Non-locality tests and quantum communication protocols using hybrid entanglement of light

Adrien Cavaillès

SORBONNE UNIVERSITÉ
CRÉATEURS DE FUTURS DEPUIS 1257

Laboratoire Kastler Brossel
Physique quantique et applications

THÈSE DE DOCTORAT DE SORBONNE UNIVERSITÉ

Spécialité : Physique

École doctorale $n°564$: Physique en Île-de-France

réalisée

au Laboratoire Kastler Brossel

sous la direction de Julien Laurat

présentée par

Adrien Cavaillès

pour obtenir le grade de :

DOCTEUR DE SORBONNE UNIVERSITÉ

Sujet de la thèse :

Tests de non-localité et protocoles de communication quantique utilisant l'intrication hybride optique

soutenue le 14 février 2019

devant le jury composé de :

M.	Marco BELLINI	Rapporteur
M.	Jean-François ROCH	Rapporteur
Mme	Eleni DIAMANTI	Examinatrice
M.	Radim FILIP	Examinateur
Mme	Agnès MAITRE	Examinatrice
M.	Julien LAURAT	Directeur de thèse

Contents

Introduction

Quantum superpositions and non-locality

The theory of quantum mechanics has been one of the most successful in the history of physics and is at the origin of numerous discoveries, including the Laser, magnetic resonance imaging (MRI) and the transistor. It retains however, one hundred years after its development, an element of mystery for the general public because it introduces a number of laws that are counter-intuitive. One consequence of these laws, now widespread in popular culture, is the "Schrödinger's cat" thought experiment [1]. Its principle is to imagine the effect of transposing the phenomenon of *quantum superposition* to the macroscopic world. Quantum mechanics posits that if a system, for example a particle, can be in two different *states*, $|0\rangle$ and $|1\rangle$, nothing forbids the existence of a state $|\psi\rangle$, called a superposition and formalized as the linear combination $|\psi\rangle \propto |0\rangle + |1\rangle$, that is intermediate between the two. In the case where the two states correspond to two possible positions for the particle, the superposition state is said to be *delocalized* and the phenomenon is called *entanglement*. A delocalized particle can only be described as being at two locations at the same time. Imagining quantum superpositions at our scale leads to absurd results, as it is in particular impossible to encounter a cat both dead and alive simultaneously.

Central to the discussion is what is meant here by "simultaneously". If one were to measure the position of a delocalized particle, one would find either one or the other location with some probability. It is therefore tempting to suppose that the superposition state describes the situation where the particle is indeed either at one position or at the other, but that its actual position is simply unknown to the scientist; that perhaps other, possibly inaccessible, factors have influenced the system to lead it into a final *set* location. This approach was followed by Einstein, Podolsky and Rosen, who proposed in 1935 [2] that quantum theory may be incomplete and that introducing independent local factors, called *hidden variables*, should explain all experimental observations. We now know that this is not the case. As was shown by Bell in 1964 [3], it is possible to devise experiments the result of which can rule out any *local* description for an entangled state. Such experiments, called *Bell non-locality tests*, have been realized under increasingly stringent constraints by Freedman *et al.* in 1972 [4], Aspect *et al.* in 1982 [5], and, as recently as in 2015, in three separate *loophole-free* experiments [6, 7, 8] in which almost no assumptions on the systems used were made. The results of these experiments are unequivocal: it is possible to realize systems, called *entangled* or *non-local*, that cannot be described as the sum of their parts but that have to be considered as a whole, no matter how distant those subsystems may be.

Distributing quantum information

While it is remarkable that there is an experimental way to prove non-locality, perhaps even more surprising is that it finds a wide range of applications. In fact, the idea of harnessing the potential of entanglement, along with that of quantum superpositions is central to the rapidly-growing research field of *quantum information* [9]. The field can be broadly divided into two main areas: *quantum computation* and *quantum communication*. The first one aims to use quantum features to obtain a computational advantage over classical systems. Quantum computing introduces a method for storing information different from that of classical computers. Instead of using bits "0 or 1" as building blocks for operations, it uses instead quantum superpositions. In the two-dimensional case they are called qu-bits and can be expressed as "0 *and* 1", or:

$$c_0 |0\rangle + c_1 |1\rangle . \tag{1}$$

The use of qu-bits instead of classical bits increases the range of possibilities for computation and allows to perform some specific tasks much more efficiently. Two famous examples are Shor's algorithm [10] which enables quick integer factorization and Grover's algorithm [11] for data exploration. The consequences of the *quantum advantage* are most striking in the case of Shor's algorithm. The RSA cryptosystem [12], widely used to secure communications, is based on the assumption that factorizing integers is a task that becomes exponentially hard as the size of the integer increases. As it solves the problem in polynomial time, Shor's algorithm would effectively render RSA encryption useless.

The field of quantum communications, which is the backdrop to this thesis, provides thankfully an alternative: *quantum cryptography* protocols that guarantee unconditionally secure communications. Since its first protocol, BB84, was introduced in 1984 by Bennet and Brassard [13], great progress has been made and quantum cryptography is now mature and commercially available. These protocols solve the issue of secure transmission of classical information. A more general aim of quantum communication is however the distribution of *quantum* information [14]. The problem is fundamentally more challenging because quantum information can only be stored and transmitted using quantum systems. This introduces several difficulties. First, it is challenging for a system to keep its quantum features for long durations or when transported over long distances. The sensibility depends on the system or the feature considered but as a general rule, a quantum system subjected to 50% of transmission loss, or attenuation, will lose its capability to present a quantum advantage. If one were for example to use light as a carrier for quantum information and send it using the best optical fibers currently available [15] (presenting losses of 0.14 $\mathrm{dB} \cdot \mathrm{km}^{-1}$), direct propagation of quantum information would be limited to 20 km. The second difficulty comes from what is called the *no-cloning theorem* [9]. This theorem states that it is impossible to create perfect copies of an unknown quantum state. As classical error-correction codes are based on redundancy, it is necessary to find adaptations in order to implement their quantum equivalent.

The solution to these two issues is to combine classical-information channels with quantum entanglement in a protocol called *quantum teleportation* [16, 17]. This protocol, instead of directly transmitting information, creates a quantum link between two parties via entanglement. As we have seen, entanglement between two modes leads to correlations between measurements performed on each mode. These correlations are used, along with a classical channel, to project quantum information present at one mode of entanglement onto the other mode. The process respects the non-cloning theorem because the initial quantum state is de-

stroyed as a result. Its advantage comes from the fact that entanglement can be propagated over long distances and still be used for quantum teleportation. The first demonstration of quantum teleportation was done by Bouwmeester et al. in 1997 [18] and since then it has been realized over increasing distances, most recently over more than 1400 km from ground to satellite [19].

Quantum teleportation opens the possibility of realizing *quantum networks*, where distant parties could share quantum information. As outlined by Kimble in his 2008 paper *The quantum internet* [20], its realization over a large scale with various actors interacting using different systems presents many challenges. This thesis enters in this general context. Through combining quantum resources of different nature in a hybrid approach, our research is aimed at studying quantum communication between parties using dissimilar systems.

Optical hybrid quantum information

This thesis work is focused on the use of light for the transfer of quantum information. Light is the system of choice for quantum communication because it presents limited interaction with external elements, serves as mediator between diverse quantum platforms and can benefit from a mature infrastructure that includes fibered networks and satellite links.

There are two complementary strategies for optical quantum information, called the continuous-variable (CV) and discrete-variable (DV) approaches, respectively linked to light's wave-like or particle-like features. In the context of qubits, these two approaches lead to different kinds of encoding for quantum information. In the discrete-variable encoding, we consider states involving single-photons and living in a space of finite dimension [21]. One example is the superposition $|\psi\rangle = c_0 |0\rangle + c_1 |1\rangle$, where $|0\rangle$ is vacuum and $|1\rangle$ is a single-photon. The continuous-variable approach focuses on encoding information using the quadratures (amplitude and phase) of a light field [22]. An example of qubit using continuous-variable encoding is the superposition of classical (coherent) light fields $|\alpha\rangle$ in opposite phases. Being a superposition of classical states, this type of qubit is sometimes called *optical Schrödinger cat state* and is written:

$$|\psi\rangle = c_+ |\alpha\rangle + c_- |-\alpha\rangle . \tag{2}$$

Although the two strategies have developed in parallel, there has been a growing drive in recent years to combine the two in the *optical hybrid approach* to quantum information [23, 24]. This hybrid approach has led to a number of innovative experiments jointly exploiting the benefits of DV and CV systems. Examples include the proposal for the teleportation of CV states using DV resources [25] and the teleportation of DV qubits using a CV method demonstrated by Takeda *et al.* in 2013 [26]. We have followed this direction as well in our group, notably with the implementation of a CV entanglement witness for DV entanglement [27] and, in parallel to its demonstration by Jeong *et al.* [28], the realization of hybrid CV-DV entanglement in 2014 [29].

Placed in this context, this thesis focuses on two main objectives: the realization of non-locality tests with hybrid entanglement and the implementation of protocols for the transmission of quantum information between discrete- and continuous-variable encodings.

Context and outline of the thesis

I joined the group of Julien as an intern in January 2015 and started my PhD in September of that year. Three PhD students in particular had preceded my arrival, Olivier Morin, Kun Huang and Hanna Le Jeannic with whom I worked during my first two years at the laboratoire Kastler Brossel (LKB). The two optical parametric oscillators (OPO) used as sources of CV and DV quantum states had been installed and calibrated by Olivier [30] and hybrid entanglement had been realized through the combined work of Olivier, Kun and Hanna [30, 31, 32]. Since its demonstration, many improvements had been realized on the experiment, and I joined in the -already well-underway- work of characterizing high-efficiency superconducting nanowire single-photon detectors (SNSPDs) obtained through a partnership with NIST and JPL. These highly-efficient detectors opened the possibility of implementing new experiments based on hybrid entanglement. The objective of my thesis was therefore to look for new protocols and pursue their implementation.

The first protocols we considered were non-locality tests. I realized a theoretical study aiming at adapting the Clauser-Horne-Shimony-Holt inequality to hybrid entanglement through a collaboration with Andreas Ketterer [33] from the group of Perola Millman and Thomas Coudreau and from discussions with Radim Filip. From there, we next considered the implementation of a Einstein-Podolsky-Rosen Steering test in collaboration with Eleni Diamanti and Damian Markham from LIP6. My work was to first adapt the Semi-Definite-Programming framework to the search of steering inequalities using hybrid entanglement. Along with Hanna and Jérémy Raskop, who was an intern at the time, we then implemented the protocol. From the measurements obtained, I performed extensive data analysis and simulations to evaluate the tomographic uncertainties associated to the protocol. In parallel to the demonstration of steering, we realized as well the protocol for remote state preparation as was first reported in [32].

In 2017, I was joined by PhD student Tom Darras and postdoctoral fellow Giovanni Guccione and together we worked on the designing and realization of hybrid quantum teleportation. This entailed significant alterations to the setup, requiring notably the introduction of a 15 m free-space delay line and a reorganization of the light paths. The setup is close to fully functional and we have already performed some data acquisition. Finally, we worked on the installation of a new cooling system for our detectors, a cryo-cooler used to reach temperatures of 1.5 K.

The present manuscript is organized as follows:

- **Part I** introduces the theoretical and experimental resources used during the course of this thesis. In Chapter 1, the theoretical concepts for state creation, characterization and measurement are presented. The second chapter introduces the functioning of optical parametric oscillators and illustrates their use in protocols for the generation of DV and CV non-Gaussian states. Finally, in Chapter 3, SNSPDs are introduced and I report on the quantum efficiency measurements performed as well as on the cooling systems used to bring them into the superconducting regime.

- **Part II** introduces hybrid entanglement of light and the non-locality tests considered and implemented. In Chapter 4, the protocol for the generation of hybrid entanglement is presented and we report on the experimental remote state preparation of arbitrary CV-encoded qubits. In Chapter 5, we start by introducing the results of the theoretical

study on Bell non-locality tests with hybrid entanglement. We then report on the first demonstration of quantum steering using hybrid entanglement.

- **Part III** is devoted to the realization of hybrid quantum teleportation. Chapter 6 introduces the concept of quantum teleportation and entanglement swapping and provides a detailed study of the difference between encoding used for quantum teleportation. It also presents our implementation for a Bell measurement using jointly photon subtraction and homodyne detection and reports on the expected quality of the protocol. Chapter 7 concludes the manuscript by detailing the setup used, including the optical delay line which is presented in details. Finally, it provides preliminary results for entanglement swapping.

List of publications

- *Demonstration of Einstein-Podolsky-Rosen Steering Using Hybrid Continuous- and Discrete-Variable Entanglement of Light.*
  A. Cavaillès, H. Le Jeannic, J. Raskop, G. Guccione, D. Markham, E. Diamanti, V.B. Verma, S.W. Nam and J. Laurat.
  Physical Review Letters **121**, 170403 (2018).

- *Remote preparation of continuous-variable qubits using loss-tolerant hybrid entanglement of light.*
  H. Le Jeannic, A. Cavaillès, J. Raskop, K. Huang and J. Laurat.
  Optica **5**, 001012 (2018).

- *Slowing Quantum Decoherence by Squeezing in Phase Space.*
  H. Le Jeannic, A. Cavaillès, K. Huang, R. Filip and J. Laurat.
  Physical Review Letters **120**, 073603 (2018).

- *High-efficiency WSi superconducting nanowire single-photon detectors for quantum state engineering in the near infrared.*
  H. Le Jeannic, V. Verma, A. Cavaillès, F. Marsili, M.D. Shaw, K. Huang, O. Morin, S.W. Nam and J. Laurat.
  Optics Letters, vol. **41**, pp. 5341-5344 (2016).

Part I

Resources for non-Gaussian states engineering

Chapter 1

Tools and formalism

This chapter aims to introduce the theoretical tools necessary to the understanding of this thesis. As such, it is far from a complete and rigorous introduction to quantum optics as was developed in many textbooks. It will serve however as an introduction to the discrete- and continuous-variable approaches to quantum optics in the context of state description and characterization. We first give some of the results of field quantization and introduce the density matrix and Wigner function formalisms. We then consider the problem of quantum measurements, and introduce usual states and operators in quantum optics. We end the chapter by presenting experimental methods for quantum state characterization.

Contents

1 The quantum description of light

The physical description of light was considered settled in the second part of the 19th century. Following a wave-like formalism for the electromagnetic field, it is at that time that the famous Maxwell's equations laid out the rules governing the interaction between charged particles and fields. This classical approach indeed provided a successful model for a wide range of experiments, with only a handful of exceptions. It is one of those exceptions however –the spectrum of blackbody radiation– that was key to the development of quantum mechanics in the beginning of the 20th century. In 1901, Planck proposed a model that accurately predicted the experimental measurements by limiting the accessible energy of the field to a discrete range of values. Einstein later interpreted this model as a particle-like description of light where the electromagnetic field is carried by photons of a fixed energy $E = h\nu$, with ν the field frequency and $h = 6.62 \cdot 10^{-34}\text{J} \cdot \text{s}$ the Planck constant.

The particle and wave descriptions were therefore seen to be appropriate in different contexts, a property called wave-particle duality. A compromise between the two approaches can be made by quantizing the electromagnetic field, starting from Maxwell's equations. Rather than rigorously derive field quantization as was done elsewhere (see for example [34, 35]), we will only review some of the results relevant to this thesis and then present two methods for quantum optical state representation.

1.1 Field quantization and modes

1.1.1 The discrete-variable approach

The quantum description of light associates to the electric field an operator $\hat{\mathbf{E}}$. This operator has to be measurable, therefore hermitian, and should be a solution of Maxwell's equations. These requirements are met classically for the particular basis of plane waves of frequency ω and wave vector $\mathbf{k}$. The quantum formalism introduces the creation $\hat{a}$ and annihilation $\hat{a}^\dagger$ operators in order to express the electric field as:

$$\hat{\mathbf{E}}(\mathbf{r}, t) = \mathbf{E}_0(\hat{a}e^{-i(\omega t - \mathbf{k}\cdot\mathbf{r})} + \hat{a}^\dagger e^{i(\omega t - \mathbf{k}\cdot\mathbf{r})}). \tag{1.1}$$

This mode of the electromagnetic field is defined on an Hilbert space $\mathcal{H}$. The operators $\hat{a}$ and $\hat{a}^\dagger$ follow the boson commutation rule $[\hat{a}, \hat{a}^\dagger] = 1$ and serve to define the *photon number operator* $\hat{N} = \hat{a}^\dagger\hat{a}$. This operator has a discrete set of eigenvalues written $|n\rangle$, with n a positive integer, that follow:

$$\hat{N}\,|n\rangle = n\,|n\rangle\,. \tag{1.2}$$

These eigenvectors are called the Fock states and describe the electromagnetic field populated by n photons. The application of the creation (respectively annihilation) operator to a Fock state increases (respectively decreases) by one its population:

$$\begin{aligned} \hat{a}\,|n\rangle &= \sqrt{n}\,|n-1\rangle \\ \hat{a}^\dagger\,|n\rangle &= \sqrt{n+1}\,|n+1\rangle\,. \end{aligned} \tag{1.3}$$

The Fock states form a complete basis for the Hilbert space H and as such any pure quantum state $|\psi\rangle$ spanning H can be written as

$$|\psi\rangle = \sum_n c_n\,|n\rangle\,. \tag{1.4}$$

The Hamiltonian associated to the electromagnetic field is the one of an harmonic oscillator and can be written as

$$\hat{H} = \hbar\omega\Big(\hat{N} + \frac{1}{2}\Big). \tag{1.5}$$

We recover from this expression the quantization of the energy of the electromagnetic field. When populated by n photons, the field has an energy

$$E(n) = \hbar\omega\Big(n + \frac{1}{2}\Big). \tag{1.6}$$

The use of the Fock basis is therefore a discrete approach. We can, as in equation (1.4), write a quantum state as a superposition of Fock states. It is therefore considered both in terms of the number of photons it contains and of its energy that can be computed from (1.6). Expressing a quantum state in these terms is called the discrete variable (DV) approach.

1.1.2 The continuous-variable approach

The electric field, being a wave, can also be described in terms of its amplitude and phase. In classical optics, one would accordingly use the Fresnel representation to express the field in terms of its real and imaginary components. There is an equivalent representation in quantum optics, called *phase space representation*, that is found by introducing the quadrature operators $\hat{x}$ and $\hat{p}$ defined as:

$$\begin{aligned} \hat{x} &= \sigma_0(\hat{a} + \hat{a}^\dagger) \\ \hat{p} &= -i\sigma_0(\hat{a} - \hat{a}^\dagger). \end{aligned} \tag{1.7}$$

The use of the term σ_0 in these definitions solves a normalization issue. There are many conventions for the expression of $\hat{x}$ and $\hat{p}$ that depend on the textbook considered (see [30] for a thorough account on this). Here we define the operators in terms of σ_0, which is equal to the standard deviation of vacuum fluctuations defined as

$$\langle 0|\, \hat{x}^2\, |0\rangle = \sigma_0^2. \tag{1.8}$$

Using the quadrature operators, we can rewrite expression (1.1) to:

$$\hat{\mathbf{E}}(\mathbf{r}, t) = \frac{\mathbf{E}_0}{\sigma_0}(\hat{x}\cos(\omega t - \mathbf{k}\cdot\mathbf{r}) + \hat{p}\sin(\omega t - \mathbf{k}\cdot\mathbf{r})). \tag{1.9}$$

The quadratures operators are equivalent to the position and momentum operators of an harmonic oscillator. From the boson commutation rule of the creation and annihilation operators, we see that $\hat{x}$ and $\hat{p}$ do not commute:

$$[\hat{x}, \hat{p}] = i2\sigma_0^2. \tag{1.10}$$

As conjugate observables, they follow the Heisenberg inequality:

$$\Delta x \Delta p \geq \sigma_0^2. \tag{1.11}$$

As a consequence, one cannot precisely measure both quadratures simultaneously. There exists a fundamental quantum noise, even for vacuum. Combining $\hat{x}$ and $\hat{p}$ in a single notation, we call *field quadrature operator at phase* θ the operator:

$$\hat{x}_\theta \hat{=} \cos(\theta)\hat{x} + \sin(\theta)\hat{p}. \tag{1.12}$$

The quadrature operators have a continuous set of orthonormal eigenvalues, written $|x, \theta\rangle$, that verify

$$\hat{x}_\theta |x, \theta\rangle = x |x, \theta\rangle . \tag{1.13}$$

They also respect the completeness relation

$$\int_{\mathbb{R}} |x, \theta\rangle \langle x, \theta| \, dx = \hat{\mathbb{1}}. \tag{1.14}$$

A quantum state can be described in terms of its projection on orthogonal quadratures, for example $|x\rangle$ and $|p\rangle$ to obtain the wave-function in the phase space:

$$\psi(x) = \langle x|\psi\rangle \qquad \psi(p) = \langle p|\psi\rangle . \tag{1.15}$$

The wave-function of a Fock state can be expressed as:

$$\langle n|x_\theta\rangle = e^{in\theta} \frac{1}{(\sqrt{2\pi}\sigma_0 2^n n!\,)^{1/2}} H_n\Big(\frac{x}{\sigma_0\sqrt{2}}\Big) e^{-(x/\sigma_0\sqrt{2})^2/2}, \tag{1.16}$$

where H_n is the n-th Hermite polynomial [36]. The wave-functions are directly linked to the probability distributions of each quadrature $P(x)$ and $P(y)$, called the *marginal distributions*. At a given phase they are defined to be

$$P(x_\theta) = |\psi(x_\theta)|^2. \tag{1.17}$$

By combining the marginal distributions of a quantum state, we can recover all of its features. The description of a quantum state in terms of its quadratures is called the *continuous variable* (CV) approach. We can use it however to recover some of the discrete features of the field, for example its population:

$$\hat{N} = \frac{1}{4\sigma_0^2}(\hat{x}^2 + \hat{p}^2 - 2\sigma_0^2). \tag{1.18}$$

1.1.3 Combining modes

The quantized expressions of equations (1.1) and (1.9) are valid for a single degree of freedom of a quantum state. In the general case however, light can have several degrees of freedom, be it polarization, frequency components or spatial modes. In this case, the total Hilbert space considered is the tensor product of each mode's Hilbert space:

$$H = H_1 \otimes H_2 \otimes H_3 \otimes \cdots. \tag{1.19}$$

The multi-modal nature of the field would in this case lead to it being expressed in the form

$$\hat{\mathbf{E}}(\mathbf{r}, t) = \sum_k \mathbf{E}_{0,k} \hat{a}_k e^{-i(\omega t - \mathbf{k}\cdot\mathbf{r})} + h.c., \tag{1.20}$$

where $h.c.$ denotes the hermitian conjugate. As the modes k live in different Hilbert spaces, they commute:

$$[\hat{a}_k, \hat{a}_{k'}^\dagger] = \delta(k, k') \qquad \forall k, k'. \tag{1.21}$$

The notation of equation (1.20) suggests a discrete sum, which is the case for different polarization or spatial modes for example, but depending on the nature of the modes considered it can also be a sum over a continuous set. One important example for this thesis is the case

of temporal modes. We can define creation operators at a specific time t. Written $\hat{a}^\dagger(t)$, this operator applied to vacuum will lead to the state "single photon at time t". Equivalently, we can also define $\hat{x}(t)$, *i.e.* the quadrature operator at time t. From this we can create a temporal mode f defined as:

$$\hat{x}_f = \int_{-\infty}^{\infty} f(t)\hat{x}(t)dt. \tag{1.22}$$

The function $f(t)$ is square-integrable such that $\int_{-\infty}^{+\infty}|f(t)|^2dt = 1$. The time operators respect the commutation relations:

$$[\hat{a}(t), \hat{a}^\dagger(t')] = \delta(t-t') \quad \text{and} \quad [\hat{x}(t), \hat{p}(t')] = i2\sigma_0^2\delta(t-t'). \tag{1.23}$$

1.2 State representation

Any pure quantum state can be defined by a state vector. One can however encounter statistical mixtures, *i.e.* classical superpositions that cannot be accurately described with a wave-function. The solution is to use the so-called *density matrix* [37] that can describe all possible pure quantum states and mixtures using a single formalism. The density matrix is fundamentally a DV representation and there is an equivalent in the CV approach: the *Wigner function* [38]. We now present both formalisms and some of their properties.

1.2.1 Density matrix

The quantum state of a system can always be characterized by a state vector. In a practical context however, an experimentalist will most often only have access to part of the total system. Their lack of knowledge can then be modelled by writing the system they have access to as a statistical mixture of pure states. This means that the observer measures a number of pure quantum states $|\psi_k\rangle$ each with probability p_k, without knowing the reason for these observed probabilities. The density matrix is used to combine the formalism of pure states and the possibility of seeing classical superpositions. In the case of a pure state, it is defined as

$$\hat{\rho} = |\psi\rangle\langle\psi|. \tag{1.24}$$

In the most general case, we can write any measured quantum state as

$$\hat{\rho} = \sum_k p_k |\psi_k\rangle\langle\psi_k|. \tag{1.25}$$

It can be rewritten on the Fock basis, on which it can present both diagonal terms, called *populations*, and cross terms of the form $|n\rangle\langle m|$ called *coherences*:

$$\hat{\rho} = \sum_{n,m} c_{n,m} |n\rangle\langle m|. \tag{1.26}$$

The populations give directly the probability of being in a given pure state. The coherences on the other hand are the terms that reflect the presence of quantum superpositions.

The density matrix has several properties:

- From equation (1.25), as the sum of probabilities is equal to one, we have

$$\mathrm{Tr}(\hat{\rho}) = 1. \tag{1.27}$$

- Equation (1.25) also ensures that the density matrix is hermitian:

$$\hat{\rho}^\dagger = \hat{\rho}. \tag{1.28}$$

- The density matrix is diagonalizable and positive semi-definite, *i.e.* it only possesses non-negative eigenvalues.
- To compute the expectation value of any operator $\hat{A}$, we take the trace of their product:

$$\langle \hat{A} \rangle = \mathrm{Tr}(\hat{A}\hat{\rho}). \tag{1.29}$$

The density matrix is a convenient tool for state characterization as it allows to compute several key parameters. Some we will consistently use are:

- The state purity. This parameter allows to quantify the distance between the measured state and a pure state. It is defined as:

$$\mathcal{P} = \mathrm{Tr}(\hat{\rho}^2) = \sum p_k^2. \tag{1.30}$$

- The fidelity between two states. In the case where an experiment's goal is the generation of a specific target state $\hat{\rho}_t$, the fidelity is used to quantify the distance between the measured $\hat{\rho}$ and target density matrix. It is defined in the case of pure states as:

$$\mathcal{F}(\hat{\rho}, \hat{\rho}_t) = \mathrm{Tr}(\hat{\rho}\hat{\rho}_t) = |\langle \psi | \psi_t \rangle|^2. \tag{1.31}$$

  In the general case, it is expressed as [39]:

$$\mathcal{F}(\hat{\rho}, \hat{\rho}_t) = \left(\mathrm{Tr}\left(\sqrt{\sqrt{\hat{\rho}}\hat{\rho}_t\sqrt{\hat{\rho}}} \right) \right)^2 \tag{1.32}$$

Because of its structure, the density matrix is mostly a DV tool for state representation and characterization. From equation (1.29) we can see that it can also be used to compute CV features. One example is the marginal distribution of a given state:

$$P(x_\theta) = \langle x, \theta | \, \hat{\rho} \, | x, \theta \rangle \, . \tag{1.33}$$

1.2.2 The Wigner function

The phase space wave-functions introduced in equation (1.15) can be jointly used to characterize a quantum state. From them one can indeed compute the marginal distributions of a state, *i.e.* the probability of observing a given quadrature result. Much like the density matrix is a single DV tool containing all the information of a quantum state, the Wigner function was introduced as a single mathematical object from which all the marginal distributions of the field can be recovered. Although less frequently used than the density matrix, the Wigner function is a more visual representation of a quantum state. It depicts the effect of imperfections such as loss or phase noise in a visual way and the formalism it introduces simplifies their computation.

The Wigner function, written $W(x, p)$, can be defined analogously to a classical phase space-distribution. It is a function of x and p that cannot be measured directly but its integration over a single quadrature leads to the marginal distribution on its conjugate:

$$P(x_\theta) = \int W(x_\theta, p_\theta) dp_\theta. \tag{1.34}$$

Unlike a classical probability distribution, it can present negative values. This feature is fundamentally quantum and leads one to see the Wigner function as a *quasi-probability* distribution. From (1.34), we see that, as for the density matrix, all the information contained in a state is accessible from the Wigner function. Both tools are therefore equivalent, and are related by the equation:

$$W_{\hat{\rho}}(x,p) = \frac{1}{2\pi\sigma_0^2}\int e^{iyp/\sigma_0^2}\,\langle x-y|\,\hat{\rho}\,|x+y\rangle\,dy. \tag{1.35}$$

The Wigner function is linear with $\hat{\rho}$. We can therefore reconstruct it using the Fock space decomposition of a state as in equation (1.26), using

$$W_{\hat{\rho}}(x,p) = \sum_{n,m} c_{n,m} W_{|n\rangle\langle m|}(x,p) \tag{1.36}$$

and

$$W_{|n\rangle\langle m|}(x,p) = \frac{(-1)^m}{2\pi\sigma_0^2}\sqrt{\frac{m!}{n!}}\left(\tfrac{x-ip}{\sigma_0}\right)^{n-m} e^{-(x^2+p^2)/2\sigma_0^2} L_m^{n-m}\left(\tfrac{x^2+p^2}{\sigma_0^2}\right), \text{ if } n \geq m. \tag{1.37}$$

In the case where $n < m$, we have

$$W_{|n\rangle\langle m|}(x,p) = W_{|m\rangle\langle n|}(x,-p). \tag{1.38}$$

Some of its properties will be useful for this thesis:

- The Wigner function of hermitian operators is real over the whole phase space.
- It is normalized to one after integration over x and p:

$$\iint_{\mathbb{R}^2} W(x,p)dxdp = 1. \tag{1.39}$$

- The expectation value of an operator $\hat{A}$ is found by integrating the product between the Wigner functions of the state and of $\hat{A}$. This is a special case of the *overlap formula*.

$$\langle\hat{A}\rangle = 4\pi\sigma_0^2 \iint_{\mathbb{R}^2} W_{\hat{A}}(x,p)W_{\hat{\rho}}(x,p)dxdp. \tag{1.40}$$

- In the case where at least one of two states $\hat{\rho}_t$ and ρ is pure, the fidelity between the two can be computed as:

$$\mathcal{F}(\hat{\rho},\hat{\rho}_t) = \mathrm{Tr}(\hat{\rho}\hat{\rho}_t) = 4\pi\sigma_0^2 \iint_{\mathbb{R}^2} dxdp W_{\hat{\rho}_t}(x,p)W_{\hat{\rho}}(x,p). \tag{1.41}$$

- In some cases, it is useful to express the Wigner function as the expectation value of the displaced parity operator $\hat{\Pi}(\alpha)$. This operator is defined as the product of displacement operators $\hat{D}(\alpha)$ (see section 3) with the parity operator $\hat{P} = e^{i\pi\hat{N}}$:

$$\hat{D}_P(\alpha) = \hat{D}(\alpha)\hat{P}\hat{D}(-\alpha). \tag{1.42}$$

  Using the shorthand $W_{\hat{\rho}}(\alpha) = W_{\hat{\rho}}(\mathrm{Re}(\alpha),\mathrm{Im}(\alpha))$, we indeed have [40]:

$$W_{\hat{\rho}}(\alpha) = \frac{1}{2\pi\sigma_0^2}\langle\hat{\rho}\hat{D}_P(\alpha)\rangle. \tag{1.43}$$

Having introduced the formalism for quantum states, we now consider the problem of quantum measurements.

2 Quantum measurements

It is one of the oddities of quantum mechanics that the theory governing the evolution of a quantum system cannot be simply used to describe a measurement apparatus. Indeed, the usual approach is to define quantum measurements in a postulate separate from the rest of the theory. The difficulty lies in the role of measurements: they provide a link between a microscopic quantum experiment and a macroscopic classical observer. A fully quantum description of the process breaks down along the way. Although there is still ongoing debate about the physical meaning of quantum measurements, we will simply use the efficient formalism of *generalized quantum measurements* and *positive operator valued measures* (POVM) operationally. We then apply the formalism to the particular examples of single-photon detection and quadrature measurements.

2.1 Generalized quantum measurements and POVMs

In its simplest form, a measurement is an operation on a quantum state $|\psi\rangle$ that leads to a result directly linked to a physical quantity. The formalism corresponding to this situation is that of *observables*: operators $\hat{A}$ that present a number of eigenvalues λ corresponding to possible measurement results and associated orthogonal eigenvectors $|\psi_\lambda\rangle$ on which the quantum state is projected after the measurement. Observables are projectors and can be expressed as

$$\hat{A} = \sum_\lambda \lambda \left|\psi_\lambda\right\rangle \left\langle\psi_\lambda\right| . \tag{1.44}$$

This model for measurements notably implies that right after the measurement has been performed, a new measurement will lead to the same result. This formalism however is inappropriate for many practical experiments. Let us take for example the case of the detection of a photon on a screen. After detection, its position has been determined but cannot be measured again, the photon being destroyed. This is an example of a *destructive* measurement, a property shared by most of the measurements we consider in this thesis. There are also other experimental situations where the formalism isn't appropriate, for instance when one doesn't directly measure a physical quantity but aims to distinguish between different quantum states (see [9] for details).

Generalized measurements address these problems by approaching the concept from the viewpoint of the results rather than the physical quantity characterized. A general measurement is defined as a set of operators $\{\hat{M}_m\}$, where m is a measurement outcome, that do not have to be projectors, orthogonal, or even hermitian. They only satisfy:

$$\sum_m \hat{M}_m^\dagger \hat{M}_m = \hat{\mathbb{1}}, \tag{1.45}$$

and are such that the probability of observing the result m is equal to

$$p(m) = \mathrm{Tr}(\hat{\rho}\hat{M}_m^\dagger \hat{M}_m). \tag{1.46}$$

Generalized measurements provide an expression for the quantum state obtained after a measurement. As we have said however, in all of our experiments we are either in the case where the measurements are destructive or where we don't worry about the state after they have been performed. In these cases, it is convenient to completely ignore the effect of the

measurement on the input state and to use the formalism of *positive operator valued measures* (POVM). A POVM $\{\hat{\Pi}_m\}$ is defined from a general measurement as

$$\hat{\Pi}_m = \hat{M}_m^\dagger \hat{M}_m \qquad \forall m. \tag{1.47}$$

POVMs are hermitian but not necessarily projectors or normalized. When the two latter properties are true, they are identical to observables. From equation (1.45), we have:

$$\sum_m \hat{\Pi}_m = \hat{\mathbb{1}}. \tag{1.48}$$

And we can compute their expectation value using

$$p(m) = \mathrm{Tr}(\hat{\rho}\hat{\Pi}_m). \tag{1.49}$$

Notably, POVMs being hermitian, their Wigner function is real and can be used to visually access some of their properties. We have as well the equation:

$$p(m) = 4\pi\sigma_0^2 \iint_{\mathbb{R}^2} W_{\hat{\Pi}_m}(x,p) W_{\hat{\rho}}(x,p) dx dp. \tag{1.50}$$

Let us consider two examples of POVMs to illustrate their use.

POVM of an on-off detector. The on-off detector model is well suited to describe most current single-photon detectors and in particular the superconducting nanowire single-photon detectors (SNSPD) used in our experiment (see chapter 3). The detection of one or more photons leads to a "click", while no click corresponds to the measurement of vacuum. The corresponding POVM is therefore the set of two operators:

$$\hat{\Pi}_{\text{no click}} = |0\rangle\langle 0| \qquad \text{and} \qquad \hat{\Pi}_{\text{click}} = \hat{\mathbb{1}} - |0\rangle\langle 0|. \tag{1.51}$$

This expression is valid in the case of perfect detectors without losses. The general case can be found by introducing a model for losses such as the one of section 3.1.3 in the expression of the detection operator [30].

POVM of a quadrature measurement. As we will see in section 4, quadrature measurements can be performed using homodyne detection. The POVM of a quadrature measurement at phase θ is in this particular case the continuous set $\{\hat{\Pi}_{x,\theta}\}_x$ such that

$$\hat{\Pi}_{x,\theta} = |x,\theta\rangle\langle x,\theta| \qquad \forall x. \tag{1.52}$$

And indeed this satisfies (1.48). We can also build POVMs from linear combinations of operators. A relevant example is the case where one considers a special detector that performs quadrature measurements at phase 0 and "clicks" when it measures a quadrature x between two values x_1 and x_2. The corresponding POVM is

$$\hat{\Pi}_{\text{click}} = \int_{x_1}^{x_2} |x\rangle\langle x| dx \qquad \text{and} \qquad \hat{\Pi}_{\text{no click}} = \hat{\mathbb{1}} - \int_{x_1}^{x_2} |x\rangle\langle x| dx. \tag{1.53}$$

2.2 Conditional preparation of a quantum state

An essential use of the POVM formalism for this thesis is the effect of conditioning on the result of measurements made on one mode of a bipartite state. Let us consider a two-mode state $\hat{\rho}_{\mathrm{AB}}$ shared by two parties, Alice and Bob, and assume that we perform a measurement on Alice's mode. The measurement is modeled by the POVM $\{\hat{\Pi}_{\mathrm{A}}^{(m)}\}_m$. If Alice obtains the outcome m, then Bob's mode is projected to:

$$\hat{\rho}_{\mathrm{B}}^{(m)} = \frac{\mathrm{Tr}_{\mathrm{A}}(\hat{\Pi}_{\mathrm{A}}^{(m)}\hat{\rho}_{\mathrm{AB}})}{\mathrm{Tr}(\hat{\Pi}_{\mathrm{A}}^{(m)}\hat{\rho}_{\mathrm{AB}})}. \tag{1.54}$$

Here we used the notation Tr_{A} for the partial trace on mode A. This property can be used to conditionally prepare specific quantum states. One only needs to wait for the measurement of m to herald the presence of $\hat{\rho}_{\mathrm{B}}^{(m)}$. Such a protocol presents the disadvantage of being probabilistic. With the Wigner formalism we can also write

$$W_{\hat{\rho}_{\mathrm{B}}^{(m)}} = \frac{\int_{\mathrm{A}} W_{\hat{\Pi}_{\mathrm{A}}^{(m)}} W_{\hat{\rho}_{\mathrm{AB}}}}{\int_{\mathrm{AB}} W_{\hat{\Pi}_{\mathrm{A}}^{(m)}} W_{\hat{\rho}_{\mathrm{AB}}}}, \tag{1.55}$$

where $\int_{\mathrm{A}}$ symbolizes the partial integration on the phase space of mode A.

In this thesis we report on experiments where we condition on single or multiple on-off detections and quadrature measurements. The expression of equation (1.55) highlights an important property of conditional preparation. In order to prepare a state with a negative Wigner function, either the input two-mode state or the measurement performed needs to have a negative Wigner function. On-off detection does present negativity of the Wigner function and can be used to prepare fundamentally quantum states. On the other hand quadrature conditioning can only lead to positive Wigner functions.

3 The usual suspects in quantum optics

In this section, we present the operators and states that will be most commonly used in this thesis. We will provide some of their properties and introduce their Wigner functions. Finally, we will consider two purely quantum features: entanglement and non-Gaussianity.

3.1 Useful states and operators

We detail therein useful quantum states and associated operators.

3.1.1 Fock states

We have already introduced in section 1 the Fock states $|n\rangle$ as eigenstates of the photon number operator. As such, they have a fixed population and form a complete basis, called the *Fock basis*. Their Wigner function is given by:

$$W_{|n\rangle\langle n|}(x,p) = \frac{(-1)^n}{2\pi\sigma_0} e^{-(x^2+p^2)/2\sigma_0^2} L_n\left(\tfrac{x^2+p^2}{\sigma_0^2}\right). \tag{1.56}$$

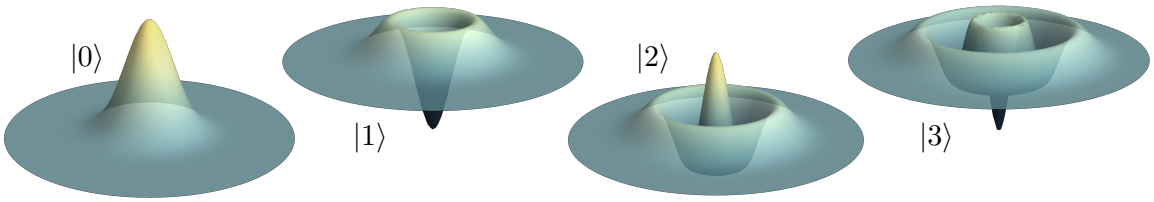

Figure 1.1: **Wigner function of the first four Fock states**. All except vacuum present negativity. In the case of odd states the maximum of negativity is at the center of phase space.

The Wigner function of the first four Fock states is plotted in Figure 1.1. We see that apart from vacuum, they all present negativity of the Wigner function. In the case of odd Fock states, the maximum negativity is at the origin of phase space. We indeed have

$$W_{|n\rangle\langle n|}(0,0) = \frac{(-1)^n}{2\pi\sigma_0}. \tag{1.57}$$

3.1.2 Coherent states and displacement operator

The coherent states are fields that, as vacuum, can be described with a classical phase distribution and provide a good approximation for what is outputted by a powerful laser (*i.e.* populated by more than a few photons). The coherent states are eigenstates of the annihilation operator.

$$\hat{a}\,|\alpha\rangle = \alpha\,|\alpha\rangle\,. \tag{1.58}$$

As such they are unaffected by photon subtraction. Their average population is

$$\langle\hat{N}\rangle = |\alpha|^2. \tag{1.59}$$

They can be defined from the displacement operator:

$$\hat{D}(\alpha) = e^{\alpha\hat{a}^\dagger - \alpha^\star\hat{a}}. \tag{1.60}$$

The displacement operator is named this way because when applied to vacuum it corresponds to a translation in phase space by the vector $(2\sigma_0\,\mathrm{Re}(\alpha), 2\sigma_0\,\mathrm{Im}(\alpha))$. All coherent states are actually displaced vacuum

$$|\alpha\rangle = \hat{D}(\alpha)\,|0\rangle\,. \tag{1.61}$$

As a result, their Wigner function is the same as that of vacuum, *i.e.* a fully symmetric Gaussian function, but translated in phase space in a direction determined by α. Two close coherent states will present overlap in their Wigner function. As the function is positive everywhere, coherent states are not orthogonal

$$|\langle\alpha|\beta\rangle|^2 = e^{-|\alpha-\beta|^2}. \tag{1.62}$$

They can be used however as a non-orthogonal overcomplete basis as they follow the completeness relation

$$\frac{1}{\pi}\int_{\mathbb{C}} |\alpha\rangle\,\langle\alpha|\,d^2\alpha = \hat{\mathbb{1}}. \tag{1.63}$$

Finally, we have the useful relation giving the decomposition of a coherent state on the Fock basis:

$$|\alpha\rangle = e^{-|\alpha|^2}\sum_{n=0}^{\infty}\frac{\alpha^n}{\sqrt{n!}}\,|n\rangle\,. \tag{1.64}$$

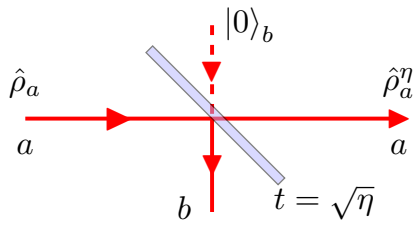

Figure 1.2: **Model for transmission losses**. The transmission channel a is coupled to an external mode b representing the environment using a beam-splitter of transmission $t = \sqrt{\eta}$.

3.1.3 Beam-splitter operator and model for transmission losses

The beam-splitter operator provides a quantum model for a beam-splitter, *i.e.* a device that couples two optical modes a and b. Its expression is

$$\hat{B}(\theta) = e^{\theta(\hat{a}^\dagger \hat{b} - \hat{a}\hat{b}^\dagger)}. \tag{1.65}$$

The reflection and transmission coefficients are defined from θ as

$$t = \cos\theta \qquad \text{and} \qquad r = \sin\theta. \tag{1.66}$$

A convenient way to model the effect of the beam-splitter is to look at how the creation operators are transformed under its application:

$$\begin{aligned} \hat{a}^\dagger &\to t\hat{a}^\dagger + r\hat{b}^\dagger \\ \hat{b}^\dagger &\to t\hat{b}^\dagger - r\hat{a}^\dagger. \end{aligned} \tag{1.67}$$

We now look at a particularly useful example: a model for transmission losses presented in figure 1.2. We start from a quantum state $\hat{\rho}_a$ propagating on a channel a. Losses occur because the state interacts in a complicated way with the environment. This interaction can however be approximated by a simple model. A beam-splitter of transmission $t = \sqrt{\eta}$ couples mode a with a single external mode b populated by vacuum. The evolution is therefore

$$\hat{\rho}_a \otimes |0\rangle\langle 0|_b \longrightarrow \hat{B}_\eta(\hat{\rho}_a \otimes |0\rangle\langle 0|_b)\hat{B}_\eta^\dagger. \tag{1.68}$$

In the case of a propagating single photon, we have

$$\hat{a}^\dagger \to \sqrt{\eta}\hat{a}^\dagger + \sqrt{1-\eta}\hat{b}^\dagger. \tag{1.69}$$

The input state $|1\rangle_a$ therefore becomes

$$|1\rangle_a \longrightarrow |1^\eta\rangle_{ab} \hat{=} \sqrt{\eta}\,|1\rangle_a|0\rangle_b + \sqrt{1-\eta}\,|0\rangle_a|1\rangle_b\,. \tag{1.70}$$

Only mode a is of interest after interaction, we therefore complete the model by tracing out mode b:

$$\begin{aligned} |1^\eta\rangle_a &= \mathrm{Tr}_b(|1^\eta\rangle\langle 1^\eta|_{ab}) \\ |1^\eta\rangle_a &= \eta\,|1\rangle\langle 1|_a + (1-\eta)\,|0\rangle\langle 0|_a\,. \end{aligned} \tag{1.71}$$

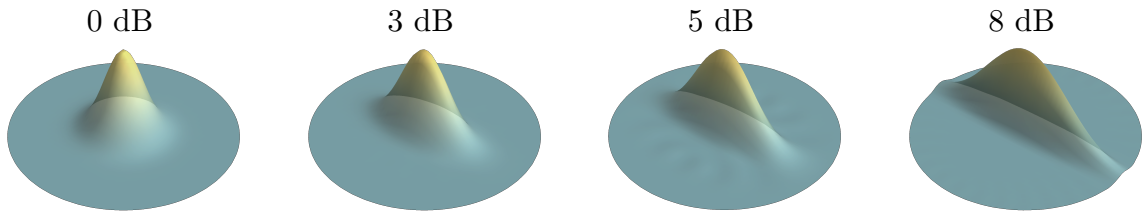

Figure 1.3: **Wigner function of squeezed vacuum states** for different squeezing factors.

3.1.4 Squeezed vacuum states

The states we considered so far present the same amount of noise fluctuations no matter the quadrature considered. In the case of vacuum, we have

$$\Delta x = \Delta p = \sigma_0. \tag{1.72}$$

Vacuum fluctuations are as low as the Heisenberg inequality allows. It is possible however to *squeeze* vacuum so that one of the quadratures will present fluctuations below the shot noise, at the expense however of the orthogonal quadrature, characterized as *anti-squeezed*. A squeezed vacuum state is characterized by its *squeezing factor* s, defined as

$$\Delta x = \sqrt{s}\sigma_0 \qquad \Delta p = \frac{1}{\sqrt{s}}\sigma_0. \tag{1.73}$$

The Wigner function of squeezed vacuum is accordingly the product of two Gaussian functions of x and p with different variances:

$$W_{\mathrm{SqVac}}(x,p) = \frac{1}{2\pi\sigma_0^2} e^{-\frac{x^2}{2s\sigma_0^2} - \frac{sp^2}{2\sigma_0^2}}. \tag{1.74}$$

We show in figure (1.3) the Wigner function of several squeezed vacuum states with different squeezing factors. In this figure and elsewhere, we typically give the squeezing amount in dB:

$$s_{\mathrm{dB}} = -10\log_{10} s. \tag{1.75}$$

We can also write squeezed vacuum on the Fock basis

$$|\mathrm{SV}\rangle = (1-\lambda^2)^{1/4} \sum_{n=0}^{\infty} \binom{2n}{n}^{1/2} \left(\frac{\lambda}{2}\right)^n |2n\rangle\,. \tag{1.76}$$

where we introduced

$$\lambda = \frac{1-s}{1+s}. \tag{1.77}$$

Squeezed vacuum is called *even* because its decomposition is only on even Fock states. The population of squeezed vacuum increases close to linearly with the squeezing factor

$$\langle \hat{N} \rangle = \frac{1}{4}\Big(s + \frac{1}{s} - 2\Big). \tag{1.78}$$

We can also write the squeezed vacuum state as the result of the application of a *single-mode squeezing operator* $\hat{S}_I(\zeta)$ on vacuum:

$$|\mathrm{SV}\rangle = \hat{S}(\zeta)\,|0\rangle\,, \tag{1.79}$$

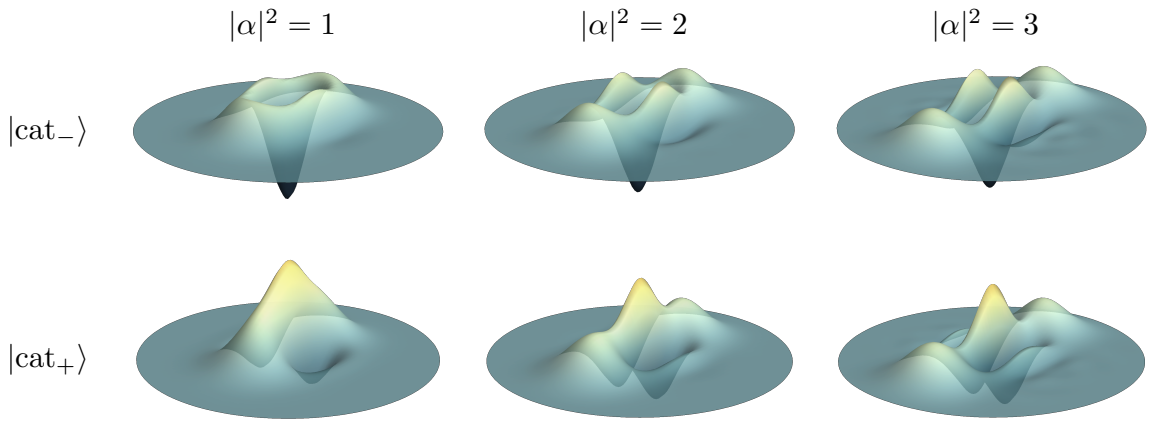

Figure 1.4: **Wigner function of odd and even cat states** of varying sizes.

where the squeezing operator is defined as

$$\hat{S}(\zeta) = e^{\frac{\zeta}{2}(\hat{a}^2 - (\hat{a}^\dagger)^2)}. \tag{1.80}$$

Squeezing by a s_{dB} amount corresponds to ζ such that

$$\zeta = \frac{\ln 10}{20} s_{\text{dB}}. \tag{1.81}$$

Two-mode squeezed vacuum. Two-mode squeezed vacuum is the state obtained when mixing two single-mode squeezed vacuum states on a balanced beam-splitter. The result is a linear combination of pairs of identically populated Fock states in two different modes:

$$|\text{TMSV}\rangle_{\text{AB}} = (1-\lambda^2)^{1/2} \sum_{n=0}^{\infty} \lambda^n |n\rangle_{\text{A}} |n\rangle_{\text{B}} . \tag{1.82}$$

This state will be key to our protocols for Fock state generation. We can define as well a two-mode squeezing operator such that

$$|\text{TMSV}\rangle_{\text{AB}} = \hat{S}_{II}(\zeta) |0\rangle_{\text{A}} |0\rangle_{\text{B}} . \tag{1.83}$$

This operator has a similar expresssion to the single-mode squeezing operator but uses creation and annihilation operators of two modes $\hat{a}, \hat{a}^\dagger$, and $\hat{b}, \hat{b}^\dagger$:

$$\hat{S}_{II}(\zeta) = e^{\frac{\zeta}{2}(\hat{a}\hat{b} - \hat{a}^\dagger \hat{b}^\dagger)}. \tag{1.84}$$

3.1.5 Optical Schrödinger cat states

The name of these states is a reference to Schrödinger's thought experiment [1] where a macroscopic protagonist –in this case, a cat– would be subjected to the laws of quantum mechanics. By entangling "its state" with that of a quantum system in superposition, one would get the absurd result of a cat dead and alive at the same time. In quantum optics, the coherent states are the closest we have to a classical system. By increasing $|\alpha|$, one indeed obtains the macroscopic field at the output of a laser. As a result, we call the superposition

of two coherent states in opposite phases an *optical Schrödinger cat state*. The reasoning is that they are a superposition of two incompatible classical states, that at the limit of $|\alpha| \gg 1$ are macroscopic. We define cat states as

$$|\text{cat}_\phi\rangle = \frac{1}{\mathcal{N}_\phi}(|\alpha\rangle + e^{i\phi}|-\alpha\rangle), \tag{1.85}$$

with the norm $\mathcal{N}_\phi$ depending on the phase of the superposition and equal to

$$\mathcal{N}_\phi = \sqrt{2(1+\cos\phi e^{-2|\alpha|^2})}. \tag{1.86}$$

In practice, this state is not macroscopic and can be realized optically only for relatively limited values of $|\alpha|$. An important feature they need to have however is a small overlap between $|\alpha\rangle$ and $|-\alpha\rangle$, which is achieved when $|\alpha| > 1$. Indeed for $|\alpha| = 1$, we have $|\langle\alpha|-\alpha\rangle|^2 \sim 2\cdot 10^{-2}$ and for $|\alpha| = 2$, we have $|\langle\alpha|-\alpha\rangle|^2 \sim 3\cdot 10^{-4}$. At smaller values of $|\alpha|$ we talk instead of *Schrödinger kittens*.

Two useful examples are the odd and even cat states, $|\text{cat}_-\rangle$ and $|\text{cat}_+\rangle$, which have the following decomposition on the Fock basis

$$\begin{aligned}
|\text{cat}_-\rangle = |\text{cat}_\pi\rangle &= \frac{2}{\mathcal{N}_-}e^{-|\alpha|^2/2}\sum_{n=0}^{\infty}\frac{\alpha^{2n+1}}{\sqrt{(2n+1)!}}|2n+1\rangle \\
|\text{cat}_+\rangle = |\text{cat}_0\rangle &= \frac{2}{\mathcal{N}_+}e^{-|\alpha|^2/2}\sum_{n=0}^{\infty}\frac{\alpha^{2n}}{\sqrt{(2n)!}}|2n\rangle\,.
\end{aligned} \tag{1.87}$$

The Wigner functions of cats of varying sizes is shown in figure 1.4. For $|\alpha|^2 > 1$ we see the two Gaussian peaks corresponding to the two coherent states. The difference to a classical superposition is evident however from the fringes observed close to the origin of phase space. These fringes are a strong evidence of non-classicality and make these states useful for quantum protocols.

3.2 (Non-)Gaussianity

As we have mentioned before, the Wigner function can only be called a quasi-probability distribution because it can present negative values (see [41] for a visual analogy of the phenomenon). Interestingly, it can be shown that this negativity is a requirement for a number of quantum protocols. In the framework of quantum computing, it is for example necessary to have states or operators whose Wigner function is negative if one wants to perform an operation that cannot be efficiently modelled classically. Another relevant example for this thesis is that of entanglement purification which is impossible without negativity of the Wigner function.

If one looks at the plots we have presented in the preceding section, one may notice that all the states without negativity of the Wigner function have a Gaussian distribution in phase space. This is in fact a general result called the *Hudson-Piquet theorem* [42]. No matter the pure state considered, its Wigner function is positive everywhere *if and only if* it is a Gaussian function. As a result we will tend to divide quantum states and operators in two categories called Gaussian and non-Gaussian depending on the existence of negative values of the Wigner function. This characterization is directly linked to the capabilities of a quantum state and, as the name of our group suggests –*"The non-Gaussian team"*–, we generally aim

for the realization of quantum states with negative values of the Wigner function.

Note that although the Hudson-Piquet theorem is true for all pure states, as soon as one considers experiments, *i.e.* mixed states, the equivalence breaks down. For example, let us consider a lossy single photon. The addition of losses means observing a mixed state between vacuum and single photon. The resulting Wigner function will be the weighted sum of the Wigner function of both states. As vacuum is Gaussian, there will come a point where no negativity of the Wigner function is observed, although the state does not follow a Gaussian distribution. The negativity remains in this case a necessary feature for some protocols so the effect of losses has to be closely monitored in experiments. In general, as soon as one observes more than 50% of losses, negativity of the Wigner function cannot be observed.

3.3 Entanglement

Another fundamentally quantum phenomenon will be of particular interest for this thesis: entanglement. As was shown for example in the expression of two-mode squeezed vacuum (1.82), it is possible to encounter states that are *inseparable*. This is in opposition to *separable* states that can be expressed in the following way:

$$\hat{\rho}_{\mathrm{AB}} = \sum_k p_k \hat{\rho}_{\mathrm{A}} \otimes \hat{\rho}_{\mathrm{B}}. \tag{1.88}$$

This equation formalizes the fact that a separable state can be defined as the combination of one or more subsystems considered independently. An inseparable state is referred to as *entangled*, which hints at the fact that it is not possible to consider its two modes separately. Entanglement and its consequences have been historically hard to accept [2], but is now experimentally proven and constitutes a key part of many protocols for quantum information and communication. One consequence of entanglement, *non-locality*, will be introduced and developed in Chapter 5 when we consider Bell and quantum steering inequalities. Another practical protocol using entanglement is quantum teleportation which will be central to chapters 6 and 7.

Here we only provide the expression of a specific quantifier of entanglement, *negativity of entanglement*. This figure of merit serves to characterize the quality of protocols where the generation of entanglement is the goal. It is defined as

$$\mathcal{N}(\hat{\rho}_{\mathrm{AB}}) = \frac{||\hat{\rho}_{\mathrm{AB}}^{T_A}|| - 1}{2}, \tag{1.89}$$

where $\hat{\rho}_{\mathrm{AB}}^{T_A}$ is the partial transpose of $\hat{\rho}_{\mathrm{AB}}$ relative to mode A and $||X||$ is the trace norm:

$$||X|| = \mathrm{Tr}(\sqrt{X^\dagger X}). \tag{1.90}$$

Entanglement negativity is a convex function that increases monotonously with entanglement. Importantly, it cannot be increased by local operations on a single mode. Even though other figures of merit exist, $\mathcal{N}$ is the one we will most consistently use, except in the cases where we go further and demonstrate steering inequality violation.

4 Quantum tomography

We have introduced so far some operators and states that we will be able to perform and create experimentally. The question remains of how to verify experimentally the quality of the created states or how to check that the desired operators have indeed been applied. The solution in our case is to perform state characterization via *quantum tomography*. The process of tomography is used in the classical world of medical imaging to obtain an image of a three-dimensional object from the measurement of its projections on different 2D planes. In Greek, $\tau o \mu \acute{o} \varsigma$ means a cut, which indeed is linked to the process of measuring different sections of an object to deduce its shape.

In the quantum optical version of tomography, the object we want to reconstruct is the Wigner function of a state and we do so by measuring its marginal distributions at different quadratures. There are two steps to this process. First, the measurement of the marginal distributions is performed using the experimental tool of *homodyne detection*. Second, from the set of quadrature measurements obtained, one has to infer the shape of the Wigner function. This inference is performed by maximizing a parameter called the *likelihood*. This parameter is a measure of the probability of getting the experimental results depending on the state measured.

In this section, we introduce first the principle of a homodyne detector and then the now-standard method used to recover the Wigner function of the state: the *Maximum-Likelihood* optimization process.

4.1 Homodyne detection

Homodyne detection is an interferential method for the measurement of quadratures. The principle is shown in figure 1.5. The state to characterize is $\hat{\rho}_s$. It interferes with a high-power field called the *local oscillator* (LO) on a balanced beam-splitter. The two output-ports of the beam-splitter are coupled to two photo-diodes, labeled 1 and 2, that record the field's power. The measurement is completed by subtracting the photo-currents of the two photo-diodes which gives a signal proportional to the quadrature of the field at the relative phase of the LO. To understand the process, we now detail the different steps using the formalism introduced in section 1.

To recover the operator corresponding to the total measurement, we first consider the expression of the annihilation operators in the two modes coupled to the photo-diodes, written $\hat{a}_1$ and $\hat{a}_2$. From the expression (1.67), we have

$$\begin{aligned} \hat{a}_1 &= \frac{1}{\sqrt{2}}(\hat{a}_{LO} + \hat{a}_s) \\ \hat{a}_2 &= \frac{1}{\sqrt{2}}(\hat{a}_{LO} - \hat{a}_s). \end{aligned} \tag{1.91}$$

The photo-currents i on both photo-diodes measure the field's power and are therefore proportional to the number operator. In consequence, we can write the corresponding operators $\hat{I}_i$ as

$$\hat{I}_{1,2} \propto \hat{a}_{LO}^\dagger \hat{a}_{LO} + \hat{a}_s^\dagger \hat{a}_s \pm \hat{a}_{LO}^\dagger \hat{a}_s \pm \hat{a}_s^\dagger \hat{a}_{LO}. \tag{1.92}$$

And then, subtracting the photo-currents, we have

$$\hat{I}_1 - \hat{I}_2 \propto \hat{a}_{LO}^\dagger \hat{a}_s + \hat{a}_s^\dagger \hat{a}_{LO}. \tag{1.93}$$

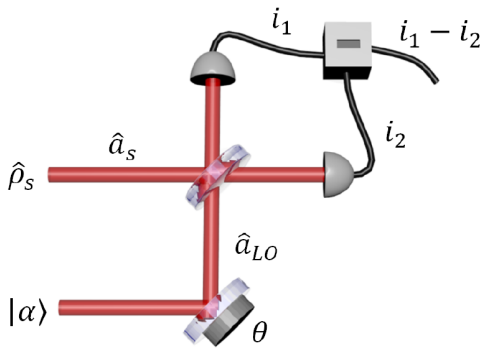

Figure 1.5: **Setup for homodyne detection**. The quantum state to characterize $\hat{\rho}_s$ is mixed with a high-power field called the local oscillator $\left|\alpha e^{i\theta}\right\rangle$ on a balanced beam-splitter. Two photo-diodes placed at the output ports of the beam-splitter provide a photo-current proportional to the field's power. The subtraction of the two photo-currents is equivalent to a quadrature measurement.

After subtraction, only the interference terms between modes s and LO remain. One simplification can then be made because the LO is a powerful coherent state $\left|\alpha e^{i\theta}\right\rangle$. This allows us to make the approximation $\hat{a}_{LO} \approx \alpha e^{i\theta}$, from which we get

$$\begin{aligned} \hat{I}_1 - \hat{I}_2 &\propto \alpha e^{-i\theta}\hat{a}_s + \alpha e^{i\theta}\hat{a}_s^\dagger. \\ \hat{I}_1 - \hat{I}_2 &\propto \alpha \hat{x}_\theta. \end{aligned} \tag{1.94}$$

This simple-in-principle apparatus therefore performs a quadrature measurement, amplified by the power of the local oscillator. It is the tool of choice for quantum tomography of optical fields.

4.2 Maximum-Likelihood reconstruction

Several methods for the reconstruction of the quantum state from tomographic measurements have been introduced over the years (see [30]). Since its introduction in 2004 [43] in the context of quantum optics, the iterative maximum-likelihood (ML) reconstruction method has however become standard. Some of its advantages include the fact that it forces the result to be a physical state (meaning in this case that it leads to a density matrix with positive diagonal elements) and that it has a high accuracy. It also enables the experimentalist to correct for losses.

Tomographic reconstruction requires accumulation of data. In our context, as homodyne detection performs $\hat{x}_\theta$ but destroys the quantum state, it means we have to create the states we want to characterize a great number of times. Then at each creation we can measure a different quadrature and from the total data set we can find the most likely state to have led to all these measurements. The principle of ML is the following.

We have a set of N quadrature measurements $\{x_n, \theta_n\}_n$, where θ_n is the local oscillator phase at event n and x_n the corresponding measured quadrature value. From this set we build the likelihood function $\mathcal{L}(\rho)$ defined as

$$\mathcal{L}(\hat{\rho}) \hat{=} \prod_{n=1}^{N} \mathrm{Tr}(\hat{\rho}\,|x_n, \theta_n\rangle\,\langle x_n, \theta_n|). \tag{1.95}$$

This function is the product of the probabilities of observing each measured POVM $|x_n, \theta_n\rangle \langle x_n, \theta_n|$ when starting from a given state $\hat{\rho}$.

The ML process is an iterative procedure that will explore different possible quantum states $\hat{\rho}_i$ and find the state $\hat{\rho}_{\mathrm{ML}}$ that maximizes $\mathcal{L}$. It requires the experimentalist to choose the dimension d of the Hilbert space he wants to explore. The algorithm is the following, starting from a density matrix $\hat{\rho}_0 = \frac{1}{d}\mathbb{1}$, we compute recursively new normalized density matrices following

$$\hat{\rho}_{n+1} \propto \hat{R}(\hat{\rho}_n)\hat{\rho}_n\hat{R}(\hat{\rho}_n), \tag{1.96}$$

where the projectors $\hat{R}(\hat{\rho})$ are defined as

$$\hat{R}(\hat{\rho}) = \sum_{n=1}^{N} \frac{|x_n, \theta_n\rangle \langle x_n, \theta_n|}{\mathrm{Tr}(\hat{\rho}\,|x_n, \theta_n\rangle \langle x_n, \theta_n|)}. \tag{1.97}$$

Making the assumption that the algorithm converges after a reasonable amount of time, it has to lead to the state $\hat{\rho}_{\mathrm{ML}}$ such that

$$\hat{\rho}_{\mathrm{ML}} \propto \hat{R}(\hat{\rho}_{\mathrm{ML}})\hat{\rho}_{\mathrm{ML}}\hat{R}(\hat{\rho}_{\mathrm{ML}}), \tag{1.98}$$

or, equivalently, such that $\hat{R}(\hat{\rho}_{\mathrm{ML}}) \to \mathbb{1}$, meaning that the probability of observing each measurements approaches $1/N$ in the case where we explore the complete set of quadratures. Although strict convergence can be reached only after an infinite number of measurements, in practice we can efficiently get close to convergence.

Taking losses into account. One advantage of the recursive procedure is that it is possible to correct for losses directly with the algorithm. How can we justify loss correction? Typically, the homodyne detection process is imperfect and introduces some losses into the measured state. As these losses are independent from the state and completely dependent on our measurement setup, correcting for them gives a fair assumption of the created state. This is of course something to use conservatively as too much loss correction will lead to overestimation of parameters of impact such as Wigner or entanglement negativity. In practice, we limit ourselves to 15% of correction, an underestimation of the losses introduced by our experimental homodyne setup.

The procedure for correction is to modify the projectors $|x_n, \theta_n\rangle \langle x_n, \theta_n|$ so that they include the losses, in effect changing the expression of the measurements into lossy quadrature operators. The exact expressions for the transformation are detailed in [30].

The challenge of error estimation. The process of tomographic reconstruction in general presents one great drawback in terms of error estimation. The density matrix or Wigner function of a quantum state contains all the possible information one can recover from measurements performed on the state. Tomography goes in the opposite direction, as from a finite number of measurements it aims to deduce the most-likely observed quantum state. The drawback is that the end result of an experiment is very often a parameter one has to deduce from the quantum state, for example the negativity of the Wigner function at the origin, the state population, entanglement negativity... As such, it is very hard to know the effect a small error in reconstruction will have on the final parameter of impact. When possible, one should acquire as much data as possible. The accumulation of data over a long period brings however issues of its own as the natural fluctuations of the experiment will

result in a degradation of the reconstructed state if we combine data over longer periods.

In the usual experimental cases, we use the threshold of 50000 events for single mode states and 100000 for two-mode states. These values give us consistent results over different experiments and lead to reasonable errors in parameters such as negativity of the Wigner function or negativity of entanglement. In some specific cases however, accumulating this many events is impossible. The violation of steering inequalities in Chapter 5 is one example, and we use in that case the method of *quantum error bars* [44]. The process, as it will be introduced in that chapter, is very time-consuming and cannot be performed systematically. Depending on the situation, we will therefore justify the need for such a complete assessment of uncertainties. In most cases this will not be necessary.

5 Conclusion

In this chapter we have introduced some useful theoretical tools, starting from field quantization to the description of quantum tomography. We have in particular presented the concepts of non-Gaussian states which are central to this thesis. Most experiments we report on in this thesis make use of this type of states and operations in various contexts.

Having introduced mostly theoretical aspects, we will now consider the experimental protocols used for the generation of non-gaussian states. One particular experimental tool is central to our methods: *the optical parametric oscillator*. This resource enables the generation of single-mode and two-mode squeezed vacuum. The next chapter will introduce this key resource and then report on its use in protocols allowing the creation of discrete- and continuous-variable states.

Chapter 2

Generation of non-Gaussian states

In the field of quantum optics, optical parametric oscillators (OPOs) are uniquely useful experimental tools as they enable the generation of both single- and two-mode squeezed vacuum states. The quantum correlations that those states exhibit make them reliable sources of entanglement [45] and they can be used to perform sensitive measurements beyond the quantum limit [46]. In our experiment, they are key to the creation of non-Gaussian states, the fundamental resource for many quantum information protocols.

In this chapter, we will present the theory of OPOs and their use for the generation of both discrete- and continuous-variable states of light. The first protocol we will detail is the heralding of high-purity single photons. While comparatively simpler, this protocol is a building block for all the experiments that will be presented in this thesis and makes for a good introduction to our experimental methods. After extending the protocol to the creation of higher-dimensional Fock states, we will also present a method for the creation of Schrödinger kitten states. These first protocols for non-Gaussian state generation are stepping stones to the creation of hybrid entanglement of light that is central to this thesis work.

Contents

1 Optical parametric oscillators as squeezing resources

The generation of both single and two-mode squeezed vacuum states is at the heart of our non-Gaussian state creation process. We introduce here the resources that enable the generation of squeezed vacuum states: optical parametric oscillators (OPO). We will first quickly introduce the theory of OPOs and then give a detailed presentation of the specifications of the two specific devices used during the course of this thesis.

1.1 Parametric down-conversion and phase-matching condition

The physical phenomenon central to the behavior of OPOs is spontaneous parametric down-conversion (SPDC), which requires the use of a non-linear medium presenting a second-order non-linear susceptibility $\chi^{(2)}$. This process consists in the conversion of a *pump* photon of frequency ω_0 into two photons (*signal* and *idler*) of lower frequencies ω_1 and ω_2. Parametric down-conversion can be observed if two conditions are met:

- $\omega_0 = \omega_1 + \omega_2$, required to ensure energy conservation.
- $\vec{k}_0 = \vec{k}_1 + \vec{k}_2$, or equivalently in the case of co-linear fields $n(\omega_0)\omega_0 = n(\omega_1)\omega_1 + n(\omega_2)\omega_2$. This is the phase matching condition that maximizes the conversion process efficiency.

Fulfilling both requirements is impossible in a normal dispersive material, as the refractive index $n(\omega)$ increases monotonically with the field frequency ω. Using a birefringent medium however, there are two possible ways to achieve phase-matching:

- **Type-I phase matching:** $n_o\omega_0 = n_e\omega_1 + n_e\omega_2$
  The pump is on the ordinary axis, and signal and idler are degenerate in polarization along the extraordinary axis.
- **Type-II phase matching:** $n_e\omega_0 = n_{e/o}\omega_1 + n_{o/e}\omega_2$
  The pump is on the extraordinary axis while signal and idler are non-degenerate in polarization.

In both cases, the SPDC hamiltonian coupling the pump, signal and idler modes can be expressed as:

$$\mathcal{H} = i\frac{\hbar g}{2}\hat{a}_i^\dagger \hat{a}_s^\dagger \hat{a}_p + \text{h.c.}, \tag{2.1}$$

where $\hat{a}_i$, $\hat{a}_s$, and $\hat{a}_p$ are the annihilation operators corresponding to the idler, signal and pump fields and g is a coupling constant. Under the right conditions, this interaction hamiltonian can lead to the creation of single- and two-mode squeezed vacuum states. This is done by having a powerful coherent state $|\alpha\rangle$ as an input pump field into the medium. This simplifies the hamiltonian, using $\hat{a}_p^\dagger \approx \alpha$, and introducing $\kappa = \alpha g$:

$$\mathcal{H} \approx i\frac{\hbar\kappa}{2}(\hat{a}_i^\dagger \hat{a}_s^\dagger - \hat{a}_i\hat{a}_s). \tag{2.2}$$

When signal and idler are degenerate in polarization and frequency, *i.e.* $\hat{a} \hat{=} \hat{a}_i = \hat{a}_s$, this is the Hamiltonian that corresponds to the application of the single-mode squeezing operator (1.80):

$$\hat{S}_I(\zeta) = e^{\frac{\zeta}{2}(\hat{a}^2 - (\hat{a}^\dagger)^2)} = e^{-i\frac{\mathcal{H}}{\hbar}\tau}, \qquad \text{for} \quad \zeta = \kappa\tau, \tag{2.3}$$

where τ is the interaction time.

Using the Heisenberg representation, one can indeed consider the evolution of both the signal and idler annihilation operators:

$$i\hbar\frac{d\hat{a}_{s/i}}{dt} = \left[\mathcal{H}, \hat{a}_{s/i}\right]. \tag{2.4}$$

This gives us, for a short interaction time τ:

$$\hat{a}_{s/i}(t+\tau) = \hat{a}_{s/i}(t) - \alpha g\tau\hat{a}_{i/s}(t)^\dagger, \tag{2.5}$$

which leads to the time-evolution:

$$\hat{a}(t) = \hat{a}(0)\,\mathrm{ch}(\kappa t) - \hat{a}^\dagger(0)\,\mathrm{sh}(\kappa t). \tag{2.6}$$

Therefore, after an interaction time τ, the quadratures $\hat{x}$ and $\hat{p}$ become:

$$\begin{aligned}\hat{x}' &= e^{-\zeta}\hat{x}\\ \hat{p}' &= e^{\zeta}\hat{p}.\end{aligned} \tag{2.7}$$

We indeed recover the effect of the application of a single-mode squeezing operator with a squeezing amount of $\zeta/2$. The quadrature $\hat{x}$ becomes squeezed and $\hat{p}$ anti-squeezed under the down conversion process. Initially populating the signal and idler mode by vacuum, we can therefore obtain single-mode squeezed vacuum with signal and idler degenerate in polarization.

In the case of non-degenerate signal and idlers, the interaction hamiltonian corresponds to a two-mode squeezing operator (1.84):

$$\hat{S}_{II}(\zeta) = e^{\frac{\zeta}{2}(\hat{a}_i\hat{a}_s - \hat{a}_i^\dagger\hat{a}_s^\dagger)}. \tag{2.8}$$

Equation (2.4) is then equivalent to

$$\frac{d(\hat{a}_s + \hat{a}_i)}{dt} = -\frac{\kappa}{2}(\hat{a}_s^\dagger + \hat{a}_i^\dagger) \tag{2.9}$$

To summarize, a single-pass SPDC process corresponds to the application of single or two-mode squeezing operators, depending on the phase-matching. Type-I phase matching leads to signal and idler fields degenerate in polarization and frequency. It corresponds in the collinear case to the application of a single-mode squeezing operator. Type-II phase matching leads to signal and idler fields degenerate in frequency but not in polarization. It corresponds to a two-mode squeezing operator.

1.2 Adding a cavity: optical parametric oscillator

It is difficult to observe SPDC because it is very inefficient in typical non-linear media. One solution to enhance its effect is to place the birefringent medium in a cavity. In that case, the setup is called an optical parametric oscillator. The cavity helps to increase the interaction time and the conversion efficiency but also adds some specific properties to the setup.

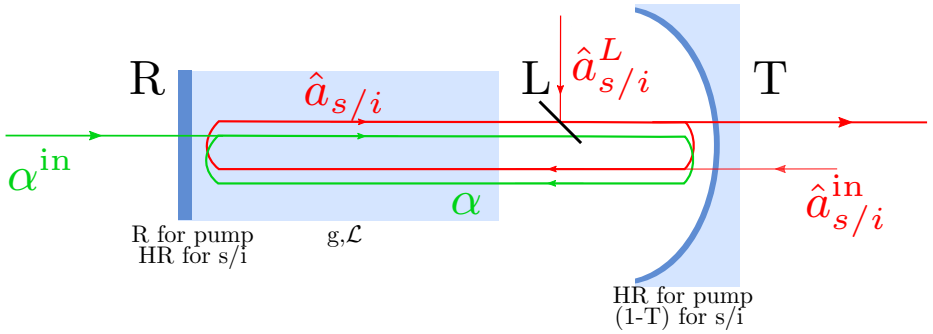

Figure 2.1: **Model of an optical parametric oscillator**. A non-linear crystal is placed in a cavity. The pump field α^{in} is sent to the cavity and from SPDC leads to the appearance of signal and idler fields s and i. The input and output mirrors have different reflection and transmission coefficients for the three fields. The input mirror is highly reflective (HR) for signal and idler and has a reflection R for the pump. The output mirror is conversely highly reflective for the pump but has a transmission T for signal and idlers. We model the intra-cavity losses by a beam-splitter of reflection L coupling the intra-cavity signal and idlers fields to the environment.

We now give a theoretical model including losses for optical parametric oscillators in order to give an expression for the time-evolution equations of the intra-cavity fields and introduce some parameters. In figure 2.1 we show a schematized OPO. The non-linear crystal characterized by g is of length l, which corresponds to a propagation time $\mathcal{L}$. The pump field α^{in} leads after down-conversion to the appearance of signal and idler fields s and i. The cavity mirrors have different reflection and transmission coefficients for ω_0 and ω_1. The input mirror has a reflection coefficient R for the pump and is highly reflective for signal and idler fields. Conversely, the output mirror is highly reflective for the pump and has a transmission of T for signal and idler fields. We model the intra-cavity losses through a beam-splitter of reflection L, which couples the modes $\hat{a}_{s,i}$ to outside modes denoted $\hat{a}^{L}_{s,i}$. We also consider possible input fields coming from the exit mirror $\hat{a}^{\text{in}}_{s,i}$.

1.2.1 Oscillation threshold

Using these notations, we compute the time-evolution of annihilation operators inside the cavity. Using equation (2.5), the annihilation operator after a round-trip of duration τ is given by:

$$\hat{a}_{s/i}(t+\tau) = \sqrt{(1-L)(1-T)}(\hat{a}_{s/i}(t) - |\alpha| g\tau' \hat{a}^{\dagger}_{i/s}(t)) + \sqrt{L}\hat{a}^{L}_{s/i} + \sqrt{T}\hat{a}^{\text{in}}_{s/i}, \tag{2.10}$$

with τ' the total interaction time equal to $2*\mathcal{L}$ and $|\alpha|$ the intra-cavity pump field. Assuming L and T to be small and introducing $g' = g\tau'$, we have

$$\hat{a}_{s/i}(t+\tau) = (1 - \frac{L+T}{2})(\hat{a}_{s/i}(t) - |\alpha| g' \hat{a}^{\dagger}_{i/s}(t)) + \sqrt{L}\hat{a}^{L}_{s/i} + \sqrt{T}\hat{a}^{\text{in}}_{s/i}, \tag{2.11}$$

which leads us to write as a first approximation

$$\frac{d\hat{a}_{s/i}}{dt} = -\frac{L+T}{2}\hat{a}_{s/i}(t) + |\alpha| g' \hat{a}^{\dagger}_{i/s}(t) + \sqrt{L}\hat{a}^{L}_{s/i} + \sqrt{T}\hat{a}^{\text{in}}_{s/i}. \tag{2.12}$$

The first consequence of adding a cavity is therefore the existence of a power threshold over which we can observe oscillation. Indeed, to have a gain in the cavity, we need to have $|\alpha|g' - \frac{L+T}{2} > 0$. The pump threshold is equal to:

$$|\alpha_{\text{th}}|^2 = \frac{(L+T)^2}{4(g')^2}. \tag{2.13}$$

We see that the threshold evolves quadratically with the output mirror transmission. It can be reduced further if the cavity is resonant for the pump. In that case, we have

$$|\alpha_{\text{th}}^{\text{in}}|^2 = \frac{(L_p+T_p)^2}{4T_p}\frac{(L+T)^2}{4(g')^2}, \tag{2.14}$$

where $T_p = 1 - R$ is the transmission of the input mirror for the pump, and L_p is the intra-cavity losses for the pump. In the case of negligible losses for the pump, we have

$$|\alpha_{\text{th}}^{\text{in}}|^2 \propto T_p T^2. \tag{2.15}$$

In all our experiments, we will remain well below the oscillation threshold.

1.2.2 Escape efficiency

An important parameter for OPOs is the escape efficiency which results from the intra-cavity losses and the output mirror transmission. It gives the probability that down-converted photons will escape the cavity through the exit mirror [47]. It is defined as

$$\eta_0 = \frac{T}{T+L}. \tag{2.16}$$

The value of the escape efficiency is directly linked to the squeezing amount obtained at the oscillation threshold $s^{\max}$ [30]:

$$s^{\max} = 1 - \eta_0. \tag{2.17}$$

It is therefore the key parameter for the evaluation of the quality of the cavity and can be measured through squeezing characterization. The escape efficiency is a concrete characterization of the intrinsic losses in the cavity. Indeed, it is directly linked to an essential parameter for protocols using conditional preparation: the *heralding efficiency*. Given the detection of a signal (respectively idler) photon outside of the cavity, the heralding efficiency is defined as the probability that the idler (respectively signal) photon has escaped the cavity. The heralding efficiency limits the quality of the state generation protocols presented in sections 2 and 3.

1.3 OPO specifications

We now give details of the OPOs used in our experiments. As in the model of figure 2.1, our OPOs are made of semi-monolithic cavities. They are pumped by a Nd:YAG laser at $\lambda_0 = 532$ nm, which leads to signal and idler fields at $\lambda_1 = 1064$ nm. The input mirror is directly coated on the non-linear crystal, has a reflection coefficient $R = 95\%$ for the pump and is highly reflective for signal and idler fields. The output mirror has a radius of curvature of 38 mm, is highly reflective for 532 nm and has a transmission of $T = 10\%$ for signal and idler fields. We use two OPOs of different phase matching. The type-II phase-matched OPO uses

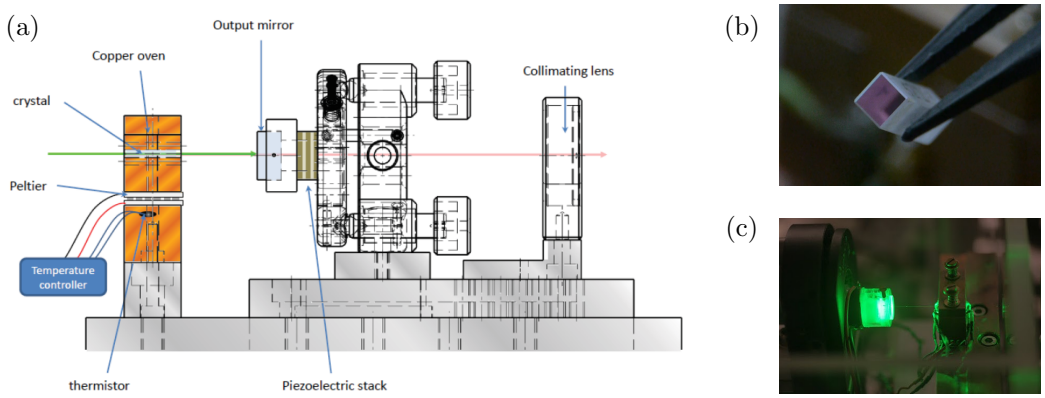

Figure 2.2: **Experimental Optical parametric oscillator**. (a): Schematics. The temperature of the non-linear crystal is tuned using a Peltier module. The mirror mount is glued to a PZT stack. All elements are fixed to a custom Invar base for thermal and mechanical stability. (b): KTP crystal from Raicol. The anti-reflection coating for 1064 nm was made by Layertech. (c): Photography of the pumped type-II OPO.

a KTP crystal of dimensions 3x3x10 mm^3, while the type-I a PPKTP crystal of dimensions 1x2x10 mm^3. Both are made by the company **Raicol** and their coatings have been realized by the company **Layertech**. In figure 2.2 (b) we show a photo of the KTP crystal used for the type-II OPO.

A detailed schematic of the cavity is shown in figure 2.2 (a). We aim to have resonance for all signals, *i.e.* double resonance for the type-I OPO and triple resonance for the type-II OPO. The output mirror is mounted on a piezo-electric transducer (PZT) in order to achieve resonance for the pump. A peltier module is used to heat an oven in which the crystal is lodged. This allows us to control the temperature of the crystal to have resonance of the idler. The cavity can be made resonant as well for the signal field in the case of the type-II OPO by tuning the laser frequency. The two OPOs have a bandwidth of 50 MHz and a free spectral range (FSR) of 4.3 GHz.

We now show the result of squeezing measurements on the type-I OPO made using homodyne detection on the type-I phase matched OPO. When going close to the threshold, we can reach high levels of squeezing. As shown on figure 2.3(a), we measure 10.5 dB of squeezing at 5 MHz and at 40 mW of pump power. At this level, the squeezing purity is necessarily degraded and we indeed see close to 19 dB of anti-squeezing. As explained before, we can deduce the escape efficiency from this measurement. Accounting for the losses introduced by the homodyne detection apparatus, we estimate the escape efficiency to be close to $\eta_0 = 92\%$.

Therefore, we have at our disposal two squeezers on the table. We next show how we use them for the heralding of non-Gaussian states. The type-I OPO allows for the generation of single-mode squeezed-vacuum and the type-II OPO for the creation of two-mode squeezed vacuum. As explained in Chapter 1, although fundamentally a non-classical state, squeezed vacuum is Gaussian. It is by combining it with a non-Gaussian operation–*photon detection*– that we are able to create non-Gaussian states that present negative values of the Wigner function. We will first look at protocols for discrete-variable state generation, and then for continuous-variable.

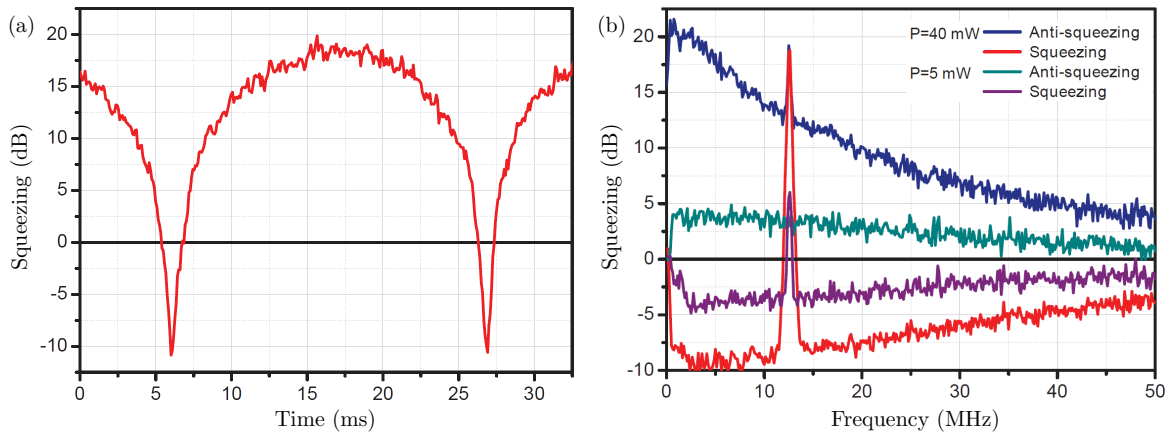

Figure 2.3: **Measured squeezing**. (a): Squeezing observed at a sideband frequency of 5 MHz when sweeping the phase of the quadrature measurement over time. We reach 10.5 dB of squeezing and 19 dB of anti-squeezing at a pump power of 40 mW (80% of the threshold). (b): Squeezing and anti-squeezing measured over the range $0-5$ MHz for a pump power of 5 mW and 40 mW, corresponding respectively to 3 dB and a maximum of 10.5 dB of measured squeezing.

2 DV state generation: heralding Fock states

The use of spontaneous parametric down-conversion for non-Gaussian state generation is now well established. In the DV context, the first realization of a localized single-photon state was made by Hong and Mandel in 1986 [48] and since then there have been several demonstration of SPDC-based non-Gaussian states. We note in particular the generation of single- [49, 50] and two-photon Fock states [51]. Following the same principle we present in this section our protocols and results for the creation of Fock states using a type-II phase matched OPO. We will see that the large escape efficiency exhibited by our OPOs enables the generation of very high-purity states.

2.1 Conditional preparation of Fock states

We aim to generate the Fock state $|n\rangle$. We use as a resource the type-II OPO pumped below threshold. We have a two-mode squeezed vacuum state at its output:

$$|\psi\rangle_{\mathrm{AB}} = (1-\lambda^2)^{1/2} \sum_{p=0}^{\infty} \lambda^p \, |p\rangle_{\mathrm{A}} \, |p\rangle_{\mathrm{B}} \, . \tag{2.18}$$

The level of pumping has to be chosen low enough that the decomposition of $|\psi\rangle_{\mathrm{AB}}$ on the Fock state basis sees negligible contributions on the eigen-modes higher than $|n\rangle$. Namely, this means that λ should be chosen such that the output state can be written as

$$|\psi\rangle_{\mathrm{AB}} \propto |0\rangle_{\mathrm{A}} \, |0\rangle_{\mathrm{B}} + \lambda \, |1\rangle_{\mathrm{A}} \, |1\rangle_{\mathrm{B}} + ... + \lambda^n \, |n\rangle_{\mathrm{A}} \, |n\rangle_{\mathrm{B}} + o(\lambda^n). \tag{2.19}$$

Here, A and B are the polarization modes corresponding to the ordinary and extraordinary axes of the non-linear crystal. Because the photons are correlated in pairs, the presence of a Fock state $|n\rangle$ in the polarization mode B can be heralded by the detection of n photons in polarization mode A. This is done using a polarizing beam-splitter (PBS) to separate the two polarizations in two spatial modes and then, using photon detectors, wait for the detection

of n photons in one of the modes. This mode, in which the n-photons are used to herald the creation of the Fock state, is called the *conditioning mode*. In the ideal case, this process is equivalent to the application of operator $|n\rangle\langle n|_A$ on $|\psi\rangle_{AB}$.

Although this method is quite efficient for the generation of small Fock states, the requirements for the state generation become more stringent as the target Fock size increases. The experimental difficulties come from the application of $|n\rangle\langle n|$ with increasing losses on the conditioning path. High-efficiency photon-number resolving detectors are not currently available for our working wavelength of 1064 nm and we use superconducting nanowire single-photon detectors that are not photon-number resolving (see Chapter 3). The application of $|n\rangle\langle n|$ therefore has to be done through splitting the conditioning path into n branches at the end of which a detector is placed. This process significantly lowers the generation rate for an increasing number of detections. The presence of losses is problematic as well because higher Fock contributions will lead to false detection events. As a consequence, the parameter λ has to be lowered to maintain the purity of the generated state which in turn lowers the generation rate. Both the transmission losses on the conditioning path and the detectors' quantum efficiency have this effect and the pumping power has to be adjusted to balance state purity and heralding rate. In practice, going beyond two-photon Fock states is still too challenging currently.

2.2 State heralding and temporal modes

The heralding process leads to the generation of states in temporal modes specific to the experimental implementation. In our case where we continuously pump an OPO, the cavity bandwidth determines the temporal shape of the generated photon wave-packet. This is due to the fact that the signal and idler fields can exit the OPO at different times. The temporal mode of the generated state can be computed as described below.

The lifetime of a down-converted photon in the cavity is directly related to the OPO bandwidth γ (FWHM). Assuming the SPDC has happened at time $t = 0$, the probability for each down-converted photon to remain inside the cavity after time t is [52]:

$$p(t) = 2\pi\gamma e^{-2\pi\gamma t}. \tag{2.20}$$

Conversely, given the presence of an idler photon at the output of the OPO at time $t = 0$, the probability that SPDC happened at time t is equal to $p(-t)$ for negative t and 0 for positive t. The probability of the signal photon being present at time t_s is therefore

$$\begin{aligned} p'(t_s) &= \int_{-\infty}^{t_i} p(-t)p(t_s - t)dt \qquad \text{if } t_s < 0 \\ p'(t_s) &= \int_{-\infty}^{0} p(-t)p(t_s - t)dt \qquad \text{if } t_s > 0. \end{aligned} \tag{2.21}$$

We end the integration at $\min(t_s, 0)$ because the SPDC has necessarily preceded the existence of either the signal or idler photon. Replacing $p(t)$ by its expression, we obtain

$$\begin{aligned} p'(t_s) &= \pi\gamma[e^{4\pi\gamma t}]_{-\infty}^{\min(0,t_s)} e^{-2\pi\gamma t_s}, \\ \text{and therefore} \qquad p'(t_s) &= \pi\gamma e^{-2\pi\gamma|t_s|}. \end{aligned} \tag{2.22}$$

The detection of an idler photon in a time interval much smaller than the cavity lifetime therefore heralds the presence of a signal photon following the probability $p'(t)$. Instead of

probabilities, and with the Heisenberg representation mindset, we typically consider the effect in terms of temporal modes. The cavity effect is indeed equivalent to a transformation of the signal creation operators following:

$$\hat{a}_{\mathrm{s}}^{\dagger} = \int_{-\infty}^{\infty} f(t)\hat{a}_{\mathrm{s}}^{\dagger}(t)dt. \tag{2.23}$$

Here f is a weight function over the set of time-dependent creation operators $\hat{a}^{\dagger}(t)$, called the *temporal mode function* of the idler state. The expression of f is directly related to p' as $|f(t)|^2 = p'(t)$. Indeed, as was shown as well in [53, 30], we have:

$$f(t) = \sqrt{\pi\gamma}e^{-\pi\gamma|t|}. \tag{2.24}$$

Any state characterization will necessarily take into account this temporal mode function. In the case of homodyne detection, this is done by applying the temporal mode directly on the quadrature measured over time:

$$\hat{x}_f = \int_{-\infty}^{+\infty} f(t)\hat{x}(t)dt. \tag{2.25}$$

The expression of f presented in equation 2.24 is valid for a perfect detection, and an ideal homodyne detection apparatus. This is of course not the case in practice and the temporal mode function will change depending on the experimental conditions. Thankfully, it is possible to infer the temporal mode of the generated state using homodyne detection [54]. This is invaluable as applying the wrong temporal mode on the homodyne data is equivalent to introducing losses. The procedure for temporal mode inference is explicited in the next section in an experimental context.

2.3 Single-photon state generation: experimental setup and resources

The single-photon state generation setup presented in figure 2.4 is one of the foundational protocols for this thesis. As its sub-parts can be found in all the other experiments we will report on, it represents a good introduction for all the non-Gaussian state generation processes we will consider. We now introduce separately the different components of the setup.

Pump and seed fields. We use a *Diabolo* Nd:YAG laser of the brand **Innolight** that has two outputs. The first one produces about 300 mW of power in the infrared at 1064 nm. Some of the infrared light is frequency doubled inside the box to 532 nm and about 600 mW of green light is available at the second output. This light is used as a pump field to the OPO. As it comes from the same source, the infrared field is coherent with the signal and idler fields of the OPO. This field serves several purposes. As a *seed beam* following the same path as the pump field it is used for monitoring the OPO resonance condition and to lock the OPO and filtering cavities. The laser is modulated at 12 MHz in order to implement the various analog locking mechanisms presented in the next paragraphs. It is also used as a local oscillator field in the homodyne detection. A mode cleaner placed at the 1064 nm output serves to filter out unwanted spatial modes. It is locked on resonance via tilt-locking [55].

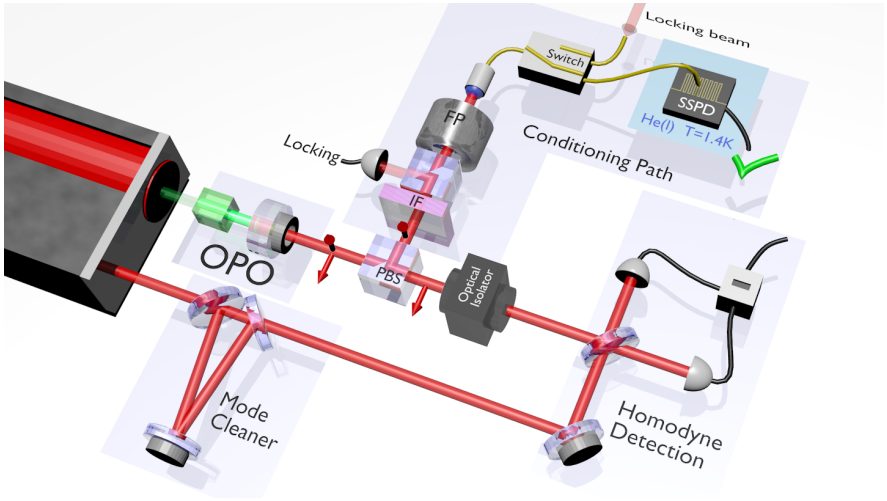

Figure 2.4: **Experimental setup for heralded generation of single-photons**. A type-II OPO is pumped at 532 nm with a power of 1 mW. At this pumping level, SPDC leads mainly to the appearance of single-photon pairs non-degenerate in polarization at the output of the OPO. The two photons are split in two spatial modes using a polarizing beam-splitter. One of its output is coupled to a conditioning path that applies frequency filtering before sending the photon to a SNSPD. The photon detection heralds the presence of a single-photon on the other spatial mode. It is characterized using homodyne detection.

Type-II phase-matched OPO. We use the KTP-based type-II phase-matched OPO described in section 1.3. We use 1 mW of pump power to be well below the threshold (estimated at 80 mW). The OPO is set to be triply resonant for the pump, signal and idler. The temperature of the crystal and the laser frequencies are adjusted manually to have resonance for the signal and idler fields. The resonance of the pump field is ensured by adjusting the size of the cavity by moving the PZT-mounted output mirror of the OPO. For that purpose, we perform *Pound-Drever-Hall* (PDH) locking [56] with the error signal obtained from the reflection of the pump field on the OPO.

Conditioning path. In the SPDC process, energy conservation requires that $\omega_0 = \omega_1 + \omega_2$, which allows for many possibilities we will label using the parameter ν such that $\omega_1 = 0.5 * \omega_0 + \nu$ and $\omega_2 = 0.5 * \omega_0 - \nu$. In our case we aim to have signal and idler degenerate in frequency, *i.e.* to have $\nu = 0$. The OPO cavity already limits the range of accessible frequencies to a frequency comb with peaks centered on the set $\{0.5\omega_0 + p\Delta\}_p$ with p and integer and $\Delta = 4$ GHz the free spectral range (FSR) of the OPO. Each peak is as broad as the OPO bandwidth: 60 MHz. The filtering process is presented in figure 2.5. The first stage of filtering is made using a **Barr Associates** interference (IR) filter. It is centered at 1064 nm and has a bandwidth of 0.5 nm (*i.e.* 125 GHz). The filter adds losses as the transmission at 1064 nm is 80% and less than 10^{-3}% outside of the transmission band. The second stage of filtering is performed using a homemade Fabry-Pérot cavity of bandwidth 350 MHz and of free spectral range 370 GHz. It presents therefore a finesse close to 1000. The cavity parameters were chosen to have a FSR at least twice as large as the bandwidth of the IR filter and a bandwidth larger than that of the OPO while narrower than the OPO FSR. The cavity is made of two mirrors of transmission $T = 0.3$ %, one flat and one spherical with a 1 m radius of curvature. The cavity length is close to 200 μm, which is why we refer to

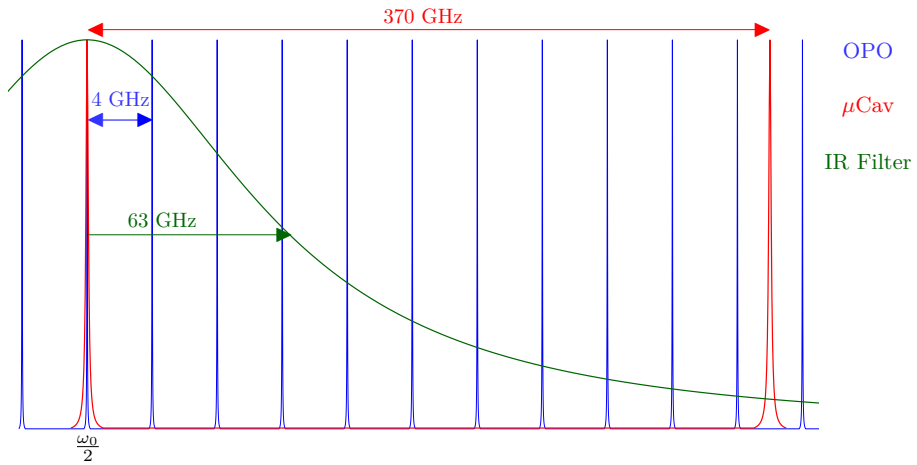

Figure 2.5: **Two-stage frequency filtering** (not to scale). The OPO cavity lets through frequencies distributed in a comb with peaks of 60 MHz bandwidth and a free spectral range (FSR) of 4 GHz. An interference (IR) filter leaves out all frequencies outside of a 0.5 nm or 126 GHz broad transmission band. The final filtering is done using a micro-cavity (μCav) of bandwidth 350 MHz and FSR 370 GHz.

it as a *micro-cavity*. The output of the micro-cavity is coupled to a fiber at the end of which is placed a high efficiency superconducting nanowire single-photon detector (see chapter 3). Overall, the conditioning path introduces about 50% of transmission losses.

Digital locking using micro-controllers. The mode cleaner and the OPO cavity are locked on resonance using analog locking procedures. The locking of the micro-cavity is however implemented using digital micro-controllers. Digital locking presents several advantages over its analogue counterpart. It is simpler to implement as it requires less material and frees one from the need to generate an error signal. It is also more suited for longer experiments as one can program automatic relocking features and peak searching sequences that are difficult to implement in purely analog systems. The price of implementation of digital locking has also dropped significantly in recent years with the development of low-cost field programmable gate arrays (FPGA) and micro-controller units (MCU). We implemented several locking procedures on the experiment using two different MCUs: The **Analog Devices** *ADUC7020* and the **Arduino** *Due* boards. Both provide 12-bit analog to digital (ADC) and digital to analog (DAC) converters, are easy to program and inexpensive. This resolution is sufficient for the locking of medium finesse cavities and interference fringes [57], and combining several converters enables us to lock reliably the high-finesse micro-cavity (see [32] for details).

Homodyne detection. The generated state is characterized using a homemade balanced homodyne detection setup. The two photodiodes used are of the brand **Fermionics** and reach quantum efficiencies above 97% at 1064 nm. We use 6 mW of power for the local oscillator which brings us 21 dB above the electronic noise (this is equivalent to 1% of loss). The monolithic structure of the OPO forces us to add an optical isolator on the path to the homodyne detector. This is because without isolation, some of the local oscillator light is reflected from the homodyne photodiodes, goes back up the infrared path all the way to the OPO and then to the conditioning path. As explained elsewhere [30], a weak displacement on the

conditioning path has for consequence a deformation of the measured marginal distribution. The optical isolator circumvents the problem but adds transmission losses. Taking this into account along with the photodiodes efficiency, the electronic noise on the homodyne signal and the overlap between the local oscillator and the signal beam, we have overall typically 15% of detection losses. Because they are intrinsic to the characterization process and are well calibrated, we can correct from them in our state tomography to evaluate the properties of the state before the optical isolator, *i.e.* as generated and available for subsequent experiments.

2.4 Single-photon state generation: data acquisition and analysis

Having presented the different devices used for the protocol, we now describe the systems used for data acquisition. We first introduce the measurement sequence used and then the acquisition settings.

Measurement sequence. Being of greatly higher power than the generated states, the seed beam cannot be introduced at the same time as the non-Gaussian states are measured. We therefore alternate between *sampling* sequences during which the micro-cavity is actively locked and the path to the SNSPD is closed, and *holding* sequences during which the seed beam is blocked, the cavity is set to hold its length and measurements are taken. Setting a longer sampling sequence or a shorter holding time increases the overall experimental duration. It is always desirable to have as short as possible experimental runs because the beams get misaligned over time and thermal fluctuations on the table will affect many locks as well as the quality of the triple resonance setting. The holding time has to be smaller than the typical time of stability of the micro-cavity. The compromise reached is to cycle between 40 ms of sampling time and 60 ms of measurements.

To open and close the seed beam paths, we use **Stanford Research Systems** (SRS) *SR475* low-noise laser shutters that have a commutation time of 5 ms. A **SRS** delay generator *DG645* is used to send the appropriate trigger signals to the shutters during the measurement cycle. Although the shutters are low-noise, there are still some mechanical vibrations that transfer to the table and that add instabilities. We therefore set them on homemade heavy mounts put on top of thick Sorbothane layers to improve mechanical isolation.

Data acquisition. All the data acquisition is made using a **LeCroy** *WaveRunner 610Zi* oscilloscope. It has a sampling rate of 20 GHz which allows us to record time evolution below the nanosecond scale. To each heralding event a voltage pulse is used as a trigger for recording the homodyne signal. During data analysis, the homodyne signal will have to be integrated over time following equation 2.24. The cavity bandwidth being $\gamma = 60$ MHz, the values of f can be neglected outside of a $4\log(10)/(\pi\gamma) \approx 50$ ns window. We record in practice 200 ns of homodyne signal for each heralding event. The heralding rate measured is of the order of 250 kHz. The data is accumulated for 50000 heralding events which corresponds to an experimental duration of less than five minutes when taking into account the duration of data recording as well as the measurement sequence.

Taking into account the temporal mode. As discussed earlier, the photon wave-packet is distributed in time following a given temporal mode function f. Although we have a theoretical expression for the expected temporal mode, it is only valid in the perfect case

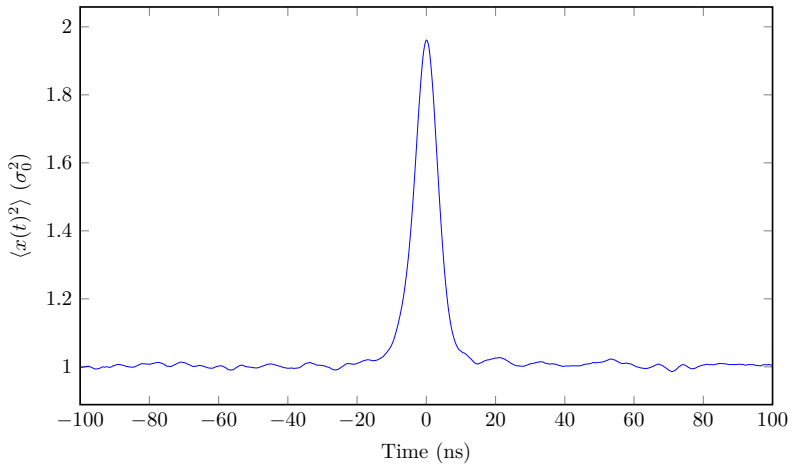

Figure 2.6: **Temporal mode**. Variance of the homodyne signal depending on time for an experimental single-photon state. At $t = 0$ the single-photon is heralded. This measurement allows us to center the temporal mode for our analysis of homodyne data.

so it is worthwhile to recover the actual function f experimentally. This can be done by trying different functions f and try to maximize a relevant quantity. Although many choices can be made, we use the optimization procedure detailed in [54]. Although an involved procedure, it broadly amounts to an optimization of f depending on the variance of the measured quadrature $\langle \hat{x}_f^2 \rangle$. This makes sense because the variance of the quadrature signal is greater for a single-photon state than for vacuum: $\langle 1| \hat{x}^2 |1\rangle = 3 \langle 0| \hat{x}^2 |0\rangle = 3\sigma_0^2$; therefore increasing the measured quadrature variance means getting closer to the state's temporal mode.

The difference in variance for vacuum and single photon states enables us as well to find the center of the temporal mode. In figure 2.6 is plotted the experimental measurement of $\langle x^2(t) \rangle$ depending on time for a heralded single-photon state. We see a peak that is due to the variance increase when the single-photon is measured. The center of the peak is used to adjust electrical delays between trigger and homodyne data recording so as to have the temporal mode centered on the recorded homodyne signal.

Pre-processed data set. Using the temporal mode function previously evaluated, we can associate to each heralding event a quadrature value following equation (2.24). There is still need for normalization of the results however as the quadrature measurement is amplified by a value depending on the local oscillator power. This is done by measuring the quadrature value of vacuum in the temporal mode f through making another measurement run where we simply block the signal path. In practice we acquire 40000 data points for vacuum before each measurements to compensate for local oscillator power fluctuations. Choosing to normalize such that vacuum has a variance of one, we finally associate to each heralding event n the value

$$\langle \hat{x}_f^{(n)} \rangle = \frac{1}{\sqrt{\langle \hat{x}_f^2 \rangle_{|0\rangle}}} \int_{-\infty}^{+\infty} f(t)\ x^{(n)}(t) dt, \tag{2.26}$$

where $x^{(n)}$ is the 200 ns-long raw homodyne data corresponding to the heralding event n and $\langle \hat{x}_f^2 \rangle_{|0\rangle}$ is the variance of vacuum in the temporal mode f averaged over all vacuum calibration events.

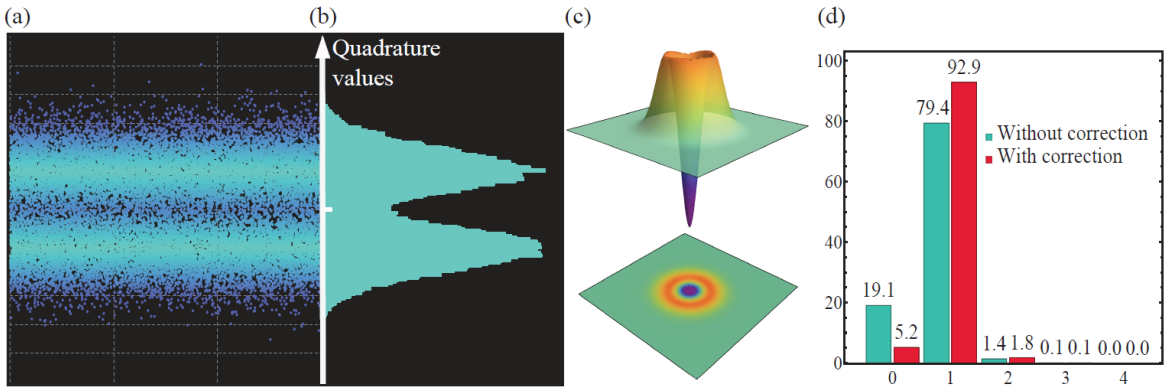

Figure 2.7: **Heralded single-photon state**. (a): Pre-processed quadrature values for all heralding events. (b): Histogram of quadrature values corresponding to the marginal distribution of the state averaged over all phases. (c): Wigner function of the reconstructed state corrected for losses. (d): Photon number distribution with and without correction for detection losses. Before characterization, we have a state with close to 93% of single-photon component and 5% of vacuum admixture.

In order to perform next the maximum-likelihood state reconstruction process, we associate to each heralding event a random phase as we assume to have a phase-independent Fock state. This is for convenience and can only decrease the measured state purity and state population. The final pre-processed data set is the table $\{n, \langle \hat{x}_f^{(n)} \rangle, \theta^{(n)}\}_n$.

State reconstruction. The final step is the reconstruction of the state using Maximum-Likelihood optimization. From the pre-processed data set, we obtain a density matrix. As for all tomographic reconstruction methods, we have to make assumptions. Here we assume to have a state with a low photon number which allows us to keep a short experiment time. For 50000 measurements, we can confidently perform the reconstruction for the space spanned by Fock states $\{|0\rangle, ..., |6\rangle\}$. Separate measurements have been made with more points to verify that higher Fock states are not populated indeed.

From the reconstructed states, we give the parameter relevant to the experiment. In the case of Fock state generation, the purity and photon number populations are the parameters of interest. As mentioned earlier, the tomographic process introduces losses around 15% that we can correct for. In practice we give the results both with and without loss correction.

2.5 Single-photon state generation: results

After reconstruction we obtain the results presented in figure 2.7 and published in [58]. Without correction from detection losses, we have less than 20% of vacuum component and close to 80% population in $|1\rangle$. Correcting for detection losses, we know that we are able to generate a single-photon state with 93% heralding efficiency and 5% vacuum component. At the heralding rate of 250 kHz enabled by our most recent SNSPD (see chapter 3), we demonstrate a spectral brightness of $0.6.10^4$ photons/(s.mW.MHz). This result makes our system one of the brightest parametric down-conversion sources to date [59], due to an intrinsic narrow bandwidth combined with the high efficiency of our heralding path. Combining with the state purity observed, our single-photon source is among the best in the published literature (see [32] for a comparison with other groups).

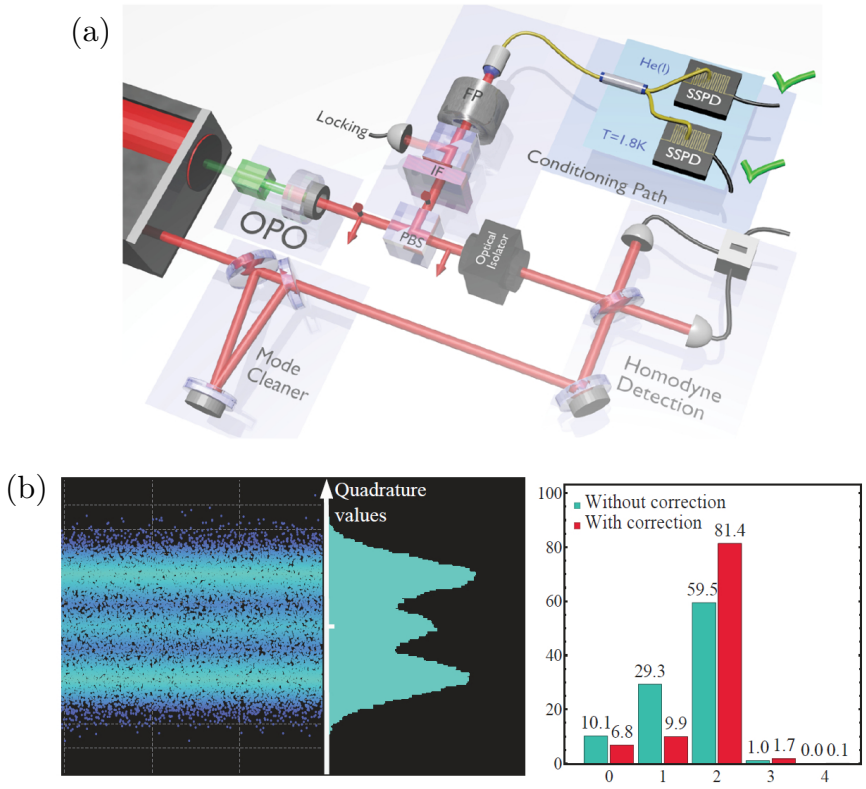

Figure 2.8: **Heralded two-photon state**. (a): Setup: This is the same setup as the one used for single-photon state generation, with the difference that two detectors are used to perform a double detection. (b): Quadrature results and photon number populations. We obtain after correction more than 80% of Fock $|2\rangle$ state, 7% of vacuum and close to 10% of single-photon component.

2.6 Two-photon Fock state generation

We also realized the experimental generation of a Fock state $|2\rangle$ with a very similar setup, by conditioning the state generation on a double detection. With our non-photon number resolving detectors, this was done, as shown in figure 2.8, by splitting the conditioning path using a fibered beam-splitter and placing one SNSPD at the end of each beam-splitter output. As explained in section 2.1, because of the losses on the conditioning path we maintain a low pumping power ($\sim$ 1 mW) to keep the double-click events rare in order to avoid detection events corresponding to Fock states $|3\rangle$ or higher. Additionally, we set a $1-$ ns acceptance window for the time-difference between coincidence clicks on the two detectors. This makes overall for a lower generation rate of 200 Hz. We obtain however a two-photon state with 80% purity (60% without correction for detection losses) as expected from the more than 90% escape efficiency of our OPO. This experiment represent the generation of the highest-purity two-photon states at the highest preparation rate published so far to our knowledge, on par with the recent demonstration in [60].

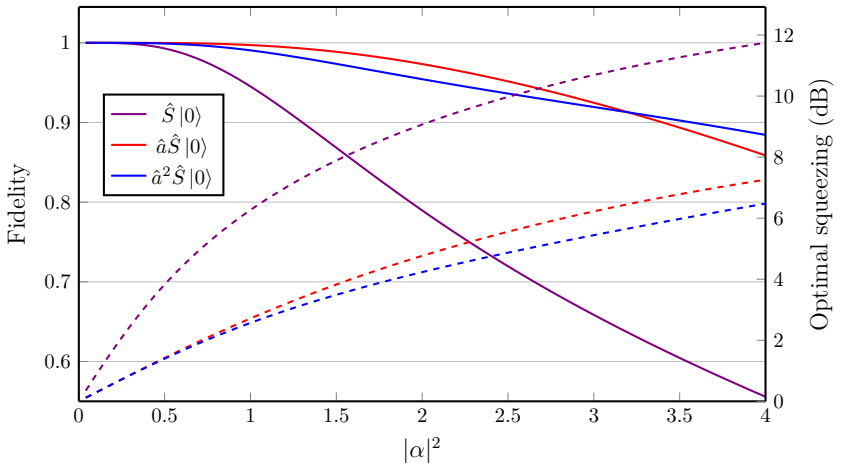

Figure 2.9: **Fidelity of photon-subtracted squeezed vacuum states with odd or even cat states** for different sizes $|\alpha|^2$. Full lines: maximum fidelity obtained over all possible squeezing amounts. Dashed lines: optimal squeezing of the photon-subtracted squeezed-vacuum state depending on the cat size.

3 CV state generation: heralding Schrödinger kitten states

As is the case for DV state generation, the use of SPDC for CV state engineering has also become established. The first two implementations were done in 2006 by Ourjoumtsev *et al.* in the pulsed regime [61] and Neergaard-Nielsen *et al.* in the continuous-wave regime [62]. The protocol used is very similar to the one presented in the last section, with the difference that we start from a type-I OPO still pumped below threshold but at a higher level. We present in this section the principle of the experiment and our results for the generation of odd Schrödinger kitten states.

3.1 Principle

Using a type-I phase-matched OPO as an initial resource, it is possible to create, with a scheme very similar to the one presented in section 2, coherent state superpositions (CSS) $|\alpha\rangle \pm |-\alpha\rangle$ of size $|\alpha|^2 \sim 1$. As we have seen in Chapter 1, at this population level, we refer to this type of states as Schrödinger kitten states. The initial idea for the generation was introduced by Dakna et al. [63] and draws from the following observation: under the right conditions, the repeated application of the annihilation operator to squeezed-vacuum leads to states that present high fidelity with Schödinger kitten states. Mathematically, and without normalization, we have indeed for lower squeezing amounts and cat sizes:

$$\begin{aligned} \hat{a}\hat{S}\,|0\rangle &\approx |cat_-\rangle \\ \hat{a}^2\hat{S}\,|0\rangle &\approx |cat_+\rangle\,. \end{aligned} \tag{2.27}$$

The approximation is valid for specific squeezing amounts and cat sizes that depend on the state considered. In figure 2.9, we plot in red (respectively violet) the fidelity of an odd (respectively even) cat state with the state $\hat{a}\hat{S}\,|0\rangle$ (respectively $\hat{a}^2\hat{S}\,|0\rangle$) for the corresponding optimal squeezing indicated by the dashed curve. One can see that in both cases and up to $|\alpha|^2 \approx 2$, we obtain fidelities above 95% with the photon-subtracted cat states for optimal

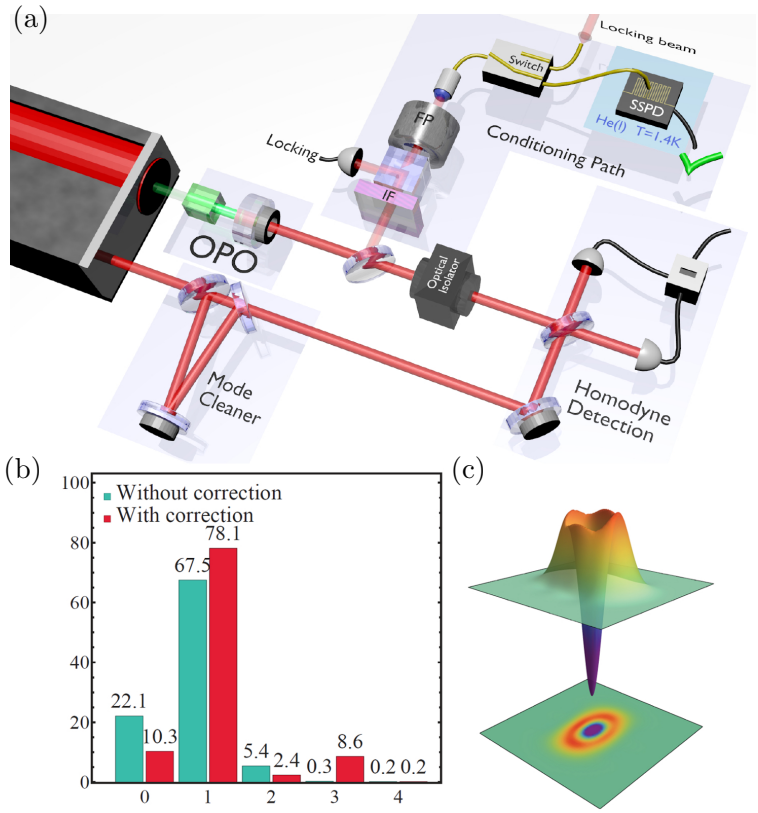

Figure 2.10: **Heralded odd cat state**. (a): The setup is similar to the single-photon state generation. We pump a type-I phase-matched OPO at 5 mW to produce 3 dB of high-purity squeezing at its output. We then approximate a single-photon detection using a beam-splitter to tap off 3% of the OPO output and conditioning on photon detection on the tapped path. (b): Photon number populations. We obtain after correction 10% of vacuum component and we observe significant population in the odd Fock states $|1\rangle$ and $|3\rangle$. (c): Wigner function of the measured kitten after correction for detection loss. We see negativity of the Wigner function at the origin, which is a strong indicator of non-classicality.

squeezing ranging up to 5 dB. We note that at lower values $|\alpha|^2 < 1$, the state $\hat{S}\,|0\rangle$ is a good approximation as well of even cat states, although higher squeezing is needed. For a squeezing of 3 dB in particular, while $\hat{S}\,|0\rangle$ is close to an even cat state of size $|\alpha|^2 = 0.4$, $\hat{a}\hat{S}\,|0\rangle$ has 99.5% fidelity with an odd cat state of size $|\alpha|^2 = 1.1$ and $\hat{a}^2\hat{S}\,|0\rangle$ has 98% fidelity with an even cat state of size $|\alpha|^2 = 1.2$.

We can therefore create odd cat states through a simple adaptation of the single-photon setup, substituting the type-II phase matched OPO by a type-I and applying a single-photon detection on the squeezed vacuum output.

3.2 Odd Schrödinger kitten state generation

The experimental apparatus is presented in figure 2.10 and is close to the setup for single-photon generation with a few differences and add-ons.

Type-I phase-matched OPO and photon subtraction. We use, as described in section 1.3, a periodically-poled KTP crystal. The pump power is set to have 3 dB of squeezing

at the output which corresponds in our case to 5 mW of green power. The cavity is set on resonance for green light using PDH locking and the temperature is adjusted to have resonance for the degenerate signal and idler fields as well. The photon subtraction is performed using a high transmission beam-splitter instead of a PBS because signal and idler are degenerate. The lower the beam-splitter reflection, the less likely it is that the conditioning event corresponds to multiple photon subtractions. The caveat is that the count rate will drop in consequence. The compromise used is to set a reflection $R = 3\%$ which corresponds to a heralding close to 100 kHz.

Phase calibration. Contrary to single-photon states, Schrödinger kitten states are not phase independent. It is therefore necessary to know the relative phase between the signal field and the local oscillator used for quadrature measurements. We use for this the seed beam initially introduced for cavity locking. The local oscillator phase is not locked but actively sweeped during the experiment by sending a voltage ramp $V(t)$ synchronized with the sampling and hold sequence to a PZT-mounted mirror placed on the LO path. During the sampling sequence, interference fringes between the LO and the seed beam are recorded using the homodyne system and will be used in the data analysis to associate to each voltage V its corresponding relative phase $\theta(V)$. During the holding sequence the seed beam is blocked so no fringes are visible but the voltage ramp is still applied to the PZT. The phase is finally recovered for each heralding event by looking at the voltage value applied at the time when the detection was made and then registering the corresponding phase. The active sweep allows us to explore the complete phase space efficiently as the heralding events arrive at random times.

Data analysis and results. As previously, we pre-process the homodyne signal and associate to each heralding event the quadrature measurement made in temporal mode f and the local oscillator phase to obtain the pre-processed data $\{n, \langle \hat{x}_f^{(n)} \rangle, \theta^{(n)}\}_n$. A Maximum-Likelihood optimization then gives us the results presented in figure 2.10 (b),(c). We have generated a state that has with correction close to 10% vacuum component. We also see that, apart from vacuum, the populations in odd photon-numbers is larger than in even components as expected from the state's parity. The Wigner function is also negative at the origin, as always a good indicator of non-classicality. We observe overall 87% fidelity with a Schrödinger kitten of size $|\alpha|^2 = 0.9$, at a generation rate of 100 kHz.

4 Conclusion

In this chapter, we have introduced optical parametric oscillators and their use in our experiment for the creation of both discrete- and continuous-variable states of light. The experimental setups presented are key components for the realization of hybrid entanglement of light but are also interesting on their own as they allow us to routinely generate high-quality Fock states and Schrödinger kittens. In Chapter 4, we will motivate the use of hybrid entanglement of light for the realization of quantum networks and detail the setup used for its realization. But first, we focus in the next chapter on the superconduction nanowire single-photon detectors used in our system and on the cooling system used to bring them into the superconducting regime.

Chapter 3

Superconducting nanowire single-photon detectors: characterization and cooling

A key component for the generation of non-Gaussian states is photon subtraction. Working at 1064 nm has historically been a disadvantage for its implementation as the quantum efficiencies of typical single-photon detectors has remained quite low until recently. In the last five years, however, there has been a lot of technological advances in this area with the development of superconducting nanowire single-photon detectors (SNSPD) working at 1064 nm. Our group took part in this effort by working jointly with V. Verma and S. W. Nam from the National Institute of Technology (NIST) and F. Marsili and M. D. Shaw from the Jet Propulsion Laboratory (JPL). The work our group was focused on was the measurement of the quantum efficiency of new detectors produced by NIST to help in the improvement of their design, which now reach quantum efficiencies above 90%. We used in particular WSi-based detectors in our common 2016 *Optics Letters* paper [58] for the generation of high-purity single-photon states. Since then we have tested new MoSi detectors that bring additional benefits.

In this chapter, we will present the properties of the detectors we currently use. We also provide details on the new cooling system we have been installing over the course of the thesis.

Contents

1 Superconducting nanowire single-photon detectors

1.1 Principle and advantages

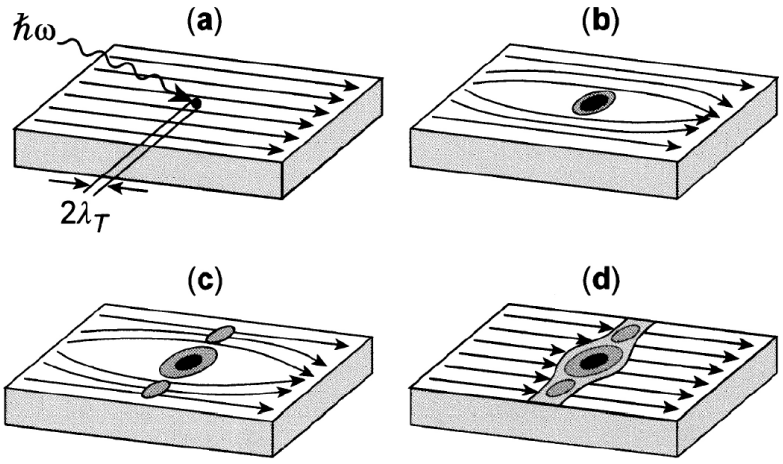

Figure 3.1: **Principle of SNSPDs**. (a): An impinging single photon creates a local hotspot on the wire, which is biased by a low amplitude DC current. (b): The current bypasses the hotspot, leading to an increase in the current density (c) and to a macroscopic resistance. A measurable voltage difference appears between the SNSDP terminals. After a short duration the temperature decreases and the hotspot returns to below the critical temperature. *Originally published in [64].*

The principle of SNSPD is presented in figure 3.1. These detectors are made of a superconducting wire of less than micro-meter thickness and a length of the order of several micro-meters. It is arranged along a sinuous path, or meander, to form a light-sensitive area as shown in figure 3.2 (a). The detection of single photons is possible because of the superconducting nature of the detector at low temperature. If a current flows through the medium at an amperage higher than a threshold called the *switching current* I_{sw}, the material will leave its superconducting state. This property is exploited by applying a current called *bias current* to the detector of value just below I_{sw}. As shown in figure 3.1, the material stays superconducting until a photon arrives at its surface and is absorbed. The energy of the photon is enough to create a resistive hotspot on the detector's surface. Because the current will then bypass the local resistance, there will be an increase in current density. The small dimensions of the wire ensures the density increase to be significant. This leads to the appearance of a macroscopic resistance of several kΩ and, in consequence, to a measurable voltage. The heat then dissipates and the detector returns to its superconducting state in a time called *dead time* that depends on the material and during which the detector is not sensitive to incoming photons. There is therefore a voltage pulse linked to the arrival of the photon that can reliably be used for triggering.

There are several parameters for which using SNSDPs instead of other single photon detectors such as Avalanche Photodiodes (APD) or Transition-Edge Sensors (TES) is advantageous. Quantum efficiency (QE) in particular is greatly superior for SNSPDs at 1064 nm than silicon-based APDs ($\approx 2\%$ of QE). It is also greater than InGaAs/InP avalanche photodiodes (up to $\sim 30\%$ at this wavelength) and SNSPDs have the additional advantage of exhibiting lower dark-count rates, *i.e.* the rate of pulses corresponding to false events. Ad-

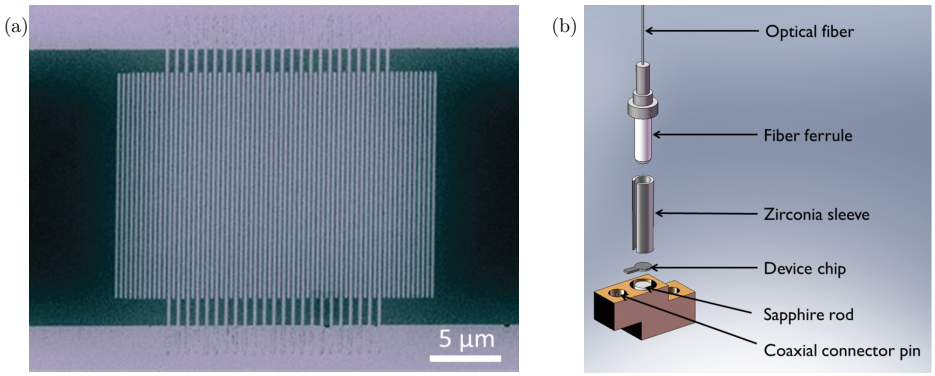

Figure 3.2: **The detectors from NIST**. (a): SEM photograph of the sensitive meander. The thickness of the wire is equal to 140 nm. (b): Detector mount design. A Zirconia sleeve is set so that an optical fiber can be directly plugged on one end to couple to the sensitive area. The active area is of dimensions $(16\ \mu m)^2$, wider than the mode field diameter of a standard mode fiber to allow for some misalignment. The nanowire is connected to a coaxial connector pin to apply the bias current.

ditionally, the dead-time of SNSPDs is of the order of 10 ns, whereas the duration for TES is of several μs. For this reason, SNSPDs have now become the detectors of choice in many laboratories and are being sold by several companies. Our group's close partnership with NIST allowed us however to take part in the parameter optimization of detectors at 1064 nm.

1.2 Properties of the detectors from NIST

Our group has been in collaboration with NIST and JPL for several years with the goal of adapting their highly efficient SNSPDs optimized for 1550 nm [65, 66] to our working wavelength of 1064 nm. We therefore received several generations of detectors made from wafers with different parameters. We measured in the lab the quantum efficiency of the detectors to help decide the parameters for the next iteration. Details of the NIST detectors design are shown in figure 3.2. The width of the nanowire is equal to 140 nm and the pitch of the serpentine structure is equal to 245 nm. The sensitive area is mounted on a copper base on which a zirconia sleeve enables us to directly plug fibers on the device. The large active area ensures a high coupling from the fiber to the detector without the need for precise alignment. Two superconducting materials were tested and used: Tungsten silicide (WSi) and, since last year, Molybdenum silicide (MoSi). Those two materials are amorphous, which is in contrast with Neobium Nitride (NbN) used in previous generations.

To measure the quantum efficiency of the detectors, we follow the procedure shown in figure 3.3. We use the power-meter OPHIR PD300-IRG(**Vega**) to assess the power at the input of the SNSPD based detection system. It is calibrated for power measurements in the range $100\ \text{pW} - 10\ \mu\text{W}$. In contrast, our SNSPDs leave the superconducting state for a power above ~ 5 pW. To make a comparison possible we therefore split the input power using a fibered beam-splitter at one output of which we place the Vega power-meter and attenuate the other by about 50 dB before sending the power to the SNSPD.

- Step A: The power ratio between the two outputs is measured by using the same power-meter alternatively on both ends and adjusting the attenuation and the input power to have $\sim 10\ \mu$W at one output and ~ 1 nW at the other.

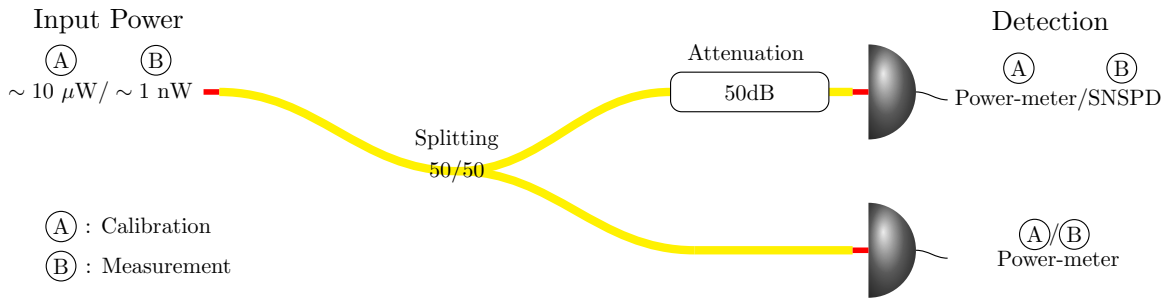

Figure 3.3: **Measuring the quantum efficiency of SNSPDs**. We use a power-meter well calibrated in the 100 pW − 10 μW range. Since the detector is suited for detection in the power range 0.5 − 5000 fW, we split the signal into two branches using a fibered beam-splitter and attenuate one path by around 50 dB. Step A: The attenuation is first calibrated by imputing a power $\sim$ 10 μW and measuring the power on both sides using the Vega power-meter. Step B: Quantum efficiency measurement of the SNSPD. We input a lower power $\sim$ 0.1 nW and measure the power on the fully transmitted output with the Vega power-meter and the count rate on the SNSPD at the attenuated output. Comparing the expected power at the exit of the attenuated path with the count rate of the SNSPD we recover the system detection efficiency of the SNSPD.

- Step B: We then couple the attenuated output to the SNSPD and place the OPHIR powermeter at the end of the other output. We then lower the input power to send $\sim$ 100 pW to the power-meter and $\sim$ 0.1 pW to the SNSPD. We have a direct evaluation of the power sent to the SNSPD and can compare with the number of triggering event obtained.

Note here that we do not measure the quantum efficiency of the detector but rather the efficiency of the complete line from the input coupler of the fiber connected to the SNSPD to the number of electrical triggers we effectively obtain on our oscilloscope. We therefore prefer to talk about *system detection efficiency* (SDE) *i.e.* the probability that an input photon will lead to a measurable pulse which comprises all the losses in the coupling system as well as the QE of the detector. The overall precision of the measurement is limited mainly by the precision of the power-meter's calibration and the non-linear behavior of the attenuators with varying power. Overall, we estimate the SDE measurement to be precise up to a $\sim$ 3% error.

The first material considered is tungsten-silicide (WSi). It is amorphous, presents advantages for the fabrication of a broad sensitive area and can reach much higher quantum efficiencies than the previously standard crystalline material NbN. The response of the best WSi detector we used is shown in figure 3.4 (a), where we plot the *system detection efficiencies* (SDE) depending on the bias current. As the bias current increases, the detector becomes more sensitive until it reaches a *plateau* where the efficiency becomes maximal. Once the bias current goes above I_{sw}, the detector is no longer sensitive. It is desirable to go as far as possible in the plateau in practice because in that regime the voltage pulses used for triggering will be more defined and have a more consistent rising edge. Once we get close to the switching current, there is however an increase in the rate of dark counts so there is a balance to reach. The WSi detectors represented a great improvement compared to the previously standard 30% of QE for typical NbN detectors, allowing us to get more than 90% of SDE with a dark count rate under 100mHz. This type of detectors enabled us to demon-

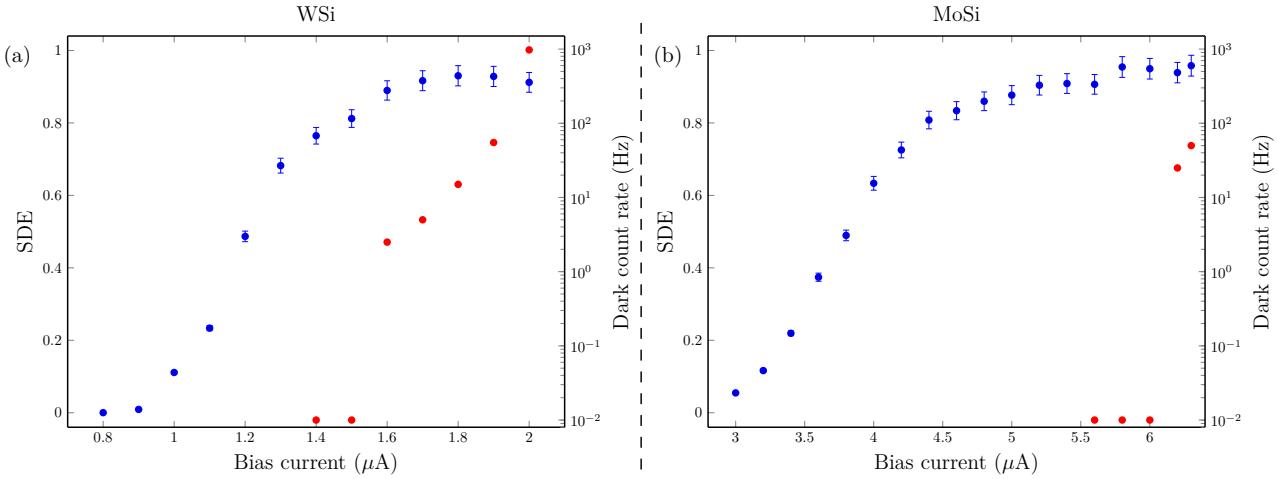

Figure 3.4: **Measured system detection efficiency**. System detection efficiency (blue) and dark count rate (red) depending on the bias current for our best WSi (a) and MoSi (b) detectors. We reach effiencies of $93\% \pm 3\%$ for both at 1064 nm. The MoSi detectors are however improved with regards to the dark count rate which stays below 0.01Hz well after the plateau has been reached, as opposed to dark counts in the 1Hz range for maximum SDE in the case of WSi. The possibility of going further in the plateau presents as well benefits for state heralding.

strate the generation of high-purity single-photon states [58] presented in the next chapter.

In the last year, further improvements have been made by NIST through the use of another material, also amorphous, Molybdenum silicide (MoSi). While they exhibit comparable SDE, these detectors have a much greater switching current and lower dark count rate. The response of our best MoSi detector is presented in figure 3.4 (b). We reach quantum efficiencies close to 93% for a dark count rate below the 100 mHz level well into the plateau. This last generation is therefore perfectly suited for our experiments. The ability to go deeper in the plateau leads to more defined triggers higher in amplitude which increases the state generation quality.

2 Cooling system: two methods

The superconducting nanowire single photon detectors need to be maintained at temperatures below 2 K to stay in the superconducting regime. Two methods for cooling were used in this thesis. The first and time-honored one consists in direct dipping into liquid helium, which presents some inconvenience including degradation of the detectors and is limited to the use of only two detectors. In consequence, we have been working on a new method. Over the last two years, we have worked on the installation of a commercial cryocooler made by the company **MyCryoFirm**. We will present in this section both methods and the current issues with the cryocooler.

2.1 First method: Dipping into helium

The apparatus, adapted from a commercial system made by **Scontel**, is presented in figure 3.5. This method consists in placing the detectors at the end of a cane surrounded by a double-wall isolated enclosure. As can be seen in figure 3.5 (a), the detectors have no

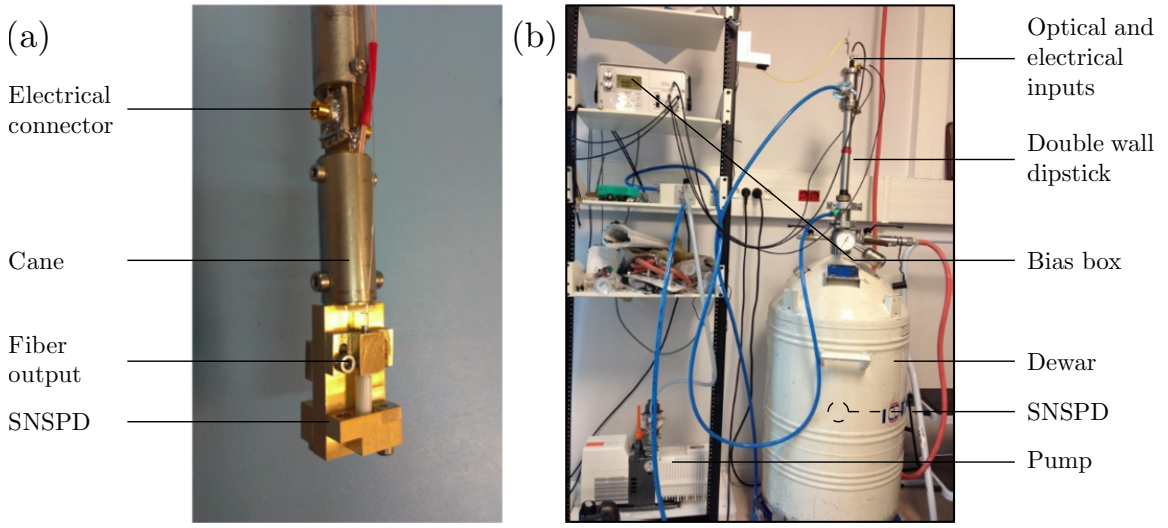

Figure 3.5: **Mounting and cooling system with the liquid helium based method**. (a): Mounting of detectors. Up to two SNSPDs can be installed at the end of the cane. Optical (electrical) connection is made through 1 m long anti-reflexion coated fibers (SMA cables) that circle around the cane all the way to the top. This allows both electrical and optical noise filtering because of the slow paced temperature drop when following the cables or fibers. (b): Cooling and measurement system. The cane is enclosed in a double wall dipstick plunged into a helium dewar. Vacuum pumping leads to a temperature decrease inside the double-wall. The bias box provides the bias current and routes the trigger voltage pulses to the experimental oscilloscope.

protective casing. The fibers are plugged directly on the ferule on one end and circle the cane all the way to the top of the double wall enclosing. SMA electrical connectors allow the application of the bias current. The double wall is directly dipped in a 60 L dewar of liquid helium, see figure 3.5 (b). The presence of a thin capillary at the bottom of the enclosure allows the inflow of helium from the dewar which submerges the detectors. The inside of the double-wall is then pumped by a Pascal SD series rotary vane pump (**Adixen**). The resulting adabiatic relaxation of the gaseous helium in the double wall leads to a drop in temperature following the Joule-Thompson effect. We can reach with this setup temperatures consistently under 1.9 K, below the critical temperatures for all detectors considered.

This method gives good results in terms of temperature and noise level when monitoring the voltage pulses. It has however some drawbacks. The rotary vane pump is rated at 15 hours of autonomy which limits the possible experimental duration. The double wall dimensions allow for just two detectors simultaneously which constrains as well the type of states that can be created. Lastly, the fact that the detectors are not protected can lead to some damage, in part because of the relative cleanliness of the liquid helium available but also because the vacuum seal's imperfections can lead to the formation of ice inside the double wall when we need to remove the detectors. In consequence, we observe a degradation of the detectors after repeated use: the anti-reflective coatings on the sensitive surface can become scratched and the micro-bondings making electrical contact between the detector and the coaxial connector can break. Although they can be bonded back, the procedure becomes complicated as the detector's surface becomes increasingly uneven.

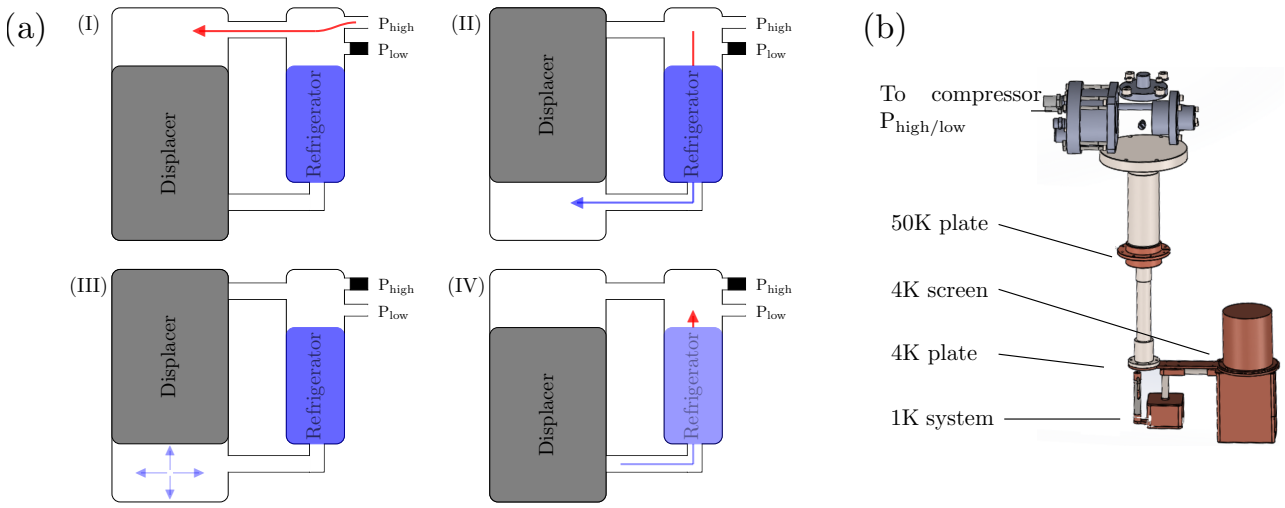

Figure 3.6: **Cooling cycle and commercial cold-head**. (a): Single stage Gifford-McMahon cooling cycle. P_{high} and P_{low} are ports linked respectively to the high and low pressure outlets of a compressor. At the beginning of the cycle and because of the previous step (IV), the refrigerator is cooler than the input gas. (I): Pressure increase at constant temperature. (II): The displacer is moved to the top which forces the gas to go through the refrigerator to the lower chamber. The refrigerator is cooler so the temperature of the gaz lowers at constant pressure. (III): The low pressure port is open so the gas expands and cools. This is the main cooling part of the cycle. (IV): The displacer is moved up which forces the cool gas to go through the refrigerator which is cooled in the process. At its output the gas is close to ambient temperature. Figure (b): 4 K cooling. The commercial RDK 101-D cold head is operated using the HC-4E2 compressor. The cold head uses two distinct Gifford-McMahon cycles. The first one cools down the 50 K plate to 50 K, the second one is used to go down below 4 K. The 4 K plate maintains the 1 K system close to 3 K.

2.2 Second method: Installation of a 1.5 K cryo-cooler

Because of the physical degradation observed on the SNSPD and in order to devise longer experiments using more detectors, we decided to transition to a cryo-cooler. The objective is to be able to cool down up to 4 detectors at less than 1.5 K continuously for up to 5 days. The installation of the whole apparatus started more than one year ago and is still not finished because the cryo-cooler was custom made for our experiment. Many issues have arisen during the implementation, among whose the breaking of two connection cables and the failure of the compressor during the summer of 2017. As of the writing of the manuscript, the setup is close to operational and some noise characterization of the triggering signals has been possible to make. The cryo-cooler was built by the company **MyCryoFirm** and is based on a commercial two-stage Gifford-McMahon [67] cooler cold head to reach 4 K. The final temperature of 1.5 K is attained through the adiabatic relaxation of He^4 in a pot in contact with the 4 K plate. We will now present the principle of the Gifford-McMahon process and then the system used to perform the Helium relaxation and go to 1.5 K.

Reaching 4 K: Two-stage Gifford McMahon cooler

To go down below 4 K, we use the RDK 101-D cold head and the water-cooled HC-4E2 helium compressors from **Sumitomo**. The cooling process is based on the Gifford-McMahon (GM) cooling cycle presented in figure 3.6 (a). Although the process presented is for a single-stage cooler, the principle is easily extended to the experimentally used two-stage cooling pro-

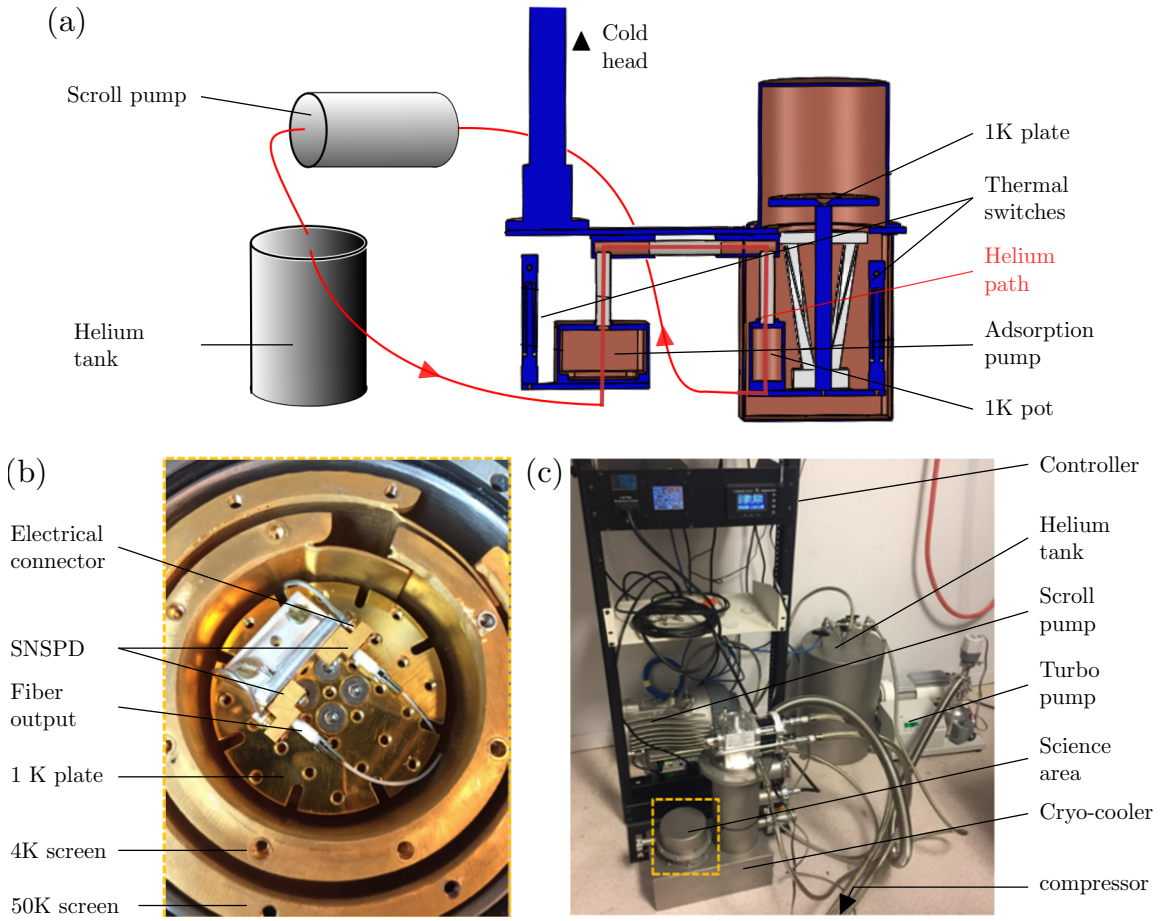

Figure 3.7: **Cryo-cooler: details**. (a): Global setup for the helium circuit. The Helium is initially kept in a tank placed outside the cryocooler. A scroll pump is used to make the helium circulate in the circuit, from the tank to the cryocooler. Inside the cryocooler, the helium goes through an adsorption pump and into a small pot. The Helium will then be liquefied to 1 K. Through the action of the thermal switch, the coal pump adsorbs the helium vapor, thus cooling down the liquid helium bath contained in the 1 K pot. It is thermally connected to the 1 K plate on which are placed the detectors. (b): Science area and detector mounting. The SNSPDs are put in thermal contact with the 1 K plate. The electrical connections with the outside are placed below the 1 K plate. We use fibers of 1.2 m and make them circle a few times around the 4 K and 50 K screens before leaving the cryo-cooler. (c): Outside arrangement. The helium tank is set next to the cryo-cooler and helium is pumped from the tank towards the 1 K pot using the scroll pump. Vacuum in the enclosure is made using the turbo pump.

cess. One only needs to use the gas cooled after the first stage as input to the second stage. There are four steps in the cooling procedure. The compressor feeds to the top chamber high pressure gas at ambient temperature. A moving piece called the *displacer* then moves up and forces the gas to go through a colder element called the *refrigerator*. Then, going back at low pressure, the gas follows an adiabatic relaxation in the lower chamber and drops in temperature. Finally the displacer forces helium through the refrigerator which is cooled down. In the next cycle the adiabatic expansion will start at a lower temperature because the refrigerator is colder, thus driving the gas to low temperatures after many cycles.

In the cold head used and pictured in figure 3.6 (b), the process is done simultaneously at two different locations. The first one cools helium down to 50 K which is then fed as input to the second where helium can go below 4 K. This is the *two-stage* process and is made by moving the two displacers in unison. Thermal screens isolate both the 50 K and 4 K stages. As can be seen in figure 3.8, the temperature of 4 K is reached in about 9 hours and the stage finally stabilizes at 3 K.

Going below 2 K

The working temperature for the detectors is reached through adsorption cooling of helium liquefied in a small pot in contact with the 4 K stage. The placement of the key components is presented in figure 3.7 (a) and (c). The helium is initially in a tank placed next to the cryo-cooler and maintained at a pressure of 800 mbar. A turbo pump drives pressure in the cryo-cooler enclosure down to $3 * 10^{-7}$ mbar for thermal isolation. A scroll pumps encourages the circulation of helium from the tank to the inside of the cryo-cooler. In figure 3.7(a) we show the path followed by Helium in the 1 K system. Inside the enclosure, the pumped helium passes through through the adsorption pump then goes into the 1 K pot before leaving. Two thermal switches can open or close thermal contact between either the adsorption pump or the sample stage with the 4 K screens. The cooling steps are then the following:

- Pre-cooling: Both thermal switches are closed, the cold-head starts to cool down the 1 K system, gaseous helium is pumped in the pot with the scroll pump.
- Once the system goes under 4.2 K, the adsorption pump thermal switch is opened. The pump is turned on which leads to degassing of helium. The pressure rises and the gas condensates in the pot.
- Once most of the helium has liquefied, the sample stage thermal switch is opened and the one connected to the pump is closed. The adsorption pump bluntly cools down and adsorbs the helium vapor. This drives down the temperature of the helium bath and goes below 2 K.

2.3 Cooling sequence and improvements

The temperature of the 1 K and 4 K stages are plotted depending on time in blue and red in figure 3.8. After 10 hours, they respectively stabilize at 1.34 K and 3 K while the pressure in the helium tank goes down as more helium is liquefied. The sample stage can be maintained at working temperature until all the helium in the outside tank has been consumed. The sample stage can now be maintained below 1.5 K with detectors plugged in for about 5 days. This represents a good improvement to the previous cooling system as we

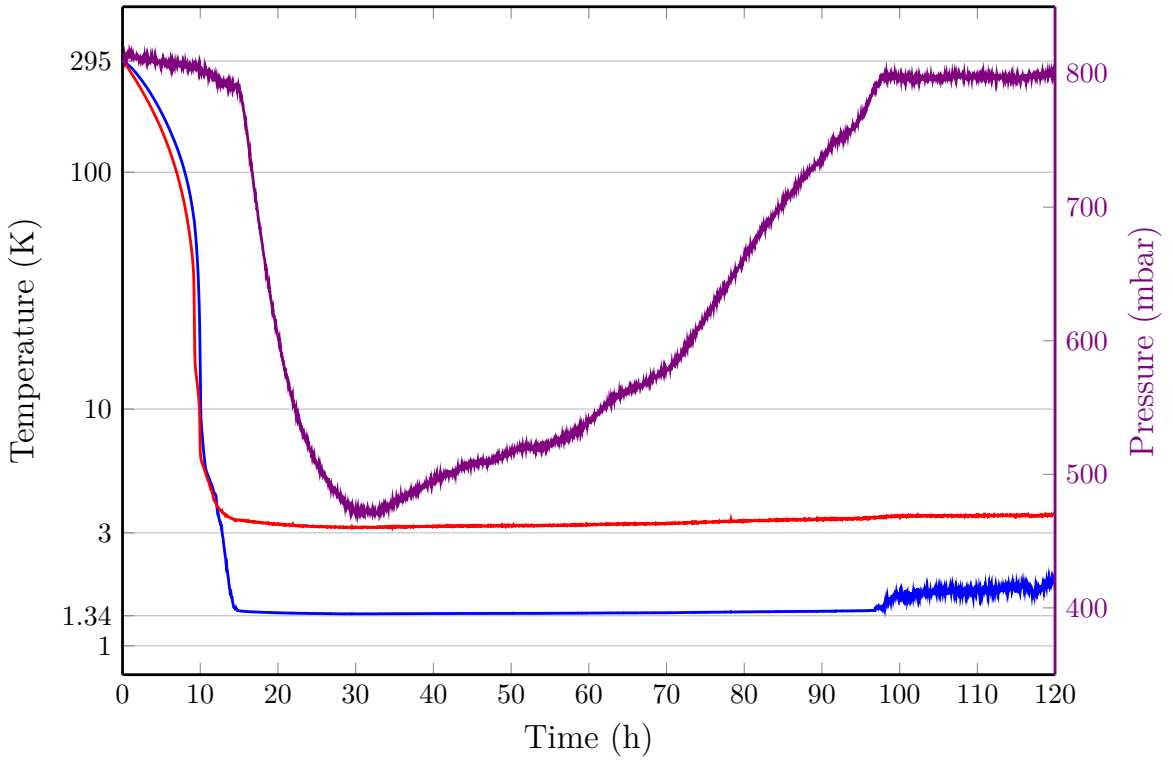

Figure 3.8: **Cooling cycle**. Red (respectively blue) curve: temperature at the 4 K (respectively 1 K) stage, depending on time. Violet curve: Pressure in the outside Dewar in mbar. When the 4 K stage reaches its working temperature of 3 K, liquefaction can start in the pot connected to the 1 K stage. This leads to a drop of pressure in the outside tank. The cold stage reaches 1.34 K after 10 hours. The temperature is maintained until all liquid helium in the 1 K pot has evaporated. The temperature then rises at a speed that depends on the thermal isolation. We reach close to five days of autonomy.

can reach lower temperature for more detectors and for longer experimental runs with a lower risk of damage. There are still some improvements to make with regards to the detectors mounting on the sample stage. An adaptation is needed in order to accommodate for more detectors. We also want to improve the mechanical isolation of the cryo-cooler as it leads to vibrations that need to be minimized.

2.4 Issues remaining

Ultimately, and in spite of these improvements, the two methods have to be compared in terms of the quality of the triggers obtained from impinging photons. In that regard, the new cooling system still needs work because we observe higher electrical noise on the triggering signal. The main noise issue concerns the scroll pump. When functioning, it introduces a lot of noise as shown in figure 3.9. Even without the scroll-pump, we observe overall a smaller signal to noise ratio on the triggers with this new apparatus even though the lower temperature translates to bigger voltage pulses. Work is still being done to improve the situation, we've noticed some grounding issues and cross-talk between the controller cables and the bias current cables. Working along with **MyCryoFirm**, we should be able to resolve these issues in the near future. We are working on a different routing of cables and consider

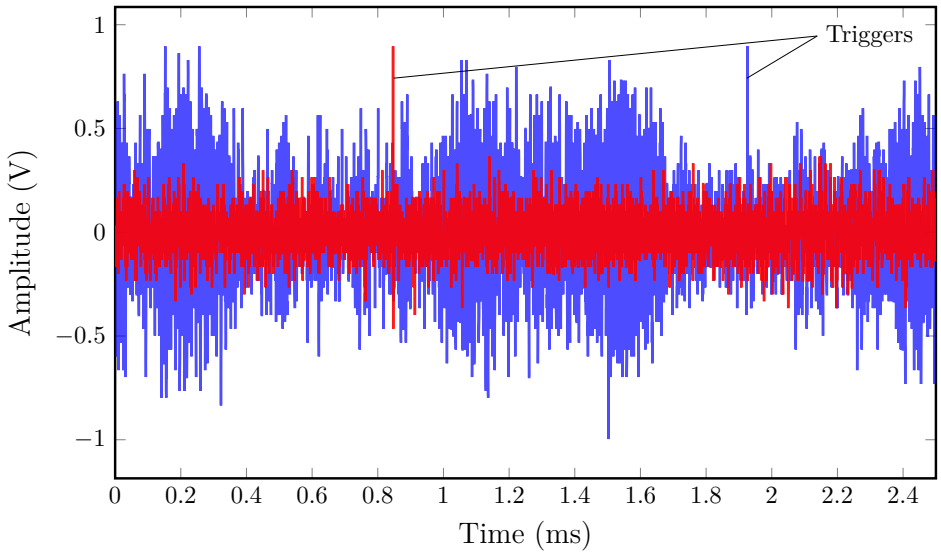

Figure 3.9: **Scroll pump noise issue**. In red is the amplitude noise visible when the scroll pump is unplugged. In blue, the scroll pump is plugged in. The noise observed is irregular and almost as high as the triggers.

the implementation of improved shielding.

In the current experimental state however, it is still preferable to use the dipstick with which we observe better overall state quality. The experiments made in the thesis were therefore limited to two detectors. As will be seen in chapter 5, it leads to longer experimental runs in the case of entanglement swapping. As we are confident in the long term viability of the cryo-cooler, we can expect an improvement in the quality of results and experimental duration once these problems are solved.

3 Conclusion

In this chapter we have introduced the principle of superconducting nanowire single-photon detectors and detailed some of their properties. We have also characterized detectors obtained as part of a collaboration with NIST and JPL. The latest detectors exhibit system detection efficiencies above 90% and dark count rates below the 100 mHz level. We also reported on two cooling systems we currently use. The first one, which consists in direct dipping into helium, enables us to use two detectors at the same time with limited noise but leads to degradation of the SNSPDs over time. The second method uses a cryocooler and allows us to use more detectors without risk of damage. There are still some noise issues however that need to be sorted before we can fully transition to this setup.

Having presented in this first part the resources available on our system and our methods for the generation of DV and CV non-Gaussian states, we now come to the description of hybrid entanglement of light. In the next chapter, we will present our method for its realization and present the first hybrid protocol realized during this thesis: the remote preparation of arbitrary CV qubits from local measurements on the DV mode of our hybrid entangled state. Finally, in Chapter 5 we consider the implementation of non-locality tests and demonstrate quantum steering using hybrid entanglement.

Part II

Hybrid entanglement and non-locality tests

Chapter 4

Hybrid entanglement of light and remote state preparation

In this chapter, we introduce hybrid entanglement of light between continuous and discrete-variable states. Its first demonstration was realized in our group in 2014 [29] and it is at the heart of most experiments performed during this thesis. We will first present some of the benefits of the hybrid approach to quantum information processing and then detail our protocol for the generation of hybrid entanglement. The procedure combines the resources presented in chapter 2 and uses two OPOs of different phase-matching. Then we report on the first protocol using hybrid entanglement we have realized: the remote preparation of arbitrary CV-encoded qubits. This work was recently published [68]. This protocol is the first step to more complicated schemes such as the demonstration of quantum steering we will report on in Chapter 5 and quantum teleportation between discrete and continuous variable encoded qubits, a necessary tool for the implementation of hybrid quantum networks.

Contents

1 Hybrid entanglement of light

In this section, we first present the hybrid approach to quantum information processing and motivate the generation of hybrid entanglement of light. We then detail the protocol used for its creation and some of the features of the state we obtain experimentally.

1.1 The hybrid context

The term hybrid characterizes any experiment that uses DV and CV resources jointly, be it states, gates or measurements performed [69]. Fully discrete or continuous variable protocols present specific advantages and drawbacks [70]. Continuous variable resources allow the implementation of deterministic gates [71]. Using homodyne detection, it also allows unambiguous state characterization that makes use of highly efficient photodetectors. Discrete variable resources allow only probabilistic gates such as photon subtraction but their implementation is less sensitive to detection loss.

The two state-generation protocols described in Chapter 2 can already be seen as hybrid experiments. In the case of the Fock state generation, the DV state is characterized using CV homodyne detection. Schrödinger kitten states on the other hand are an example of DV qubits encoded on CV coherent states: $c_\alpha |\alpha\rangle + c_{-\alpha} |-\alpha\rangle$. Their generation is dependent as well on photon-subtraction, an inherently DV process. The difference in encoding leads to practical advantages as it enables fault tolerant quantum computing [72] using simpler resources than DV-state encoded qubits when $|\alpha| > 1.2$ [73] —but with higher sensitivity to channel loss as a trade-off.

More generally, the hybrid approach was proved fruitful in recent years as many protocols have been advanced and implemented [24]. Of particular note are the proposed DV teleportation of CV states [25] and the experimentally realized CV teleportation of DV qubits [26]. These two examples highlight the advantages of going hybrid: The former enables teleportation of CV states with high-fidelities which would be in a CV-only context possible only in the limit of infinite squeezing and the latter is a first demonstration of the otherwise inaccessible deterministic teleportation of DV qubits. Other experiments have demonstrated Gaussian entanglement distillation using single-photon subtraction [74, 75, 76]. In our group we have used homodyne detection as a CV entanglement witness for DV entanglement [27]. Going further, we can hope for the implementation of nearly deterministic universal gate operations thanks to the hybrid approach for $\alpha \approx 1$ [77]. It is also useful for quantum computation protocols using cluster states [78] or following the quantum bus method [79] as well as for quantum key distribution [80, 81]. Many of the proposed protocols use as key resource what is the core of this thesis: hybrid entanglement of light. We will now introduce it as an essential component for the realization of heterogeneous quantum networks.

1.2 Definitions and goals

In the context of quantum networks, the hybrid approach entails communication between parties working with different encodings as schematized in figure 4.1 (a). Users of CV and DV resources can interact through the use of hybrid entanglement generated in a central node. Although many types of hybrid entanglement exist [82], our focus is on two-mode pure states of the form

$$|\Psi\rangle = \sum_n |n\rangle_{\mathrm{DV}} |\psi_n\rangle_{\mathrm{CV}} \tag{4.1}$$

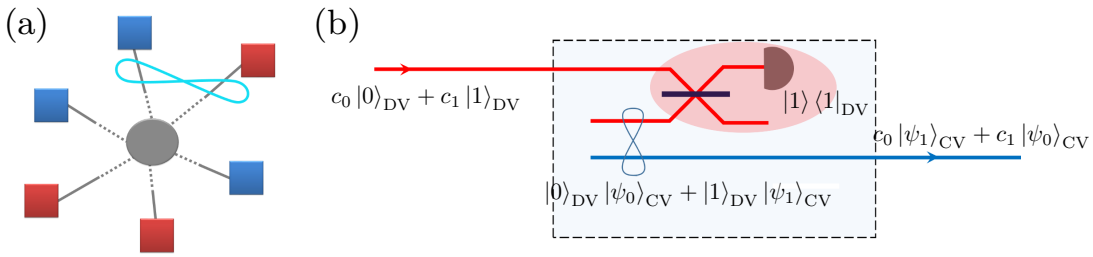

Figure 4.1: **The hybrid approach**. (a): Hybrid quantum network. The interaction between nodes based on different encodings, *i.e.* CV in blue and DV in red, is possible thanks to hybrid entanglement. (b): DV to CV quantum converter. The conversion is done through quantum teleportation by mixing the DV mode of hybrid entanglement with the qubit to teleport then applying a Bell state measurement. The qubit information becomes encoded on qumodes $|\psi_0\rangle_{CV}$ and $|\psi_1\rangle_{CV}$.

where $\{|n\rangle_{DV}\}_n$ is the complete orthonormal basis for the DV mode and the $|\psi_n\rangle_{CV}$ are infinite-dimensional qumodes. Depending on the setup used by the interacting parties and the protocol chosen, the router has to adapt its entangled state. The DV eigenstates can be polarizations $|H\rangle$ and $|V\rangle$ or Fock states for example.

Hybrid entangled states are essential to the implementation of hybrid networks as they allow in particular the realization of quantum teleportation between two encodings. As an illustration, the principle of a DV to CV quantum converter is shown in figure 4.1 (b). This protocol allows the conversion of an input DV-encoded qubit $c_0 |0\rangle_{DV} + c_1 |1\rangle_{DV}$ into a CV-encoded qubit $c_0 |\psi_1\rangle_{CV} + c_1 |\psi_0\rangle_{CV}$. This is achieved by the application of a joint Bell measurement on the DV-encoded qubit and the DV mode of the hybrid entangled state which then results in the creation of the corresponding CV-encoded qubit (up to a Pauli operator in the general case). This protocol represents one of our group's main goals and we will present in Chapter 6 the progress towards its implementation. It is however just one example of the possibilities afforded by hybrid entanglement of light and we have performed several protocols during this thesis. We will report in this chapter on the remote preparation of arbitrary CV-encoded qubits, in Chapter 5 on the realization of Einstein-Podolsky-Rosen steering, and finally in Chapter 6 and 7 on preliminary results of entanglement swapping between encodings.

Before this, we will present the experimental setup used for the generation of hybrid entanglement of light and the results obtained as published by the group in the 2014 paper by Morin *et al* [29].

1.3 Generation of hybrid entanglement

The hybrid-entangled state we can generate with our resources is given by:

$$|\Psi\rangle = \frac{1}{\sqrt{2}}(|+\rangle |\alpha\rangle + e^{i\phi} |-\rangle |-\alpha\rangle), \tag{4.2}$$

with $|\pm\rangle = 1/\sqrt{2}(|0\rangle \pm |1\rangle)$ two equal-weight qubits in the basis spanned by vacuum and single-photon Fock states. This state is well suited for the implementation of quantum protocols with the non-Gaussian resources introduced in Chapter 2 but has some specific advantages and drawbacks compared to other types of hybrid entanglement. The realization of nearly deterministic universal gates with hybrid entanglement when using a polarization encoding on

the DV side $|\pm\rangle = |H\rangle \pm |V\rangle$ [77] but is not guaranteed for the state of equation (4.2) as there is no deterministic and linear way to flip between vacuum and single-photon states. It presents however the benefit of being more resilient to losses, for example in quantum teleportation protocols [83] because the DV mode will always remain in the $\{|0\rangle, |1\rangle\}$ subspace when adding losses. This loss-resilience is of great interest for our goals of performing proof-of-principle experiments. The creation of a polarization based hybrid entangled state is however also among our goals, however it remains a longer term objective as it requires the installation of a third OPO.

1.3.1 Experimental implementation

The experimental setup is presented in figure 4.2. It combines the two previously-introduced Fock and cat state generation experiments by joining their conditioning paths in an indistinguishable fashion so that the heralding click is nonlocal. Namely, the tapped mode at the output of the type-I phase-matched OPO (OPO I) is mixed with the idler mode of type-II phase-matched OPO (OPO II) before the filtering and detection is performed. If the tapped and idler mode are indistinguishable, the detection of a photon can be due either the presence of a single-photon on the DV mode or a photon-subtracted squeezed vacuum state on the CV mode. A detection event therefore heralds the state

$$|\Psi\rangle \propto |0\rangle_{\mathrm{DV}} \hat{a}\hat{S} |0\rangle_{\mathrm{CV}} + e^{i\phi} |1\rangle_{\mathrm{DV}} \hat{S} |0\rangle_{\mathrm{CV}}, \tag{4.3}$$

here $\hat{a}$ and $\hat{S}$ act on the CV mode. As we have seen in Chapter 2, we have $\hat{a}\hat{S}|0\rangle \approx |cat_-\rangle$ and $\hat{S}|0\rangle \approx |cat_+\rangle$ for different values of α depending on the squeezing amount. We set the pump power to have 3 dB of squeezing at the output of OPO I. In these conditions, and as shown in Figure 2.9, the heralded state has high fidelity with the hybrid state:

$$|\Psi\rangle \propto |0\rangle_{\mathrm{DV}} |cat_-\rangle_{\mathrm{CV}} + e^{i\phi} |1\rangle_{\mathrm{DV}} |cat_+\rangle_{\mathrm{CV}}. \tag{4.4}$$

Although the fidelities of the odd and even CV states are highest with state of different size ($|cat_-\rangle$ with $|\alpha|^2 = 1.1$ and $|cat_+\rangle$ with $|\alpha|^2 = 0.4$) we should expect a good fidelity for both kittens set to $|\alpha|^2 \approx 0.8$. Then a rotation of the DV basis leads to the expression in equation 4.2.

Nonlocal conditioning. The main difficulty of implementation is in making the heralding modes indistinguishable in all degrees of freedom. It is therefore necessary to match the heralding rates of both OPOs. This is done first by rotating the tapped mode of OPO I into a horizontal polarization and mixing on a PBS with the vertically polarized idler mode of OPO II. The mixed mode is then projected using a half wave-plate and PBS on an intermediate polarization set such that both heralding rates are identical. The lost signal is used for phase locking on photo-diode P3. It is also required to match the bandwidth of the two OPOs. Being of similar structure, the cavity lengths of both OPOs are finely adjusted by matching the temporal modes observed separately.

Phase locking and monitoring. The matching of both heralding modes will only lead to a mixed state if the relative phase between the two is not fixed at each realization. It is therefore locked using the interference fringes between the two seed beams. We choose to lock to a relative phase $\phi = \pi$. The state characterization is done as usual using homodyne detection. In this case it is necessary to monitor the phase of both modes. The lock at

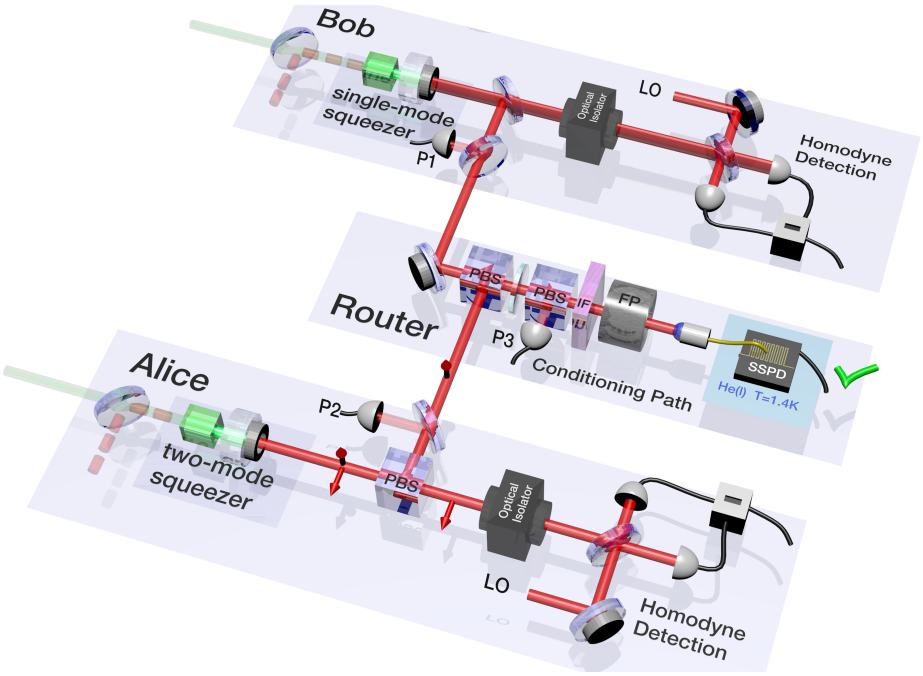

Figure 4.2: **Experimental setup for hybrid entanglement generation**. Two OPOs of type-I (OPO I) and type-II (OPO II) phase matching are pumped well below threshold. OPO I produces 3 dB of squeezed vacuum at its output and OPO II sees the creation of pairs of single photon. The idler mode of OPO II is mixed with 3% of tapped signal from the output of OPO I before sent on the conditioning path. The mixed mode is then filtered in frequency using a Fabry-Pérot cavity and an IR filter before being fiber-coupled to a SNSPD. The two heralding modes are indistinguishable through fine tuning of both OPOs' bandwidth and the balancing of their respective heralding rates. The creation of the same state at every heralding click is ensured by phase locking between the two conditioning paths at P3. The detection of a single photon can therefore herald the creation of either a CV or DV state thus generating hybrid entanglement.

P3 allows us fix the relative phase between the two-modes and perform two-mode state reconstruction.

Data set and state reconstruction. We record for each heralding event the homodyne data on both modes and apply the temporal mode function on and normalize to the variance of vacuum each raw signal to obtain quadrature results. We acquire 100 000 data events labeled by n to obtain the pre-processed table $\{n, \langle\hat{x}_{\mathrm{I},f}^{(n)}\rangle, \langle\hat{x}_{\mathrm{II},f}^{(n)}\rangle, \theta_{\mathrm{I}}^{(n)}, \theta_{\mathrm{II}}^{(n)}\}_n$, where n is the heralding event's number. Where the subscripts I and II refer to the mode on which was made the quadrature measurement at the corresponding local oscillator phase. The state reconstruction is done using the usual Maximum-Likelihood optimization but for a two-mode state. We set the optimization for the Hilbert space spanned by $\{|0\rangle, ... |6\rangle\}$ for the DV mode and $\{|0\rangle, ... |10\rangle\}$ for the CV mode, well beyond the subspace we expect to be populated. We also give result both with and without correction for detection losses which is fixed at 15% on both modes. At the end of the reconstruction we obtain a 77-by-77 two-mode density matrix that can be analyzed.

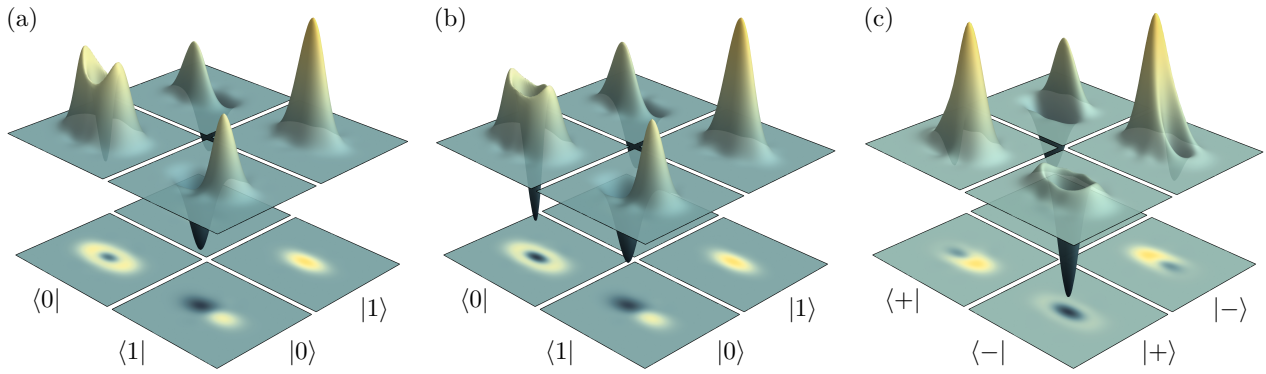

Figure 4.3: **Experimental results**. Panels (a) and (b): Wigner functions of the reduced density matrices $\langle i|\,\hat{\rho}\,|j\rangle_{\mathrm{DV}}$ with $i,j \in \{0,1\}$. The coherence terms $i \neq j$ lead to complex values of the Wigner function so we plot the real and imaginary part of $\langle 0|\,\hat{\rho}\,|1\rangle_{\mathrm{DV}}$ respectively in the top and bottom square. The results are presented with no correction in panel (a), with correction for 15% detection loss in (b). (c): Results in the rotated $\{|+\rangle, |-\rangle\}$ basis corrected for detection loss.

1.3.2 Results

Symmetric case. The Wigner function of the entangled state is four-dimensional which makes it complicated to represent it on a 2D plane. The 77-by-77 density matrix formalism does not provide immediate insight on the state created as well. We therefore present results: we show the Wigner functions of the single-mode density matrices obtained by projecting the DV mode on the Fock basis $\langle i|\,\hat{\rho}\,|j\rangle$, with $i,j \in \{0,1\}$. This is valid if the higher dimensional modes on the DV side are not populated. As they account for less than 2% of the total trace, the experimental data is accurately represented.

In figure 4.3 (a), we show the results without correction for detection loss. The diagonal projections indeed correspond to even and odd cat states. The Wigner function of the odd cat state is negative at the origin of phase space as expected with $W(0,0) = -0.053$. We also note the presence of non-negligible coherence terms which is consistent with a measured entanglement negativity (see chapter 1) of $\mathcal{N} = 0.27$. Next we consider the state when corrected for 15% of transmission loss in figure 4.3 (b). We see a stronger negativity of the Wigner function for the odd cat state $W(0,0) = -0.169$ and measure a strong entanglement negativity $\mathcal{N} = 0.38$, to be compared to $\mathcal{N}_0 = 0.5$ which is the maximum value that can be reached theoretically. The panel (c) of figure 4.3 finally presents the corrected results in the qubit basis $\{|+\rangle, |-\rangle\}$. We see overall a fidelity of 77% with the target state of equation (4.2) for $\phi = \pi$ and $\alpha = |0.9|$. This experiment was the first published demonstration of hybrid entanglement of light [29].

Asymmetric case. The maximally entangled state is obtained by matching the heralding rates of both OPOs. It will however be useful in some protocols such as remote state preparation and quantum steering to have an asymmetric hybrid state to compensate for other experimental biases. By rotating the projecting half-wave plate, we can adjust the heralding rates and create the state

$$|\Psi\rangle = \sqrt{R}\,|0\rangle_{\mathrm{DV}}\,|cat_-\rangle_{\mathrm{CV}} + e^{i\phi}\sqrt{1-R}\,|1\rangle_{\mathrm{DV}}\,|cat_+\rangle_{\mathrm{CV}}\,, \tag{4.5}$$

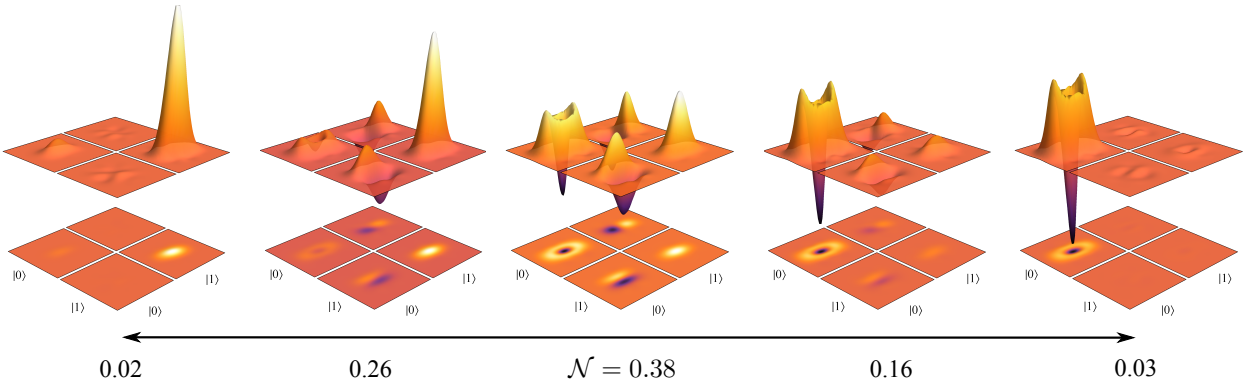

Figure 4.4: **Asymmetric states and entanglement negativity**. Hybrid state and negativity of entanglement depending on the heralding rate bias. By rotating the mixing half-wave plate, we can go from fully separable $|1\rangle |cat_+\rangle$ on the left to the maximally entangled hybrid state and then back to fully separable $|0\rangle |cat_-\rangle$ on the right. The corresponding entanglement negativities are shown below the plots

where the probability of having the heralding click coming from OPO I is $R/(1-R)$ times as big as the probability of it coming from OPO II. As shown in figure 4.4, we can vary from maximally entangled hybrid state to fully separable single photon or odd cat state by varying the angle of the mixing wave plate.

This hybrid resource is the foundation for most protocols we report on in this thesis. The first one we will present is the remote preparation of arbitrary CV-qubits. It is a natural extension of our experiment in that it is linked to the representations we use to show our hybrid entangled state. One can see from the figure 4.3 that if we perform local projections on $|0\rangle$, $|1\rangle$, or $|\pm\rangle$ on the DV side, we generate remotely on the CV mode respectively odd or even cat states and coherent states. Extending the concept, it is possible to project on any qubit on the DV mode to remotely prepare any CV-encoded qubit.

2 Remote preparation of arbitrary CV-encoded qubits

In this section we report on the first protocol we implemented using hybrid entanglement and that was recently published in [68]: the remote preparation of arbitrary CV-encoded qubits. Harnessing hybrid entanglement allows us to go further than what was possible using our protocol for Schrödinger kitten state generation because it enables the remote creation of any superposition of $|\alpha\rangle$ and $|-\alpha\rangle$ rather than evenly-weighted states. After a quick presentation of remote state preparation and its uses, we will detail our implementation and the results we have obtained.

2.1 Principle

2.1.1 Context

The most versatile method for the transmission of quantum information in a network is quantum teleportation which allows the transfer of an unknown quantum state to a distant party [16]. As presented earlier (see figure 4.1 (b)), it requires the application of local Bell measurements jointly on one mode of an entangled resource and on the state to be transferred to retrieve the input state on the other entangled mode. The initial state is recovered —up to a Pauli operator that depends on the result of the Bell measurement. It is therefore necessary to send classical information to the teleported mode so as to know which operator to apply to complete the teleportation process. In practice, two bits of classical information need to be transferred to the distant party to fully recover the unknown quantum state.

In contrast, remote state preparation (RSP) refers to a different type of protocol for the transfer of quantum information in which the sender has complete knowledge of the state to be be communicated. It presents the advantage of requiring the transmission of less classical information than quantum teleportation [84], in practice one classical bit to recover a pure qubit [85, 86, 87]. RSP finds a variety of applications, ranging from long-distance quantum communication to loss-tolerant quantum-enhanced metrology [88]. In recent years, a number of optical demonstrations have been realized in DV and CV systems. Remote state preparations of polarization qubits were demonstrated based on polarization entanglement [89, 90, 91]. Transfer of single-photon and vacuum superpositions was also achieved based on single-photon entanglement [92] and continuous-variable RSP was demonstrated using Einstein-Podolsky-Rosen entangled beams [93, 94, 95]. These works were also extended to the preparation of multiqubit states [96, 97].

2.1.2 The hybrid approach

As our implementation is the first RSP demonstration in an hybrid DV-CV context, we will present the principle starting from ideal hybrid entanglement. Alice and Bob are two parties sharing the hybrid-entangled state $|\Psi\rangle$ of equation (4.2). In our case Alice, which has access to the DV mode (labeled A) of $|\Psi\rangle$, aims to remotely prepare arbitrary CV encoded qubits $c_+ |\alpha\rangle + c_- |-\alpha\rangle$ on Bob's CV mode (labeled B). To that end she locally performs the projective measurement $\hat{\Pi}_{\mathrm{A}}(\theta,\phi) = |\pi(\theta,\phi)\rangle \langle\pi(\theta,\phi)|_{\mathrm{A}}$, with

$$|\pi(\theta,\phi)\rangle_{\mathrm{A}} = \cos(\theta)\,|0\rangle_{\mathrm{A}} + e^{i\phi}\sin(\theta)\,|1\rangle_{\mathrm{A}}\,. \tag{4.6}$$

This results in the preparation on the CV mode of the state

$$\hat{\rho}(\theta,\phi) = \frac{\mathrm{Tr_A}(\hat{\Pi}_\mathrm{A}(\theta,\phi)\,|\Psi\rangle\,\langle\Psi|)}{\mathrm{Tr}(\hat{\Pi}_\mathrm{A}(\theta,\phi)\,|\Psi\rangle\,\langle\Psi|)}, \tag{4.7}$$

which gives us

$$\begin{aligned}\hat{\rho}(\theta,\phi) \propto \mathrm{Tr_A}\Big(\Big(\,|\pi(\theta,\phi)\rangle\,\langle\pi(\theta,\phi)|_\mathrm{A} \otimes \mathbb{1}_\mathrm{B}\Big) \times \Big(\,|0\rangle\,\langle 0|_\mathrm{A}\,|cat_-\rangle\,\langle cat_-|_\mathrm{B} \\ + |0\rangle\,\langle 0|_\mathrm{A}\,|cat_+\rangle\,\langle cat_-|_\mathrm{B} + (|0\rangle\,\langle 1|_\mathrm{A}\,|cat_-\rangle\,\langle cat_+|_\mathrm{B} + h.c.)\Big)\Big),\end{aligned} \tag{4.8}$$

and finally

$$\begin{aligned}\hat{\rho}(\theta,\phi) = \cos^2\theta\,|cat_-\rangle\,\langle cat_-| + \sin^2\theta\,|cat_+\rangle\,\langle cat_+| \\ + \frac{1}{2}\sin 2\theta(e^{i\phi}\,|cat_-\rangle\,\langle cat_+| + e^{-i\phi}\,|cat_+\rangle\,\langle cat_-|\,).\end{aligned} \tag{4.9}$$

In the case of big cat states $|cat_\pm\rangle \propto |\alpha\rangle \pm |-\alpha\rangle$ with $|\alpha| \gg 1$, we can rewrite equation (4.9) in the coherent-state basis as

$$\begin{aligned}\hat{\rho}(\theta,\phi) \propto (1+\sin 2\theta\cos\phi)\,|\alpha\rangle\,\langle\alpha| + (1-\sin 2\theta\cos\phi)\,|-\alpha\rangle\,\langle-\alpha| \\ + \Big((\cos 2\theta + i\sin 2\theta\sin\phi)\,|\alpha\rangle\,\langle-\alpha| + \mathrm{h.c.}\Big).\end{aligned} \tag{4.10}$$

With the right choice of θ and ϕ, we can therefore prepare in the limit of $|\alpha| \gg 1$ any CV-encoded qubit at the distant CV node. This protocol is a good example of the benefits of using hybrid entanglement. In the case of a polarization encoded hybrid state, it is straightforward to apply the operators $\hat{\Pi}(\theta,\phi)$ with linear optical components [89]. It is a bit more difficult in our case but still advantageous as compared to other schemes for CV-encoded qubits generation as they require several conditioning measurements [98].

2.2 Experimental implementation

The experimental setup is presented in figure 4.5 (a). Starting from a hybrid-entangled state, we can approximate the operators $\hat{\Pi}(\theta,\phi)$ using quadrature measurements done via homodyne detection on the DV mode. The operator is performed by conditioning, *i.e.* the measurement of appropriate quadrature values heralds the application of $\hat{\Pi}(\theta,\phi)$.

Conditioning on homodyne detection. To understand the general idea of this method, the marginal distributions of the quadrature corresponding to the single-photon and vacuum states are plotted in figure 4.5(b) in the ideal case. The measurement of a quadrature outcome equal to zero on Alice's side has to come from the vacuum component and will therefore project Bob's state onto the state $|\mathrm{cat}_-\rangle$. Similarly, a large value quadrature result, which most likely comes from the single-photon component, will project Bob's state onto the state $|\mathrm{cat}_+\rangle$. By choosing a given phase ϕ and a quadrature value Q, Alice can then remotely prepare any superposition of the form $c_+|\mathrm{cat}_+\rangle + e^{i\varphi}c_-|\mathrm{cat}_-\rangle$. In the ideal case and large $|\alpha|$ values, a quadrature measurement equal to $+1$ projects the state onto the equally-weighted superposition $|\mathrm{cat}_+\rangle + |\mathrm{cat}_-\rangle \sim |\alpha\rangle$, i.e., a coherent state. The remote preparation is therefore probabilistic, but heralded, as the right state is created only when the right result is obtained.

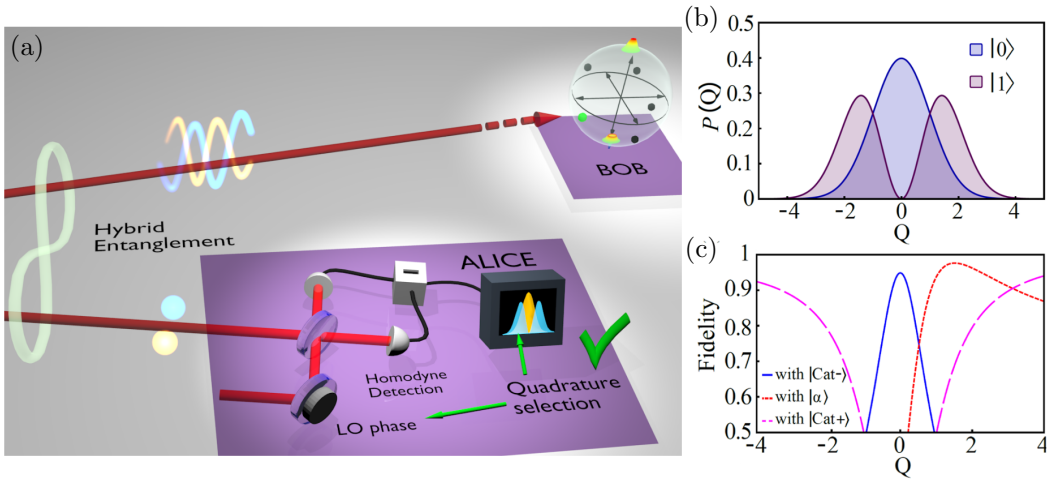

Figure 4.5: **Remote preparation of CV-encoded qubits using hybrid entanglement**. (a): Experimental setup. Alice and Bob located at two distant nodes share an entangled state $|0\rangle_A|\text{cat}_-\rangle_B + |1\rangle_A|\text{cat}_+\rangle_B$. Conditional on a specific quadrature measurement via homodyne detection, Alice remotely prepares any arbitrary superposition $c_+|\text{cat}_+\rangle + e^{i\varphi}c_-|\text{cat}_-\rangle$ on Bob's node. The measured quadrature is chosen by locking the local oscillator phase on a value ϕ and the preparation is heralded by the occurrence of a preselected value Q within an acceptance window of width Δ (typically taken equal to 20% of the shot noise value). The prepared state is characterized by homodyne detection, with an overall efficiency $\eta = 85\%$. (b) Marginal distributions of vacuum and single-photon states. (c) Theoretical fidelity of the remotely prepared state with different targeted superpositions as a function of the quadrature value Q, with $\phi = 0$ and $|\alpha| = 0.7$.

The classical piece of information that Alice needs to send to Bob is therefore whether or not the event is to be kept.

The superposition coefficients can be calculated as follows. The measurement implemented by Alice can be written in the form of the quadrature operator $\hat{Q}_\phi = \hat{X}\cos\phi + \hat{P}\sin\phi$ where $\hat{X}$ and $\hat{P}$ denote the canonical position and momentum observables. The measurement of a quadrature value Q projects the entangled state onto a quadrature eigenstate $\langle Q_\phi|$:

$$|\Phi\rangle_B \propto \langle Q_\phi|\Psi\rangle_{AB} = \langle Q_\phi|0\rangle_A|\text{cat}_-\rangle_B + \langle Q_\phi|1\rangle_A|\text{cat}_+\rangle_B \tag{4.11}$$

with

$$\langle Q_\phi|0\rangle_A = \frac{1}{(2\pi)^{1/4}}e^{-Q^2/4} \quad \text{and} \quad \langle Q_\phi|1\rangle_A = \frac{Qe^{i\phi}}{(2\pi)^{1/4}}e^{-Q^2/4}.$$

The remotely prepared state on Bob's side can finally be written after normalization as:

$$|\Phi\rangle_B = \frac{1}{\sqrt{1+Q^2}}\left(|\text{cat}_-\rangle + Qe^{i\phi}|\text{cat}_+\rangle\right). \tag{4.12}$$

By associating with equation (4.9), we see that with a chosen quadrature value Q following $Q = \tan^2\theta$ and a local oscillator phase ϕ, we recover the operator $\hat{\Pi}(\theta,\phi)$. Figure 4.5(c) provides the expected fidelities to different targeted states as a function of the measured quadrature value Q. For this calculation, we consider our experimental case for which the mean photon number is limited due to the initial approximation in the entangled state generation. The fidelities are calculated for $|\alpha| = 0.7$. As a result, for instance at $Q = 0$, the fidelity

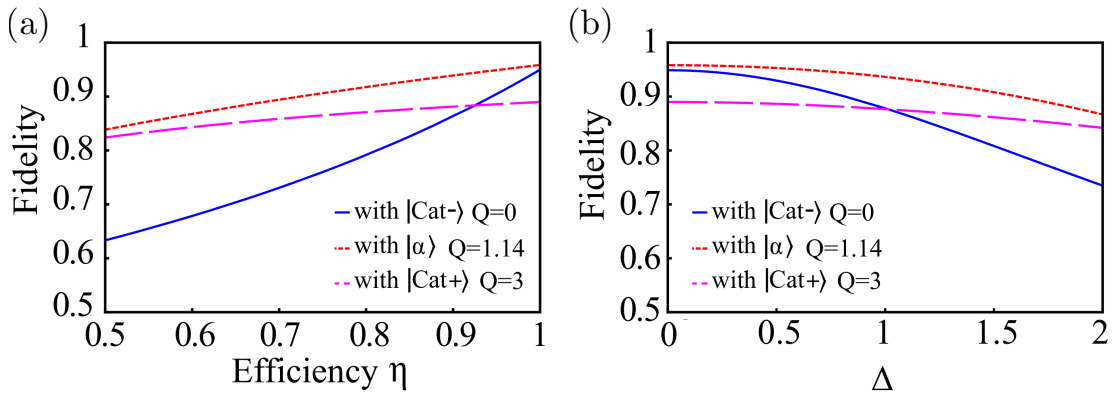

Figure 4.6: **Fidelity of the prepared states with the experimental imperfections**. (a): Theoretical fidelity as a function of the efficiency of the heralding homodyne detection. (b): Theoretical fidelity as a function of the window width Δ. The normalization is such that the variance of vacuum is $\sigma_v = 1$.

of the prepared state to $|\text{cat}_-\rangle$ is equal to 95%. For other values of Q, all superposition can be generated, and the measurement angle ϕ comes into play. In particular, for $Q = \pm 1.14$ and $\phi = 0$, one can obtain the coherent state $|\pm\alpha\rangle$. This conditioning value $|Q|$ is slightly larger than 1 due to the limited size $|\alpha|^2$.

Impact of losses and conditioning window. Experimentally, two parameters can lead to a reduction of fidelity [93]. The first one is the finite efficiency of the detection used for heralding, as shown in figure 4.6 (a). We see that the effect varies depending on the state one wishes to generate, the odd cat state is more sensitive to losses than the even cat state. This is because the former corresponds to a conditioning on vacuum and therefore is triggered in the case where the DV mode was initially populated by a single photon then lost in the environment. The latter will also be impacted but less significantly. The main effect of losses for this state is a drop in preparation rate as less events will be registered as positive. This in turn leads to a decrease in fidelity because the vacuum component will rise and there is a non-zero probability to obtain higher quadrature values when vacuum is measured. Alice can however adjust her conditioning choice Q so as to maintain good state fidelity with increased losses at the cost of a lower preparation rate.

The second parameter is the acceptance window in quadrature values. Indeed, to have a non-zero preparation rate, we condition not on a precise Q value but on a range of quadrature values $q \in [Q - \Delta/2, Q + \Delta/2]$. This leads to a loss of fidelity on the state generation as we herald

$$\hat{\rho} \propto \int_{Q-\Delta/2}^{Q+\Delta/2} dq \, \text{Tr}_\text{A}(|qe^{i\phi}\rangle\langle qe^{-i\phi}|\Psi\rangle \langle\Psi|). \tag{4.13}$$

The selection width Δ results in a trade-off between preparation rate and fidelity. However, the reduction in fidelity is only of second order with the width (see figure 4.6 (b)). This enables us to take Δ equal to 20% of the shot noise value. For such a selection band, centered for instance in Q=0, the success rate is around 5% while the fidelity is only decreased by a few percents.

Conditioning and state reconstruction. The homodyne conditioning is performed on the DV side by an active locking of the local oscillator (LO) relative phase desired. The locking is digital and performed using Arduino DUE microcontrollers. To prepare a larger range of CV-encoded qubits, we aim to lock the LO phase at many values. This is achieved by sweeping the LO phase during the sampling sequence fast enough to see a complete interference fringe with the seed beam on the homodyne signal then actively lock at the target power. The initial sweeping serves as calibration to recover the maximum and minimum of intensity and adjust the target intensity accordingly. It is necessary because of misalignment and thermal fluctuations that lead to changes of fringe visibility. During the holding sequence, the piezo-transducers are kept fixed as in previous setups. We estimate the phase noise to be below 3%.

To verify the quality of the prepared states, we also perform homodyne detection on the CV mode. At a given LO phase, many states can be prepared depending on the quadrature results obtained. The conditioning is applied after all homodyne data on both sides has been acquired. We acquire around 10^6 heralding events for each phase ϕ which leads to the pre-conditioned and pre-processed data $\{n, \langle\hat{x}^{(n)}_{\mathrm{I},f}\rangle, \langle\hat{x}^{(n)}_{\mathrm{II},f}\rangle, \theta^{(n)}_{\mathrm{I}}, \phi^{(n)}_{\mathrm{II}}\}_n$. We then keep only the events where $\langle\hat{x}^{(n)}_{\mathrm{II},f}\rangle \in [Q-\Delta/2, Q+\Delta/2]$ and perform single-mode tomography on the conditioned data which typically comprises 40000 events depending on the state prepared. Some of the experimental results for the preparation of different states therefore come from the same initial data run. The difference to the ideal experiment is only practical, one could send for example the CV mode in a delay line for long enough to get the quadrature results on the DV mode and decide to let it be sent or not.

2.3 Results

We come to the experimental results. A set of remotely-prepared states are presented in Fig. 4.7, inserted in a Bloch sphere where the poles are defined by the orthogonal states $|\mathrm{cat}_+\rangle$ and $|\mathrm{cat}_-\rangle$, with $|\alpha|= 0.7$. In order to graphically represent the states, for each prepared state $\hat{\rho}_{\mathrm{exp}}$ we determine the maximal fidelity with the state $\cos(\phi/2)|\mathrm{cat}_+\rangle + e^{i\varphi}\sin(\phi/2)|\mathrm{cat}_-\rangle$ and obtain thereby the spherical coordinates $\{\phi, \varphi\}$. The distance d to the center scales with the purity of the state, $d = \sqrt{2\mathrm{Tr}[\hat{\rho}^2_{\mathrm{exp}}] - 1}$. Each prepared state is represented by a number located in the sphere at the corresponding distance from the center d and we give next to it the corresponding experimental Wigner function. Table 4.1 gives a summary of the conditioning parameters used to prepare these states and the fidelity with the targeted state to be transferred. As these results show, our procedure enables the remote preparation of arbitrary CV qubits with a large fidelity to the target states. Fidelities above 80% are obtained, except for the state numbered 2, i.e., for a $|\mathrm{cat}_-\rangle$ target. As we explained earlier, this reduced fidelity is generally true for states lying closer to the south pole. We note also that the states numbered 3 and 4 are close to coherent states with opposite phase, as expected. However, they are not exactly lying on the sphere equator but slightly out of this plane due to the limited mean photon number $|\alpha|^2 < 1$. This smaller value of α also explains the small dip in values close to the origin of phase space.

We now investigate in more detail the control of the prepared superpositions as a function of the conditioning parameters. Figure 4.8 provides projections of the Bloch sphere along two planes, i.e., XZ and XY. Rotation of the states in these planes are controlled by independent parameters, namely the quadrature value Q and the phase θ, respectively. In figure (a), we

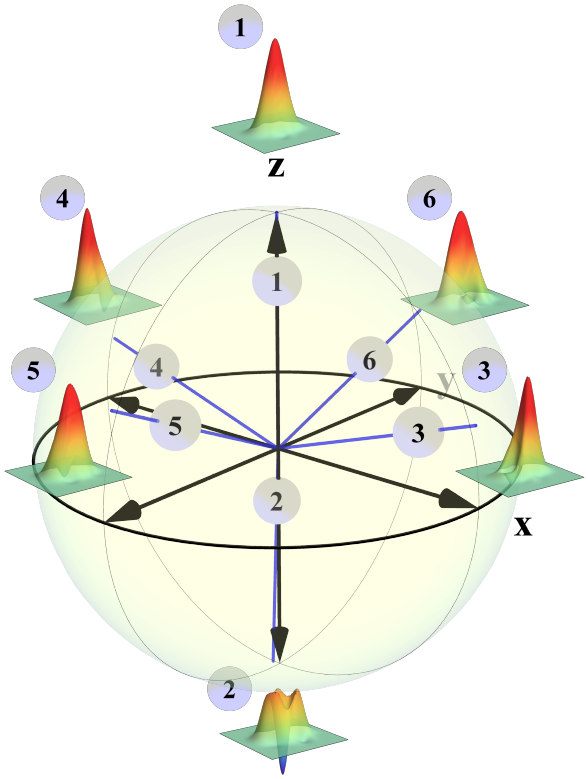

Figure 4.7: **Remotely prepared states** represented on a Bloch sphere and associated Wigner functions. The poles are the two orthogonal states $|\text{cat}_+\rangle$ and $|\text{cat}_-\rangle$, with $|\alpha|= 0.7$. The results are corrected for the $\eta = 85\%$ detection efficiency.

#	Target	Q, θ	$\mathcal{F}_{\lvert\alpha\rvert=0.7}$	Rate
1	$\lvert\text{Cat}+\rangle$	$\lvert Q\rvert\geq 2$, $\theta = 0$	86%	13.8 kHz
2	$\lvert\text{Cat}-\rangle$	$Q = 0$, $\theta = 0$	65%	9.6 kHz
3	$\lvert\alpha\rangle$	$Q = 1.14$, $\theta = 0$	85%	9.4 kHz
4	$\lvert-\alpha\rangle$	$Q = -1.14$, $\theta = 0$	85%	9.4 kHz
5	$\lvert\alpha\rangle + i\lvert-\alpha\rangle$	$Q = -1.14$, $\theta = \pi/2$	81%	9.4 kHz
6	$\lvert\alpha\rangle - i\lvert-\alpha\rangle$	$Q = 1.14$, $\theta = \pi/2$	80%	9.4 kHz

Table 4.1: **Features of the remotely prepared states**. Summary of the prepared states corresponding to each point on Fig. 4.7. The targeted states appear in the second column as well as the experimental fidelities $\mathcal{F}$ for $|\alpha|= 0.7$. Q and θ correspond to the quadrature value in unit of shot noise and to the local oscillator phase. For the points 2 to 6, the acceptance window Δ is equal to 0.2. The error bar on the fidelity is $\pm 3\%$. The last column provides the heralding rate.

can see the change of the weight of the superposition. We plot the Wigner function of several prepared states, each reconstructed from 40000 separate quadrature measurements. We can go from an odd cat state (number #2) to an even cat state (number #1) with intermediate

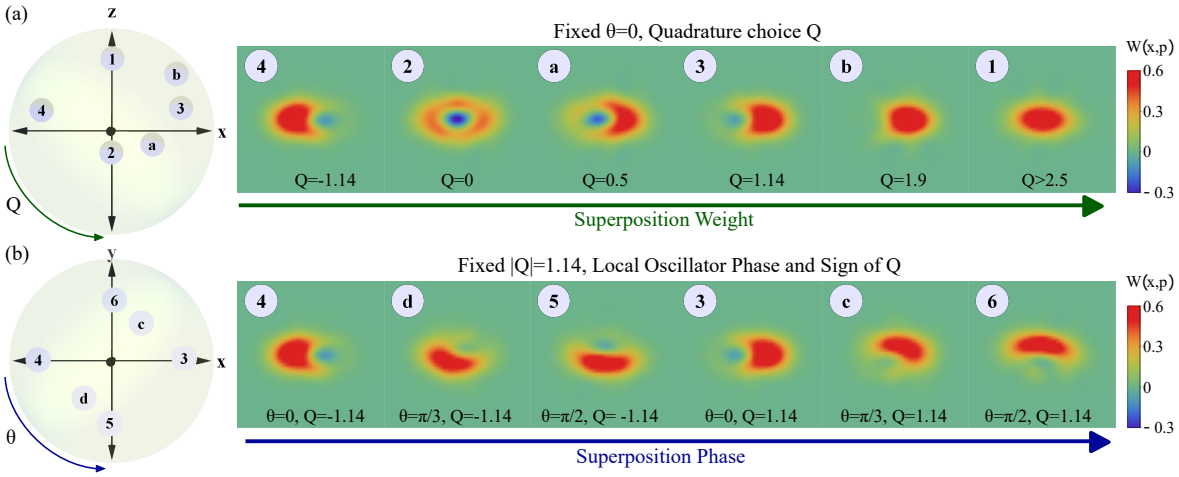

Figure 4.8: **Exploring the Bloch sphere**. Control of the remotely-prepared superposition via tuning of (a) the selected quadrature value Q and (b) the local oscillator phase θ. The left figures provide the location of the prepared states projected onto the XZ and XY plane of the Bloch sphere respectively. The rows show the evolution of the associated Wigner functions when the conditioning parameter is tuned. We note that the sign flip of Q is equivalent to a π phase shift. The results are corrected for the $\eta = 85\%$ detection efficiency and reconstructed from 40 000 samples.

superpositions between the two all at a fixed relative phase $\theta = 0$. In figure (b), we stay close to the equator of the Bloch sphere by fixing $Q = 1.14$ and then modify the local oscillator phase. This allows us to create a balanced superposition between even and odd cat states at different relative phases. We see indeed a rotation of the states from number #4 to number #6 which illustrates the quantum state engineering capability in phase space offered by our scheme.

3 Conclusion

In this chapter, we presented hybrid entanglement of light and the first protocol making use of it: the remote preparation of any CV-encoded qubit by performing local measurements on the DV mode. The performance is limited by the losses we introduce on the DV mode which are mostly due to the presence of the optical isolator. Future implementations, with for example a bow-tie OPO cavity, could significantly lower those losses and increase the fidelity of the prepared states with their respective target. This first hybrid-entanglement-based protocol being successful, we can now explore more advanced schemes. The strong negativity of entanglement measured and the RSP capability first led us to probe the nonlocal properties of our resource. In the next chapter we present a theoretical study for the implementation of Bell tests and our experimental demonstration of quantum steering with hybrid entanglement.

Chapter 5

Non-locality tests on hybrid entanglement

The realization of remote state preparation of arbitrary CV-qubits is a clear manifestation of the robust entanglement present in our hybrid entangled resource. In this chapter, we address the possibility of performing non-locality tests with this hybrid state.

First, we give the account of a theoretical study of the possibility of implementing Bell tests with our setup. To that end, several approaches are considered, and we conclude on the loss-requirements for the violation of Bell inequalities in a hybrid context. We then consider the intermediate scenario of quantum steering. The main result of the chapter is the success in demonstrating Einstein-Podolsky-Rosen steering for the first time using hybrid entanglement, a result that has been published in [99]. We present the experimental setup used for this demonstration as well as a detailed account of the computation of error bars associated to the measurement. We finally find our state to be distant from the local bound by more than five standard deviations.

Contents

1 Entanglement and non-locality

The existence of entangled states has for consequence a counter-intuitive phenomenon. As described by Einstein, Podolsky and Rosen in 1935 [2], in the case where an entangled state is shared by two arbitrarily distant nodes, the results of measurements made by one of the parties will be strongly correlated with the result of future measurements performed on the other mode. This situation is possible in classical physics if there exists a prior history shared by the two parties, which may be unknown, but that has a causal influence on the results of measurements made on the two modes. In quantum theory however, although all the information about an entangled state is contained in its density matrix, the latter does not determine the outcome of local measurements on its subsystems. This led the authors of [2] to assume quantum theory to require a more complete description.

This property is however now well-accepted and has been demonstrated in numerous experiments. We note in particular the first observation of a Bell inequality violation by Freedman *et al.* [4], the first demonstration ruling out the locality loophole by Aspect *et al.* [5] and the three loophole-free experiments published in 2015 [6, 7, 8]. In this section, we first introduce the concept of non-locality and then detail some of the practical uses of non-local states.

1.1 Bell non-local states

We define here non-locality using the approach and the formalism outlined in [100]. A Bell test [3] can be described as follows. We consider two systems having previously interacted and measured by two observers Alice and Bob. To do so, they perform measurements, labeled x for Alice and y for Bob that lead to some outcomes denoted respectively a and b. After enough measurements, they can reconstruct separately the conditional probabilities $p(a|x)$ and $p(b|y)$, while by comparing their results they can compute the distributions $p(ab|xy)$. In the case where they observe $p(ab|xy) \neq p(a|x)p(b|y)$, a classical, meaning here *local*, explanation entails the existence of a set of parameters λ that have influenced both systems during their interaction. These so-called *hidden* variables condition the results of Alice and Bob's measurements *prior* to their implementation. A local model for the situation can therefore be written as:

$$p(ab|xy) = \int_{\Lambda} d\lambda p(a|x\lambda)p(b|y\lambda)q(\lambda), \tag{5.1}$$

where we integrate over the set Λ of hidden variables that condition the observer's measurements. These variables are not necessarily constant throughout the experiment and is taken into account by introducing the probability distribution $q(\lambda)$.

Any quantum state that follows equation (5.1) is compatible with a local description. Quantum theory allows however the existence of experiments for which a local description is impossible [100]. These scenarios, *i.e.* successful Bell tests, involve the use of states called *non-local*. The original Bell test consisted in Alice and Bob measuring correlations on subparts of a pure entangled state through two possible measurements each, respectively x_i and y_j with $i, j \in \{0, 1\}$. The results of their measurements a_i and b_j would then be assigned to two possible values: $a_i, b_j \in \{+1, -1\}$. One can show [101], that assuming equation (5.1) to be true leads to the Clauser-Horne-Shimony-Holt inequality:

$$\mathcal{B} = |\langle a_0 b_0\rangle + \langle a_0 b_1\rangle + \langle a_1 b_0\rangle - \langle a_1 b_1\rangle| \leq 2. \tag{5.2}$$

This inequality is however not verified in general for quantum states where the upper limit becomes $2\sqrt{2}$ [100]. Any entangled state for which one can perform measuremements violating equation (5.2) is non-local.

1.2 Non-locality of entangled states

As defined in Chapter 1, a bipartite state $\hat{\rho}$ spanning the Hilbert space H is entangled if it is impossible to write it as a linear combination of tensor products of states belonging to parties Alice (A) and Bob (B):

$$\hat{\rho} \neq \sum_k p_k \hat{\rho}_A^k \otimes \hat{\rho}_B^k. \tag{5.3}$$

Entanglement and non-locality are closely related concepts. We can first see this by computing the conditional probabilities $p(ab|\hat{x}\hat{y})$ for a separable state:

$$\begin{aligned} p(ab|\hat{x}\hat{y}) &= Tr(\hat{\rho}\hat{x} \otimes \hat{y}) \\ &= \sum_k p_k Tr(\hat{\rho}_A^k \hat{x}) Tr(\hat{\rho}_B^k \hat{y}) \\ &= \sum_k p_k p(a|\hat{x}, k) p(b|\hat{y}, k). \end{aligned} \tag{5.4}$$

As the conditional probability can be written in the form of equation (5.1), we conclude that it is possible to obtain non-local correlations from measurements on a quantum state only if it is entangled.

A question that is still open is whether the reverse is true. It has been demonstrated that all pure entangled states are non-local [102, 103, 104]. The question is more complicated however for mixed states. For instance, there exists a class of mixed entangled states, called the Werner states [105], that admit a local model for any possible local measurements. This does not fully settle the question however as one can reveal the non-local features of a quantum states through different strategies. One is to perform entanglement distillation and it was conjectured by Peres [106] in 1999 that undistillable bibartite entangled states admit a local model. However this was disproven more recently [107, 108] and it is possible that in fact every entangled state can be revealed non-local through more elaborate strategies (See [100] for the description of non-locality subgroups corresponding to different strategies).

1.3 Non-locality in practice: Device independence

Although the link between entanglement and non-locality has yet to be fully characterized, the practical realization of key quantum protocols between untrusted parties has been so far proven to be secure only through the use of non-local states. These include random number generators and quantum key distribution (QKD). To see the added value of non-locality, it is interesting to look at the differences between two early QKD protocols: **BB84** and **E91**. The first one was introduced in 1984 by Bennet and Brassard [13], was garanteed secure because of the non-cloning theorem and was later extended to the use of entanglement [109]. The second protocol, detailed by Ekert in 1991 [110], uses a maximally entangled state and its success is ensured by the violation of a CHSH inequality. Initially, this second protocol was intended to be a more practical implementation of QKD as it would rely on similar setups used for Bell violation. The answer of Bennet and Brassard was to update **BB84** to a version relying on entanglement without needing a Bell inequality violation. This protocol

was proven as secure as **E91** *if* one assumes perfect control of the experiment, *i.e.* if all its components have been characterized and are trusted.

The fundamental advantage of Ekert's protocol is therefore that one does not need to make any assumption on the measurements implemented. Security is ensured by looking at correlations between the results of measurements no matter what is actually performed. This frees one of the necessity of having characterized perfectly both his setup and the one of the party with whom he wants to share a key. This was explicited first in [111, 112] under the name self-testing and is now called *device independence* (DI). Later, device independent protocols for quantum key distribution (DIQKD) were introduced that rely only on the no-signaling assumption, *i.e.* the assumption that Alice has no way of knowing which measurements was chosen by Bob and *vice versa* [113, 114]. Similar development has been made towards protocols for DI random number generation [115].

2 Towards device-independent use of hybrid entanglement of light

We have seen that proving an entangled state to be non-local demonstrates its usefulness for a wider range of protocols. In particular, it opens the possibility of implementing fully device-independent and secure quantum communication channels. In the context of quantum networks where untrusted actors using different encodings interact, it is worthwhile to study the non-local features of hybrid entanglement.

In this section we study the requirements for the realization of a Bell test with our hybrid resource. In the context of the CHSH inequality, we consider and compare a number of strategies for the demonstration of its non-local nature.

2.1 Framework of the study: Adapting the CHSH inequality to hybrid entanglement

The Bell tests we considere are in the framework of the CHSH inequality. As seen in section 1.1, in this scenario two measurements are performed on each mode, leading to two possible results to which we associate the values ± 1. Originally, the CHSH inequality was applied to two-dimensional DV states such as entangled spin or polarization qubits for example. In that case, the POVMs associated to Alice and Bob's measurements span the Pauli operator basis. Meaning one could write with no loss of generality the CHSH inequality as

$$\mathcal{B} = |\langle \hat{\sigma}_{\mathbf{a}_0} \otimes \hat{\sigma}_{\mathbf{b}_0} \rangle + \langle \hat{\sigma}_{\mathbf{a}_1} \otimes \hat{\sigma}_{\mathbf{b}_0} \rangle + \langle \hat{\sigma}_{\mathbf{a}_0} \otimes \hat{\sigma}_{\mathbf{b}_1} \rangle - \langle \hat{\sigma}_{\mathbf{a}_1} \otimes \hat{\sigma}_{\mathbf{b}_1} \rangle| \leq 2, \tag{5.5}$$

where the $\mathbf{a}_i$ and $\mathbf{b}_j$ are 3-dimensional vectors and $\hat{\sigma}_{\mathbf{x}} = \mathbf{x} \cdot (\hat{\sigma}_X, \hat{\sigma}_Y, \hat{\sigma}_Z)$. In the rest of the section, we are looking to adapt the inequality to hybrid entanglement. To do so we consider several different operators on the DV and CV modes as a number of possible Bell tests. In an experimental context, we compare in particular their resilience to losses. We outline the impact the choice of encoding made for the DV mode has on the ease of implementation of Bell tests and then consider various operators on the CV mode.

2.2 Loss-tolerance of a Bell test

Managing losses is crucial to an experimental demonstration of non-locality. The goal of our study is therefore to compute the loss-requirements in the system for a successful Bell

violation. In effect, we compare different strategies in terms of the maximum amount of losses we can add to the system before the Bell test fails.

We have seen in previous chapters one principal source of loss for our state: the $\eta_0 \approx 90\%$ escape efficiency of the OPOs. The parameter chosen for our plots is the overall efficiency η defined as the product of the efficiency on both modes $\eta_o = \eta_{\mathrm{CV}}\eta_{\mathrm{DV}}$, where $\eta_{DV}(\eta_{CV})$ is the transmission efficiency on the DV(CV) mode. In the experimental context we have in the best case an overall efficiency $\eta_o = \eta_0^2 \approx 81\%$. The overall efficiency needs however to include as well the losses introduced by the imperfect measurements performed. For example and as we show in Section 2.3, the implementation of a Pauli operator using homodyne detection has to take into account the $\eta_{\mathrm{HD}} = 15\%$ detection losses of the experimental setup. When considering the results of the study, one therefore has to add the losses inherent to his measurement's implementation. There is a theoretical loss threshold for all two-mode experiments under which the CHSH inequality cannot be violated. The lowest efficiency allowing for any implementation of the CHSH test a Bell violation is $\tilde{\eta}_i = 2/3$ on each mode $i \in \{1, 2\}$ (*i.e.* a global efficiency of $\tilde{\eta}_o = \tilde{\eta}_1\tilde{\eta}_2 = 4/9$) in a symmetric (or close to symmetric case) [116]. Lower thresholds can be reached only for very asymmetric cases where one measurement has a close to perfect implementation, a situation out of reach for us.

2.3 Implementing Pauli operators on the DV mode depending on the encoding

Our goal is to adapt the CHSH inequality to hybrid entanglement and in particular to our specific implementation to see the loss-requirements for our system. As presented in Chapter 4, we currently use the photon-number encoding $\{|0\rangle, |1\rangle\}$ on the DV mode and the squeezing encoding $\{\hat{S}|0\rangle, \hat{a}\hat{S}|0\rangle\}$ on the CV mode. Note however that there are other possible choices and, notably, one of the goals of our group is to realize hybrid entanglement using the polarization encoding $\{|H\rangle, |V\rangle\}$ on the DV mode. Although we give a comprehensive account of the differences between encodings in Chapter 6 (Section 1.2), the change relevant to the context of the CHSH inequality is the implementation of Pauli operators on the DV mode. To keep our study more general and valid for the future implementation of hybrid entanglement, we outline the difference between the two encodings here and will consider perfect Pauli operators in the remainder of the section.

While it is possible to perform all Pauli operators in the polarization encoding using polarizing beam-splitters and single-photon detectors, in the photon-number basis it is only possible to approximate $\hat{\sigma}_X$ and $\hat{\sigma}_Y$ when using linear systems. One possible method is to perform homodyne measurements at phase ϕ and then sign-binning the result. This approximates the Pauli operator $\hat{\sigma}(\phi) = \cos(\phi)\hat{\sigma}_X + \sin(\phi)\hat{\sigma}_Y$. Indeed, if we consider the Fock state decomposition of the corresponding measurement $\hat{\pi}(\phi)$:

$$\begin{aligned}
\langle n|\hat{\pi}(\phi)|m\rangle &= \langle n|\left(\int_0^{+\infty} |x_\phi\rangle\langle x_\phi| dx - \int_{-\infty}^{0} |x_\phi\rangle\langle x_\phi| dx\right)|m\rangle \\
&= \int_0^{+\infty} e^{i\phi(n-m)}\psi_n(x)\psi_m^*(x)dx - \int_{-\infty}^{0} e^{i\phi(n-m)}\psi_n(x)\psi_m^*(x)dx \\
&= \sqrt{\frac{2}{\pi}}\langle n|\hat{\sigma}(\phi)|m\rangle \qquad \forall n, m \in \{0, 1\}. \qquad (5.6)
\end{aligned}$$

Even in the case of a lossless homodyne detector, this is an approximation because of the prefactor $\sqrt{2/\pi}$. The probability of performing the right operator is equal to $1/2(1 + \sqrt{2 * \eta/\pi})$,

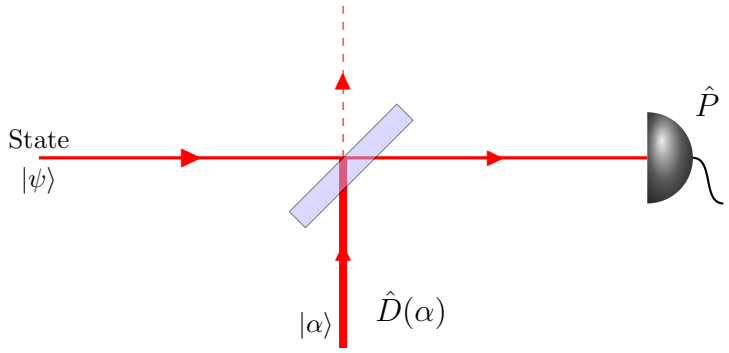

Figure 5.1: **Displaced parity measurement**. The state to measure $|\psi\rangle$ is mixed mith a coherent state $|\alpha\rangle$ on a beam-splitter. Then, a photon-number resolving detector measures the parity of the mixed field.

with η the homodyne efficiency [117]. There is therefore an intrinsic drawback to the use of the photon-number encoding on the DV mode for Bell tests: A realistic implementation of a Pauli measurements will introduce additional losses when compared to hybrid entanglement with polarization encoding. As said earlier and for generality, our study is in the case of perfect Pauli measurements on the DV mode. When using the photon-number encoding, one needs to include additional losses to recover the loss-resilience of the Bell test.

Keeping this in mind, we now consider the CV mode. As it populates a greater Hilbert space than the DV mode, we need to look for different observables. Those can be either extensions of the Pauli formalism to higher dimensions or linked to the phase-space representations. In the following, we consider several of these operators as a number of possible strategies.

2.4 Comparing strategies: using different observables on the CV mode

We now consider several Bell tests devised for high-dimensional systems in order to find the most suitable one for our experiment. The following work was realized in collaboration with the group of Thomas Coudreau and Perola Milman from the university Paris Diderot and in particular with Andreas Ketterer whose doctoral thesis [33] provides important theoretical details along with simulations using displaced parity measurements on the CV mode. What we detail here extends the simulations performed therein from the target hybrid state $|+\rangle|\alpha\rangle + |-\rangle|-\alpha\rangle$ to the one experimentally implemented $\hat{S}|0\rangle|1\rangle + e^{i\pi}\hat{a}\hat{S}|0\rangle|0\rangle$. We also add the study of other observables based on displacements and imperfect detectors.

2.4.1 First test: the Wigner function as an observable

Historically and to the best of our knowledge, Banaszek and Wódkiewicz [118] were the first to outline a link between phase-space distribution and non-locality. Considering the expression of the Wigner function as a displaced parity operator as seen in Chapter 1, they showed that one can devise an experimental setup for measuring one point of the Wigner function. As shown in figure 5.1, the setup consists in applying a displacement to the incoming field and then, using a photon number sensitive detector, in measuring the photon number parity of the resulting field.

The POVM corresponding to this measurement is the displaced parity operator:

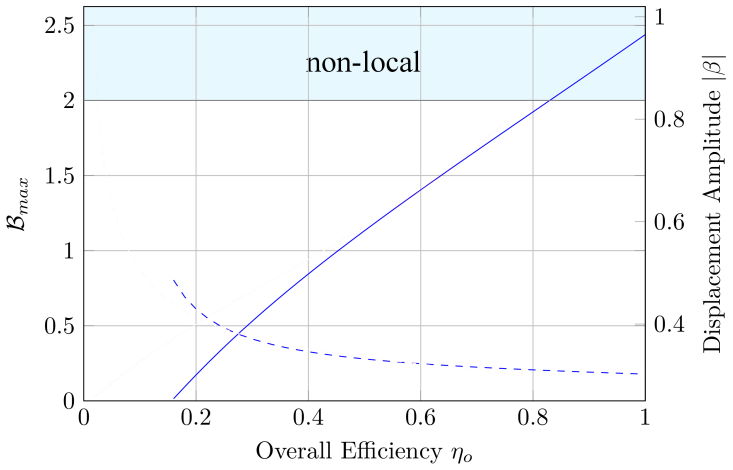

Figure 5.2: **Loss-tolerance using displaced-parity operators**. Expected Bell parameter value depending on the global efficiency for a hybrid state with 3 dB of squeezing using displaced-parity operators. Full lines: maximum value of the Bell parameter. Dashed lines: optimum displacement amplitude $|\beta|$ when applying operator $\hat{D}(\beta)\hat{P}\hat{D}(-\beta)$ on the CV mode. On the DV mode we apply either of the operators $\hat{\sigma}_Z$ and $\hat{\sigma}_X$. On the CV mode we choose between operators $\hat{\Pi}(\beta)$ and $\hat{\Pi}(-\beta)$, with $|\beta|$ given by the dashed curve. The corresponding Bell inequality is violated starting from a global efficiency $\eta_o = 83\%$.

$$\hat{\Pi}(\alpha) = \hat{D}(\alpha)\hat{P}\hat{D}(-\alpha). \tag{5.7}$$

As we have seen in equation (1.43) of Chapter 1, this operator is proportional to the Wigner function at the point in phase space (x, p) as, using the notation $W_{\hat{\rho}}(x, p) = W_{\hat{\rho}}(\alpha = x + ip)$, we have

$$W_{\hat{\rho}}(\alpha) = \frac{1}{2\pi\sigma_0^2} Tr\left(\hat{\rho}\hat{D}(\alpha)\hat{P}\hat{D}(-\alpha)\right) \tag{5.8}$$

Therefore, as generalized in [119], one can test the non locality of a two mode state using the following CHSH inequality:

$$\mathcal{B} = |\langle\hat{\Pi}(\alpha)\otimes\hat{\Pi}(\beta)\rangle + \langle\hat{\Pi}(\alpha')\otimes\hat{\Pi}(\beta)\rangle + \langle\hat{\Pi}(\alpha)\otimes\hat{\Pi}(\beta')\rangle - \langle\hat{\Pi}(\alpha')\otimes\hat{\Pi}(\beta')\rangle| \leq 2, \tag{5.9}$$

or equivalently, using the shorthand $W(\alpha = x_\alpha + ip_\alpha, \beta = x_\beta + ip_\beta)$ for the two-mode Wigner function $W(x_\alpha, p_\alpha, x_\beta, p_\beta)$,

$$\mathcal{B}(\alpha, \alpha', \beta, \beta') = 4\pi^2\sigma_0^4|W(\alpha, \beta) + W(\alpha', \beta) + W(\alpha, \beta') - W(\alpha', \beta')| \leq 2. \tag{5.10}$$

From there a straightforward hybridization of inequalities (5.5) and (5.10) is the following hybrid CHSH inequality:

$$\mathcal{B}(\mathbf{a}_0, \mathbf{a}_1, \beta, \beta') = |\langle\hat{\sigma}_{\mathbf{a}_0}\otimes\hat{\Pi}(\beta)\rangle + \langle\hat{\sigma}_{\mathbf{a}_0}\otimes\hat{\Pi}(\beta')\rangle + \langle\hat{\sigma}_{\mathbf{a}_1}\otimes\hat{\Pi}(\beta)\rangle - \langle\hat{\sigma}_{\mathbf{a}_1}\otimes\hat{\Pi}(\beta')\rangle| \leq 2, \tag{5.11}$$

where we apply Pauli operators on the DV mode and displaced-parity operator on the CV mode. We now consider the effect of losses on the possibility of observing a Bell inequality violation.

In figure 5.2, we plot the maximum violation attainable for a theoretical hybrid-entangled state, depending on the global efficiency $\eta_o = \eta_{DV}\eta_{CV}$. We consider the symmetric case

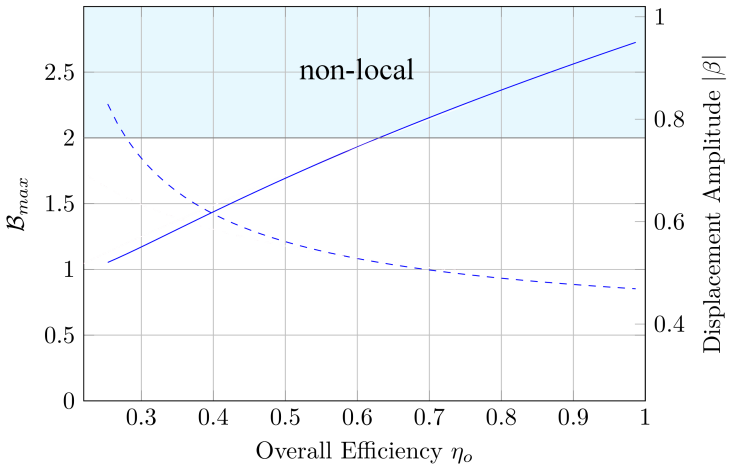

Figure 5.3: **Loss-tolerance using displaced-detection operators**. Expected Bell parameter value depending on the global efficiency for a hybrid state with 3 dB of squeezing using displaced-detection measurements. Full lines: maximum value of the Bell parameter. Dashed lines: Optimum displacement amplitude $|\beta|$ when applying operator $\hat{M}(\beta)$ on the CV mode. On the DV mode we apply either of the operators $\hat{\sigma}_Z$ and $\hat{\sigma}_X$. On the CV mode we choose between operators $\hat{M}(\beta)$ and $\hat{M}(-\beta)$, with $|\beta|$ given by the dashed curve. The corresponding Bell inequality is violated starting from global efficiency $\eta_o = 63\%$.

$\eta_{DV} = \eta_{CV}$. We see that the minimum global efficiency needed for a violation is around $\eta_o = 83\%$. At maximum efficiency, the Bell parameter reaches $\mathcal{B} = 2.44$, below the quantum limit of $2\sqrt{2}$. Although our initial optimization was made over all possible $(\mathbf{a}_0, \mathbf{a}_1, \beta, \beta')$, we find that the particular combination $\{\mathbf{a}_0 = (0,0,1), \mathbf{a}_1 = (1,0,0), \beta = r, \beta' = re^{i\pi}\}$ gives us the maximum attainable value of $\mathcal{B}$ for all efficiencies, up to an adjustment of the norm $r = |\beta| = |\beta'|$. The dashed plot gives the value of this optimal norm at each particular global efficiency value η_o. Those values range between $r = 0.48$ at low efficiency and $r = 0.3$ for perfect transmission. These results are in good agreement with the calculations performed by Andreas Ketterer as part of our collaboration and detailed in [33]. The slight difference can be explained by the use of a squeezing encoding for the CV mode in our case. The threshold for global efficiency using the displaced-parity operators is therefore quite high as it is above the best-case-scenario efficiency of our setup $\eta_0^2 = 81\%$. This first strategy is therefore not suited to our system and we need to consider alternatives.

2.4.2 Adaptation: displaced-detection measurements

Implementing the parity operator is challenging using most current single-photon detectors, including our SNSPDs as they are not photon-number resolving. An adaptation of the measurement in figure 5.1 to realistic detectors would therefore need to rule out any parity measurement. The alternative we consider is to condition not on the parity of the photon-number measured but on whether or not photons have been detected. One assigns for example the result -1 to the detection of one or more photons and $+1$ to the alternative. The operator associated to the latter case being the projector $|\alpha\rangle\langle\alpha|$, one can write the former measurement as $Id - |\alpha\rangle\langle\alpha|$. The overall POVM is therefore $M(\alpha) = 2|\alpha\rangle\langle\alpha| - Id$. This approach was introduced in [120] for $\alpha = 1$, in effect implementing $\hat{\sigma}_X$ for a 2D DV state , then generalized in [117] to different α values and Hilbert spaces of greater dimension and

finally used in [121] for an experimental demonstration of EPR steering. In the context of a two-mode squeezed state, these operators $\hat{M}(\alpha)$ have been shown to be very loss-tolerant as they reach the minimum efficiency threshold $\tilde{\eta}$ for all symmetric apparatuses [122]. This promising result led us to do the same study of loss-tolerance using these observables in a hybrid context. We plot in figure 5.3 the maximum value of $\mathcal{B}$ attainable for a hybrid state with 3 dB of squeezing depending on the overall efficiency η_o.

We indeed observe a greater loss-tolerance than with the previous displaced-parity measurements as one can see a violation with a global efficiency as low as $\eta_o = 63\%$. We find optimal settings analogous to the displaced-parity method: $\{\mathbf{a}_0 = (0,0,1), \mathbf{a}_1 = (1,0,0), \beta = r, \beta' = re^{i\pi}\}$ with slightly different suitable values of $r = |\beta|$. This represents a great improvement over the previous method but this still represents a challenging demonstration well above the theoretical bound $\tilde{\eta}_o = 45\%$.

We now consider two other strategies following a different approach. Instead of finding high-dimensional operators to apply on the complete CV subspace, we project the CV mode onto a two-dimensional space.

2.4.3 Third method: mapping on generators of the CV subspace

We know that Pauli operators are well suited for a discrete-variable CHSH inequality violation. Using them one can maximally violate Bell inequalities and they constitute, along with the identity operator, a basis for all $2D$ observables. In this subsection and as our next approach, we'll look at analogous operators that span the infinite-dimensional CV space that have similar properties and that can be implemented as the previously considered observables.

The idea is to restrict the CV mode to a subspace spanned by two infinite-dimensional states. These two generators should be chosen such that most of the features of the CV mode are kept when projecting on the subspace. In short we want to map our CV mode and operators on a 2D basis formed by two CV vectors: $\{|0_{CV}\rangle, |1_{CV}\rangle\}$. Ideally, one would need to have $|0_{CV}\rangle$ and $|1_{CV}\rangle$ strictly or close to orthogonal. Then we can build on this basis Pauli-type operators:

$$\begin{aligned}
\hat{\Sigma}_I &= |0_{CV}\rangle\langle 0_{CV}| + |1_{CV}\rangle\langle 1_{CV}|, \\
\hat{\Sigma}_z &= |0_{CV}\rangle\langle 0_{CV}| - |1_{CV}\rangle\langle 1_{CV}|, \\
\hat{\Sigma}_x &= |0_{CV}\rangle\langle 1_{CV}| + |1_{CV}\rangle\langle 0_{CV}|, \\
\hat{\Sigma}_y &= -i\,|0_{CV}\rangle\langle 1_{CV}| + i\,|1_{CV}\rangle\langle 0_{CV}|.
\end{aligned} \tag{5.12}$$

For coherent states superpositions, the basis to consider is $\{|0_{CV}\rangle = |\beta\rangle, |1_{CV}\rangle = |-\beta\rangle\}$. In this case, $|\beta\rangle$ and $|-\beta\rangle$ are not strictly orthogonal but this issue can be alleviated by going to higher values of $|\beta|$. This particular case is well suited to experimental implementation as it is possible to measure the corresponding operators of equation 5.12 by combining displaced-parity measurements. This approach was used in particular in [123] to demonstrate a Bell inequality violation with entanglement between an artificial atom and a cat state. If we look at the expression of $\hat{\Pi}(\alpha)$ on the CV basis $\{|\beta\rangle, |-\beta\rangle\}$:

$$\begin{aligned}
\langle\beta|\,\hat{\Pi}(\alpha)\,|\beta\rangle &= \langle\beta-\alpha|\alpha-\beta\rangle \\
\langle\beta|\,\hat{\Pi}(\alpha)\,|-\beta\rangle &= e^{2(\alpha\beta^*-\alpha^*\beta)}\,\langle\alpha|-\alpha\rangle.
\end{aligned} \tag{5.13}$$

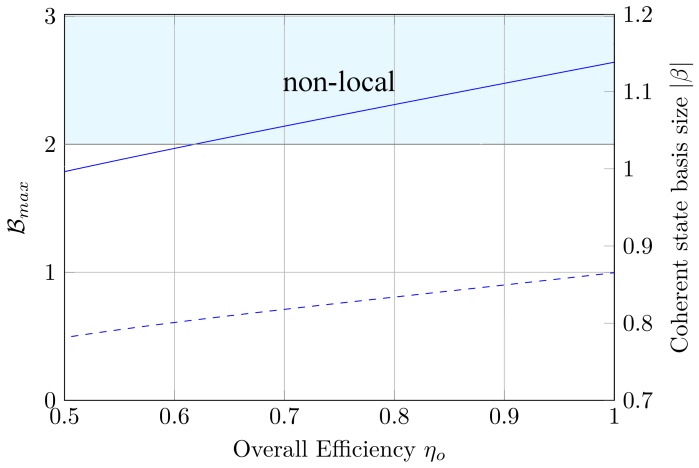

Figure 5.4: **Loss-tolerance using mapping on coherent state basis**. Full line: expected Bell parameter value depending on the global efficiency for a hybrid state with 3 dB of squeezing using a mapping to a coherent states basis. Dashed line: optimum coherent state amplitude $|\beta|$ for the CV basis. On the DV mode we apply either of the operators $\hat{\sigma}_Z$ and $\hat{\sigma}_X$. On the CV mode we choose between operators $\hat{\Sigma}_x^\beta$ and $\hat{\Sigma}_y^\beta$, with $|\beta|$ given by the dashed curve. The corresponding Bell inequality is violated starting from global efficiency of $\eta_o = 62\%$.

As a consequence, on the subspace spanned by $\{|\beta\rangle, |-\beta\rangle\}$, we have [123]:

$$\begin{aligned}
\hat{\Sigma}_I &\approx \hat{\Pi}(\beta) + \hat{\Pi}(-\beta) \\
\hat{\Sigma}_x &\approx \hat{\Pi}(0) \\
\hat{\Sigma}_y &\approx \hat{\Pi}(\frac{i\pi}{8\beta}) \\
\hat{\Sigma}_z &\approx \hat{\Pi}(\beta) - \hat{\Pi}(-\beta)
\end{aligned} \tag{5.14}$$

Because Pauli operators are generators of a 2D basis, one can measure any operator on the CV subspace spanned by $\{|\beta\rangle, |-\beta\rangle\}$ by combining displaced parity measurements. There is however the caveat that they therefore cannot all be implemented in a single shot measurement using this method. Indeed, in the case of $\hat{\Sigma}_I$ and $\hat{\Sigma}_z$ it is necessary to combine the result of multiple measurements. This rules out a loophole free demonstration of Bell non-locality.

Under this basis, we can compute new expectation values for the Bell parameter $\mathcal{B}$, as shown in figure 5.4. This leads us however to a narrow improvement on the previous method as in this case a violation is possible starting from $\eta_o = 62\%$. The underwhelming improvement from the displaced detection method can be explained by the way we implement cat states experimentally *i.e.* using squeezed vacuum and photon subtractions. $\hat{S}|0\rangle$ and $\hat{a}\hat{S}|0\rangle$ are close to unity fidelity for $s = 3$ dB with coherent state superpositions of different sizes $|\alpha|$. Fidelity between $\hat{S}|0\rangle$ and $|\text{cat}_+\rangle$ is maximal for $|\alpha_+| \approx 0.6$ while it is for $|\alpha_-| \approx 1$ that $\hat{a}\hat{S}|0\rangle$ and $|\text{cat}_-\rangle$ are the closest. Any basis $\{|\beta\rangle, |-\beta\rangle\}$ will therefore be inadequate for a simultaneous mapping of $\hat{S}|0\rangle$ and $\hat{a}\hat{S}|0\rangle$. This argument is underpinned by the fact that the optimum values of $|\beta|$ found are close to 0.8, *i.e.* around halfway between $|\alpha_+|$ and $|\alpha_-|$.

The next step is therefore to adapt the operators of equation 5.12 to our implementation of CSS and use the basis $\{|0_{CV}\rangle = \hat{S}|0\rangle, |1_{CV}\rangle = sh(\zeta)^{-1}\hat{a}\hat{S}|0\rangle\}$. No matter the squeezing amount applied, the basis is orthonormal. The results are shown in figure 5.5.

With this method, we can hope to reach a Bell violation for global efficiencies as low as

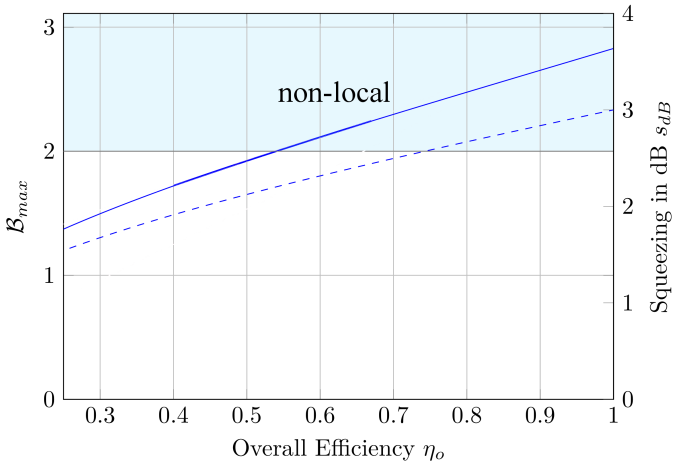

Figure 5.5: **Loss-tolerance using mapping on squeezed-states basis**. Full line: expected Bell parameter value depending on the global efficiency for a single-click hybrid state with $3dB$ of squeezing using a mapping to a squeezed states basis. Dashed line: optimum squeezing in dB to apply for the CV basis measurement. On the DV mode we apply either of the operators $\hat{\sigma}_Z$ and $\hat{\sigma}_X$. On the CV mode we choose between operators $\hat{\Sigma}_x^s$ and $\hat{\Sigma}_y^s$, with s_{dB} the optimal amount of squeezing given by the dashed line. The corresponding Bell inequality is violated starting from global efficiency of close to $\eta_o = 54\%$ for both the symmetric and asymmetric cases.

$\eta_o = 54\%$. However we leave open the question whether this can be implemented experimentally or not. The mismatch between $|\alpha_+|$ and $|\alpha_-|$– the size of coherent state superpositions our implemented "cat" states are closest in fidelity to– is at the origin of the problem. While we can approximate $\hat{\Sigma}_z^s$ and $\hat{\Sigma}_I^s$, defined as $\hat{S}\,|0\rangle\langle 0|\,\hat{S}^\dagger \pm sh(\zeta)^{-1}\hat{a}\hat{S}\,|0\rangle\langle 0|\,\hat{S}^\dagger\hat{a}^\dagger$ well with:

$$\begin{aligned}\hat{\Sigma}_z^s &\approx \hat{\Pi}(\alpha_+) + \hat{\Pi}(-\alpha_+) - \hat{\Pi}(\alpha_-) - \hat{\Pi}(-\alpha_-) + 2\hat{\Pi}(0)\\ \hat{\Sigma}_I^s &\approx \hat{\Pi}(\alpha_+) + \hat{\Pi}(-\alpha_+) + \hat{\Pi}(\alpha_-) + \hat{\Pi}(-\alpha_-),\end{aligned} \tag{5.15}$$

displaced parity measurements seem insufficient to approximate $\hat{\Sigma}_x^s$ and $\hat{\Sigma}_y^s$, because they involve the measurement of $|\alpha_+\rangle\langle\alpha_-|$. Displaced detection measurements fall short as well on this as we haven't found a way to improve on single shot measurements through the combination of 2 or more observables. This result is an example of the drawbacks of using the squeezing encoding instead of the coherent state basis for the CV mode. The implementation of some measurements is more challenging because of the difference of population between the two eigenstates of the basis.

We now come to the last strategy considered: the use of pseudo-spin operators. This method also provides a mapping onto a two-dimensional subspace, although without a projective operation. Although there are to our knowledge no easy way to implement this last strategy, it gives us the minimum efficiency threshold for Bell inequality violation using hybrid entanglement.

2.4.4 Minimal bound for loss-resilience: using pseudo-spin operators

The underlying idea of the Pauli-type CV operators introduced previously is that we consider only the projection of the CV mode onto a 2 dimensional subspace, spanned by

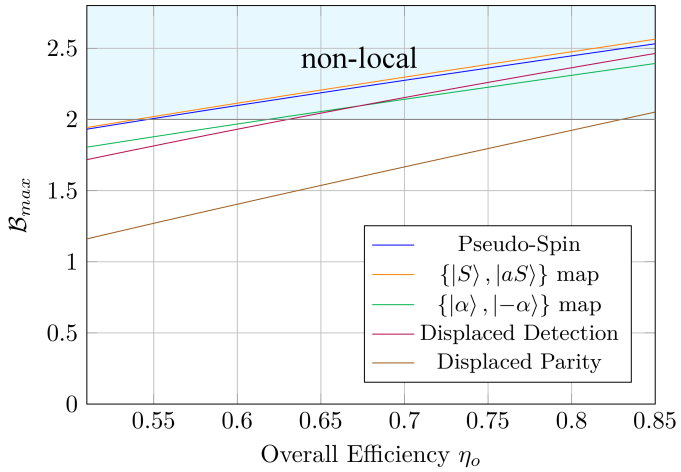

Figure 5.6: **Loss-tolerance for all methods**. Expected Bell parameter value depending on the global efficiency for a hybrid state with 3 dB of squeezing using all methods. Pseudo-spin operators and mapping to a squeezing basis lead to the most tolerant Bell tests. On the DV part, we implement Pauli operators $\hat{\sigma}_x$ and $\hat{\sigma}_z$.

coherent states. This is in effect a mapping of our CV mode onto a lower dimension subspace but with the problem that we use only part of the two-mode state for the search of non-local features, which may not be optimal. A more general alternative is the use of pseudo-spin operators [124], an extension of Pauli operators to dimensions higher than 2. They are expressed as:

$$\begin{aligned}
\hat{S}_x &= \sum_{n=0}^{\infty} (|2n\rangle \langle 2n+1| + |2n+1\rangle \langle 2n|) \\
\hat{S}_y &= \sum_{n=0}^{\infty} (-i\,|2n\rangle \langle 2n+1| + i\,|2n+1\rangle \langle 2n|) \\
\hat{S}_z &= \sum_{n=0}^{\infty} (-1)^n\,|n\rangle \langle n|\,.
\end{aligned} \tag{5.16}$$

These operators follow the Pauli matrix algebra and can be used to map a CV mode onto the 2D density matrix [125]:

$$\rho_2 = \frac{1}{2}(Id + \hat{\sigma}_{\mathbf{S}(\rho_{CV})}), \tag{5.17}$$

where $\mathcal{S}$ is the vector with components $(\mathcal{S})_i(\rho_{CV}) = Tr(\rho_{CV}\hat{S}_i)$. Tracing the product of ρ_{CV} with any linear combination $\sum_i c_i\hat{S}_i$ amounts to measuring $\sum_i c_i\hat{\sigma}_i$ on ρ_2. Indeed we have:

$$\begin{aligned}
Tr(\hat{\sigma}_i\rho_2) &= \sum_j Tr(\rho_{\mathrm{CV}}\hat{S}_i)Tr(\frac{1}{2}\hat{\sigma}_i\hat{\sigma}_j) \\
&= Tr(\rho_{\mathrm{CV}}\hat{S}_i)Tr(\frac{1}{2}\hat{\sigma}_i^2) \\
&= Tr(\rho_{\mathrm{CV}}\hat{S}_i).
\end{aligned} \tag{5.18}$$

Therefore, any pseudo-spin measurement on ρ_{CV} is equivalent to a Pauli measurement on the corresponding 2D density matrix $\rho_2(\rho_{\mathrm{CV}})$. The interesting thing is that one can devise a local

CV measurement	Min. efficiency	Implementation
Displaced-parity (DP)	83%	Requires photon-number resolving detectors
Displaced-detection (DD)	63%	Works with on-off detectors
$\{\|\alpha\rangle, \|-\alpha\rangle\}$ map	62%	Combined DP measurements
$\{\hat{S}\|0\rangle, \hat{a}\hat{S}\|0\rangle\}$ map	54%	—
$\{\hat{a}\hat{S}\|0\rangle, \hat{a}^2\hat{S}\|0\rangle\}$ map	54%	Approximately with combined DP measurements.
Pseudo-spin	54%	—

Table 5.1: **Comparison of all methods**. Loss-resilience and requirements for the implementation of different strategies for Bell inequality violation.

and unconditional Hamiltonian for the mapping $\rho_{CV} \rightarrow \rho_2(\rho_{\mathrm{CV}})$ which has for consequence that $\rho_{DV} \otimes \rho_2(\rho_{\mathrm{CV}})$ must present the same non-local properties as $\rho_{DV} \otimes \rho_{\mathrm{CV}}$ [125]. As Pauli operators, along with the identity operator, form a complete basis for the 2D space, we arrive at the conclusion that by using the pseudo-spin basis we should be at the limit of what can be achieved with a CHSH inequality applied to our hybrid state. To our knowledge, there is no easy way to implement the mapping Hamiltonian but we can use this to look at how far from the limit we are when using the previous methods.

In figure 5.6 we give the results for this method and compare them to the previously considered strategies. We find the same threshold than for the mapping on a squeezing basis.

2.5 Comparison of all methods and conclusion

We compare all methods in Figure 5.6 and Table 5.1. The most loss-resilient strategy is the projection on a squeezing mapping. However, as we have seen, the Pauli-type operators can be reliably implemented only if the two eigenstates of the basis have a similar population. We therefore do not provide a strategy for mapping on the $\{\hat{S}|0\rangle, \hat{a}\hat{S}|0\rangle\}$ but we can approximate the projection on the $\{\hat{a}\hat{S}|0\rangle, \hat{a}^2\hat{S}|0\rangle\}$ basis by combining displaced-parity measurements. Starting from our experimental hybrid-entangled state, the best compromise is therefore the displaced-detection method. In this case a minimum of 63% overall efficiency is required and there is no need for photon-number resolving detectors. This condition is however too challenging to fulfill experimentally at the current stage. The use of a polarization-based hybrid entanglement would make the demonstration more accessible. Indeed in that case, the implementation of Pauli operators on the DV mode could then be made in a more efficient manner.

In the meantime, we consider an intermediate test of non-locality: Einstein-Podolsky-Rosen (EPR) steering. In the next section we present the principle of EPR steering and report on its experimental demonstration with hybrid entanglement of light.

3 Einstein-Podolsky-Rosen steering with hybrid entanglement

The difficulty of implementing true device independent (DI) protocols led to the development of intermediate scenarios. In the context of QKD for example, one intermediate use case would consist in the transfer of a secret key between two nodes, one of them fully characterized and the other untrusted. This type of protocol is called *one-sided device independent* (1SDI) and is useful in a number of contexts including random number generators [126, 127], entanglement estimation [128], and entanglement verification for quantum networks [129, 130]. Similar to how the realization of a Bell test certifies device independence, there exists a class of protocols for 1SDI certification, called *steering* tests. In this section, we first introduce the principle of quantum steering and then we report on its demonstration using hybrid entanglement.

3.1 Einstein-Podolsky-Rosen steering

The term of *quantum steering* was coined by Schrödinger in his answer [131] to the EPR paradox introduced in [2]. While Einstein, Podolsky and Rosen proposed the introduction of local hidden variables (LHV) as a resolution to the supposed incompleteness of quantum mechanics, Schrödinger believed that the wavefunction provides a complete description of a local system. In his view, it was incomplete only when describing delocalized entangled states. In the context of 1SDI protocols, we will consider EPR steering as a test of the validity of a local model as introduced in [132].

3.1.1 Local hidden state model

In a steering scenario, Alice and Bob share an entangled state and Alice, who cannot be trusted, has to convince Bob that she can remotely steer his system. To this end she performs one out of a set of m_{A} measurements labeled θ, which yields a result a from a set of o_{A} possible outcomes. This information is then sent to Bob. Depending on the measurement and its result, Bob's system is projected to the state $\hat{\rho}_{a|\theta}$ with probability $p(a|\theta)$. Whether steering is observed or not will be determined by the information contained in the set $\{p(a|\theta), \hat{\rho}_{a|\theta}\}_{a,\theta}$ obtained after repeated measurements. Equivalently, we consider the set of unnormalized states $\{\hat{\sigma}_{a|\theta}\}_{a,\theta}$, called *assemblage*, defined by $\hat{\sigma}_{a|\theta} = p(a|\theta)\hat{\rho}_{a|\theta}$.

One property required for all admissible assemblages is the *non-signaling condition*. It aims to ensure that Bob cannot have any knowledge of Alice's measurement choice beforehand to avoid the possibility of supraluminal communications. In our context it means that the mixed state Bob observes without any information coming from Alice should be independent from θ:

$$\sum_a \hat{\sigma}_{a|\theta} = \sum_a \hat{\sigma}_{a|\theta'} \qquad \forall \theta, \theta'. \tag{5.19}$$

The steering test is successful if the assemblage measured by Bob couldn't have been obtained by a *local hidden state* (LHS) model. Such a model, sketched in figure 5.7, supposes that Bob receives a *local* quantum state $\hat{\rho}_\lambda$ while Alice receives a related piece of classical information λ that will determine the result a of her measurement θ according to a probability $p(a|\theta, \lambda)$. In the general case, we have a set of possible λ distributed according to probability distribution $\mu(\lambda)$. An assemblage $\{\hat{\sigma}_{a|\theta}\}$ following an LHS model satisfies

$$\hat{\sigma}_{a|\theta} = \int d\lambda \mu(\lambda) p(a|\theta, \lambda) \hat{\rho}_\lambda \qquad \forall\, a, \theta. \tag{5.20}$$

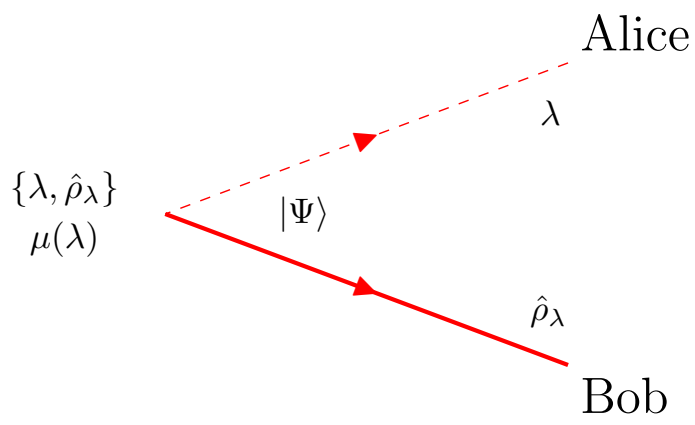

Figure 5.7: **Local hidden state model**. Correlations between the measurements made by Alice and the state measured by Bob are explained by Alice receiving a classical piece of information λ when Bob receives the state ρ_λ. The possible λ follow the probability distribution $\mu(\lambda)$.

To know if steering has indeed occured, Bob therefore has to perform tomographic measurements on his local state. After the measurements have been performed, Alice will send the complete history of her measurement choices and results from which Bob will split his data accordingly and reconstruct his assemblage. Crucially, and because Bob's measurements are trusted, he can take into account the losses introduced by his system and correct for them. Then is left the task of checking for a possible LHS model for the experimental assemblage.

3.1.2 Expressing the local hidden state model as a semi-definite program

Checking an assemblage against any LHS representation is hard in the general case [133], but it is possible to simplify the problem when the number of measurements and outputs made by Alice is finite. The idea is to rewrite $p(a|\theta,\lambda)$ using *deterministic* probability distributions. These distributions are defined using a set of functions λ' that assign to each measurement $\theta \in \{1,...,m_\mathrm{A}\}$ a fixed result $a \in \{1,...,o_\mathrm{A}\}$. There are $o_\mathrm{A}^{m_\mathrm{A}}$ possible such λ', each associated to a list of outcomes $\{a^{\lambda'}_{\theta=1}, a^{\lambda'}_{\theta=2}..., a^{\lambda'}_{\theta=m_\mathrm{A}}\}$. For every measurement made by Alice and its result, there exists a corresponding λ'. The conditional probability $p(a|\theta,\lambda)$ can be written using these functions:

$$p(a|\theta,\lambda) = \sum_{\lambda'} p(\lambda'|\lambda)\delta_{a,\lambda'(\theta)}, \tag{5.21}$$

keeping only the λ' for which $\lambda'(\theta) = a$. The $\delta_{a,\lambda'(\theta)}$ are deterministic probability distributions equal to one if $a = \lambda'(\theta)$ and otherwise equal to zero. The advantage of this formulation is that all the $\delta_{a,\lambda'(\theta)}$ are fixed, only $p(\lambda|\lambda')$ is undetermined. Injecting the expression (5.21) in the LHS model (5.20), we obtain

$$\begin{aligned}
\hat{\sigma}_{a|\theta} &= \sum_{\lambda'} \int d\lambda \mu(\lambda) p(\lambda'|\lambda)\delta_{a,\lambda'(\theta)}\hat{\rho}_\lambda \\
\hat{\sigma}_{a|\theta} &= \sum_{\lambda'} \delta_{a,\lambda'(\theta)}\hat{\sigma}_{\lambda'}, \\
\hat{\sigma}_{a|\theta} &= \sum_{\substack{\lambda' \\ a=\lambda'(\theta)}} \hat{\sigma}_{\lambda'},
\end{aligned} \tag{5.22}$$

where we define $\hat{\sigma}_{\lambda'} = \int d\lambda \mu(\lambda) p(\lambda'|\lambda) \hat{\rho}_\lambda$. In consequence, all $\hat{\sigma}_{\lambda'}$ are positive and that $\sum_{\lambda'} Tr(\hat{\sigma}_{\lambda'}) = 1$.

We therefore find that an assemblage following a LHS representation has to admit the expression (5.22), with the condition that the $\{\sigma_{\lambda'}\}$ are positive. It is actually always possible to find an expression in the form of (5.22) if we accept $\{\sigma_{\lambda'}\}$ that are negative [133]. The possibility of having a LHS model depends therefore only on the sign of the maximum value μ for which we can find a set $\{\sigma_{\lambda'}\}$ that verifies (5.22) and $\sigma_{\lambda'} \geq \mu * Id$ for all λ'. If μ is negative, no LHS model can account for the experiments results. The problem of searching for the maximum value of μ is in this context a particular instance of a general class of problems called *semi-definite programs* (SDP) that are well-known and can be solved in polynomial time [134]. The corresponding SDP formulation is:

$$\begin{aligned} \text{given} \quad & \{\hat{\sigma}_{a|\theta}\}_{a,\theta}, \{\delta_{a,\lambda'(\theta)}\}_{\lambda'} \\ \max_{\{\hat{\sigma}_{\lambda'}\}} \quad & \mu \\ \text{s.t.} \quad & \sum_{\lambda'} \delta_{a,\lambda'(\theta)} \hat{\sigma}_{\lambda'} = \hat{\sigma}_{a|\theta} \qquad \forall a, \theta, \\ & \hat{\sigma}_{\lambda'} \geq \mu * Id \qquad \forall \lambda'. \end{aligned} \tag{5.23}$$

The process can be described as: Given a set of conditioned states $\hat{\sigma}_{a|\theta}$ and all possible measurements θ and associated outcomes a, find the maximum value μ such that $\{\hat{\sigma}_{a|\theta}\}$ verifies equation (5.22). Obtaining a negative μ is impossible if there exists a LHS model, therefore if the result of the program is a negative number, a local description is ruled out and quantum steering is demonstrated. In the experimental context, SDP gives us a practical way, using existing libraries such as the one given in [133], to solve the problem of checking whether a LHS model can explain the measured assemblage.

3.1.3 From SDP to steering inequalities

The reformulation of a steering test as a SDP is convenient in an operational context but one can approach it differently to see the connection between Bell tests and quantum steering. Similar to how the violation of a Bell inequality proves a state to be Bell non-local, there exists inequalities that are respected for all LHS models. These are called *steering inequalities*, and can be found through the following re-expression of the SDP in equation (5.23). Let us consider a set of positive operators $\{\hat{F}_{a|\theta}\}_{a,\theta}$ and suppose we have a LHS model for the assemblage $\{\hat{\sigma}_{a|\theta}\}$. Then let us apply each operator to the corresponding state and sum over all a and θ. We obtain the following quantity:

$$\begin{aligned} \mathcal{S} &\hat{=} \ \text{tr}\Big(\sum_{a,\theta} \hat{F}_{a,\theta} \hat{\sigma}_{a|\theta}\Big) \\ \mathcal{S} &= \text{tr}\Big(\sum_{a,\theta,\lambda'} \hat{F}_{a,\theta} \delta_{a,\lambda'(\theta)} \hat{\sigma}_{\lambda'}\Big). \end{aligned} \tag{5.24}$$

All $\{\hat{F}_{a|\theta}\}$ being positive, in the case where a LHS model is valid, we have

$$\mathcal{S} = \text{tr}\Big(\sum_{a,\theta} \hat{F}_{a,\theta} \hat{\sigma}_{a|\theta}\Big) \geq 0. \tag{5.25}$$

This is an example of a steering inequality, the violation of which therefore demonstrates the observation of EPR steering. This is linked to SDPs as it can be shown [133] that SDP (5.23)

is equivalent to the following program:

$$\begin{aligned} \text{given} \quad & \{\hat{\sigma}_{a|\theta}\}_{a,\theta}, \{\delta_{a,\lambda'(\theta)}\}_{\lambda'} \\ \min_{\{\hat{F}_{a|\theta}\}} \quad & \mathcal{S} = \mathrm{tr}\,(\sum_{a,\theta} \hat{\sigma}_{a|\theta}\hat{F}_{a|\theta}) \\ \text{s.t.} \quad & \sum_{a,\theta} \hat{F}_{a|\theta}\delta_{a,\lambda'(\theta)} \geq 0 \qquad \forall\lambda', \\ & \mathrm{tr}\,(\sum_{a,\theta,\lambda'} \hat{F}_{a|\theta}\delta_{a,\lambda'(\theta)}) = 1. \end{aligned} \tag{5.26}$$

The SDP can therefore be seen as an optimization process over all possible $\{\hat{F}_{a|\theta}\}$, *i.e.* steering inequalities, in order to find the minimum value $\mathcal{S}_{min}$. If $\mathcal{S}_{min}$ is negative, the steering test is successful. The first condition ensures the positivity of $\mathcal{S}$ for LHS model compatible assemblages while the second normalization amounts to a scaling condition that allows one to compare between different steering inequalities.

Semi-definite programming allows the exploration of a much wider range of inequalities than we have considered for Bell tests. That being said, it is still necessary to find the appropriate measurements on Alice's mode independently. Indeed, the SDP only extracts the most suitable set of operators to apply on Bob's conditional states. We now present the experiment realized for the violation of a steering inequality using hybrid entanglement.

3.2 Performing EPR steering with our hybrid state

In this section, we first present the protocol used for quantum steering with hybrid entanglement, motivate some of the experimental settings and give the expected steering inequality violation. We then provide details on the experimental implementation and present the measured assemblage.

3.2.1 The setup

In the context of this experiment, and for generality, we start from *asymetric* hybrid entanglement, *i.e.* we assume that Alice and Bob share the hybrid non-maximally-entangled optical state $|\Psi\rangle_{\mathrm{AB}}$

$$|\Psi\rangle_{\mathrm{AB}} = \sqrt{R}\,|0\rangle_{\mathrm{A}}|\mathrm{Cat}_-\rangle_{\mathrm{B}} - \sqrt{1-R}\,|1\rangle_{\mathrm{A}}|\mathrm{Cat}_+\rangle_{\mathrm{B}}\,, \tag{5.27}$$

where R can be tuned by adjusting the heralding rates of both OPOs. The setup chosen is shown in figure 5.8. The measuremens performed on the DV mode are the Pauli operator approximations $\hat{\pi}(\theta)$ introduced in section 2.3: Quadrature measurements followed by sign-binning of the result. We therefore have $a \in \{+,-\}$. Bob separately performs tomographic measurements by recording the relative phase of his local oscillator and the quadrature value obtained at each event $\#N$. Having no information from Alice for this particular event, Bob cannot see the effect of her measurements yet. It is only after associating Alice's observations $\{\theta, a\}_N$ to the corresponding heralding events that he is able to split his data into $2m_{\mathrm{A}}$ subsets. He can then reconstruct the states $\{\rho_{a|\theta}\}_{a,\theta}$ and obtain the assemblage $\{\sigma_{a|\theta}\}_{a,\theta}$. EPR steering is demonstrated if the assemblage is impossible to describe with a LHS model, in which case Bob will be convinced and the test successful. In a loophole-free steering experiment, Alice's measurements need to be randomly chosen at a late enough time so that there

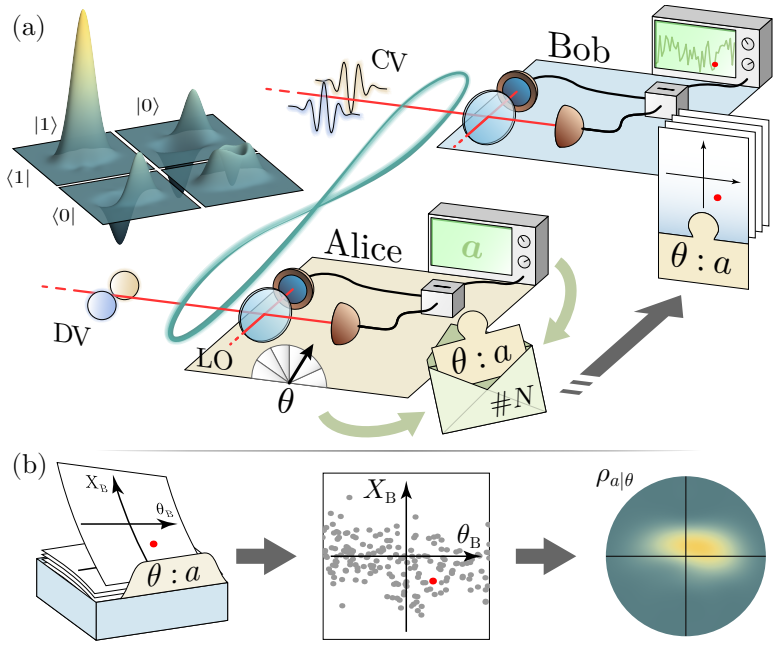

Figure 5.8: **Steering scenario with hybrid CV-DV entanglement of light**. (a) The two-mode hybrid entangled state is shared between Alice, who cannot be trusted, and Bob. On the DV mode, Alice locally performs quadrature measurements using homodyne detection at different phases θ of her local oscillator (LO) and registers the sign-binned measurement result $a = \pm$. She then sends the information to Bob, who uses it to sort his own quadrature measurements depending on the phase choice and sign result $\{\theta, a\}$. (b) Via quantum state tomography, Bob is able to reconstruct each conditional state $\rho_{a|\theta}$ and the associated Wigner functions. As detailed in the text, he obtains the assemblage $\{\sigma_{a|\theta}\}_{a,\theta}$ and tests it against any LHS model to prove that EPR steering has occurred.

can be no causal link between her measurement results and that of Bob. We chose not to follow these requirements in our implementation as implementing a sufficient time-separation between both modes would entail adding a significant amount of transmission losses. Indeed, changing Alice's measurement means going from one LO phase to another, a transition that follows the response time of our piezo-transducers. Being free from this requirement, we perform Alice's measurements in sequence. A consequence of this implementation is that the non-signaling condition is not necessarily respected and will have to be checked. Note however that, because we keep all quadrature measurement results, we are not subject to the detection loophole.

We now consider the expression of Bob's assemblage to see how the measurement settings can be tuned to get the best possible steering demonstration. The two possible conditionning for each of Alice's measurements $\hat{M}_\theta^+$ and $\hat{M}_\theta^-$ corresponding to a positive or negative quadrature measurement defined as:

$$\begin{aligned} \hat{M}_\theta^+ &= \int_0^{+\infty} \left|qe^{i\theta}\right\rangle \left\langle qe^{-i\theta}\right| dq \\ \hat{M}_\theta^- &= \int_{-\infty}^{0} \left|qe^{i\theta}\right\rangle \left\langle qe^{-i\theta}\right| dq. \end{aligned} \tag{5.28}$$

Following equation (1.54) of chapter 1, the corresponding conditional states are defined by

$$\rho_{a|\theta} = \frac{Tr_A(\hat{M}^a_\theta \left|\Psi\right\rangle \left\langle\Psi\right|_{\mathrm{AB}})}{Tr(\hat{M}^a_\theta \left|\Psi\right\rangle \left\langle\Psi\right|_{\mathrm{AB}})}, \tag{5.29}$$

which gives

$$\begin{aligned}\rho_{a|\theta} \propto a\ R \int_0^{a\infty} dq |\langle 0|q\rangle|^2 \left|\mathrm{Cat}_-\right\rangle \left\langle\mathrm{Cat}_-\right| + a\ (1-R) \int_0^{a\infty} dq |\langle 1|q\rangle|^2 \left|\mathrm{Cat}_+\right\rangle \left\langle\mathrm{Cat}_+\right| \\ + a\sqrt{R(1-R)}(e^{i\theta} \int_0^{a\infty} dq \left\langle 1|q\right\rangle \left\langle q|0\right\rangle \left|\mathrm{Cat}_-\right\rangle \left\langle\mathrm{Cat}_+\right| + h.c.).\end{aligned} \tag{5.30}$$

$|\langle 0|q\rangle|^2$ and $|\langle 1|q\rangle|^2$ are even functions of q normalized to an integration over $\{-\infty, +\infty\}$ so we have

$$a \int_0^{a\infty} dq |\langle 0|q\rangle|^2 = a \int_0^{a\infty} dq |\langle 1|q\rangle|^2 = 0.5. \tag{5.31}$$

The odd integral can be evaluated to

$$\begin{aligned} a \int_0^{a\infty} dq \left\langle 1|q\right\rangle \left\langle q|0\right\rangle &= \frac{1}{\sqrt{2\pi}\sigma_0\sqrt{2}} a \int_0^{a\infty} dq 2q e^{-(\frac{q}{\sqrt{2}\sigma_0})^2} \\ &= \sqrt{\frac{1}{2\pi}} a \int_0^{a\infty} 2ue^{-u^2} du, \qquad \text{where} \qquad u = \frac{q}{\sqrt{2}\sigma_0} \\ &= \sqrt{\frac{1}{2\pi}}. \end{aligned} \tag{5.32}$$

We finally obtain the following expression for Bob's assemblage:

$$\begin{aligned}\hat{\sigma}_{a|\theta} =& p(a|\theta)(R \left|\mathrm{Cat}_-\right\rangle\left\langle\mathrm{Cat}_-\right| + (1-R) \left|\mathrm{Cat}_+\right\rangle\left\langle\mathrm{Cat}_+\right| \\ &+ a\sqrt{2R(1-R)/\pi}(e^{i\theta} \left|\mathrm{Cat}_-\right\rangle \left\langle\mathrm{Cat}_+\right| + e^{-i\theta} \left|\mathrm{Cat}_+\right\rangle \left\langle\mathrm{Cat}_-\right|)),\end{aligned} \tag{5.33}$$

where $p(a|\theta) = 1/2$ for all a and θ as positive and negative quadrature measurements are equally likely.

To implement the best possible steering test, we did simulations using the **Matlab** implementation of a SDP tailored for steering tests supplied in [133] to determine what parameters to use. We first consider the optimum number of measurements Alice needs to perform and then the impact of losses and state asymmetry on the value of $\mathcal{S}$.

3.2.2 Experimental imperfections: transmission loss and phase noise

As seen in section 2, we have to consider transmission losses on Alice's and Bob's mode, respectively denoted as η_{A} and η_{B}. The escape efficiency of both OPOs is estimated to be 90%, which directly translates to 10% of intrinsic loss on both modes. Additionally, the homodyne detection setups introduce overall 15% of detection loss. The asymmetry of the steering scenario has however for consequence that these losses will not have the same impact for the two parties. Indeed in the steering context, because Bob trusts his apparatus, he can correct for these 15% detection losses when performing the tomographic reconstruction of his assemblage. On the other hand, no assumption can be made with regards to Alice's measurements, meaning that a similar correction process is not acceptable.

The second imperfection we take into account in the model is phase noise. This is done by

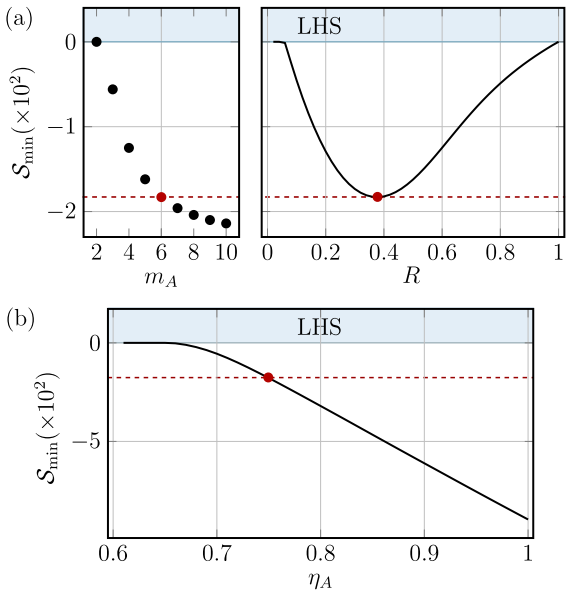

Figure 5.9: **Expected maximum steering inequality violation**. (a) Left: maximum violation depending on the number of measurements m_{A} performed by Alice, calculated at the optimal ratio R. Right: expected violation as a function of R for $m_{\mathrm{A}} = 6$. In both panels the overall efficiencies are assumed to be $\eta_{\mathrm{B}} = 90\%$ for Bob and $\eta_{\mathrm{A}} = 75\%$ for Alice. (b) Maximum violation as a function of Alice's efficiency η_{A} for $m_{\mathrm{A}} = 6$, $\eta_B = 90\%$, and $R = 0.37$. The red dot indicates the maximal violation possible in our experimental conditions.

modeling each conditional state $\hat{\sigma}_{a|\theta}$ as a mixture of conditional states of phases distributed as a Gaussian centered on θ with a standard deviation of δ_θ of 3°, mirroring the observed standard deviation of phases during the acquisition:

$$\hat{\sigma}'_{a|\theta} = \frac{1}{\sqrt{2\pi}\delta_\theta} \int_{-\infty}^{+\infty} \hat{\sigma}_{a|\theta'} e^{-\frac{(\theta-\theta')^2}{2\delta_\theta^2}} d\theta'. \tag{5.34}$$

Having established the model for the expected assemblage, we now use the SDP to see if steering is achievable.

3.2.3 Choosing the experimental settings

We first consider the number m_{A} of measurements performed by Alice. The left panel of Fig. 5.9 (a) shows the largest violation as a function of m_{A} when maximizing over all possible R. In our experimental conditions, one can see that a steering inequality violation is possible starting from three measurements. More measurements translate to a larger theoretical violation, with diminishing returns. Implementing a greater number of measurements leads however to issues because of the experimental fluctuations. As all different measurements are taken in sequence, we aim to combine data from independent runs made at different times. We have to keep the overall experimental duration as short as possible to respect the non-signaling condition. The compromise chosen is to perform a set of $m_{\mathrm{A}} = 6$ measurements. The variation of $\mathcal{S}_{\min}$ as a function of R for $m_{\mathrm{A}} = 6$ is then given on the right panel of Fig. 5.9(a). Because of the asymmetry in transmission losses for the CV and DV modes, equal balance between the two heralding rates is not optimal and the best violation is found for an unbalanced ratio $R = 0.37$.

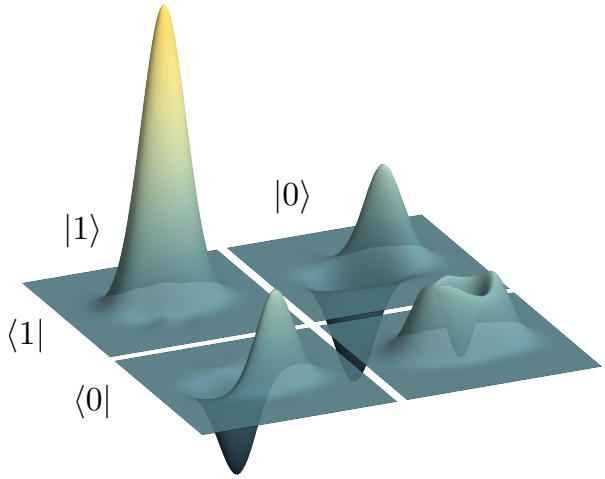

Figure 5.10: **Asymmetric hybrid state**. Wigner function for the asymmetric state with $R = 0.36$ corrected for detection losses on both modes. Its negativity of entanglement is $\mathcal{N} = 0.28$.

For these parameters, Figure 5.9(b) finally presents the best violation attainable depending on the transmission efficiency on Alice's side, which is not possible to correct for. One can see that our demonstration of EPR steering is challenging since it requires a transmission efficiency on Alice's mode higher than $\eta_{\mathrm{A}} = 65\%$. In the experimental conditions $\eta_{\mathrm{A}} \approx 75\%$, a steering violation can be expected.

3.2.4 Generation of the asymmetric hybrid state and steered assemblage

We generated the hybrid entangled state aiming for $R = 0.37$, in line with our simulation for optimal violation by tuning the ratio between the heralding rates of both modes. The state, which was heralded at a rate of 200 kHz, was first checked using the homodyne setups available on both the CV and DV modes, and the two-mode Wigner function was reconstructed using a MaxLik algorithm. Overall, including experiment reset, the whole data set has been captured in a couple-hour span. The single-mode Wigner functions of the four projections on the DV mode $\langle i| \rho_{\mathrm{AB}} |j\rangle$ with $i, j \in \{0, 1\}$ are plotted in Fig. 5.10. We find that higher-photon-number components in the DV mode are limited to 2% and the measured asymmetry is $R = 0.364$. The entanglement negativity reaches $\mathcal{N} = 0.28 \pm 0.01$ when corrected for detection losses. This value is lower than the negativity of entanglement obtained for a symmetric hybrid state $\mathcal{N} \approx 0.38$ but as we have seen in figure 5.9, the asymmetry comes from the possibility of correcting for losses on Bob's mode.

Having characterizing the hybrid state, we then performed the steering test with $m_{\mathrm{A}} = 6$ measurements made in sequence by Alice, corresponding to 6 values of her LO's relative phase $\theta = n \times \frac{\pi}{6}$ with $n \in [0, 5]$. We accumulated 120000 quadrature measurements on Bob's side for each value θ. Through a Maximum Likelihood optimization, we then reconstructed the complete assemblage $\{\sigma_{a|\theta}\}_{a,\theta}$. The experimental Wigner functions of each normalized subset of the assemblage are displayed in Fig. 5.11. The unconditioned state is shown at the center, $\hat{\sigma}_\theta = \sum_a \hat{\sigma}_{a|\theta}$. The Wigner functions of the 12 conditional states are displayed along the perimeter of the disc, at the angle and in the half space respectively corresponding to Alice's choice θ and result $a = \pm$. Depending on Alice's measurements, Bob's conditional state rotates around the phase-space origin.The non-signaling condition $\sum_a \sigma_{a|\theta} = \sum_a \sigma_{a|\theta'}$

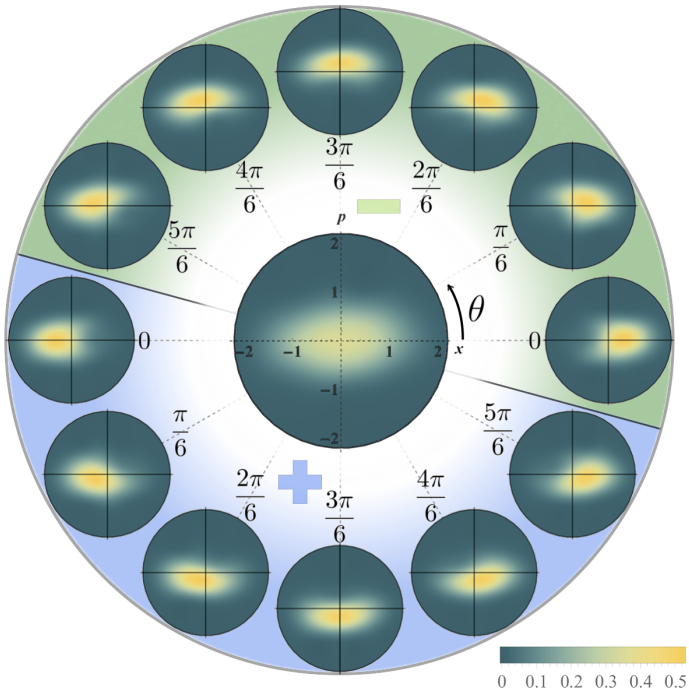

Figure 5.11: **Experimental steered states**. The Wigner function of Bob's unconditioned state is shown at the center of the disk. When Alice makes measurement $\theta \in \{n.\frac{\pi}{6}\}$ and gets result $a = \pm$, Bob's state is projected to the corresponding $\rho_{a|\theta}$. The associated Wigner function is displayed at the angle θ and in the half-space corresponding to a. The steering resulting from Alice's measurements translates into a rotation of Bob's state around the phase-space origin.

for all θ, θ' needs to be checked here. We find an average fidelity between unconditioned states $\mathcal{F}(\sigma_\theta, \sigma_{\theta'}) = 99.7 \pm 0.1\%$, within the bounds of the typical uncertainties associated with a MaxLik reconstruction.

We therefore have a clear visual representation of the impact of Alice's measurements. We can now confront this assemblage to a steering inequality to see whether the test is successful.

3.3 Finding the best inequality for our experimental assemblage

Our goal is to find the optimal steering inequality, meaning the best set of operators $\{\hat{F}^{opt}_{a|\theta}\}$ for our experimental data run. The most straightforward way to do so would be to input our experimental assemblage directly in the SDP and obtain from it $\{\hat{F}^{opt}_{a|\theta}\}$. This is however impossible in our case because of the slight deviation we have from the non-signaling condition. The optimum operators found by the SDP in this case are unphysical. They exploit the tiny differences between $\sigma_{+|\theta}$ and $\sigma_{-|\theta}$'s higher-dimensional components to give unbounded steering violations. In consequence, even close to identical states would see very different values of $\mathcal{S}$ for these operators, thereby proving their unphysical nature.

The alternative we followed is schematized in figure 5.12 and consists in building an assemblage $\hat{\sigma}^{\text{th}}_{a|\theta}$ as close as possible to the experimental one $\hat{\sigma}^{\text{exp}}_{a|\theta}$ but still verifying the non-signaling condition. Then apply the SDP to this assemblage and use the output optimum operators on the experimental assemblage to see whether steering has occurred. The valid-

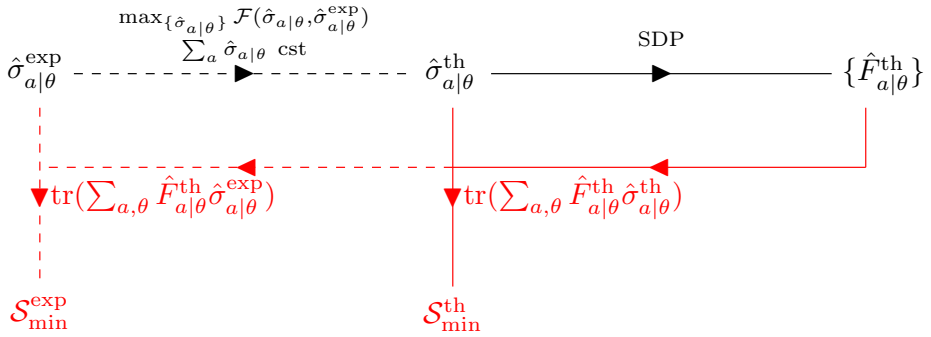

Figure 5.12: **Finding steering inequalities**. Scheme to get the optimal steering inequality for the experimental assemblage. Full lines represent processes that lead with certainty to the optimal result, whereas dashed lines stand for processes that may be suboptimal. As the experimental assemblage $\{\sigma^{\text{exp}}_{a|\theta}\}$ presents a slight deviation from the non-signaling condition, it cannot be directly used in a SDP. We therefore build a theoretical assemblage $\{\sigma^{\text{th}}_{a|\theta}\}$ following equation (5.33) and optimize parameters such as squeezing amount, asymmetry and losses to get as close as possible to $\{\sigma^{\text{exp}}_{a|\theta}\}$ while preserving the non-signaling condition. We model the process as a search for the maximum of a function $\mathcal{F}(\sigma, \sigma')$ which outputs a general parameter evaluating how close σ and σ' are. We then perform SDP on the theoretical assemblage maximizing $\mathcal{F}$ to obtain the optimal steering inequality associated to the operators $\{\hat{F}^{\text{th}}_{a|\theta}\}$. These operators are then applied to the experimental assemblage to find the experimental steering parameter $\mathcal{S}^{\text{exp}}_{\text{min}}$. Note that the function $\mathcal{F}$ can be the fidelity but not necessarily; it is judged only on the value of $\mathcal{S}^{\text{exp}}_{\text{min}}$ at the end of the global process, and therefore may be dependent on $\hat{\sigma}^{\text{exp}}_{a|\theta}$.

ity of the $\hat{F}_{a|\theta}$ is ensured by the non-signaling condition and verified by the stability of the value of $\mathcal{S}$ when applying the operators to the experimental assemblage with the addition of variable small noise. Actually finding the set of $\hat{\sigma}^{\text{th}}_{a|\theta}$ that will lead to the minimum value of $\mathcal{S}^{\text{exp}}_{\text{min}}$ is tricky because neither higher average fidelities with the experimental conditional states nor lower $\mathcal{S}^{\text{th}}_{\text{min}}$ values ensure lower $\mathcal{S}^{\text{exp}}_{\text{min}}$. This two-step process also prevents us from concluding that the best operators found are the optimal ones.

Iterative trials finally led to a set of operators that result in a negative $\mathcal{S}^{\text{exp}}_{\text{min}}$. We limited ourselves to an assemblage following the expected structure of equation (5.33) and optimizing on parameters such as experimental losses, squeezing and asymmetry. The most suitable theoretical assemblage found does not correspond however to the expected states and the operators $\{\hat{F}^{\text{th}}_{a|\theta}\}$ differ from the operators found in the previous simulations for our experimental model. The $\{\hat{F}^{\text{th}}_{a|\theta}\}$ are the optimal operators for a non-signaling assemblage with an asymmetry of $R = 0.24$ (instead of 0.37) and a squeezing before losses of 2.7 dB (instead of 3 dB), although with accurate losses $\eta_A = 0.75$ and $\eta_B = 0.89$. Whether this deviation from the actual assemblage is due to the suboptimal processes in our derivation of the operators or due to other types of losses we failed to take into account remains to be determined. Although our model is imperfect, the difference is too big to be solely due to a mischaracterization of our apparatus.

In the end, we obtain a maximum steering inequality violation of $\mathcal{S}^{\text{exp}}_{\text{min}} = -0.00755$ for a set of operators that when applied to their source non-signaling assemblage give the result $\mathcal{S}^{\text{th}}_{\text{min}} = -0.011$. Both results are below the expected violation $\mathcal{S} \approx -0.018$ found in section 3.2.3, which indicates that the process of finding the optimal operators can be significantly improved. The steering test can however only be successful after evaluating the

associated error bar. We now present the method we followed to evaluate the uncertainties associated to the tomographic reconstruction.

3.4 Evaluating the error bars for our steering test

In this section, we will detail some of the calculations made in order to evaluate the uncertainties associated to our steering test. Because the steering parameter $\mathcal{S}_{\min}^{\exp}$ is obtained through a multi-stage process, as opposed to being directly measured, we have to be particularly careful with regards to error propagation.

The main error source to consider here is the tomographic reconstruction of the assemblage $\{\hat{\sigma}_{a|\theta}\}$, which results from the combination of 12 Maximum-Likelihood (ML) optimization processes. Each ML process is irreversible and in effect destroys a lot of the available information contained in the complete set of quadrature measurements. We will describe two approaches we followed to estimate the uncertainties associated to the ML process: the frequently used Bootstrap method, and then an application of the so-called quantum error bars method recently proposed in [44].

3.4.1 Notations and error sources to consider

As Alice's measurements are not trusted, we do not need to consider imperfections in her implementation as it will only change the set of operators $\{\hat{F}_{a|\theta}\}$ we will use in our steering test. On Bob's side, it is the tomographic reconstruction process that has to be evaluated.

After his quadrature measurements, Bob obtains a data set for each experimental run. It consists of quadrature measurements at given local oscillator phases ϕ: $\{q_\phi, \phi\}_{N_{a|\theta}}^{a|\theta}$, with $N_{a|\theta}$ the number of measurement events from which will be reconstructed the corresponding conditional state, which we will denote as $\hat{\rho}_{a|\theta}^{\mathrm{ML}}$ to highlight the fact that it is obtained after a ML optimization. At this step, errors in the evaluation of ϕ and, to a lesser extent, of q_ϕ can arise. We suppose however that those errors will never improve the steering violation observed with our assemblage. In the case of ϕ, they will instead introduce more phase noise while errors on q_ϕ are linked to the centering of the temporal mode and will be equivalent to additional transmission losses. This supposition is validated by experimental observations: a more accurate phase fitting process led to a significant increase of the measured violation.

On the other hand, the MaxLik reconstruction can lead to an over-estimation of the steering violation. A first reason for this is that it outputs the density matrix most susceptible to have lead to the observation of the set $\{q_\phi, \phi\}_{N_{a|\theta}}^{a|\theta}$, $\hat{\rho}_{a|\theta}^{\mathrm{ML}}$, not the "actual" experimental state $\hat{\rho}_{a|\theta}^{0}$. One therefore has to evaluate the chance that the measurement of $\{q_\phi, \phi\}_{N_{a|\theta}}^{a|\theta}$ is an unlikely event, *i.e.* how different can $\hat{\rho}_{a|\theta}^{\mathrm{ML}}$ and $\hat{\rho}_{a|\theta}^{0}$ realistically be. A second reason is that we use loss correction during the ML process for 15% of transmission loss. This can lead to an overestimation of $|\mathcal{S}_{\min}^{\exp}|$.

In consequence, it is necessary to evaluate the uncertainties associated to the MaxLik optimization. To that end, we present two different methods considered. We first consider the parametric bootstrap method, which is often used for practical error estimation (for example in the steering test reported on in [135]), and then follow a more accurate –but also more time-consuming– method recently introduced in [44]: the derivation of so-called quantum error bars.

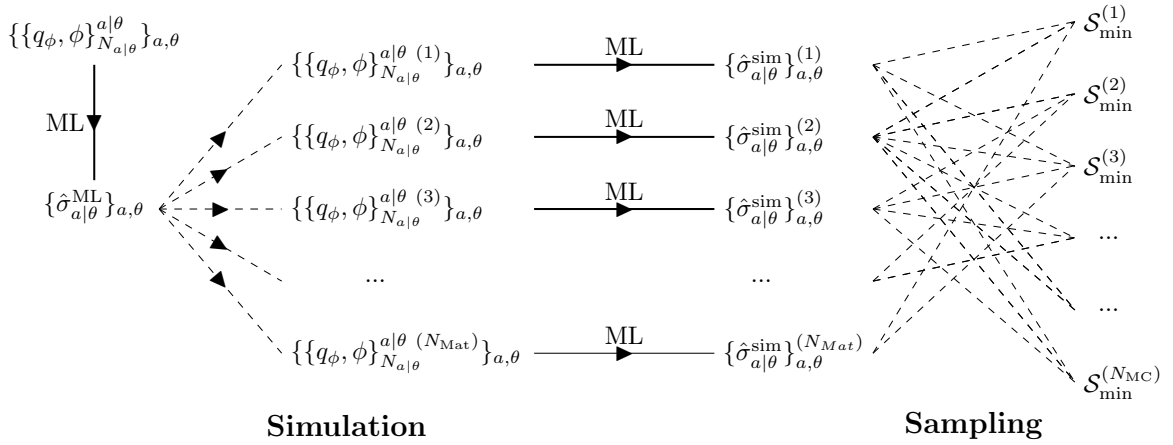

Figure 5.13: **Parametric bootstrap method**. Full lines represent the irreversible process of Maximum-Likelihood optimization while dashed lines stand for processes that can be optimized: simulation and data sampling. We start from the set of homodyne measurements $\{q_\phi, \phi\}^{a|\theta}_{N_{a|\theta}}$ and perform MaxLik optimization to get the state $\hat{\rho}^{\mathrm{ML}}_{a|\theta}$ most likely to have led to these results. From this state, we generate a set of N_{Mat} simulated measurements $(\{q_\phi, \phi\}^{a|\theta\ (j)}_{N_{a|\theta}})_j$. Each simulated measurement set has the same size as the experimental data $\{q_\phi, \phi\}^{a|\theta}_{N_{a|\theta}}$. We then perform MaxLik optimization on each simulated data set to recover N_{Mat} simulated assemblages. We complete the process by randomly sampling N_{MC} sets of 12 $\sigma^{\mathrm{sim}}_{a|\theta}$ to compute N_{MC} steering parameter values $\mathcal{S}^{(j)}$. The standard deviation of the final set is used to assess the tomographic uncertainties.

3.4.2 Error bar estimation using the parametric bootstrap method

Principle The first process we consider is a parametric Bootstrap method [136]. The advantages it presents are speed of computation and simplicity. The principle is shown in the diagram of figure 5.13. We construct from $\hat{\rho}^{\mathrm{ML}}_{a|\theta}$ (itself reconstructed from $\{q_\phi, \phi\}^{a|\theta}_{N_{a|\theta}}$) many measurement sets $(\{q_\phi, \phi\}^{a|\theta\ (j)}_{N_{a|\theta}})_j$, with j varying from 1 to N_{Mat} the total number of sets built. Then, combining 12 assemblage members chosen randomly from all sets for all a and θ we obtain an ensemble of assemblages $\{\hat{\sigma}^{\mathrm{sim}}_{a|\theta}\}_k$ corresponding to $\mathcal{S}^k_{\mathrm{min}}$, with k varying from 1 to N_{MC}, the number of sampled steering parameter values. Building a histogram of $\mathcal{S}_{\mathrm{min}}$ values, denoted as $H^{N_{\mathrm{MC}},N_{\mathrm{Mat}}}_{\mathcal{S}}$, finally enables us to evaluate the standard deviation associated to the ML reconstruction.

The bootstrap method is parametric in that it is a resampling of the initial data set $\{q_\phi, \phi\}^{a|\theta}_{N_{a|\theta}}$ biased by $\hat{\rho}^{\mathrm{ML}}_{a|\theta}$. The method depends strongly on the first maximum-likelihood process and therefore doesn't take into account the possibility of having made an outlier measurement. It means that although it will give a reasonably accurate value of standard deviation, the mean value $\overline{\mathcal{S}_{\mathrm{min}}}$ can be far off. Because of the quick computational time, it was done first however to get an idea of the quality of our violation.

Simulation of quadrature measurements The quadrature measurement simulation consists in the generation of quadratures randomly with the weight of the probability distribution $P(q, \phi)$ computed from $\hat{\rho}^{\mathrm{ML}}_{a|\theta}$. To do so we divide the (q, ϕ) space in a grid of dimensions $D_\phi * D_q$. We then assign numbers to each of these subdivisions so that $N(q;;q+dq,\phi;;\phi+d\phi) = P(q,\phi)*N_{tot}$, where N_{tot} is a parameter tuning the discretisation of $P(q, \phi)$. Any num-

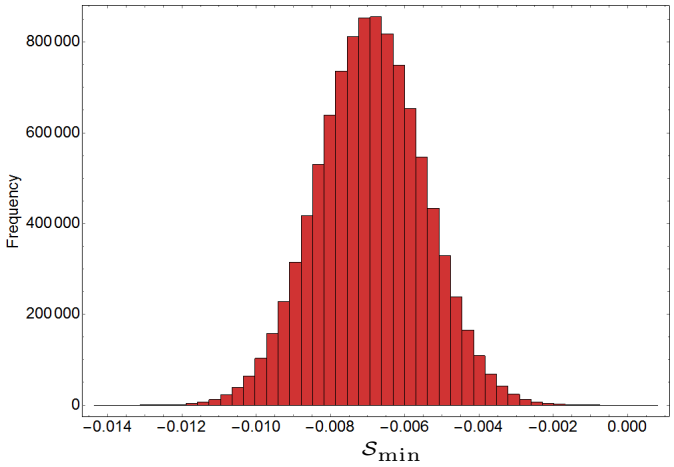

Figure 5.14: **Results using the Bootstrap method**. Histogram of the steering parameter values using the parametric Bootstrap method. We use a sample of $N_{\text{MC}} = 10^7$ points out of a set of $N_{\text{Mat}} = 12 * 2 * 10^4$ density matrices. We obtain a Gaussian distribution centered on $\mathcal{S} = -0.00691$ with a standard deviation $\sigma = 0.00144$.

ber between 1 and N_{tot} will therefore correspond to a given subdivision. The mapping between the number and the subdivision is surjective but not injective, the divisions corresponding to the most probable quadrature measurements being the ones that have the biggest number of preimages. We therefore choose a random number between 1 and N_{tot}, find the associated subdivision and choose a random quadrature measurement $(q_j, \phi_j) \in [q;;q+dq, \phi;;\phi+d\phi]$. We repeat this process $N_{a|\theta}$ times for each conditional state to have as many simulated measurements as we had experimentally. In practice we had converging results well before settling to our final choice of $D_\phi = D_q = 3000$ and $N_{tot} = 10^9$.

Results For each set $\{a, \theta\}$, we simulated 20000 matrices. We then computed 10^7 values of $\mathcal{S}$ randomly choosing assemblages through the set of $12 * 2 * 10^4$ density matrices. The results are shown in figure 5.14. We obtain $\mathcal{S} = -0.00691 \pm 0.00144$ which corresponds to a violation of 4.8σ. With these settings, and in the condition that we trust the bootstrap method, we have a steering violation at a distance close to five standard deviation from the local bound. Interestingly, the average value is not the one of the experimental data, *i.e.* the result obtained when applying the operators $\hat{F}_{a|\theta}$ on $\{\hat{\rho}^{\text{ML}}_{a|\theta}\}$ which is $\mathcal{S}^{\text{ML}}_{\min} = -0.00755$. The validity of only considering $12 * 2 * 10^4$ density matrices and a number of samples of $N_{\text{MC}} = 10^7$ is developed in appendix 5A.

This first result is a very strong indicator of the success of our steering test. As we see from figure 5.13 however, it introduces many times the MaxLik procedure which is inherently irreversible. For this reason, it is worthwhile to consider a different method: the computation of so-called *quantum error bars*.

3.4.3 The metropolis-hastings method: quantum error bars

As shown in section 3.4.2, the bootstrap method we used includes many iterations of the maximum-likelihood algorithm. The ML process can cause issues in cases where the number of measurements is insufficient. Those include the impossibility of constructing confidence regions because the most likely state found can be at the border of physical states, see [137] for a discussion on these issue. The question is whether or not we have enough measurements to be confident in the repeated use of ML. Because the density matrix contains all possible information about a state, it is impossible to say *a priori* whether enough information has been accumulated for a particular measurement, be it negativity of the Wigner function or, in our case, the value of $\mathcal{S}_{\min}$. For most state characterization made in this thesis, we had confidence enough in the results, because of their consistency over repeated experiments but also because they involve ML at most once. In the case of steering, we found it worthwhile to use a recently introduced [44] method for uncertainty estimation called *quantum error bars*.

Principle The idea behind the method is to keep the likelihood function $\mathcal{L}$ in use as long as possible during the error estimation process as it contains all the information obtained from our measurements. From the set of quadrature measurements made, we write the likelihood function of each conditional state using the corresponding set of operators $\{M_{a|\theta}^{(k)}\}_{N_{a|\theta}}$:

$$\mathcal{L}_{a|\theta}(\hat{\rho}) = \prod_{k=1}^{N_{a|\theta}} \mathrm{Tr}(M_{a|\theta}^{(k)}\hat{\rho}). \tag{5.35}$$

Keeping the likelihood function, we will not only consider the most likely matrix $\hat{\rho}^{\mathrm{ML}}$ but also density matrices for which the likelihood function is close to maximum. The objective is to find the probability distribution $\mu(\mathcal{S}_{\min})$ of parameter $\mathcal{S}_{\min}$. To do so, we compute separately the probability distributions associated to the measurement of each operator $\hat{F}_{a|\theta}$ as this can only lead to an overestimation of uncertainties. This is done by integrating the values of $f_{a|\theta}(\rho)\hat{=}p(a|\theta)\,\mathrm{tr}(\hat{F}_{a|\theta}\hat{\rho})$ over a large range of density matrices $\hat{\rho}$, using the likelihood function $\mathcal{L}_{a|\theta}$ as bias:

$$\mu(f_{a|\theta}) \propto \int \mathcal{L}_{a|\theta}(\hat{\rho})\delta(f_{a|\theta}(\hat{\rho}) - f_{a|\theta})d\hat{\rho} \tag{5.36}$$

Here the likelihood $\mathcal{L}_{a|\theta}$ is no longer viewed as a function but as a distribution $\mathcal{L}_{a|\theta}(\hat{\rho})d\hat{\rho}$. This is done by multiplying it by a prior distribution $\pi(\rho)d\rho$. This prior distribution represents the knowledge we have of our state prior to the experiment. In the context of the steering test we consider, we chose a fully indifferent prior, i.e., we make no prior assumption on the states observed and postulate $\pi(\hat{\rho})d\hat{\rho} = \frac{1}{c}d\hat{\rho}$, with c a normalizing factor such that $\int \frac{1}{c}\mathcal{L}(\hat{\rho})d\hat{\rho} = 1$. The challenging part in the computation of $\mu(f_{a|\theta})$ is actually finding the normalization constant c. The difficulty is avoided by the use of a Metropolis-Hastings (MH) algorithm to reconstruct $\mu(f_{a|\theta})$.

The MH algorithm amounts to a random walk in state space biased by the likelihood function to obtain a set of density matrices $\{\hat{\rho}_i\}$. At every step, a candidate density matrix ρ_c is chosen according to a jump distribution $Q(\hat{\rho}_c|\hat{\rho}_i)$ centered on ρ_i. Whether $\hat{\rho}_c$ will be kept depends on its likelihood. The iterative process is the following:

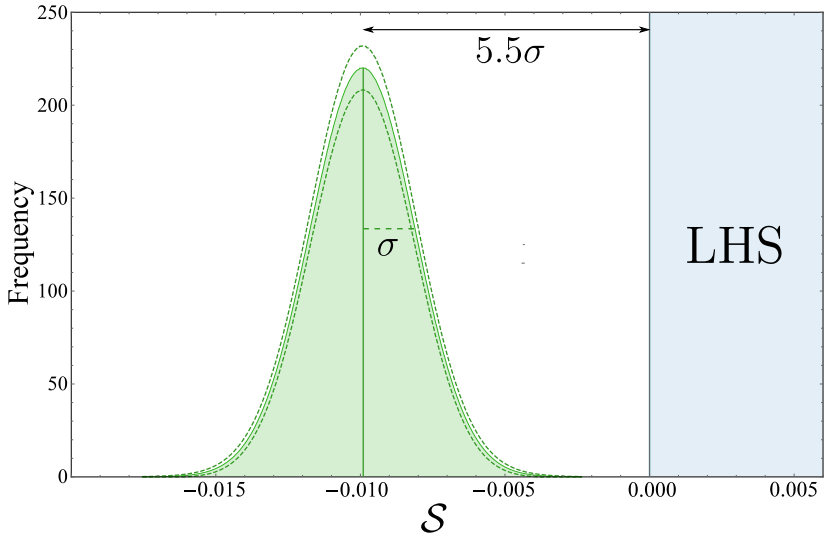

Figure 5.15: **Results using the quantum error bar method**. Histogram of the steering parameter values using the Metropolis-Hastings method. We use a sample of $N_{\text{MC}} = 5 * 10^8$ points out of a set of $N_{\text{Mat}} = 12 * 10^4$ density matrices. The dashed lines correspond to one standard deviation from the average histogram. We measure a separation to the local bound of $-5.48\sigma \pm 0.18\sigma$.

Given $\hat{\rho}_i$,

- Choose randomly a candidate density matrix $\hat{\rho}_c$ according to $Q(\hat{\rho}_c|\hat{\rho}_i)$
- Compute $a = \frac{\mathcal{L}_{a|\theta}(\hat{\rho}_c)}{\mathcal{L}_{a|\theta}(\hat{\rho}_i)}$.
- If $a > 1$, then $\hat{\rho}_{i+1} = \hat{\rho}_c$.
- Else, set $\hat{\rho}_{i+1} = \hat{\rho}_c$ with probability a and $\hat{\rho}_{i+1} = \hat{\rho}_i$ with probability $1 - a$

After a great number of iterations where the values $f_{a|\theta}(\rho_i)$ are recorded, the distribution obtained will converge to a distribution $\tilde{\mu}(f_{a|\theta})$ directly related to $\mu(f_{a|\theta})$. The difference between the two distributions is due to the MH process and can be corrected for. In our case however, because we combine twelve of these $\tilde{\mu}(f_{a|\theta})$, their respective skewing will compensate one-another and, as detailed in appendix 5D, we found this last process unnecessary. Other bias sources have been considered as well, as discussed in appendices 5A and 5B.

Results and comparison with BootStrapping. We chose a gaussian jump distribution $Q(\hat{\rho}_c|\hat{\rho}_i)$ with a standard deviation adjusted during the exploration so that we would observe a jump close to 23% of the time, the ideal value to efficiently explore the state space [138]. Recording one out of a thousand density matrices during the iterative process, we obtained $N_{\text{Mat}} = 10^4$ matrices for each conditional state. From them, we computed 5.10^8 $\mathcal{S}_{\text{min}}$ values whose histogram is shown in figure 5.15. This is exactly the distribution $\mu(\mathcal{S})$ described in [44]. It should be a skewed gaussian function, the skewing being due to the exploration process induced by the Metropolis Hastings algorithm but the skewing is not noticeable and a secondary source of error in our final histogram, (see Appendix 5D). The final fitting of our data is a gaussian of mean $x_0 = -0.00992 \pm 0.00010$ and standard deviation $\sigma = 0.00181 \pm 0.00004$,

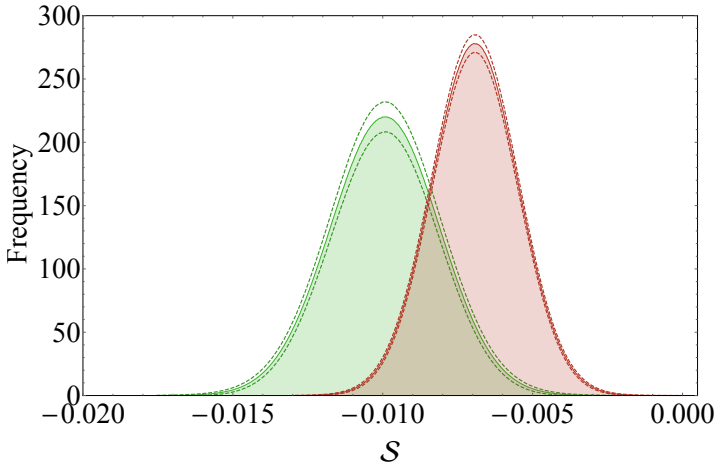

Figure 5.16: Histogram of the steering parameter values for 5.10^8 points out of a set of $12 * 2 * 10^4$ density matrices using the bootstrap method (in red) and using a set of $12 * 10^4$ density matrices using the quantum error bar approach (in green).

which gives a separation to the local bound of $-5.48\sigma \pm 0.18\sigma$.

Comparing now to the BootStrap process in 5.16 we see that we have both a higher violation and a larger standard deviation using the second method of quantum error bars. Interestingly neither of the two method is centered on the $\mathcal{S}$ value of the initial $\rho^{\mathrm{ML}}_{a|\theta}$ assemblage, which was $S^{\mathrm{exp}}_{\mathrm{min}} = -0.00755$. However we are closer in the case of the MH method to the violation we expected for the theoretical non-signalling assemblage closest to our experimental data: $S^{\mathrm{th}}_{\mathrm{min}} = -0.01103$. The MH procedure outputs an ensemble of density matrices for which the steering test result is the one of a non-local assemblage. Note that one could apply to each density matrix a different steering inequality and get an increased violation. This is however very time consuming and the distance to the local bound we observe is enough that this was not deemed necessary.

Overall, we are confident in the observation of EPR-Steering at more than 5σ as seen when using the Metropolis-Hastings method. The bootsrap method is known to be not fully accurate [44] especially in our case where we made the weak hypothesis of having ρ^{ML} as a root matrix. This result represents a clear demonstration of EPR steering and a robust entanglement certification with one untrusted party.

4 Conclusion

In this chapter, we have evaluated the non-local features of hybrid entanglement. We first started with a study of the loss-requirements for the realization of a Bell test using several different strategies. We find the implementation of a Bell test challenging with our current implementation of hybrid entanglement using photon-number encoding on the DV mode. The planned generation of hybrid entanglement with polarization encoding would however make the demonstration accessible. We then considered the intermediate scenario of quantum steering and we report on the violation of a steering inequality by more than five standard deviations, for the first time using hybrid entanglement.

The demonstration of EPR steering with optical hybrid entanglement proves its usefulness for a wider range of quantum information protocols. It opens in particular the possibility of

realizing one-sided device independent protocols. These would be particularly useful in the context of heterogeneous quantum networks where disparate physical platforms and encoding would interact at different levels of trust. It encourages us as well to try and implement other protocols. In the next two chapters we present the current progress towards the realization of one of the group's long-standing objective: hybrid quantum teleportation.

5 Appendix

5A. Adjusting the number of matrices $N_{\mathbf{Mat}}$ and the number of samples $N_{\mathbf{MC}}$

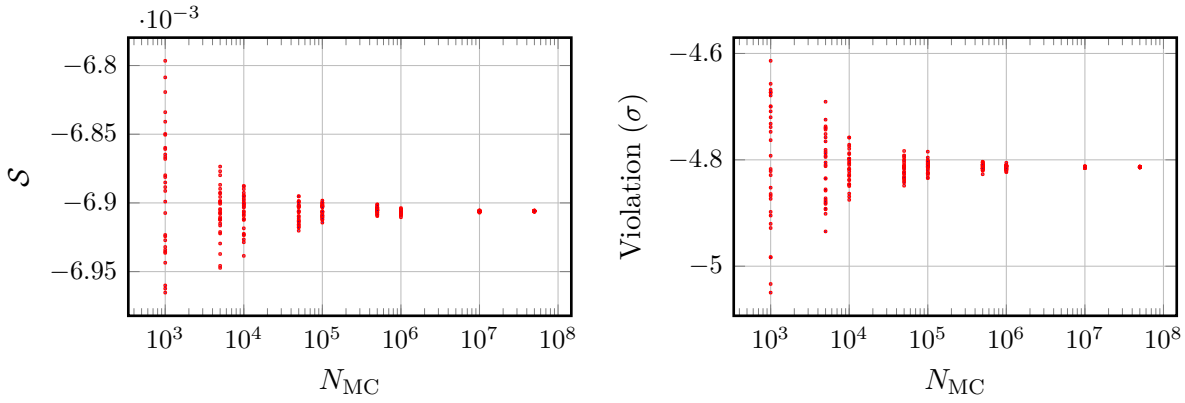

Figure 5.17: (a): Mean value of $\mathcal{S}$ for histograms of N_{MC} points. (b): Mean value of separation to the local bound in terms of standard deviations for histograms of N_{MC} points. In both cases $N_{\mathrm{Mat}} = 10^4$ and we computed 30 histograms for each N_{MC}.

This appendix gives some details on the sampling process used in the methods for error estimation. Two parameters have to be chosen such that convergence is observed, N_{Mat} and N_{MC}. The first one refers in the case of bootstrapping to the number of simulated quadrature measurement sets and the second one in both cases to the number of samples taken to build the final histogram. We demonstrate their effect in the context of bootstrapping, keeping in mind that the conclusions for N_{MC} will be valid for both methods.

In the end we want to have a probability distribution of $\mathcal{S}$, but since we generate density matrices and then compute the associated steering value, we have to choose two parameters: N_{Mat} the number of each density matrix (so we have up to N_{Mat}^{12} possible assemblages) and N_{MC} the number of values $\mathcal{S}^j$ we compute to construct an histogram of violations $H_{\mathcal{S}}^{N_{\mathrm{MC}},N_{\mathrm{Mat}}}$. One can see N_{Mat} as an indicator of the size of the space we are exploring to find a N_{MC} points error distribution. To accurately recover the actual error distribution associated to the MaxLik reconstruction, both numbers should be as high as possible. However, for computational reasons, we limited N_{Mat} to the order of 10^4. This gives us a great number of possible permutations but one has to check that we are well beyond a point of convergence for the obtained values of $\mathcal{S}$ and associated histograms $H_{\mathcal{S}}^{N_{\mathrm{MC}},10^4}$.

The first thing we check is the number of points N_{MC} in our histogram we need to have to accurately represent the steering parameter distribution of our set of $12 * N_{\mathrm{Mat}}$ matrices. In Fig. 5.17 (a) we looked at the influence of the number of points in histograms of $\mathcal{S}$ on their mean value. Each point corresponds to the mean value of an histogram $H_{\mathcal{S}}^{N_{\mathrm{MC}},10^4}$, we did 30 histograms for each value N_{MC}. Fig. 5.17 (b) presents the same results but looking at the distance to the local bound in terms of standard deviations. One can see that for values of N_{MC} above 10^6 the $H_{\mathcal{S}}^{N_{\mathrm{MC}},10^4}$ will give consistent results.
We conclude from this that 10^6 $\mathcal{S}$ values chosen randomly is a sufficient sampling of our set of $12 * 10^4$ matrices constructed through the Monte-Carlo simulation. That being said, we also have to check the validity of considering only $12 * 10^4$ matrices. In Fig. 5.18, we do

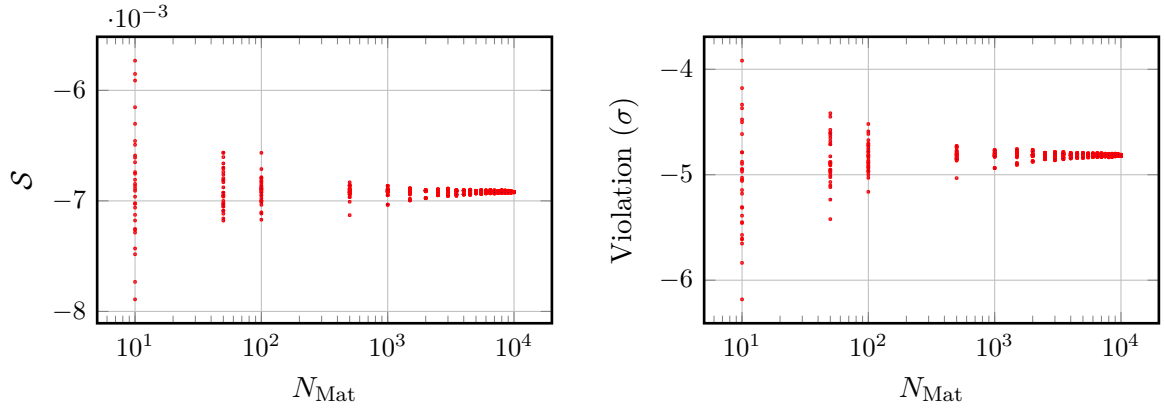

Figure 5.18: (a): Mean value of $\mathcal{S}$ for histograms of N_{Mat} points. (b): Mean value of separation to the local bound in terms of standard deviations for histograms of N_{Mat} points. In both cases $N_{\text{MC}} = 10^6$ and we computed 30 histograms for each N_{Mat}.

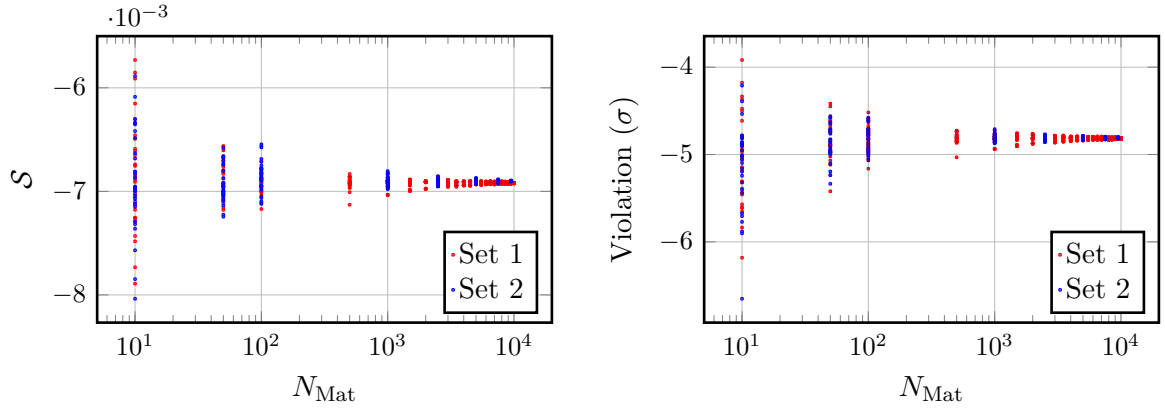

Figure 5.19: (a): Mean value of $\mathcal{S}$ for histograms of N_{Mat} points for two sets of global size $12 * 10^4$. (b): Mean value of separation to the local bound in terms of standard deviations for histograms of N_{Mat} points for two sets of global size $12 * 10^4$. In both cases $N_{\text{MC}} = 10^6$ and we computed 30 histograms for each N_{Mat} of each set.

the same study by fixing the value of N_{MC} to 10^6 and then investigating the consistency of histogram results depending on the size of the space we are exploring through the variation of N_{Mat}. Note that for each point we are constructing $H_{\mathcal{S}}^{N_{\text{MC}},N_{\text{Mat}}}$ from the set $\{n\}$ of values respecting $\{n\} \in [n_r; n_r + N_{\text{Mat}}(\mod 10^4)]$ with n_r a random integer between 1 and 10^4.

We seem to reach convergence at around $N_{\text{Mat}} \approx 5 * 10^3$ but we have to keep in mind that we are bound by the global set of matrices of size $12 * 10^4$. This mainly means that a set of $12 * 5 * 10^3$ matrices is a good sampling of the space spanned by the whole $12 * 10^4$ set. Here we are really limited to the computation time of all these matrices but we decided to compute 10^4 additional ones to obtain two different spaces of size $12 * 10^4$ and compare the previous analysis in both cases. The results are plotted in Fig. 5.19.

Although there is a visible difference when looking at the absolute $\mathcal{S}_{\text{min}}$ value, taking into account the standard deviation shows that the distance to the local bound of the two sets are for our practical purpose identical.
This concludes our study of the appropriate number of density matrices to reach convergence

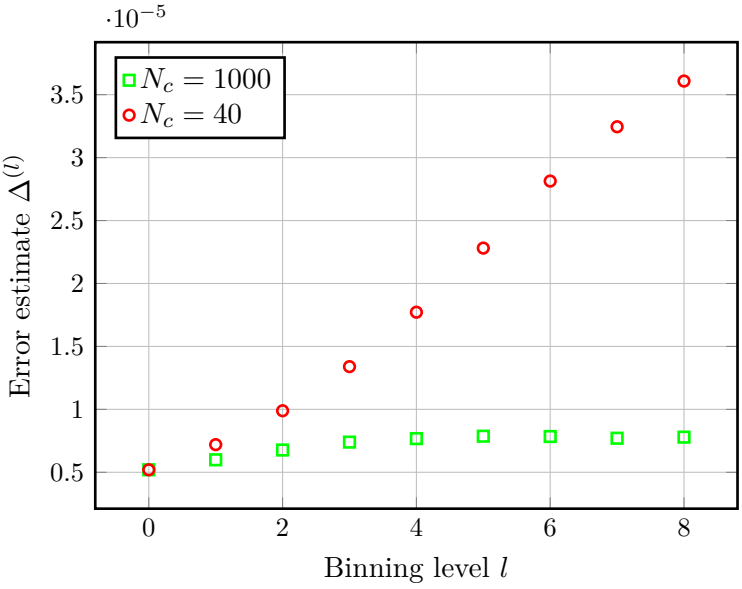

Figure 5.20: Binning analysis of $f_{a|\theta}(\rho)$ averaged over a and θ for two data sets of size $M = 10000$ with different sample rejection rates N_c. We can see that convergence is reached only for the sample build with $N_c = 1000$ for a binning level $l \geq 5$. This data allows the computation of the integrated auto-correlation time of each data set $A^{(0)}_{a|\theta}$ as the error bars on $\mu(f_{a|\theta})$.

of results when reconstructing density matrices through a parametric bootstrap process. With the setting of $N_{\text{Mat}} = 10^4$ and $N_{\text{MC}} = 10^6$ we feel that the errors still left on this distance to the local bound estimation are linked more to the validity of realising a parametric bootstrap than to the limited number of iterations we are bound to do.

5B. Sample correlation in the Metropolis-Hastings exploration

As the MH algorithm is an iterative process, correlations between samples have to be taken into account and in our case keeping only one out of $N_c = 1000$ values of $f_{a|\theta}(\rho_i)$ and accumulating $M = 10000$ samples was enough to circumvent their effect. This was verified by computing the sample set's *integrated autocorrelation time* τ_A [139]. This parameter indicates the distance between two uncorrelated samples in the data set and can be computed through a binning analysis. This process consists in creating, from the original data set $A^{(0)}_{a|\theta} = \{f_{a|\theta}(\rho_i)\}_{i \leq M}$, several binned series by averaging consecutive entries following:

$$A^{(l)}_{a|\theta} = \frac{1}{2}\{A^{(l-1)}_{a|\theta,2i-1} + A^{(l-1)}_{a|\theta,2i}\}_{i \leq M/2^l}. \tag{5.37}$$

For each of these $A^{(l)}_{a|\theta}$ we can then compute the error estimate $\Delta^{(l)}_{a|\theta} = \sqrt{Var(A^{(l)}_{a|\theta}) * 2^l/M}$. To show the effect of N_c, we compared two data sets of size $M = 10000$ constructed independently with parameters $N_c = 40$ and $N_c = 1000$. We denote as $\Delta^{(l)}$ the average over θ and a of $\Delta^{(l)}_{a|\theta}$. In Fig. 5.20 we show the evolution of $\Delta^{(l)}$ with l for both sets. Only the second set sees convergence for $l \geq 5$ which ensures the sampling to be adequate and allows

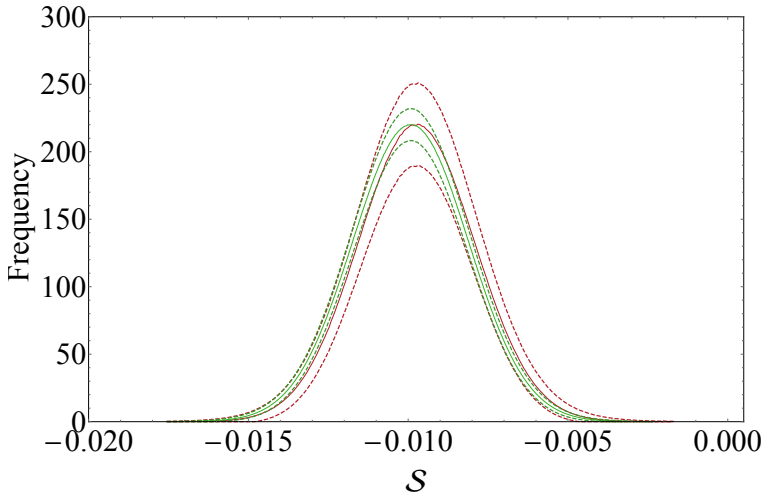

Figure 5.21: Histogram of the steering parameter values for $N = 5 \times 10^8$ points out of two data sets of size $M = 10^4$ computed with parameters $N_c = 40$ in red and $N_c = 1000$ in green. The area delimited by dashed lines encompass possible histograms at less than one standard deviation from the average. The green histogram is the final evaluation of the error bars associated to the steering inequality violation. We observe a distance to the local bound of more than 5 standard deviations.

us to compute $\tau_A = \frac{1}{2}((\frac{\Delta^{(\infty)}}{\Delta^{(0)}})^2 - 1) \approx 0.65$. This means the sample neighbours are typically uncorrelated on average for all θ and a. The histogram $\mathcal{H}(f_{a|\theta}, M)$ obtained from the data set $A^{(0)}_{a|\theta}$ is therefore a valid evaluation of $\mu(f_{a|\theta})$ up to a deviation that can be computed using $\tau_{a|\theta}$. Considering the histogram as the data set $\{p_n, \mathcal{I}_n\}$, with p_n the normalized number of values $f_{a|\theta}$ comprised in the interval $\mathcal{I}_n$, the error on each p_n is estimated by

$$\delta_{a|\theta}(n) = \sqrt{\frac{p_n - p_n^2}{M/(1 + 2\tau_{a|\theta}) - 1}}.$$

By summing random members of all $A^{(0)}_{a|\theta}$ data sets N times we then obtained $A_{\mathcal{S}}$, our final set of $\mathcal{S}$ values. To ensure an accurate sampling of our data, we chose $N = 5 * 10^8$ and were then able to compute the corresponding histogram $\mathcal{H}(\mathcal{S}, N)$. As $\mathcal{S}(\rho) = \sum f_{a|\theta}(\rho)$, the error on each point of $\mathcal{H}(\mathcal{S}, N)$ was evaluated to be

$$\delta(n) = \sqrt{\frac{1}{12^2} \sum_{a,\theta} \delta_{a|\theta}(n)^2}.$$

Using this information, $\mathcal{H}(\mathcal{S}, N)$ is shown in green in Fig. 5.21 along with the sets $\{p_n \pm \delta(n)/2, \mathcal{I}_n\}$ that bound the area containing $\mu(\mathcal{S})$ with a confidence of one standard deviation. As a comparison, the same evaluation was done using $N_c = 40$ and is shown in red. The results for both independent sets are compatible and show the relevance of moving to a higher sample rejection rate for a more precise evaluation of our error bars. A numerical fitting of $\mu(\mathcal{S})$ shows good agreement with a gaussian distribution so no deskewing procedure [44] was found necessary. As a result the standard deviation of our data set $A_{\mathcal{S}}$ is a direct evaluation of the errors associated to our MaxLik reconstruction. The final fitting of our data is a gaussian of mean $x_0 = -0.00992 \pm 0.00010$ and standard deviation $\sigma = 0.00181 \pm 0.00004$, which gives a separation to the local bound of $-5.48\sigma \pm 0.18\sigma$.

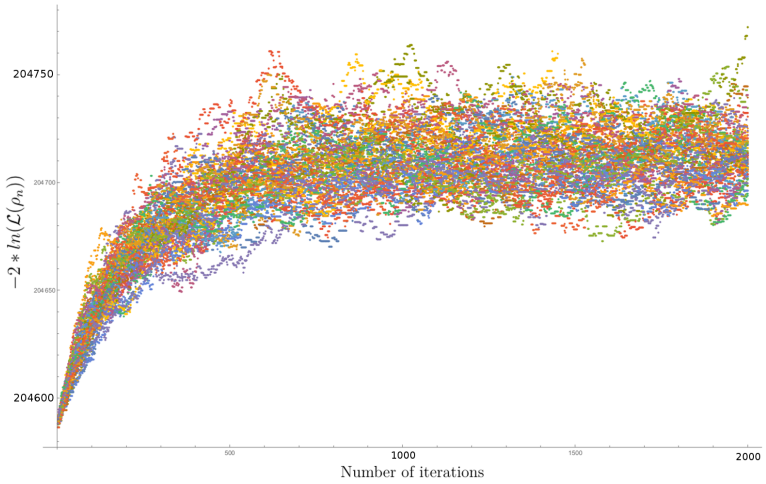

Figure 5.22: Exploration of the likelihood space of $\hat{\rho}^{exp}_{-|0}$ starting from $\hat{\rho}^{\mathrm{ML}}_{-|0}$ for 50 different beginnings of the Metropolis-Hastings algorithm. The thermalization is considered to be reached after 1250 iterations.

5C. Thermalization

In order to consider relevant density matrices in our final error estimation we need to wait for the computation to thermalize, that is to reach an area where the likelihood is not negligible. One might think that starting from ρ^{ML} would ensure that we are in the right zone of the likelihood space from the beginning. This is however not the case as we are performing a biased random walk in a likelihood space of high dimension. The function computing the number of ρ_n at a given likelihood distance from $\hat{\rho}^{\mathrm{ML}}$, $N(\mathcal{L})$, therefore increases sharply with $\mathcal{L}$, so much so that the algorithm will thermalize quite far from $\hat{\rho}^{\mathrm{ML}}$. This is visible in figure 5.22 where are shown 50 different iterations of the Metropolis-Hastings Algorithm starting from $\hat{\rho}^{\mathrm{ML}}$ with the same jump probability up to 2000 steps. The algorithm will drift away from $\hat{\rho}^{\mathrm{ML}}$ in any direction but will settle in a zone at log-likelihood distance of around $\Delta\lambda = -2\Delta ln(\mathcal{L}) \approx 100$. In terms of probability this means that the states in the area are much less likely to have been observed than $\hat{\rho}^{\mathrm{ML}}$ as the ratio of likelihood is $\mathcal{L}(\hat{\rho}_n)/\mathcal{L}(\hat{\rho}^{\mathrm{ML}}) \approx e^{-50}$. This gives an idea of the very sharp increase of $N(\mathcal{L})$: because we are staying in this region a balance is reached between the density of states and the probability to observe them. On a given experimental data set, this $\Delta\lambda$ is constant no matter the number of measurements performed (although $\lambda(\hat{\rho}^{\mathrm{ML}})$ changes) so we are inclined to think that it is direcly linked to $N(\mathcal{L})$.
From this plot we decided to set the thermalization waiting time as $N_\theta = 1250$.

After thermalization we will stay in a region of space at a distance $\Delta\lambda$ from $\hat{\rho}^{\mathrm{ML}}$. We can therefore worry that it will take a huge amount of time to explore the space as we are on a hypersphere of radius $\Delta\lambda$ whose size we ignore. This wouldn't be too much of a problem if the function we actually want to compute $\mathcal{S}$ were not too dependent on the direction in the likelihood space but it is possible that it changes dramatically depending on the direction we left ρ^{ML}. To check this we looked at the values of the steering parameter after n steps $0.5\,\mathrm{tr}(\hat{F}_{-|0}\hat{\rho}_i)$ for 50 iterations of the algorithm as is presented in figure 5.23. For the case of $\rho^{\mathrm{exp}}_{-|0}$ there doesn't seem to be any difference on the explorations of the values of $\mathcal{S}_{\mathrm{min}}$ no matter which direction we drift to. We observe this as well for the other subsets of the

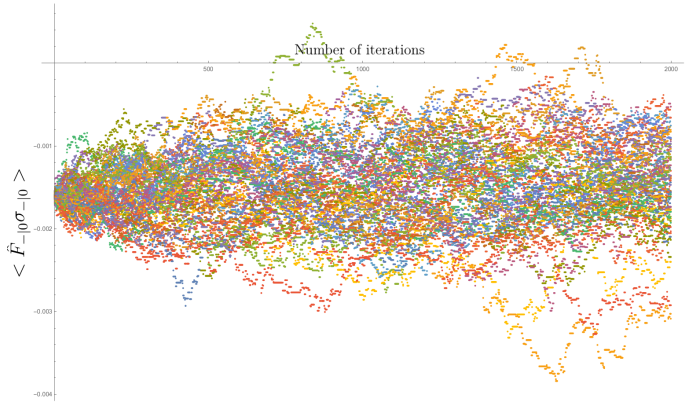

Figure 5.23: Values of $0.5\,\mathrm{tr}(\hat{F}_{-|0}\hat{\rho}_i)$ after n steps of the Metropolis-Hastings algorithm starting from $\hat{\rho}^{\mathrm{ML}}$ for 50 iterations of the algorithm.

assemblage, so this will not affect our final result.

5D. Skewing of the probability distribution

The MH algorithm introduces some deformation of the measured function μ as a result of a competition between the exponential decrease of the likelihood function which we want to fit and the ever increasing density of states away from $\hat{\rho}^{\mathrm{ML}}$. We have to check if the model developped in [44] describes well our results. This can help to precise our model but also is a good indicator of the validity of the whole MaxLik processs as it would be very unlikely to observe data in agreement with the model if $\hat{\rho}^{\mathrm{ML}}$ were close to the boundary of physical states for example.
First we considered the fitting of a single subset $0.5\,\mathrm{tr}(\hat{F}_{a|\theta}\hat{\rho}_i)$. In figure 5.24 we plotted the values corresponding to the state $\theta = \pi/6$ and $a = -$. In red we can see the full fitting according to the model developped in [44] which is in quite good agreement. Of course we pay here for the size of our data set limited to 10^4 for computational reasons so this fitting is not perfect, but we can also see the corresponding deskewed gaussian in green and it is quite close to our full model fit.

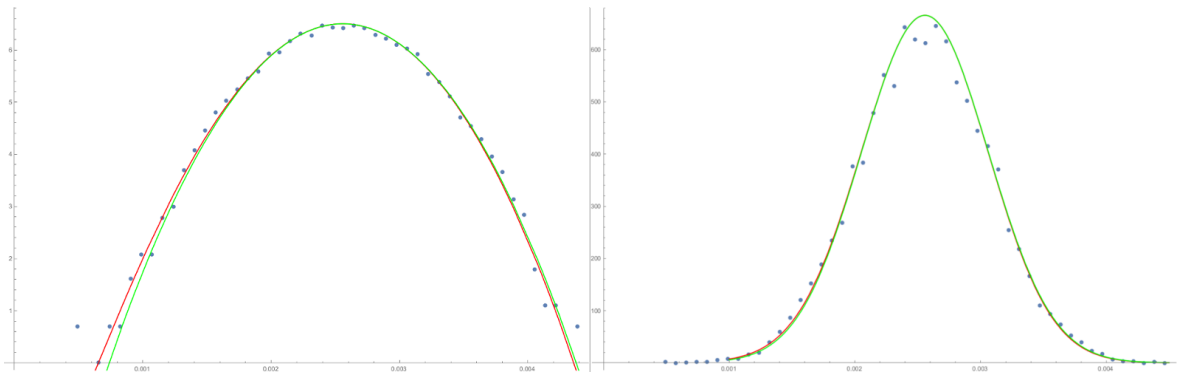

Figure 5.24: Fitting of the histogram obtained through the MH algorithm. Left: logarithmic plot, right regular scaling. In red is the complete fitting model and in green the corresponding deskewed gaussian.

The results are similar for all measurement choices and results so we logically find in figure 5.25 that the full fitting is a narrow improvement over a gaussian fit when considering the final steering parameter.

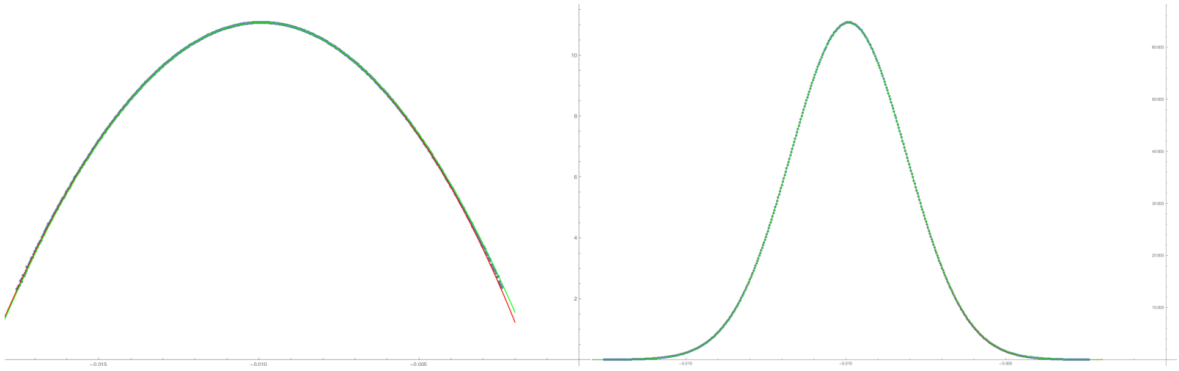

Figure 5.25: Fitting of the histogram obtained through the MH algorithm for the full steering parameter. Left: logarithmic plot, right regular scaling. In red is the complete fitting model and in green the corresponding deskewed gaussian.

In the end the combination of all the subsets of the assemblage does not need any adjustment in the fitting. It may be because the skewing averages out when combining all subsets or that we don't have enough points in our histogram for each subset to effectively fit the data.

In part II, we have introduced hybrid entanglement of light, presented different methods for non-locality tests and reported on a protocol for the remote preparation of arbitrary CV qubits. A central result is the demonstration of a steering inequality violation which proves our hybrid resource suitable for use in one-sided device independent protocols. Having characterized hybrid entanglement, we now consider its use for quantum teleportation between DV and CV encodings. In Chapter 6 we provide some insights into the protocol considered and detail the differences between possible implementations. Finally in Chapter 7 we present the current experimental setup to be used for the realization of quantum teleportation from DV to CV encoding and report on preliminary result giving us confidence in the future success of the experiment.

Part III

Hybrid quantum teleportation

Chapter 6

Hybrid quantum teleportation: Principle and model

We now come to the final protocol considered in this manuscript: quantum teleportation between CV and DV encodings. This experiment has been a goal of the group for several years now, and we started its implementation in the last year of my thesis. It represents a significant step-up in complexity from the previous protocols because it requires multiple heralding events: three separate detection events and one homodyne conditioning. In this chapter, we first present the principle and motivations behind quantum teleportation. We then introduce a new method for the realization of a Bell measurement that combines DV and CV resources and present its benefits and drawbacks. We conclude by a theoretical account of the expected results of a quantum teleportation protocol using our resources.

Contents

1 Quantum teleportation

Quantum teleportation (QT) is one of the most versatile and prevalent uses of entanglement and an example of a quantum protocol in which a purely non-classical feature, inseparability, is a necessary requirement. As opposed to remote state preparation, QT allows the transfer of an unknown quantum state between two nodes sharing entanglement, using only a classical communication channel. Given the infinite number of measurements necessary to characterize a quantum state, the fact that only two-bits of classical information are sufficient for recovering the initial state is the reason for the protocol's name which draws from popular science fiction. The quantum information was not physically transported between the two nodes using either a classical or a quantum causal channel, hence the name *teleportation*. Note that the same cannot be said for RSP protocols as once one of the parties knows the state to be transferred, a finite amount of classical information could allow the receiver to generate independently the desired output. In the case of a qubit for example, once the basis is known, only 2 parameters are sufficient to perfectly describe the state

Since proposed in 1993 by Bennet *et al.* [16], QT has become a staple of quantum information protocols and has been shown to be crucial to the development of many technologies. In quantum computing schemes, QT allows for straightforward and practical universal quantum computation [140] and one-way computing using cluster-states [141]. In the field of quantum communication, it enables the creation of quantum repeaters [142] necessary for long distance communication and the realization of scalable quantum networks [20].

1.1 Principle and definitions

1.1.1 Qubit teleportation

The most general principle of quantum teleportation is shown in figure 6.1 (a). Two parties Alice and Bob share an entangled state $|\Psi\rangle_{\mathrm{AB}}$. An unknown quantum state $|\psi_{\mathrm{in}}\rangle_{\mathrm{C}}$ is sent to Alice who performs a joint Bell measurement between her mode A and mode C. The result of the measurement is then sent to Bob who applies accordingly an operator $\hat{U}$ on his mode to recover the input state $|\psi_{\mathrm{in}}\rangle_{\mathrm{B}}$. Although this scheme can work in higher dimensions or using CV entanglement, we explain the principle in the case of DV qubits in two dimensions, without specifying the continuous or discrete nature of the encoding used for generality. The entangled state is written

$$|\Psi\rangle_{\mathrm{AB}} = \frac{1}{\sqrt{2}}(|0\rangle_{\mathrm{A}}|1\rangle_{\mathrm{B}} + |1\rangle_{\mathrm{A}}|0\rangle_{\mathrm{B}}), \tag{6.1}$$

where $\{|0\rangle, |1\rangle\}$ is the basis of the Hilbert space and can stand for DV-encoded (on a polarization or Fock basis for example) or equivalently CV-encoded qubits (for example on states $|\pm\alpha\rangle$ or $|\mathrm{cat}_{\pm}\rangle$). The input state is a qubit $|\psi_{\mathrm{in}}\rangle_{\mathrm{C}} = c_0|0\rangle_{\mathrm{C}} + e^{i\phi}c_1|1\rangle_{\mathrm{C}}$ so the global three-mode system is given by

$$|\Psi\rangle_{\mathrm{ABC}} = \frac{1}{\sqrt{2}}(c_0|0\rangle_{\mathrm{C}} + e^{i\phi}c_1|1\rangle_{\mathrm{C}}) \otimes (|0\rangle_{\mathrm{A}}|1\rangle_{\mathrm{B}} + |1\rangle_{\mathrm{A}}|0\rangle_{\mathrm{B}}). \tag{6.2}$$

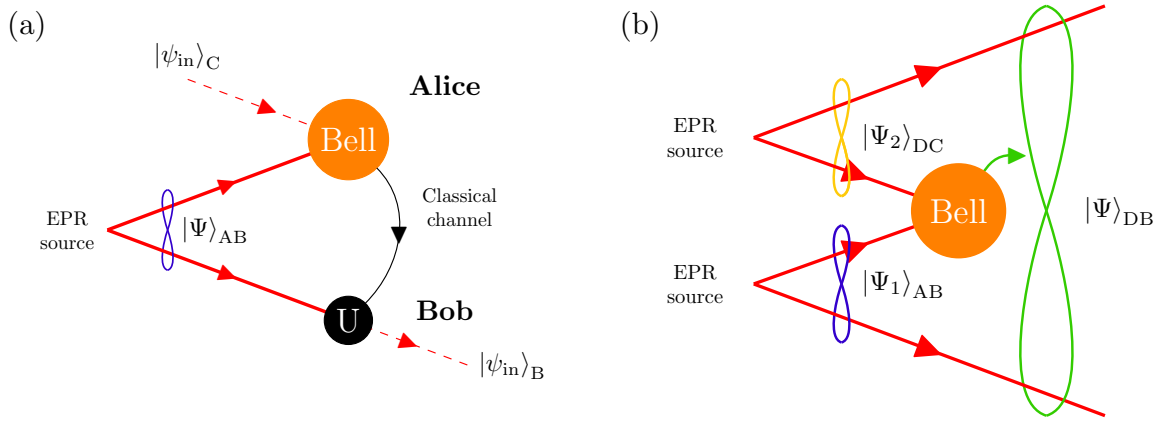

Active teleportation Entanglement swapping

Figure 6.1: **Principle of two quantum teleportation protocols**. (a): Active teleportation. Alice and Bob are two parties that have access to one mode (respectively A and B) of an entangled state $|\Psi\rangle_{\text{AB}}$ and can be arbitrarily distant from each-other. Using this resource they will teleport an unknown state $|\psi_{\text{in}}\rangle_{\text{C}}$ propagating on mode C and given to Alice. To do so, she performs a Bell measurement on the two modes A and C and then transmits the result to Bob through a classical channel. Depending on the information received, Bob performs an operation U on his mode and recovers the initial state $|\psi_{\text{in}}\rangle_{\text{B}}$. (b): Entanglement swapping. Here the input mode C is entangled with another mode D. The application of a Bell measurement on A and C leads to entanglement between modes D and B even though they have never directly interacted.

One can rewrite the system in terms of the Bell states on mode C and A $\left|\Psi^{(\pm)}\right\rangle_{\text{CA}}$ and $\left|\Phi^{(\pm)}\right\rangle_{\text{CA}}$ introduced in Chapter 1:

$$\begin{aligned}|\Psi\rangle_{\text{ABC}} =& \frac{1}{2}\Big(\left|\Psi^{(-)}\right\rangle_{\text{CA}} \otimes (c_0 |0\rangle_{\text{B}} - e^{i\phi} c_1 |1\rangle_{\text{B}}) \\ &+ \left|\Psi^{(+)}\right\rangle_{\text{CA}} \otimes (c_0 |0\rangle_{\text{B}} + e^{i\phi} c_1 |1\rangle_{\text{B}}) \\ &+ \left|\Phi^{(-)}\right\rangle_{\text{CA}} \otimes (-e^{i\phi} c_1 |0\rangle_{\text{B}} + c_0 |1\rangle_{\text{B}}) \\ &+ \left|\Phi^{(+)}\right\rangle_{\text{CA}} \otimes (e^{i\phi} c_1 |0\rangle_{\text{B}} + c_0 |1\rangle_{\text{B}})\Big). \end{aligned} \tag{6.3}$$

We notice that this is the sum, up to Pauli operators, of tensor products between the input state and each Bell state. We can indeed write, with the notation $|\psi_{\text{in}}\rangle_{\text{B}} = c_0 |0\rangle_{\text{B}} + c_1 e^{i\phi} |1\rangle_{\text{B}}$,

$$\begin{aligned}|\Psi\rangle_{\text{ABC}} =& \frac{1}{2}\Big(\left|\Psi^{(-)}\right\rangle_{\text{CA}} \otimes \hat{\sigma}_Z |\psi_{\text{in}}\rangle_{\text{B}} + \left|\Psi^{(+)}\right\rangle_{\text{CA}} \otimes |\psi_{\text{in}}\rangle_{\text{B}} \\ &+ e^{-i\pi/2} \left|\Phi^{(-)}\right\rangle_{\text{CA}} \otimes \hat{\sigma}_Y |\psi_{\text{in}}\rangle_{\text{B}} + \left|\Phi^{(+)}\right\rangle_{\text{CA}} \otimes \hat{\sigma}_X |\psi_{\text{in}}\rangle_{\text{B}} \Big). \end{aligned} \tag{6.4}$$

The strategy becomes clear from expression 6.4. Alice performs a Bell measurement leading to either of the POVMs $\left|\Psi^{(\pm)}\right\rangle\left\langle\Psi^{(\pm)}\right|_{\text{CA}}$ and $\left|\Phi^{(\pm)}\right\rangle\left\langle\Phi^{(\pm)}\right|_{\text{CA}}$ which projects Bob's mode into $\hat{U} |\psi_{\text{in}}\rangle_{\text{B}}$, with $\hat{U}$ a Pauli operator depending on the Bell measurement. Alice therefore tells him using the classical channel which Bell operator was measured and Bob applies the corresponding $\hat{U}$ to its mode to recover $|\psi_{\text{in}}\rangle_{\text{B}}$.

From this ideal protocol, we introduce some definitions to distinguish between different possible implementations:

- If Alice performs a complete Bell measurement, *i.e.* all possible Bell projections can be performed, the protocol is *deterministic* as opposed to *probabilistic* in the inverse case.
- If the Pauli operator is applied by Bob in real time, the protocol is called *active*, whereas if it is applied a posteriori or not at all it is *passive*.

1.1.2 Entanglement swapping

A particular case of quantum teleportation where the mode to be teleported is part of an entangled state is especially relevant for this thesis. This situation, first explicitly formalized in [143], is called *entanglement swapping* (ES) and presented in figure 6.1 (b). Starting from two entangled states $|\Psi_1\rangle_{\mathrm{AB}}$ and $|\Psi_2\rangle_{\mathrm{CD}}$, Alice applies a joint Bell measurement between the two modes A and C. This entangles the two remaining modes B and D even though they have never directly interacted. Using the same reasoning as before, and in the case where $|\Psi\rangle_{\mathrm{ABCD}} = \left|\Psi^{(-)}\right\rangle_{\mathrm{AB}} \otimes \left|\Psi^{(-)}\right\rangle_{\mathrm{CD}}$, we have

$$\begin{aligned}|\Psi\rangle_{\mathrm{ABCD}} = -\frac{1}{2}\Bigg(&\left|\Psi^{(-)}\right\rangle_{\mathrm{AC}} \otimes \left|\Psi^{(-)}\right\rangle_{\mathrm{BD}} - \left|\Psi^{(+)}\right\rangle_{\mathrm{AC}} \otimes \left|\Psi^{(+)}\right\rangle_{\mathrm{BD}} \\ &- \left|\Phi^{(-)}\right\rangle_{\mathrm{AC}} \otimes \left|\Phi^{(-)}\right\rangle_{\mathrm{BD}} + \left|\Phi^{(+)}\right\rangle_{\mathrm{AC}} \otimes \left|\Phi^{(+)}\right\rangle_{\mathrm{BD}} \Bigg).\end{aligned} \tag{6.5}$$

Similarly to before, the modes B and D are initially uncorrelated. After Bell measurements have been applied however, they become entangled. Classical information on which measurement has been applied needs to be transmitted to modes B and D however to make further operations –for example teleportation between the two remaining modes. Discrete-variable entanglement swapping enables entanglement between parties distant from each other further than would be possible by directly propagating an entangled state. For this reason it is key to the realization of several technologies for long distance quantum communications such as quantum repeaters [142] or quantum relays [144].

1.1.3 Thresholds for successful teleportation protocols

In any practical implementation of QT, the teleported state will differ from the one sent. As there exist different protocols able to approximate the input qubit, a successful teleportation protocol should lead to an ouptut state so close to the input qubit that QT is advantageous compared to other possible methods. Traditionally, the fidelity between the two states is used as figure-of-merit for the protocol. As the QT protocol works for an unknown quantum state, the fidelity to consider is the average for all possible input quantum states, *i.e.* for pure states:

$$\mathcal{F} = \int_{\psi_{\mathrm{in}}} |\langle\psi_{\mathrm{in}}|\psi_{\mathrm{out}}(\psi_{\mathrm{in}})\rangle|^2 d\psi_{\mathrm{in}}, \tag{6.6}$$

with $|\psi_{\mathrm{out}}(\psi_{\mathrm{in}})\rangle$ the output state created depending on the input state $|\psi_{\mathrm{in}}\rangle$. As all input states cannot be tested experimentally, one either measures the output fidelity for an ensemble of input states accurately representing all possible qubits (typically all mutually unbiased basis states of the Bloch sphere) or performs the integration over the ensemble the protocol

has been tested on.

The threshold for certification of QT depends on the experiment and the competing protocols considered. The usual threshold considered is the one of classical teleportation (CT). In such a protocol, Alice makes a measurement of the input state $|\psi_{\text{in}}\rangle$ and sends the retrieved information to Bob using the classical channel so that Bob creates an output state accordingly. For a qubit, the most information one can retrieve on average with a single measurement of the input state leads to an average fidelity of $\mathcal{F} = 2/3$ [145]. This is the fidelity threshold typically used in practice.

A more stringent threshold for a successful QT rules out other quantum protocols where the input qubit may not have destroyed. An example is the following protocol: Alice creates a copy of the input qubit as faithfully as possible and then performs QT on the copy using the entangled state she shares with Bob. Quantum cloning machines [146] allow the realization of copies of quantum states with a higher fidelity than is possible using CT (In the case of qubits, one can go as high as $\mathcal{F} = 5/6$). It is therefore possible for Bob to receive a quantum state presenting a fidelity with the input qubit above the classical threshold all while Alice has retained the original quantum state. This scenario is sometimes called a *quantum fax* [147] and depending on the experimentalist's goals, one may want to rule out this situation by going above the quantum cloning limit. This ensures Bob obtains the best copy of the input state.

One should also note that, as fidelity evaluation is a measurement that destroys part of the available information, other figures of merit can be used to rule out a classical protocol. In fact, similarly to the case of quantum steering, semi-definite programs can be used to certify the teleportation as being quantum [148]. This is the least stringent requirement and is in fact equivalent to demonstrating the existence of entanglement between Alice and Bob. Finally, in the case of entanglement swapping, the feature of interest is the generation of entanglement between the two output modes even though they have never directly interacted. It is therefore natural to consider entanglement negativity as a figure of merit as it proves the presence of entanglement between the two output modes.

1.2 Encoding choice

The teleportation process we presented is valid for various types of encoding. Depending on the encoding used however, the implementation of quantum teleportation will present specific differences with the ideal deterministic active protocol. We therefore present the advantages and drawbacks of choosing one of several encodings that are directly related to our experiment. First, among DV encodings, there are differences between dual-rail encoding (for example on a polarization basis $\{|H\rangle, |V\rangle\}$), and single-rail encoding (*e.g.* vacuum and single photon $\{|0\rangle, |1\rangle\}$). With CV encoding we also distinguish the coherent-state basis $\{|\alpha\rangle, |-\alpha\rangle\}$ and the squeezed basis $\{\hat{S}|0\rangle, \hat{a}\hat{S}|0\rangle\}$. The different properties we consider when comparing encodings are: completeness of the Bell measurement (deterministic or probabilistic), the possibility of implementing the Pauli operator (active or passive), the robustness of the protocol with regards to decoherence, the attainable fidelities and the corresponding classical fidelity bound.

Polarization encoding $\{|H\rangle, |V\rangle\}$. It is possible to perform the two Bell measurements $\left|\Psi^{(\pm)}\right\rangle$ using a 50:50 beam-splitter, two polarizing beam-splitters (PBS) and single-photon

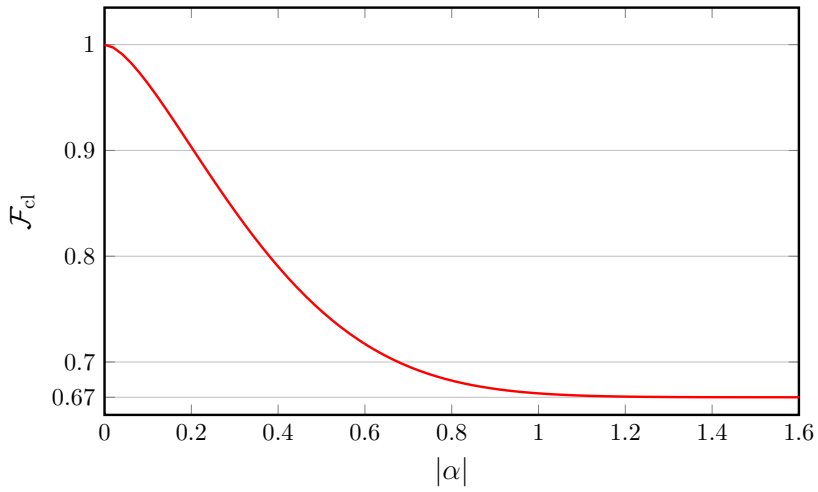

Figure 6.2: **Classical bound of fidelity when using a coherent-state basis** depending on the size of $|\alpha|$. For $|\alpha| > 1$, we recover the limit for an orthogonal basis. As $|\alpha|$ goes to zero, the states are closer to vacuum and harder to discriminate which can be exploited in a classical teleportation scenario.

detectors (not necessarily photon-number resolving) [149]. However, the two other Bell measurements are not accessible with linear optics [150]. This makes the QT protocol inherently probabilistic. The application of the Pauli operators on the other hand can be performed easily using dephasing ans PBSs. As we use an orthonormal encoding basis, the maximum fidelity achievable through classical teleportation is $\mathcal{F}_{\text{cl}} = 2/3$.

Vacuum and single-photon encoding $\{|0\rangle, |1\rangle\}$. This encoding suffers from the same issue as the previous one regarding completeness of the Bell measurement, only $\left|\Psi^{(\pm)}\right\rangle$ are theoretically accessible using a 50:50 BS and photon-number resolving detectors. In the absence of this last resource, they can be approximated –as we will see in section 2.2– using a single-photon detector and an homodyne-detection setup. This encoding presents another issue as it is difficult to implement $\hat{\sigma}_X$ and $\hat{\sigma}_Y$ because it requires a flip from vacuum to single photon which cannot be performed with linear systems. It does however present an advantage in terms of fidelity. The classical bound is still limited to $\mathcal{F}_{\text{cl}} = 2/3$ but teleportation to qubits in this basis is known to be more resilient to losses [83].

Coherent-state encoding $\{|\alpha\rangle, |-\alpha\rangle\}$. The main advantage of this CV encoding is that it enables the implementation of complete Bell measurements for all values of $|\alpha|$ [151]. We will show the reasoning here in the case where $|\alpha| \gg 1$ and considering the Bell state $\left|\Psi^{(+)}\right\rangle \propto |\alpha\rangle_{\text{A}} |-\alpha\rangle_{\text{C}} + |-\alpha\rangle_{\text{A}} |\alpha\rangle_{\text{C}}$. The measurement can be performed by first mixing the two modes on a 50:50 beam splitter. This leads to the unnormalized state:

$$\begin{aligned} \left|\Psi^{(+)}\right\rangle_{\text{AC}} &\xrightarrow{\text{BS}} |\alpha - \alpha\rangle_{\text{A}} |2\alpha\rangle_{\text{C}} + |-\alpha + \alpha\rangle_{\text{A}} |-2\alpha\rangle_{\text{C}} \\ &= |0\rangle_{\text{A}} \left|\text{cat}_{+}^{2\alpha}\right\rangle_{\text{C}}, \end{aligned} \tag{6.7}$$

Encoding	Bell measurement	State recovery	$\mathcal{F}_{\text{cl}}$	Losses
$\{\|H\rangle, \|V\rangle\}$	50%, *probabilistic*	100%, *active*	2/3	Sensitive
$\{\|0\rangle, \|1\rangle\}$	50%, *probabilistic*	$\hat{\sigma}_Z$, *incomplete*	2/3	Resilient
$\{\|\alpha\rangle, \|-\alpha\rangle\}$, $\|\alpha\| \lesssim 1$	100%, *deterministic*	$\hat{\sigma}_X, \hat{\sigma}_Y$, *incomplete*	$> 2/3$	Less sensitive
$\{\|\alpha\rangle, \|-\alpha\rangle\}$, $\|\alpha\| \gg 1$	100%, *deterministic*	100%, *active*	$\sim 2/3$	More sensitive
$\{\hat{S}\|0\rangle, \hat{a}\hat{S}\|0\rangle\}$	Low fidelity	$\hat{\sigma}_X, \hat{\sigma}_Y$, *incomplete*	2/3	Less sensitive
$\{\hat{a}\hat{S}\|0\rangle, \hat{a}^2\hat{S}\|0\rangle\}$	$\sim 100\%$, *deterministic*	$\hat{\sigma}_X, \hat{\sigma}_Y$, *incomplete*	2/3	Less sensitive

Table 6.1: Features of the best possible qubit quantum teleportation protocols depending on the encoding used. In column Bell measurement, we give the proportion of measurements that can be performed with linear systems. In State recovery, we detail which Pauli operators can be implemented in the same context. The threshold given is the one corresponding to classical teleportation protocols. Finally, in the last column we qualify the resilience to losses of the created qubits. Except for the limit case of coherent-state encoding at $|\alpha| \gg 1$, protocols limited to a single encoding can be either deterministic or active but not both.

with $\left|\text{cat}_{\pm}^{\beta}\right\rangle_{\text{C}} \propto |\beta\rangle_{\text{C}} \pm |-\beta\rangle_{\text{C}}$. Both the A and C mode are populated by even parity states. The same calculation for the other Bell states gives

$$\begin{aligned} \left|\Psi^{(-)}\right\rangle_{\text{AC}} &\xrightarrow{\text{BS}} |0\rangle_{\text{A}} \left|\text{cat}_{-}^{2\alpha}\right\rangle_{\text{C}} \\ \left|\Phi^{(\pm)}\right\rangle_{\text{AC}} &\xrightarrow{\text{BS}} \left|\text{cat}_{\mp}^{2\alpha}\right\rangle_{\text{A}} |0\rangle_{\text{C}} . \end{aligned} \tag{6.8}$$

With two parity resolving detectors on mode A and C, it is therefore possible to discriminate between all Bell operators. Contrary to the polarization encoding however, it is not easy to implement the $\hat{\sigma}_Z$ operator, although it can be approximated with a displacement but only at high values of $|\alpha|$ [151].
In terms of fidelity, the classical bound is strictly higher than 2/3 (see [152]) because the basis is not orthonormal $|\langle\alpha|-\alpha\rangle| \neq 0$, but as $\alpha \to \infty$ it converges to 2/3. The dependency of $\mathcal{F}_{\text{cl}}$ on $|\alpha|$ is shown in figure 6.2.

Squeezing encoding $\{\hat{S}|0\rangle, \hat{a}\hat{S}|0\rangle\}$ and $\{\hat{a}\hat{S}|0\rangle, \hat{a}^2\hat{S}|0\rangle\}$. As we have seen states of the form $\hat{a}^n\hat{S}|0\rangle$ present good fidelity with cat states at low values of $|\alpha|$. Their use as a basis for qubit encoding does not however present the same properties than the coherent-state basis in the general case. This is most evident in the case of encoding on $\{\hat{S}|0\rangle, \hat{a}\hat{S}|0\rangle\}$. As seen in Chapter 2 (figure 2.9), the two states are close to cat states of different sizes we note $|\alpha_+|$ and $|\alpha_-|$ (at 3 dB, $|\alpha_+| \sim 0.6$ and $|\alpha_-| \sim 1.0$). In that case, we consider Bell states of the form

$$\begin{aligned} \left|\Psi^{(\pm)}\right\rangle &\propto \hat{S}|0\rangle_{\text{A}} \hat{a}\hat{S}|0\rangle_{\text{C}} \pm \hat{a}\hat{S}|0\rangle_{\text{A}} \hat{S}|0\rangle_{\text{C}} \\ &\propto (|\alpha_+\rangle + |\alpha_+\rangle)(|\alpha_-\rangle - |\alpha_-\rangle) \pm (|\alpha_-\rangle - |\alpha_-\rangle)(|\alpha_+\rangle + |\alpha_+\rangle), \end{aligned} \tag{6.9}$$

and

$$\left|\Phi^{(\pm)}\right\rangle \propto (|\alpha_+\rangle + |\alpha_+\rangle)(|\alpha_+\rangle + |\alpha_+\rangle) \pm (|\alpha_-\rangle - |\alpha_-\rangle)(|\alpha_-\rangle - |\alpha_-\rangle), \tag{6.10}$$

Using the same reasoning as in equation (6.7), mixing the two-modes of $\left|\Phi^{(\pm)}\right\rangle$ on a 50:50 beam splitter leads to

$$\left|\Phi^{(\pm)}\right\rangle \xrightarrow{\text{BS}} (\left|\text{cat}_+^{2\alpha_+}\right\rangle_{\text{A}} \pm \left|\text{cat}_+^{2\alpha_-}\right\rangle_{\text{A}}) \left|0\right\rangle_{\text{C}} + \left|0\right\rangle_{\text{A}} (\left|\text{cat}_+^{2\alpha_+}\right\rangle_{\text{C}} \pm \left|\text{cat}_+^{2\alpha_-}\right\rangle_{\text{C}}). \tag{6.11}$$

In the case where $\alpha_+ = \alpha_-$ the application of an Hadamard gate on each mode will allow one to discriminate both operators using parity-sensitive detectors. However in the general case the two Bell states cannot be perfectly discriminated. The distance to the perfect implementation of the Bell measurement depends on $|\alpha_+ - \alpha_-|$. The same conclusion can be reached for $\left|\Psi^{(\pm)}\right\rangle$. The two encodings are therefore not equal, it is hard to perform a complete Bell measurement with $\{\hat{S}\left|0\right\rangle, \hat{a}\hat{S}\left|0\right\rangle\}$ but, because in this case $|\alpha_-| \sim 1.0$ and $|\alpha_+| \sim 1.1$, the encoding $\{\hat{a}\hat{S}\left|0\right\rangle, \hat{a}^2\hat{S}\left|0\right\rangle\}$ allows for deterministic teleportation with good fidelity. The difference with the coherent state encoding is also visible with regards to fidelity. The classical bound for fidelity is $\mathcal{F}_{\text{cl}} = 2/3$ in this case because the basis is orthonormal.

We summarize these features in table 6.1, with the addition of a characterization of the sensitivity of qubits to transmission losses or decoherence. Their influence is typically linked to the population number of the states considered, at greater values of $|\alpha|$ the state will be more sensitive to losses. The effect is not only due to the encoding chosen at the output, but in the case of hybrid teleportation between encodings, it also depends on the encoding used at the input mode. We therefore only give a rough idea of the effects which are fully detailed in [152, 83].

Overall, only the case of a coherent-state basis encoding at high values of $|\alpha|$ can be used both as input and output encoding and still lead to a deterministic active teleportation protocol, other encodings require a tradeoff in the implementation of QT. Note however that if we allow for additional complexities in the systems considered, there are some methods to improve on the results presented in table 6.1. Examples include encoding the qubit on multiple degrees of freedom [153], the use of additional ancillary qubits [154] or using a CV entangled resource [26] in order to perform a near complete Bell measurement with a DV encoding.

1.3 Previous implementations and state of the art

There have been many experiments demonstrating qubit quantum teleportation in different contexts. Tin this section, we detail some of the relevant experiments for our study.

1.3.1 Quantum teleportation protocols with fixed encoding

With DV encoding, the first demonstration was by Bouwmeester *et al.* in 1997 using polarization qubits [18]. In the following year, the first deterministic [153] and the first active protocols [155] were implemented. Teleportation using vacuum and single-photon states as basis was realized a bit later [156]. Teleportation using the coherent state encoding was proposed in 2001 [157] and has not been fully implemented yet. A close protocol –equivalent to QT at vanishing losses–, *tele-amplification*, was however realized more recently [158]. Since these proof-of-concept experiments, much progress has been made and teleportation protocols have now been realized over practical distances ranging up to 143 km on earth [159] and recently 1400 km from ground to satellite [19].

From the different features of CV and DV encodings presented in table 6.1, hybrid entanglement seems to be an appropriate resource for the implementation of a fully deterministic and active protocol by joining their benefits. Such a protocol, introduced and theoretically studied in [152], would perform the deterministic teleportation of coherent-state qubits onto a polarization encoding. Beyond these ideal properties, hybrid quantum teleportation would be very useful even in an imperfect implementation as a conversion process between two opposing encodings, a process impossible to implement otherwise. In that context the teleportation from a photonic qubit on a coherent-state basis presents the advantage of leading to higher fidelities more efficiently [160] and is directly accessible using our hybrid resource.

1.3.2 Current progress towards teleportation between encodings

Two recent experiments in particular explore QT between two different encodings. The first one considers teleportation from a CV qubit to a $\{|0\rangle, |1\rangle\}$ basis [161] and the second one from polarization to CV encoding [162]. Although they represent a good step in the direction of hybrid QT, their implementation introduced approximations that should be alleviated to go beyond their proof-of-concept status. As our goals are closely related to these experiments, we will now expand on the compromises they introduce in order to see what can be improved upon in our implementation.

- In the first experiment, the hybrid state is generated using a similar method to ours and as such uses the $\{\hat{S}|0\rangle, \hat{a}\hat{S}|0\rangle\}$ encoding, albeit with a squeezing of 1.56 dB. This encoding is closest to $\{|cat_+^{\alpha+}\rangle, |cat_-^{\alpha-}\rangle\}$ with $|\alpha_+| = 0.42$ and $|\alpha_-| = 0.72$. At these amplitude levels, the population of squeezed vacuum is close to zero and $\hat{a}\hat{S}|0\rangle$ has a higher although low single-photon component. The Bell measurement of [151] can in that case be adapted and implemented using only a single photon detector instead of parity-sensitive detectors. The Bell measurement therefore presents the disadvantage of being only valid in the limit of low amplitudes and the scheme cannot be extended to a practical context. Furthermore, the quality of the teleportation depends on the state to teleport. Another strong compromise is made for the qubit prepared as an input odd cat state is simulated by a low amplitude coherent state.

- In the second experiment, one Bell measurements out of four is performed on the DV encoding and the protocol is extendable to a coherent-state basis of greater population. An issue however is that the inherent low count rate of their generation limits their acquisition to 1500 events overall. Given that the state characterization is done by correcting for more than 50% of detection losses, the derivation of the fidelity is very prone to errors, all the more so that it is inferred from a set of measured values on an incomplete ensemble of input states using an approximate model. We also note that in this experiment even though entanglement swapping is mentioned as an interpretation, it is performed only once the final entangled DV mode is measured. This therefore does not constitute a proper ES experiment as the final entanglement is destroyed as soon as it is heralded.

Overall, the main issues in these experiments that should be solved for a practical QT protocol are the lack of scalability to a coherent state basis of higher population for the first one and the acquisition of a small number of data points for the second one. In the former experiment, entanglement swapping was also not demonstrated in an operational manner. Finally, and

seeing the large amount of loss correction applied, a study of uncertainties associated to the tomographic reconstruction would be of interest.

1.4 Our goal for hybrid quantum teleportation

Our goal is to perform both qubit quantum teleportation and entanglement swapping using our hybrid state. We therefore have two possibilities for hybrid teleportation using our system. Teleportation from $\{|0\rangle, |1\rangle\}$ to $\{\hat{S}|0\rangle, \hat{a}\hat{S}|0\rangle\}$ or in the reverse direction. As we aim for scalability, the implementation of a Bell measurement on the CV mode is out of reach without parity-sensitive photon detectors. We decided in consequence to perform the Bell measurement on the DV mode to teleport towards a CV encoding. This protocol has not been performed yet by other groups and allows us to increase the amount of squeezing used so as to have a greater count rate. In that setting, the protocol presents the disadvantage that it cannot be performed deterministically or actively. As said earlier it is still of interest on its own as a converter between encodings and could find uses in practical quantum protocols. The fidelity bound that needs to be reached will be in this case $\mathcal{F}_{\text{cl}} = 2/3$ as shown in table 6.1.
As mentioned earlier, entanglement swapping was never realized with a hybrid entangled state. Performing, as for qubit QT, the Bell measurement on the DV modes of two different entangled states leaves us with several possibilities to explore:

- Swapping between two hybrid entangled states to entangle two CV modes, a process which we describe with the notation

$$\text{CV}\infty\text{DV} \otimes \text{DV}\infty\text{CV} \longrightarrow \text{CV}\infty\text{CV}. \tag{6.12}$$

- Swapping between an hybrid entangled state and DV entanglement to remotely prepare hybrid entanglement:

$$\text{CV}\infty\text{DV} \otimes \text{DV}\infty\text{DV} \longrightarrow \text{CV}\infty\text{DV}. \tag{6.13}$$

Both of these cases can be realized with our experimental setup. However, for practical reasons we will present in Chapter 7, the latter case is easier to perform and will be our first experiment of entanglement swapping. As for qubit QT, the protocol cannot be deterministic and as a first try will not be active either. In both situations, the quality of implementation will be assessed from measurements of negativity of entanglement for both the input states and the generated entangled state.

Having established the goals and the corresponding figures-of-merit for our experiment, we now present the protocol used, starting with the implementation of a partial Bell measurement on the photonic encoding.

2 Bell measurement

In this section, we present the method used to perform the Bell measurement and study the influence of some experimental parameters on the quality of its implementation. Finally we give an estimation of the expected values of the figures-of-merit appropriate to qubit QT and entanglement swapping in a practical experiment.

2.1 Mixing CV and single-rail DV modes

We implement a Bell measurement on the DV mode which needs to discriminate with certainty some Bell states from the others. To see the process, we adapt the expression of the system for qubit QT shown in equation (6.2) to the hybrid context with encodings $\{|0\rangle, |1\rangle\}$ for modes A and C and $\{|\text{cat}_+\rangle, |\text{cat}_-\rangle\}$ for mode B:

$$|\Psi\rangle_{\text{ABC}} = \frac{1}{\sqrt{2}}(c_0 |0\rangle_{\text{C}} + e^{i\phi} c_1 |1\rangle_{\text{C}}) \otimes (|0\rangle_{\text{A}} |\text{cat}_-\rangle_{\text{B}} + |1\rangle_{\text{A}} |\text{cat}_+\rangle_{\text{B}}). \tag{6.14}$$

This can be rewritten, as in equation (6.3), as

$$\begin{aligned} |\Psi\rangle_{\text{ABC}} = \frac{1}{2}\Big(& \left|\Psi^{(-)}\right\rangle_{\text{CA}} \otimes (c_0 |\text{cat}_+\rangle_{\text{B}} - e^{i\phi} c_1 |\text{cat}_-\rangle_{\text{B}}) \\ & + \left|\Psi^{(+)}\right\rangle_{\text{CA}} \otimes (c_0 |\text{cat}_+\rangle_{\text{B}} + e^{i\phi} c_1 |\text{cat}_-\rangle_{\text{B}}) \\ & + \left|\Phi^{(-)}\right\rangle_{\text{CA}} \otimes (-e^{i\phi} c_1 |\text{cat}_+\rangle_{\text{B}} + c_0 |\text{cat}_-\rangle_{\text{B}}) \\ & + \left|\Phi^{(+)}\right\rangle_{\text{CA}} \otimes (e^{i\phi} c_1 |\text{cat}_+\rangle_{\text{B}} + c_0 |\text{cat}_-\rangle_{\text{B}})\Big). \end{aligned} \tag{6.15}$$

To differentiate Bell states, we first mix modes A and C on a balanced beam-splitter. This leads to the transformation

$$\begin{aligned} \hat{a}^\dagger &\xrightarrow{50:50} \frac{1}{\sqrt{2}}(\hat{a}^\dagger + \hat{c}^\dagger) \\ \hat{c}^\dagger &\xrightarrow{50:50} \frac{1}{\sqrt{2}}(\hat{c}^\dagger - \hat{a}^\dagger). \end{aligned} \tag{6.16}$$

Where $\hat{a}^\dagger$ and $\hat{c}^\dagger$ are the creation operators for modes A and C respectively. Applied to the Bell states, this gives us

$$\begin{aligned} \left|\Psi^{(-)}\right\rangle_{\text{CA}} &\xrightarrow{50:50} |0\rangle_{\text{C}} |1\rangle_{\text{A}} \\ \left|\Psi^{(+)}\right\rangle_{\text{CA}} &\xrightarrow{50:50} |1\rangle_{\text{C}} |0\rangle_{\text{A}} \\ \left|\Phi^{(-)}\right\rangle_{\text{CA}} &\xrightarrow{50:50} \frac{1}{\sqrt{2}}\Big(|0\rangle_{\text{C}} |0\rangle_{\text{A}} + \frac{1}{\sqrt{2}}(|0\rangle_{\text{C}} |2\rangle_{\text{A}} - |2\rangle_{\text{C}} |0\rangle_{\text{A}})\Big) \\ \left|\Phi^{(+)}\right\rangle_{\text{CA}} &\xrightarrow{50:50} \frac{1}{\sqrt{2}}\Big(|0\rangle_{\text{C}} |0\rangle_{\text{A}} + \frac{1}{\sqrt{2}}(|2\rangle_{\text{C}} |0\rangle_{\text{A}} - |0\rangle_{\text{C}} |2\rangle_{\text{A}})\Big). \end{aligned} \tag{6.17}$$

If one can perform the operators $|1\rangle\langle 1|_{\text{C}}$ or $|1\rangle\langle 1|_{\text{A}}$, it is possible to discriminate $\left|\Psi^{(-)}\right\rangle_{\text{CA}}$ and $\left|\Psi^{(+)}\right\rangle_{\text{CA}}$ from all other Bell states. Note also that, as expected, there is no way to discriminate $\left|\Phi^{(-)}\right\rangle_{\text{CA}}$ and $\left|\Phi^{(+)}\right\rangle_{\text{CA}}$ from all other Bell states, even with the use of photon-number resolving detectors on both modes.

The use of parity-sensitive photo-detectors on modes A and C would complete the Bell measurement as the detection of an odd population in either mode heralds the corresponding Bell operation. As these are not available in our system, we use a different method that can approximate the operation by using both a single-photon detector and an homodyne-detection system. Additionally, we choose to perform only one of the two available Bell

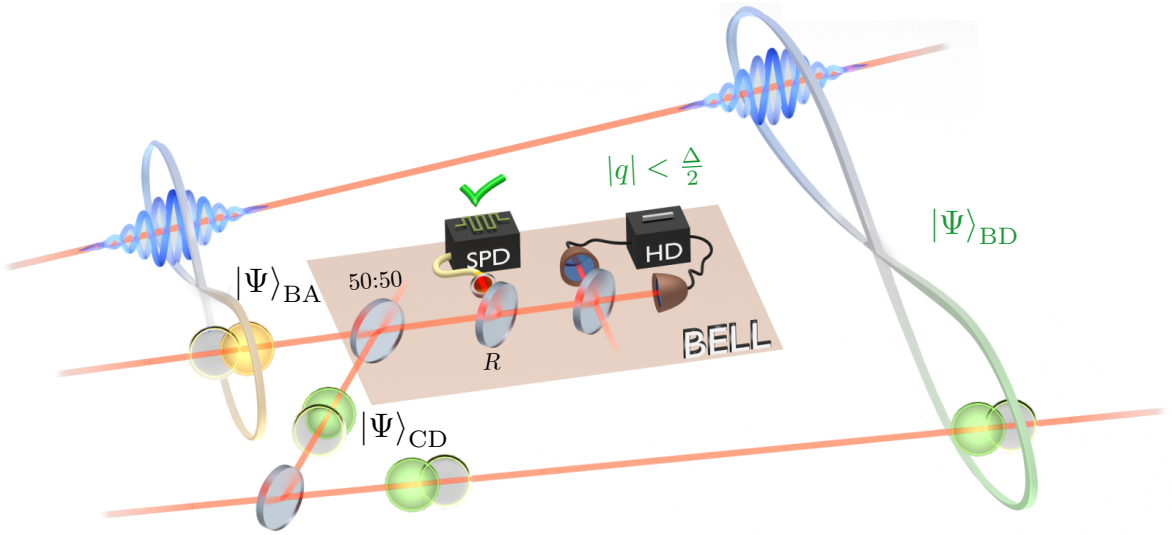

Figure 6.3: **Bell measurement in the context of entanglement swapping**. The two modes A and C are first mixed on a 50:50 beamsplitter. Then a beamsplitter of low reflectivity $R \ll 1$ taps part of one of the output ports of the balanced beamsplitter and sends it to a SNSPD. The detection of a single photon heralds the presence of either vacuum or single photon in the untapped mode. An homodyne detection serves to discriminate both cases by performing quadrature measurements. The Bell measurement is completed by conditioning on the measurement of quadratures close to zero, *i.e.* following $|q| < \Delta/2$ with Δ small compared to the variance of vacuum.

measurements by monitoring the output of mode C to perform $\left|\Psi^{(+)}\right\rangle_{CA}$. This decreases the success probability of the protocol from 50% to 25% but we will show it necessary for our practical implementation. Monitoring mode C rather than A presents the benefit of removing the requirement of applying an operator on the CV mode to retrieve the original qubit.

2.2 Experimental implementation of the Bell measurement

The process is shown in figure 6.3 in the particular case of entanglement swapping. The Bell measurement is successful if we rule out the presence of $|0\rangle_C$ or $|2\rangle_C$. Vacuum is first ruled out by inserting a beam splitter and conditioning on the detection of at least a photon on the reflected mode using a SNSPD. The insurance that the click was not due to a double detection is given by the low reflectivity of the beam-splitter. As was done at the output of OPO I, this operation approximates the application of operator $\hat{a}$ on mode C. From this step, Bell state $\left|\Psi^{(-)}\right\rangle_{CA}$ is ruled out, and the system can be described by

$$\begin{aligned}|\Psi\rangle_{ABC} \propto & |0\rangle_C |0\rangle_A \otimes (c_0 |\text{cat}_+\rangle_B + e^{i\phi} c_1 |\text{cat}_-\rangle_B) \\ & -\frac{1}{2} |1\rangle_C |0\rangle_A \otimes (-e^{i\phi} c_1 |\text{cat}_+\rangle_B + c_0 |\text{cat}_-\rangle_B) \\ & +\frac{1}{2} |1\rangle_C |0\rangle_A \otimes (e^{i\phi} c_1 |\text{cat}_+\rangle_B + c_0 |\text{cat}_-\rangle_B). \end{aligned} \tag{6.18}$$

As was done for remote state preparation, the homodyne detection is then used to condition on $|0\rangle_C$. The detection of a quadrature measurement result q close to zero being more likely for vacuum than for a single photon, waiting for such an event biases the state teleported in

mode B towards the target $c_0 \left|\text{cat}_+\right\rangle_\text{B} + e^{i\phi} c_1 \left|\text{cat}_-\right\rangle_\text{B}$. In the case of entanglement swapping, the same reasoning can be applied starting from equation (6.5) and we recover the entangled state $\left|\Psi^{(+)}\right\rangle_\text{BD}$. In the perfect case of vanishing reflectivity R and selection window width Δ, the Bell measurement is exactly performed. As for remote state preparation, we need to make compromises in order to have a significant count rate. In the next subsections, we consider the impact R and Δ have on the Bell measurement fidelity, the fidelity of the teleported state with the target and the negativity of entanglement in the case of entanglement swapping.

2.2.1 Bell measurement fidelity

The fidelity between the measurement shown in figure 6.3 and the ideal Bell measurement depends on several parameters: first on the reflectivity of the tapping beam splitter R and the width of the selection window on the homodyne signal Δ but also on the losses on mode C and, importantly, on the input state. To show this, we now detail the calculations in the imperfect case. We start by combining equations (6.4) and (6.17) and keep only the relevant terms where mode C is populated by either $|1\rangle$ or $|2\rangle$ to obtain

$$|\Psi\rangle_\text{ABC} = \frac{1}{2}\Big(|1\rangle_\text{C} |0\rangle_\text{A} \otimes |\psi_\text{in}\rangle_\text{B} + \frac{1}{2} |2\rangle_\text{C} |0\rangle_\text{A} \otimes (i\hat{\sigma}_Y |\psi_\text{in}\rangle_\text{B} + \hat{\sigma}_X |\psi_\text{in}\rangle_\text{B})\Big). \tag{6.19}$$

With $|\psi_\text{in}\rangle_\text{B} = c_0 \left|\text{cat}_+\right\rangle_\text{B} + e^{i\phi} c_1 \left|\text{cat}_-\right\rangle_\text{B}$ and $\hat{\sigma}_X$, $\hat{\sigma}_Y$ the Pauli operators in the basis $\{\left|\text{cat}_+\right\rangle_\text{B}, \left|\text{cat}_-\right\rangle_\text{B}\}$, we have

$$i\hat{\sigma}_Y |\psi_\text{in}\rangle_\text{B} + \hat{\sigma}_X |\psi_\text{in}\rangle_\text{B} = 2e^{i\phi} c_1 \left|\text{cat}_+\right\rangle_\text{B}, \tag{6.20}$$

and therefore

$$|\Psi\rangle_\text{ABC} = \frac{1}{2}(|1\rangle_\text{C} |0\rangle_\text{A} \otimes |\psi_\text{in}\rangle_\text{B} + e^{i\phi} c_1 |2\rangle_\text{C} |0\rangle_\text{A} \otimes \left|\text{cat}_+\right\rangle_\text{B}). \tag{6.21}$$

Now we introduce the beamsplitter coupling mode C with a new mode D. We label its transmission and reflection factors t and r such that $|r|^2 = R$ and $|t|^2 = 1 - R$. We apply the beamsplitter transformation $c^\dagger \to tc^\dagger + rd^\dagger$ to obtain

$$\begin{aligned} |\Psi\rangle_\text{ABCD} = \frac{1}{2}\Big(&(t |1\rangle_\text{C} |0\rangle_\text{D} + r |0\rangle_\text{C} |1\rangle_\text{D}) \otimes |0\rangle_\text{A} |\psi_\text{in}\rangle_\text{B} \\ &+ e^{i\phi} c_1 (t^2 |2\rangle_\text{C} |0\rangle_\text{D} + r^2 |0\rangle_\text{C} |2\rangle_\text{D} + \sqrt{2} tr |1\rangle_\text{C} |1\rangle_\text{D}) \otimes |0\rangle_\text{A} \left|\text{cat}_+\right\rangle_\text{B} \Big). \end{aligned} \tag{6.22}$$

Then, we apply a detection event on the SNSPD on mode D and trace out on mode A. This leads to the density matrix ρ_BC equal to

$$\rho_\text{BC} = \frac{\text{Tr}_{\text{A,D}}(\sum\limits_{n\geq 1} |n\rangle \langle n|_\text{D} |\Psi\rangle \langle\Psi|_\text{ABCD})}{\text{Tr}(\sum\limits_{n\geq 1} |n\rangle \langle n|_\text{D} |\Psi\rangle \langle\Psi|_\text{ABCD})}. \tag{6.23}$$

We obtain

$$\begin{aligned} \rho_\text{BC} \propto &|0\rangle \langle 0|_\text{C} |\psi_\text{in}\rangle \langle\psi_\text{in}|_\text{B} + c_1^2 \Big(2t^2 |1\rangle \langle 1|_\text{C} + r^2 |0\rangle \langle 0|_\text{C}\Big) \left|\text{cat}_+\right\rangle \left\langle\text{cat}_+\right|_\text{B} \\ &+ c_1 t\sqrt{2} \Big(e^{-i\phi} |0\rangle \langle 1|_\text{C} |\psi_\text{in}\rangle \left\langle\text{cat}_+\right|_\text{B} + e^{i\phi} |1\rangle \langle 0|_\text{C} \left|\text{cat}_+\right\rangle \langle\psi_\text{in}|_\text{B}\Big). \end{aligned} \tag{6.24}$$

We see here the effect of the detection. At small r, all the non-negligible terms left are incompatible with the presence of vacuum in mode C *except* the first term which corresponds

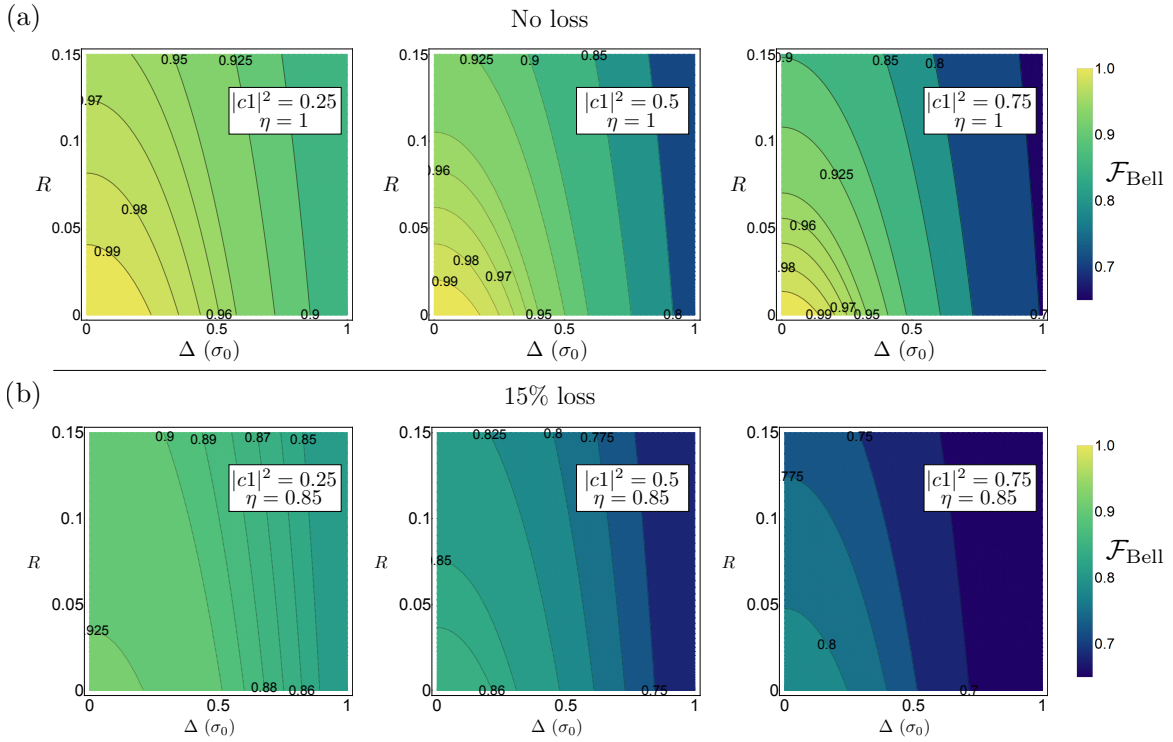

Figure 6.4: **Probability of performing the right Bell measurement** depending on the width of the selection window Δ used for the homodyne conditioning and on the beam splitter reflectivity R. As the probability depends on transmission losses and on the coefficients of input qubit $c_0 |0\rangle + c_1 |1\rangle$, we plot the measurement fidelity depending on the experimental parameters for three values of c_1 without losses in (a) and for the experimentally relevant 15% of losses introduced by the homodyne detection system in (b). Δ is normalized to the variance of vacuum.

to a successful teleportation. If R is too big however, there is no way to discriminate between the first and third terms of equation (6.24) through measurements on mode C.

The final step is homodyne conditioning that can be computed as was done for RSP and quantum steering. The operator corresponding to the selection of quadratures $|q| \leq \Delta/2$ is

$$\hat{M} = \int_{-\frac{\Delta}{2}}^{\frac{\Delta}{2}} |q\rangle \langle q| \, dq. \tag{6.25}$$

Applied to the state given in equation (6.24), we finally obtain the expression of the teleported state after the measurement:

$$\rho \propto A_{00}^{\Delta} |\psi_{\text{in}}\rangle \langle \psi_{\text{in}}|_{\text{B}} + c_1^2 \Big(2 * (1-R) A_{11}^{\Delta} + R A_{00}^{\Delta} \Big) |\text{cat}_+\rangle \langle \text{cat}_+|_{\text{B}} \,, \tag{6.26}$$

where we used the notation

$$A_{ij}^{\Delta} = \int_{-\frac{\Delta}{2}}^{\frac{\Delta}{2}} \langle i|q\rangle \langle q|j\rangle \, dq \tag{6.27}$$

and noticed that $A_{10}^{\Delta} = A_{01}^{\Delta} = 0$ for all Δ. It is also possible to include the losses before the homodyne detection to get the most general result. As usual, we model the losses by a

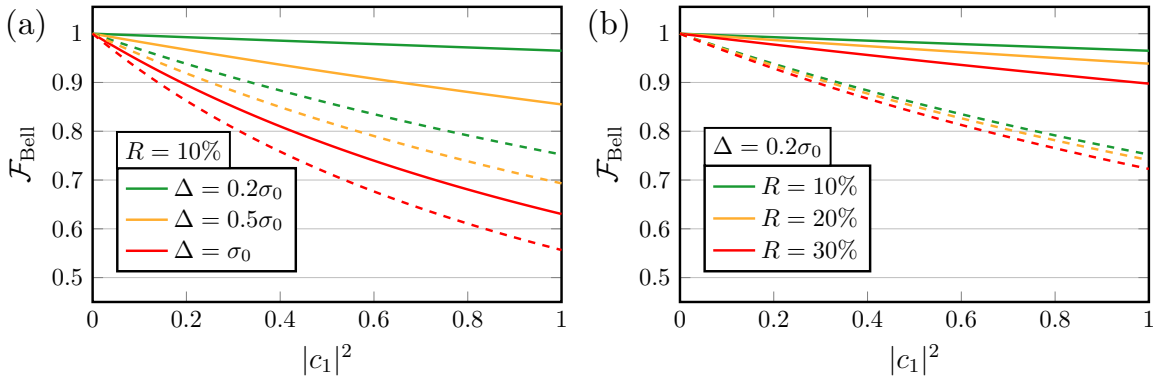

Figure 6.5: **Fidelity of the Bell measurement** depending on $|c_1|^2$. Full lines: no losses, dashed lines: 15% transmission loss. In figure (a), the evolution is plotted for a fixed value of reflectivity $R = 10\%$ and different values of Δ and in figure (b) Δ is fixed to 20% of the variance of vacuum σ_0 and we show the influence of changes in R.

beam-splitter of transmission η coupling mode C with another mode that is then traced out. This gives us the final expression:

$$\rho \propto A_{00}^{\Delta} \left|\psi_{\text{in}}\right\rangle \left\langle\psi_{\text{in}}\right|_{\text{B}} + c_1^2 \Big(2(1-R)(\eta A_{11}^{\Delta} + (1-\eta) A_{00}^{\Delta}) + R A_{00}^{\Delta} \Big) \left|\text{cat}_+\right\rangle \left\langle\text{cat}_+\right|_{\text{B}} . \tag{6.28}$$

The quality of the Bell measurement depends therefore on the ratio $A_{00}^{\Delta}/A_{11}^{\Delta}$, R and η as expected. We also notice the main difference between the measurement and the ideal Bell operator: its quality depends on the state to teleport as is visible through the presence of c_1^2. Unsurprisingly, the requirements for a good teleportation of vacuum are not severe.

The effect of experimental parameters on the quality of the Bell measurement can be visualized first in the loss-less case in figure 6.4(a). We plot the fidelity $\mathcal{F}_{\text{Bell}}$ between the measurement performed and the ideal Bell measurements depending on R and Δ for different values of coefficients c_1. We see that the fidelity drops when c_1 increases, as expected. Without loss and for $R < 15\%$, the fidelity depends more strongly on Δ than R but is quite high for all values of c_1, and is greater than 90% for $R = 10\%$ and a conditioning window as narrow as the one used for RSP, *i.e.* 20% times the variance of vacuum. Next, in figure 6.4(b), we show the same plots when accounting for the experimental 15% additional losses introduced on the homodyne detection path. We see that this effect is the strongest and significantly lowers the measurement fidelity. It remains however greater than 75% for all c_1 using as before $R = 10\%$ and $\Delta = 0.2\sigma_0$. The fact that the Bell measurement quality depends on the qubit being sent is also shown in figure 6.5 where the Bell measurement is shown depending on c_1 for different values of Δ and R. These plots confirm the stronger dependence on Δ than on R for $\mathcal{F}_{\text{Bell}}$ and the strong impact of losses on the homodyne detection. For $\Delta = 0.2\sigma_0$, the fidelity remains higher than 90% for all qubits for R as big as 30% without losses. In the case of 15% loss the fidelity drops below 50% for $|c_1|^2 = 0.4$ for $\Delta = 0.2\sigma_0$ and $R = 10\%$.

In summary, we conclude from these simulations that the fidelity of the Bell measurement presents the disadvantage of being qubit dependent. This issue is however alleviated at the limit of lower Δ and R, the former being the parameter having the most impact. Losses also have a significant impact on $\mathcal{F}_{\text{Bell}}$ and an appropriate implementation will lower the value of Δ depending on the losses considered. Note that the effect is not as problematic in terms

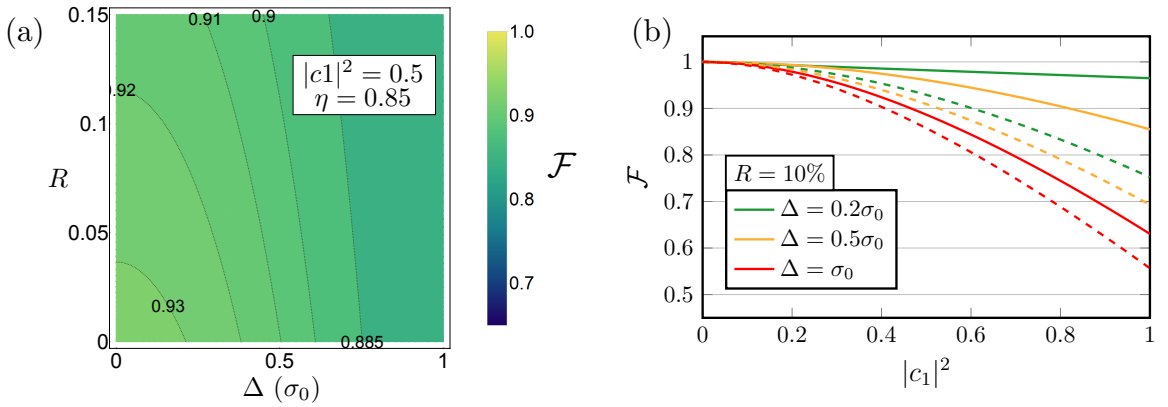

Figure 6.6: **Fidelity of the teleported state with the target CV qubit depending on experimental conditions**. (a): State fidelity depending on Δ and R for $|c_1|^2 = 0.5$ and 15% transmission loss. (b): State fidelity depending on $|c_1|^2$ for a fixed value of reflectivity $R = 10\%$ and different values of Δ. Full lines: no losses, dashed lines: 15% transmission loss.

of count rate as could be expected at first glance. Indeed, the presence of losses leads to an increase of the number of quadrature measurements close to zero as the vacuum component increases. Lowering the size of Δ is a strategy that amounts in effect to discriminating between vacuum and lossy single-photons (rather than between $|0\rangle$ and $|1\rangle$) which leads to a similar count rate with or without losses when the effect is exactly compensated. These results show the interest of using dual-rail encoding for the DV mode instead of single-rail. In the case of polarization encoding for example, the Bell measurement fidelity is independent from c_1 and can be very close to one. That being said, choosing the lowest possible Δ and R in our implementation can bring us close to this ideal situation.

What is missing from these simulations is how the Bell measurement fidelity value translates in terms of the final parameters of interest: state fidelity and negativity of entanglement. This is the subject of the next two subsections.

2.2.2 State fidelity

In the case of qubit teleportation the final parameter of interest is the fidelity of the teleported state with the target CV qubit:

$$\mathcal{F} = \langle\psi_{\text{in}}|\,\rho\,|\psi_{\text{in}}\rangle_{\text{B}}\,. \tag{6.29}$$

This fidelity is different from $\mathcal{F}_{\text{Bell}}$ because the state teleported when the wrong Bell measurement is performed is not orthogonal to the target state:

$$|\langle\psi_{\text{in}}|cat_+\rangle_{\text{B}}|^2 = 1 - c_1^2. \tag{6.30}$$

From equation (6.28) we can compute the state fidelity:

$$\mathcal{F} = \frac{A_{00}^{\Delta} + c_1^2(1-c_1^2)(2(1-R)(\eta A_{11}^{\Delta} + (1-\eta)A_{00}^{\Delta}) + RA_{00}^{\Delta})}{A_{00}^{\Delta} + c_1^2(2(1-R)(\eta A_{11}^{\Delta} + (1-\eta)A_{00}^{\Delta}) + RA_{00}^{\Delta})}. \tag{6.31}$$

This expression is close to the Bell state fidelity but gives higher values for qubits of lower c_1. The precise effect of each parameter can be seen in figure 6.6 where we plot in (a) $\mathcal{F}$

depending on Δ and R for $|c_1|^2 = 0.5$ and in (b) depending of $|c_1|^2$ for different values of Δ at $R = 10\%$. The range of values spanned by $\mathcal{F}$ is the same as for $\mathcal{F}_{\text{Bell}}$ but the state fidelity remains higher for lower values of c_1. In the particular case of $\Delta = 0.2\sigma_0$ and $R = 10\%$, $\mathcal{F}$ is above 90% for $|c_1|^2 \leq 0.6$ which is to compare with the limit of $|c_1|^2 \leq 0.4$ for $\mathcal{F}_{\text{Bell}}$.

Following the same reasoning as in [161, 162], this model for losses is useful to infer the fidelity of the teleportation protocol averaged over all c_1 even when tested for a sub-ensemble of input qubits. To do so, one has to measure the experimental fidelity for an as-large-as-possible set of different input qubits and then compute the average for the model best-fitting the experimental data.

2.2.3 Negativity of entanglement for entanglement swapping

In the case of entanglement swapping, the final expression of the teleported entanglement can be computed using the same procedure as for qubit teleportation. We show the calculation in the case of equation (6.13) where the input entangled state is DV∞DV and not necessarily balanced, meaning we use as initial four-dimensional state:

$$|\Psi\rangle_{\text{ABCD}} = \left|\Psi^{(+)}\right\rangle_{\text{AB}} \otimes (c_0 \,|0\rangle_{\text{C}} \,|1\rangle_{\text{D}} + c_1 e^{i\phi} \,|1\rangle_{\text{C}} \,|0\rangle_{\text{D}}), \tag{6.32}$$

with $\left|\Psi^{(+)}\right\rangle_{\text{AB}}$ the usual hybrid entanglement. This state can be rewritten as

$$\begin{aligned} |\Psi\rangle_{\text{ABCD}} =& \frac{1}{2}\Big(\left|\Psi^{(-)}\right\rangle_{\text{CA}} \otimes (c_0 \,|\text{cat}_+\rangle_{\text{B}} \,|1\rangle_{\text{D}} - e^{i\phi} c_1 \,|\text{cat}_-\rangle_{\text{B}} \,|0\rangle_{\text{D}}) \\ &+ \left|\Psi^{(+)}\right\rangle_{\text{CA}} \otimes (c_0 \,|\text{cat}_+\rangle_{\text{B}} \,|1\rangle_{\text{D}} + e^{i\phi} c_1 \,|\text{cat}_-\rangle_{\text{B}} \,|0\rangle_{\text{D}}) \\ &+ \left|\Phi^{(-)}\right\rangle_{\text{CA}} \otimes (-e^{i\phi} c_1 \,|\text{cat}_+\rangle_{\text{B}} \,|0\rangle_{\text{D}} + c_0 \,|\text{cat}_-\rangle_{\text{B}} \,|1\rangle_{\text{D}}) \\ &+ \left|\Phi^{(+)}\right\rangle_{\text{CA}} \otimes (e^{i\phi} c_1 \,|\text{cat}_+\rangle_{\text{B}} \,|0\rangle_{\text{D}} + c_0 \,|\text{cat}_-\rangle_{\text{B}} \,|1\rangle_{\text{D}}) \Big). \end{aligned} \tag{6.33}$$

From this expression and as before, we have the relevant terms after mixing modes A and C:

$$|\Psi\rangle_{\text{ABCD}} = \frac{1}{2}\Big(|1\rangle_{\text{C}} \,|0\rangle_{\text{A}} \otimes |\psi_{\text{in}}\rangle_{\text{BD}} + \frac{1}{2} \,|2\rangle_{\text{C}} \,|0\rangle_{\text{A}} \otimes (i\hat{\sigma}_Y^B \,|\psi_{\text{in}}\rangle_{\text{BD}} + \hat{\sigma}_X^B \,|\psi_{\text{in}}\rangle_{\text{BD}}) \Big). \tag{6.34}$$

Here we use the notation $|\psi_{\text{in}}\rangle_{\text{BD}} = c_0 \,|\text{cat}_+\rangle_{\text{B}} \,|1\rangle_{\text{D}} + e^{i\phi} c_1 \,|\text{cat}_-\rangle_{\text{B}} \,|0\rangle_{\text{D}}$ and as before the Pauli operators $\hat{\sigma}_X^B$ and $\hat{\sigma}_Y^B$ are applied on mode B. In this case the entangled state corresponding to the wrong Bell measurements is

$$i\hat{\sigma}_Y^B \,|\psi_{\text{in}}\rangle_{\text{B}} + \hat{\sigma}_X^B \,|\psi_{\text{in}}\rangle_{\text{B}} = 2e^{i\phi} c_1 \,|\text{cat}_+\rangle_{\text{B}} \,|0\rangle_{\text{D}} \,. \tag{6.35}$$

From then, the exact same reasoning as the one used for qubit QT leads us to the expression of the teleported entanglement in the case of losses:

$$\begin{aligned} \rho \propto & A_{00}^{\Delta} \,|\psi_{\text{in}}\rangle \,\langle\psi_{\text{in}}|_{\text{BD}} \\ &+ c_1^2 \Big(2(1-R)(\eta A_{11}^{\Delta} + (1-\eta) A_{00}^{\Delta}) + R A_{00}^{\Delta} \Big) \,|\text{cat}_+, 0\rangle \,\langle\text{cat}_+, 0|_{\text{BD}} \,. \end{aligned} \tag{6.36}$$

From equation (6.36) we see that the negativity of entanglement $\mathcal{N}$ will be below the one presented by the initial entangled state, the second term of the equation corresponds to losses directly added onto the teleported entanglement. We remark that, as the lossy term

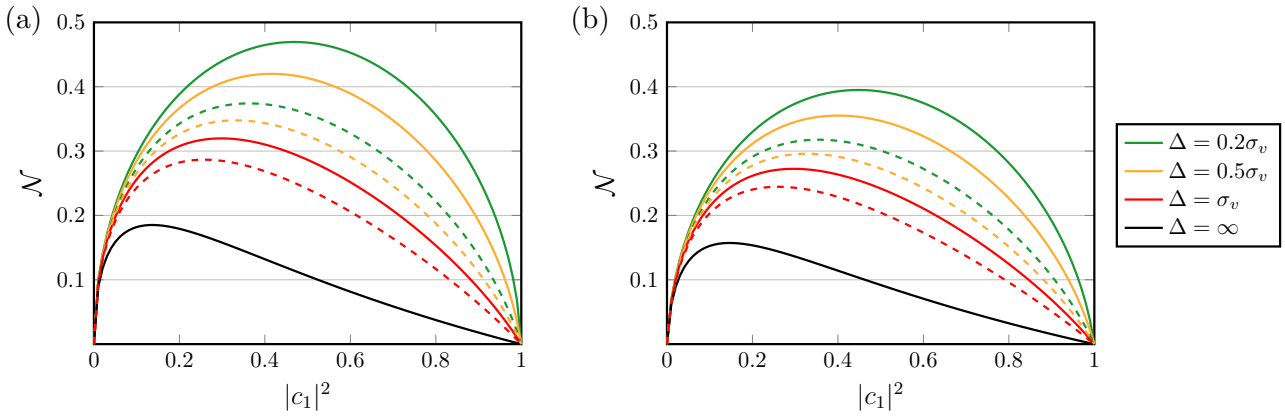

Figure 6.7: **Entanglement negativity of the swapped state** depending on c_1 for different conditioning windows Δ and $R = 10\%$. Full lines: No losses, dashed lines: 15% of detection losses. Figure (a): In the case of a perfect hybrid entangled state with $\mathcal{N} = 0.5$ and a loss-less DV∞DV entangled state. Figure (b): Starting from the experimental hybrid entangled state with $\mathcal{N} = 0.38$ and a perfect DV entangled state mixed with 20% of vacuum. In all cases, starting from a perfectly balanced DV entangled state $|c_1|^2 = 0.5$ doesn't lead to the highest possible negativity on the swapped entanglement. Applying a bias enables one to compensate for the imperfections introduced by the approximate Bell measurement. We see in (a) that even starting from two maximally entangled states, we cannot reach maximum $\mathcal{N}$ on the teleported states and we are limited to $\mathcal{N} = 0.47$ without losses and $\mathcal{N} = 0.37$ with losses for $\Delta = 0.2\sigma_0$. Starting from the experimental hybrid entanglement in (b) we can reach $\mathcal{N} = 0.4$ without loss and $\mathcal{N} = 0.32$ with 15% losses. Note that in both cases, even without conditioning on the homodyne, the detection of a photon is enough to generate entanglement although with a value of negativity roughly half of what can be achieved when performing the homodyne conditioning.

depends on c_1, starting with the maximally entangled balanced state $c_1 = 1/\sqrt{2}$ doesn't necessarily lead to the state with the highest $\mathcal{N}$ after swapping. The dependence can be seen in figure 6.7. In figure (a) we show the value of $\mathcal{N}$ on the swapped entanglement in the case of a maximally entangled hybrid state depending on c_1 and in figure (b) the same evolution in the case where we start with the experimental hybrid entanglement with $\mathcal{N} = 0.38$ and a DV entangled state mixed with 20% of vacuum. In this more realistic case, we can expect to reach quite high values of negativity, up to $\mathcal{N} = 0.32$ when accounting for the losses on the homodyne detection path. The observation of negativity is overall quite forgiving in terms of Bell measurement quality. Even without any conditioning on the homodyne detection, we can still reach $\mathcal{N} = 0.15$.

2.2.4 Entanglement purification

A particular use of entanglement swapping is entanglement purification. If the Bell measurement performed has a good fidelity with the ideal Bell measurement, it is possible to increase the amount of entanglement above that of the input state or even above the negativity of both initial entangled states. Achieving this increase of negativity is a strong indicator of quality for any ES protocol. In our experimental conditions, it is challenging to reach this regime as can be seen in figure 6.8. In the figure we show the negativity of the swapped state depending on the negativity of the input DV state and for the experimental hybrid entangled state with $\mathcal{N}_{\text{CV}\infty\text{DV}} = 0.38$. Without losses on the homodyne detection both regimes where we have $\mathcal{N}$ greater than for the input state (shaded in green) or greater than for the input and

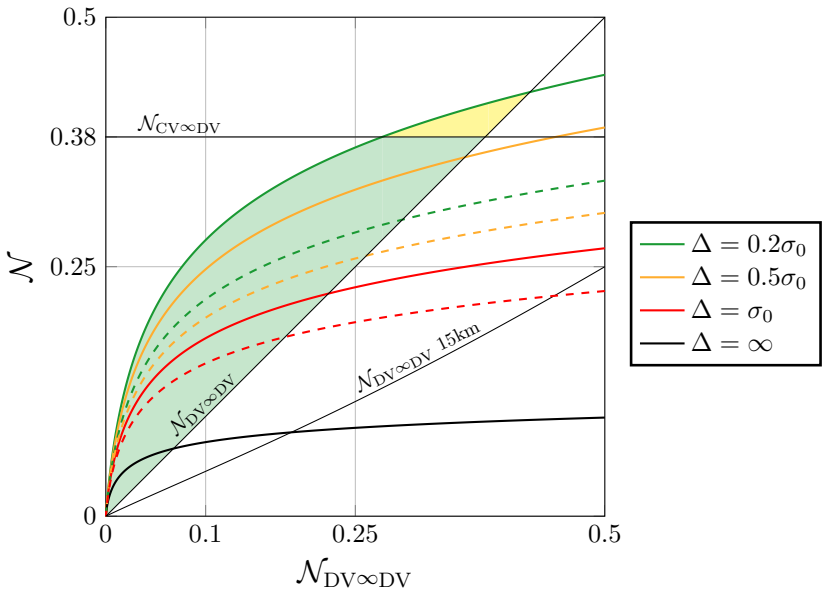

Figure 6.8: **Entanglement negativity after swapping** depending on the negativity of the initial DV-entangled state $\mathcal{N}_{\mathrm{DV}\infty\mathrm{DV}}$ for different values of Δ and for the experimental hybrid state presenting $\mathcal{N}_{\mathrm{CV}\infty\mathrm{DV}} = 0.38$ and $R = 10\%$. Full lines: no loss, dashed lines: 15% losses on the homodyne detection. Depending on the initial conditions, it is possible to obtain a final state presenting a negativity greater than $\mathcal{N}_{\mathrm{DV}\infty\mathrm{DV}}$. For example at $\Delta = 0.2\sigma_0$ and without loss, this case corresponds to the green area. As shown by the dashed line, this situation is possible even with a lossy homodyne detection for $\mathcal{N}_{\mathrm{DV}\infty\mathrm{DV}} < 0.3$. In that case, swapping lead to a purification of the input entanglement. In the perfect case without losses, it is even possible to obtain a higher negativity than that of both the input state and the hybrid entanglement used. This corresponds to the yellow area. Because of the 15% detection loss induced by the homodyne detection, this case is impossible to achieve experimentally. Finally we plot the negativity of the input state after propagation in a commercial optical fiber for 15km. This distance of 15km corresponds to the $\approx 50\%$ losses separating the CV and DV modes of the hybrid-entangled state (assuming 0.2 dB/km loss). When $\mathcal{N}$ is above that line, swapping is beneficial compared to a direct propagation of the input state. This is the case for most input entangled states in the case of $\Delta < 1$.

hybrid-entangled states (shaded in yellow) are accessible. However, the 15% losses introduced by the homodyne limit the possibilities as shown by the dashed green line. In that case it is still possible to improve on the input entanglement but not on both. For input entangled states with lower $\mathcal{N}_{\mathrm{DV}\infty\mathrm{DV}}$, our scheme both purifies and converts the entanglement from DV∞DV to CV∞DV.

Once we consider the effective distance between the CV and DV modes of hybrid entanglement, the protocol appears even more advantageous. Indeed, as we have seen there are losses on the conditioning mode used to herald hybrid entanglement. These losses, which are due to frequency filtering and coupling to the heralding SNSPD are close to 30% which roughly corresponds to 7.5 km of transmission through a commercial optical fiber. These losses mainly have an impact on the rate of generation of the hybrid state (there is only a marginal impact on the quality of the state because the number of false positive increases relatively to good events). From that viewpoint the CV and DV modes of entanglement can be considered to be 15 km distant from each other (the distance is doubled because losses have to be counted both for the CV and DV conditioning paths). From this we conclude

that the swapping protocol is advantageous if it leads to a better negativity than what would have been reached by a direct propagation for 15 km of one mode of the input entanglement. This limit is plotted as well in figure 6.8 and we see that for all input qubits the negativity reached is well above that threshold if $\Delta \leq 0.5\sigma_0$.

A realistic entanglement swapping experiment would therefore allow the purification of entanglement when compared to a direct transmission even in our hybrid case. This is possible because of the nature of the Bell measurement used. As it is done by conditioning on measurement results, it trades efficiency for entanglement quality. This feature is the reason why quantum repeaters can work, the combination of several ES operations allows a linear decrease of entanglement instead of the exponential decrease when using direct transmission [163].

3 Conclusion

In this chapter, we have introduced the principle of quantum teleportation and presented the advantages and drawbacks presented by different encoding basis for its implementation. We have also motivated the realization of hybrid quantum teleportation and presented a protocol for teleportation from a DV photon-number basis to a CV coherent-state encoding. A theoretical study leads us to conclude that a hybrid implementation of QT is possible with our resources. In the case of qubit quantum teleportation, this protocol should lead to fidelities above the classical limit. Entanglement swapping can also be performed and would realistically lead to a swapped state presenting entanglement negativity greater than achievable through direct transmission. In the next Chapter we will present the progress made towards the realization of both protocols and some preliminary results for entanglement swapping.

Chapter 7

Experimental implementation of hybrid quantum teleportation

In this chapter, we present the complete experimental setup for hybrid quantum teleportation that was built during the course of this thesis. We have seen how to generate hybrid entanglement in Chapter 4 and the previous chapter detailed how the Bell measurement can be implemented. The last remaining component for a practical demonstration of quantum teleportation is the generation of the input state. All the resources necessary to its creation have been presented in prior chapters and are available for our experiment. We could indeed complete the protocol by adding more OPOs, SNSPDs and homodyne detection systems on the table. We followed however a different approach and installed a new resource: an optical delay line. This delay line allows us to use the same OPOs both for the generation of the input state and of hybrid entanglement by letting the input state propagate into the delay line before mixing it with an hybrid-entangled state generated at a later time.

We will first present the complete setup for hybrid QT and then give details on the delay line's implementation and features. We conclude the chapter by reporting on encouraging preliminary results for hybrid entanglement swapping.

Contents

1 Complete setup for hybrid quantum teleportation

Our complete protocol is in two stages. The first one is the creation of the input state, either a photon-number qubit or DV∞DV entanglement, in a delay line. The second stage is the teleportation protocol presented last chapter. In this section we give details on the complete protocol, starting with the method used for the consecutive generation of single-photon states and hybrid entanglement.

1.1 Consecutive creation of a single photon and hybrid entanglement using the same source

Our goal is to first herald the presence of a single photon on the DV mode at time t_1 and then to create hybrid entanglement at a later time t_2. As shown in figure 7.1, this can be done using two SNSPDs placed at the output ports of a beam-splitter coupling both conditioning paths. One of these detector will herald the creation of hybrid entanglement while the other will herald the presence of a single-photon on the DV mode. This is possible because the rate of detection of parametric down-conversion events coming from OPO II is in practice much greater than for OPO I. This means that when mixing on the beam splitter the two conditioning paths, balancing the two rates at one of its output will lead to a strong imbalance at the other output. As the imbalance is in favor of OPO II, detecting PDC events at this other port most likely corresponds to the presence of single photons.

Let us look at a particular example. We write the PDC rates for OPO I and OPO II respectively $\mathcal{R}_{\mathrm{I}}$ and $\mathcal{R}_{\mathrm{II}}$. At the typical pumping power of 1mW for OPO II and 5mW of pumping power for OPO I and when tapping 3% off its output, we have $\mathcal{R}_{\mathrm{II}}/\mathcal{R}_{\mathrm{I}} \approx 3$. The balanced hybrid entangled state is created by mixing both conditioning paths on a beam-splitter of reflectivity R_0. At the end of one of the beam splitter output is the SNSPD that serves to herald hybrid entanglement. The maximally entangled state is heralded on this detector when photons detected are equally likely to have come from both OPOs. With the arrangement shown in figure 7.1, this is achieved in the condition that the beam-splitter reflectivity follows

$$R_0 = \frac{\mathcal{R}_{\mathrm{I}}}{\mathcal{R}_{\mathrm{I}} + \mathcal{R}_{\mathrm{II}}}. \tag{7.1}$$

At the other output port the ratio between the number of clicks coming from OPO II and that of OPO I, which we write $N_{\mathrm{II/I}}$, is equal to

$$N_{\mathrm{II/I}} = \frac{1-R}{R}\frac{\mathcal{R}_{\mathrm{II}}}{\mathcal{R}_{\mathrm{I}}} \tag{7.2}$$

Combining this with equation (7.1), we find that

$$N_{\mathrm{II/I}} = (\frac{\mathcal{R}_{\mathrm{II}}}{\mathcal{R}_{\mathrm{I}}})^2. \tag{7.3}$$

In the case where $\mathcal{R}_{\mathrm{II}}/\mathcal{R}_{\mathrm{I}} = 3$, we obtain $N_{\mathrm{II/I}} = 9$, meaning that, if we consider only the DV mode, the state heralded when we observe a detection at this output port is

$$\rho_{\mathrm{DV}} = 0.9\,|1\rangle\langle 1|_{\mathrm{DV}} + 0.1\,|0\rangle\langle 0|_{\mathrm{DV}}\,. \tag{7.4}$$

We obtain a mixed state with 90% of single-photon component. This is in the ideal case but, even starting from our experimental high-purity single photons, we manage to recover

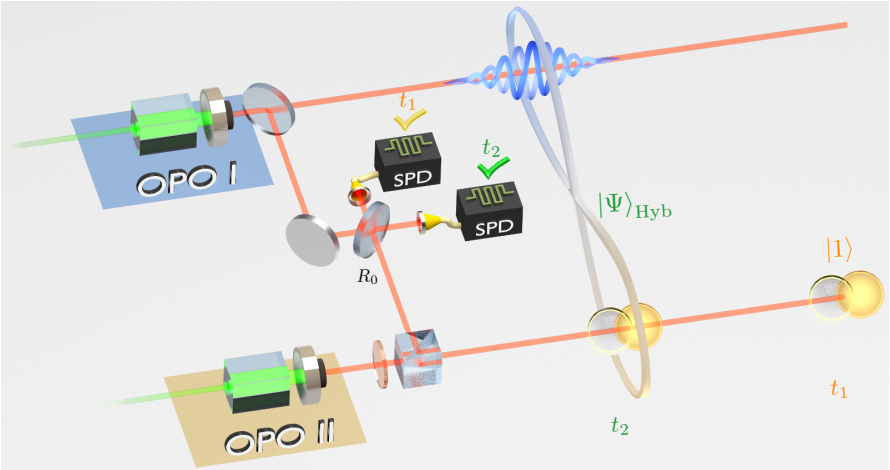

Figure 7.1: **Consecutive generation of single-photon and hybrid entanglement**. The beam-splitter joining the two conditioning paths is imbalanced and has a reflectivity R_0. This imbalance, along with the different heralding rates of both OPOs, allows the configuration where events detected on the SNSPD on the right or equally likely to come from both OPOs while photons detected by the SNSPD on top are most likely to come from OPO II. At time t_1, we herald a single photon on the DV mode via a click on the top detector and at time t_2 the second detector heralds the creation of hybrid entanglement.

a state with a 84% single-photon component. This is already a very good single-photon but if necessary it can be made purer by tuning $\mathcal{R}_{\text{I}}$ and $\mathcal{R}_{\text{II}}$. This can be done by adjusting the pump power on both OPOs or by tuning the tapping percentage at the output of OPO I. This setup is therefore very close to having two independent sources of hybrid entanglement and single-photon states, at different times, with no compromise in terms of count rate for hybrid entanglement.

The ideal strategy for QT is to first herald a single-photon and from it manufacture the input state for teleportation which is then stored. The second step is to wait for a click heralding hybrid entanglement to retrieve the input state after which quantum teleportation can finally be performed. These steps are difficult to implement with this setup because the DV mode of hybrid entanglement is the same as the mode on which the single-photon can be created. The solution is to use the same beam splitter to create the input state, to send that input state to a delay line and then to perform the Bell measurement for QT.

1.2 Protocol for quantum teleportation

We now present the complete strategy for hybrid teleportation. It combines the method we just presented for the generation in sequence of a single-photon state and then hybrid entanglement with the method for Bell measurement detailed in section 2.2. The only thing missing is the generation of the input state and how to store until it can be teleported. The experimental setup is shown in figure 7.2. It presents the addition of a delay line coupled to the DV mode by a $50:50$ beam-splitter. This delay line is used for storage of the input state which will then be teleported.

There are several steps to the teleportation protocol that we now show. We first explain the protocol in the case of qubit QT and then we will present what adjustments are necessary

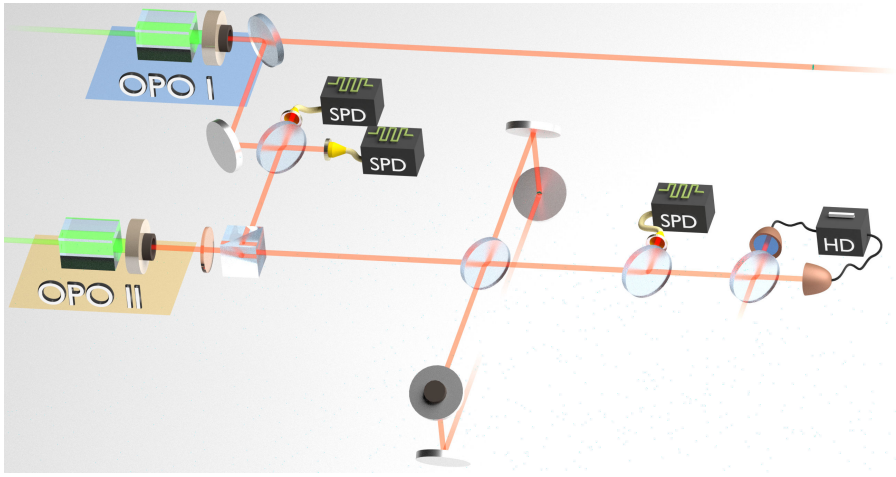

Figure 7.2: **Full setup for hybrid qubit quantum teleportation and entanglement swapping**. The exact protocol for teleportation is presented step-by-step in figure 7.3. The two OPOs are used both for the generation of hybrid entanglement and the input state, at different times. The added feature is a delay line coupled to the DV mode by a balanced beam-splitter. This delay line is used to store the input qubit and send it back to the same beam-splitter to be teleported.

for entanglement swapping.

1.2.1 Qubit quantum teleportation

The step-by-step protocol is shown in figure 7.3. There are four steps overall for the realization of QT. The first two are necessary for the creation of the input qubit and its storage in a delay line. The final two steps consist in the hybrid teleportation protocol we presented earlier.

Generation of the input qubit The method is shown in figures 7.3 (a) and 7.3 (b). The first step shown in (a) consists in heralding a single photon on mode A at time $t = 0$ following the method presented in section 1.1 and send it to a $50:50$ beam-splitter used to couple mode A with another mode C. This generates DV∞DV entanglement between modes A and C, thus creating the state

$$\left|\Psi^{(+)}\right\rangle_{\mathrm{CA}} = |0\rangle_{\mathrm{C}}|1\rangle_{\mathrm{A}} + |1\rangle_{\mathrm{C}}|0\rangle_{\mathrm{A}}\,. \tag{7.5}$$

From this DV-entanglement, the input qubit can be created by remote state preparation. This is shown in figure 7.3 (b). As in Chapter 4, once the mode A of the DV entanglement reaches the homodyne detection at time $t = t_{\mathrm{HD}}$, we condition on the observation of a given quadrature result q and lock the local oscillator phase to a value ϕ. This leads to the remote preparation of the qubit

$$|\psi_{\mathrm{in}}\rangle_{\mathrm{C}} = |1\rangle_{\mathrm{C}} + qe^{i\phi}|0\rangle_{\mathrm{C}}\,. \tag{7.6}$$

Storage of the qubit in a delay line The input qubit is sent on a delay line and returned to the other input of the balanced beam-splitter. The teleportation process can continue if hybrid entanglement is heralded at the exact moment where the qubit finishes its propagation through the delay line (see figure 7.3 (c)). We note the time of propagation through the delay

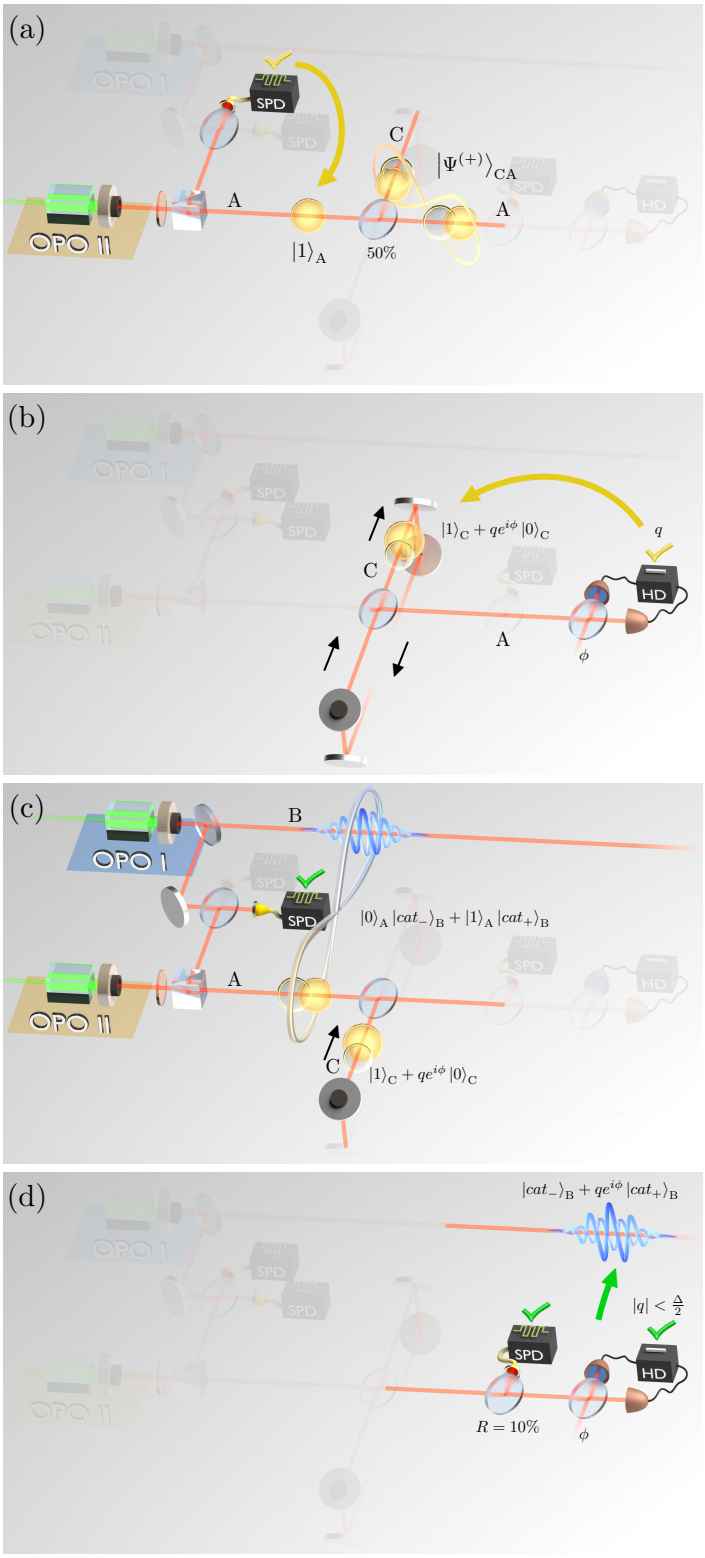

$t = 0$: Single-photon creation

- A click from the top SNSPD heralds the presence of a single-photon on the DV mode A.
- The photon is then split on a balanced beam-splitter coupling mode C to the DV mode. DV entanglement $|\Psi^{(+)}\rangle_{CA} = |0\rangle_C|1\rangle_A + |1\rangle_C|0\rangle_A$ is created.

t_{HD} : RSP, qubit in delay line

- Mode A of the DV entanglement is measured on the homodyne detection.
- RSP is performed using the homodyne locked at phase ϕ. Conditioning on measurement q prepares the input qubit $|1\rangle_C + qe^{i\phi}|0\rangle_C$. The qubit is sent in the delay line.

t_{DL} : Start of teleportation

- Hybrid entanglement is heralded using the second SNSPD.
- The qubit finishes propagating through the delay line and is ready to be teleported.

$t_{DL} + t_{Bell}$: Bell measurement

- The Bell measurement is completed by a local subtraction and homodyne conditioning.
- The input qubit is teleported to the CV mode: $|cat_-\rangle_B + qe^{i\phi}|cat_+\rangle_B$

Figure 7.3: **Detailed protocol for QT using the delay line**. (a) and (b) lead to the creation and storage of the DV qubit. (c) and (d) correspond to its teleportation on a CV encoding.

line t_{DL}. Our use of the delay line is quite close to the setup introduced in two recent paper by Bouillard *et. al* [164] and Takeda *et. al* [165]. Their implementations add the possibility of storing quantum states in the loop for several passes which gives more flexibility to their resources. Our particular protocol doesn't fundamentally require this capability.

Qubit Quantum teleportation Finally we arrive in figure 7.3 (c) at the starting point for hybrid quantum teleportation. The qubit and hybrid entanglement (HE) are mixed on the 50 : 50 beam-splitter. The phase of the delay line has to be locked to maintain a constant dephasing between the two inputs, this is done uzing a PZT on the final mirror of the delay line. Then in figure 7.3 (d) the teleportation is completed. We use a beam-splitter of reflectivity $R = 10\%$ and wait for a detection on the reflected mode. This approximates the application of the annihilation operator. Then we condition on the measurement of quadratures close to zero $|q| \leq \Delta/2$. The combination of the two operations is close to the application of operator $|1\rangle\langle 1|_{\mathrm{C}}$, *i.e.* the projector corresponding to the Bell measurement $\left|\Psi^{(+)}\right\rangle$. The input qubit is directly teleported on the CV encoding without the need for the application of a Pauli operator on the CV mode.

1.2.2 Entanglement swapping

The protocol for entanglement swapping is very close to the one used for qubit QT and uses the same setup. The first step is identical to the one realized in figure 7.3 (a) and leads to the creation of DV-entanglement. This is the input state that will be swapped. The second step in figure 7.3 (b) is therefore not performed. Instead, the homodyne detection serves to perform quantum tomography on one half of the input state. Accordingly, we sweep the local oscillator phase instead of locking it. The other mode of DV entanglement propagates through the delay line and the rest of the protocol is identical to that of figure 7.3. The difference with the ideal entanglement swapping protocol is that the swapped DV mode is measured –and destroyed– before the Bell measurement is performed. The correlations are still present between the final hybrid entanglement but it cannot be further propagated and used in other protocol without changes to the setup. This is however only a practical issue and simple changes to the setup would solve this problem. A possible solution is to introduce a variable transmissivity beam splitter on mode A that would be used in place of the second step shown figure 7.3 (b) to fully reflect mode A of the DV entanglement. During the time of propagation in the delay line, it would then be switched to full transmission to complete the protocol. The one implemented in [165] can be switched in 10 ns from $T = 0$ to $T = 1$, which is well below our value for t_{DL} (see 2.1.1).

2 Adding a delay line

Although the delay line was introduced as a short term solution for the realization of quantum teleportation, it represents a promising enhancement of our setup. For example,it opens the possibility of realizing protocols using time-bin entanglement. We therefore devote a section to a presentation of some of its features and study in particular the effect of transmission losses, first in the continuous pumping regime and then in the context of quantum teleportation. We finally present in details our experimental implementation and characterize its transmission loss and stability.

2.1 Parameters of the delay line

The introduction of a delay line in the setup leads to some modifications in the protocol. In the particular case of entanglement swapping, we've seen that it limits the use of the swapped DV mode for further experiments. In this section we consider the limitations it imposes on the quality of the input states we can create. We start by detailing the design constraints on the delay line and then assess the quality of the input states that can be generated for ES and qubit QT. We then conclude on the advantages of the method when compared to using coherent states as input.

2.1.1 Length of the delay line

The length of the delay line is constrained because of the temporal modes of the input qubit and hybrid entanglement. Indeed, as we have seen in chapter 2, the detection of a click at time $t = 0$ is correlated to the presence of a single photon at any given time t' around $t = 0$, most likely in the range -20 ns $\leq t' \leq 20$ ns. The same is true for hybrid entanglement. We wait for two heraldings in sequence at time $t = 0$ and t_{DL}. The Bell measurement comprises a detection event that has to be made at $t = t_{\mathrm{DL}} + t_{\mathrm{Bell}}$, where t_{Bell} is the time it takes for a photon heralded at $t = 0$ to go straight through the balanced beam-splitter and all the way to be detected for the Bell measurement. If t_{DL} is smaller than or comparable to 20 ns, a click observed at that time could have originated from the mixing of hybrid entanglement with the input qubit as expected. It could however as well have happened if HE was created first. In that case its DV mode would have propagated through the delay line and then would have been mixed with the single photon created later. Although this process still corresponds to a Bell measurement between a qubit and hybrid entanglement, it leads to losses for several reasons. First, the DV mode of HE goes through 50% of transmission loss because of the balanced beam-splitter, and second, the qubit in question is a single photon which limits the range of qubits to teleport.

Interestingly, even without the two previous issues, this would still lead to losses because the qubit and HE go through different input ports of the beam-splitter than in the normal protocol. As a consequence, from equation (6.17) we see that the Bell measurement we perform is $\left|\Psi^{(-)}\right\rangle$ instead of $\left|\Psi^{(+)}\right\rangle$. We have interference between the two possible paths followed by the qubit and HE which is equivalent to losses.

In the end we chose to build a delay line of 15 m, which corresponds to $t_{\mathrm{DL}} = 50$ ns. This also allows us to discriminate during the Bell measurement between the right sequence and all other possible paths such as multiple passes through the delay line for the qubit or for hybrid entanglement.

2.1.2 Characterizing the losses: continuous wave regime

The transmission losses in the delay line will directly impact on the quality of the input state. Here, we study the behavior of the delay line in the continuous regime in order to characterize its losses. The next section will look at the effect of these losses on the quantum input. The model used is presented in figure 7.4 (a). The delay line configuration resembles a Sagnac interferometer where two ports of the beam-splitter have been exchanged. In this configuration, there is only one direction of propagation for the light inside the delay line which can be considered to be a cavity. As presented in the figure, we model the losses by a beam-splitter of transmission η. At stability we have the system of equations linking the

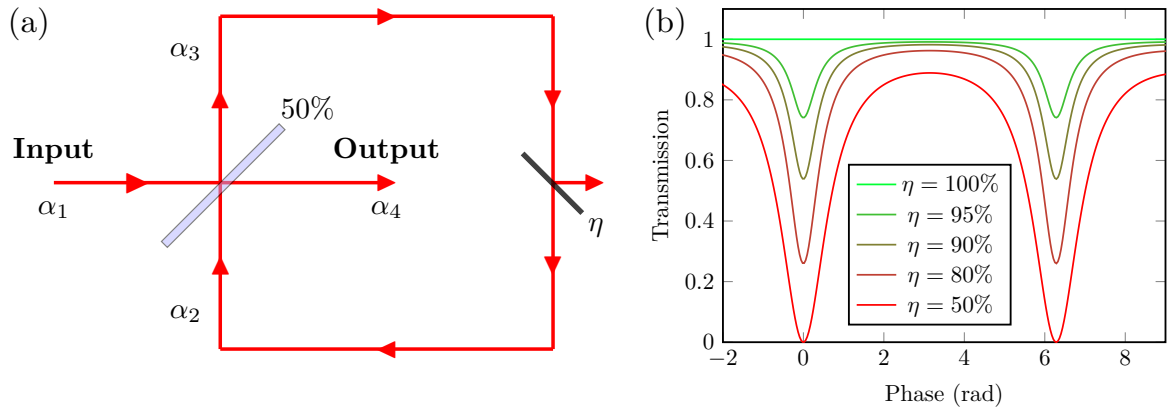

Figure 7.4: **Lossy delay line**. (a): Model. Losses are represented by a beam splitter of transmission η. (b): Transmission depending on the phase for different values of intra-cavity loss $1 - \eta$.

field amplitudes involved α_i:

$$\begin{aligned}\alpha_3 &= \frac{1}{\sqrt{2}}(\alpha_1 + \alpha_2)\\ \alpha_4 &= \frac{1}{\sqrt{2}}(\alpha_1 - \alpha_2)\\ \alpha_2 &= \sqrt{\eta}e^{i\phi}\alpha_3,\end{aligned} \tag{7.7}$$

where ϕ is the phase acquired after one pass through the delay line. Solving the system leads to the expression of the internal field's amplitude:

$$\frac{\alpha_2}{\alpha_1} = \frac{\sqrt{\eta}e^{i\phi}}{\sqrt{2} - \sqrt{\eta}e^{i\phi}}.. \tag{7.8}$$

From this we can compute the expression of the power inside the cavity

$$\frac{I_2}{I_1} = |\frac{\alpha_2}{\alpha_1}|^2 = \frac{\eta}{(\sqrt{2} - \sqrt{\eta}\cos(\phi))^2 + \eta\sin^2(\phi)}. \tag{7.9}$$

And we get at the output:

$$\begin{aligned}\frac{\alpha_4}{\alpha_1} &= \frac{1 - \sqrt{2\eta}e^{i\phi}}{\sqrt{2} - \sqrt{\eta}e^{i\phi}}\\ T \hat{=} \frac{I_4}{I_1} &= \frac{(1 - \sqrt{2\eta}\cos(\phi))^2 + 2\eta\sin^2(\phi)}{(\sqrt{2} - \sqrt{\eta}\cos(\phi))^2 + \eta\sin^2(\phi)}.\end{aligned} \tag{7.10}$$

The evolution of the transmission T with the phase is presented in figure 7.4 (b) for different values of η. We have a transmission T of 100% at all phases in the ideal case but with intra-cavity losses, T drops the most for $\phi = 2\pi n$, with $n \in \mathbb{N}$. It is possible to phase-lock the delay line only in the presence of small losses.

This behavior allows us to estimate the delay line losses by simply monitoring the power transmitted while sweeping the cavity. Note that, in the experimental context, the losses do not depend on the phase of the delay line. Indeed, we are heralding a quantum state with a narrower temporal mode than the delay line length and therefore are not in a continuous regime where interferences would arise when recombining the input field with itself.

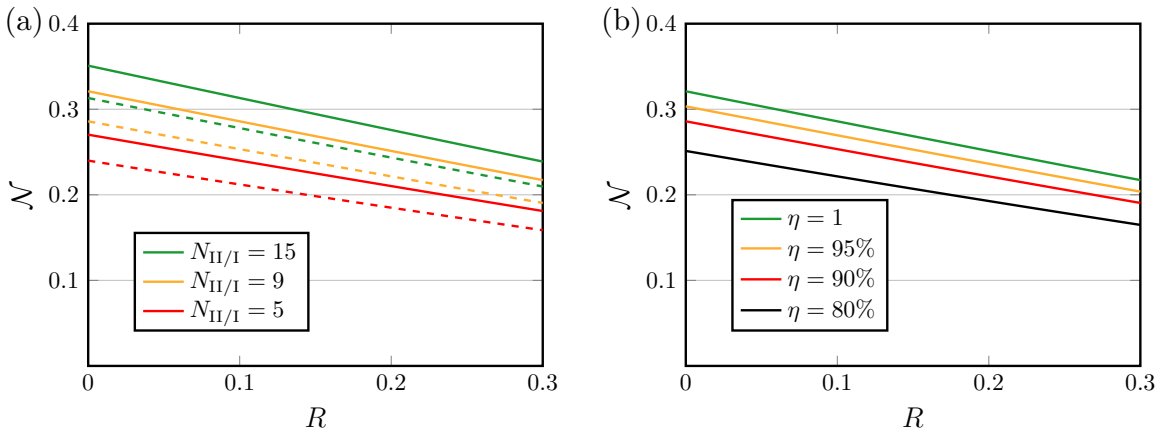

Figure 7.5: **Negativity of entanglement for the input** DV∞DV state depending on the reflectivity R of the tapping beam-splitter in the Bell measurement. (a): Evolution depending on the value of $N_{\mathrm{II/I}}$. Full lines: no losses on the delay line, dashed lines: 90% transmission on the delay line. At the typical value of $N_{\mathrm{II/I}} = 9$, we are close to the maximum possible negativity given the escape efficiency of OPO II. (b): Evolution for different values of transmission in the delay line.

2.2 Quality of the input and teleported states

We have seen that our implementation of the QT protocol has two main differences with the ideal protocol presented in section 2.2: First, the use of the same OPOs for the generation of hybrid entanglement and the input state, and second the delay line. These two differences have a direct impact on the quality of the input state created. We now apply the results of subsections 2.2.2 and 2.2.3 to our implementation to evaluate the quality of the input state depending on two new parameters: The ratio $N_{\mathrm{II/I}}$ of heralding rates from OPO II and OPO I, and the losses $1-\eta$ in the delay line. Overall this leads to four parameters when considering, for the Bell measurement, the reflectivity of the tapping beam-splitter R and the width of the conditioning window on the homodyne detection Δ.

The expression of the single photon state generated is, following the reasoning in section 1.1:

$$\rho \propto N_{\mathrm{II/I}} \left|1\right\rangle \left\langle 1\right| + \left|0\right\rangle \left\langle 0\right| . \tag{7.11}$$

To this we must add the losses due to the limited escape efficiency of OPO II $\eta_0 \approx 0.9$. This corresponds to the state

$$\rho \propto 0.9 N_{\mathrm{II/I}} \left|1\right\rangle \left\langle 1\right| + (1 + 0.1 N_{\mathrm{II/I}}) \left|0\right\rangle \left\langle 0\right| . \tag{7.12}$$

After the 50 : 50 beam-splitter, we obtain the normalized DV-entangled state before propagation in the delay line:

$$\rho_{\mathrm{CA}} = \frac{1}{N_{\mathrm{II/I}} + 1} (0.9 N_{\mathrm{II/I}} \left|\Psi^{(+)}\right\rangle \left\langle\Psi^{(+)}\right|_{\mathrm{CA}} + (1 + 0.1 N_{\mathrm{II/I}}) \left|00\right\rangle \left\langle 00\right|_{\mathrm{CA}}). \tag{7.13}$$

After propagation of mode C over the delay line with losses $1-\eta$, we get:

$$\rho_{\mathrm{CA}} = \frac{1}{N_{\mathrm{II/I}}+1}\Big(\frac{0.9N_{\mathrm{II/I}}}{2}(\,|01\rangle\langle 01|_{\mathrm{CA}} + \eta\,|10\rangle\langle 10|_{\mathrm{CA}} + \sqrt{\eta}(|01\rangle\langle 10|_{\mathrm{CA}} + h.c.)) \\ + (1+0.1N_{\mathrm{II/I}} + (1-\eta)\frac{0.9N_{\mathrm{II/I}}}{2})\,|00\rangle\langle 00|_{\mathrm{CA}}\Big). \tag{7.14}$$

From then, the quality of the Bell measurement comes into play. We proceed to compute the expression of the input states first for entanglement swapping, and then for qubit QT.

Entanglement swapping For entanglement swapping, the value of the reflectivity R of the beam splitter on mode A will add $\sqrt{1-R}$ worth of losses. Although we typically account for detection losses, these cannot be corrected for as they are inherent to our system and, unless we modify the setup to add for example a variable transmissivity beam-splitter on mode A as proposed earlier, we consider them to be part of the created DV-entanglement. We can still correct for the 15% losses used for the state characterization however. In consequence, the input state for entanglement swapping can finally be written:

$$\rho_{\mathrm{CA}} = \frac{1}{N_{\mathrm{II/I}}+1}\Big(\frac{0.9N_{\mathrm{II/I}}}{2}((1-R)\,|01\rangle\langle 01|_{\mathrm{CA}} + \eta\,|10\rangle\langle 10|_{\mathrm{CA}} \\ +\sqrt{(1-R)\eta}(|01\rangle\langle 10|_{\mathrm{CA}} + h.c.)) \\ +(1+0.1N_{\mathrm{II/I}} + \frac{0.9N_{\mathrm{II/I}}}{2}(1-\eta+R))\,|00\rangle\langle 00|_{\mathrm{CA}}\Big). \tag{7.15}$$

Although R only had a marginal effect in terms of the quality of the Bell measurement, it has a larger impact in terms of the accessible negativity of entanglement for the input state. We plot in figure 7.5 the negativity of the input state depending on R for different values of $N_{\mathrm{II/I}}$ and losses on the delay line. Overall the effect of both these parameters is quite limited compared to the initial loss of negativity due to the escape efficiency of the OPO. As long as $\eta \leq 90\%$ and $R \leq 10\%$ we have an input entanglement of negativity $\mathcal{N} \geq 0.27$, quite close to the best possible value with 90% of escape efficiency $\mathcal{N} = 0.35$. Comparing to figure 6.7, we should be able to reach a regime where the negativity of the teleported entanglement is higher than the input if $\Delta \leq 0.2\sigma_v$ and well above the negativity of the input state propagated over 15 km of fiber.

Qubit quantum teleportation Finally, for qubit quantum teleportation, we perform remote state preparation on the state in equation (7.15) to obtain the input qubit. As we did in Chapter 4, we get a good approximation of the remotely prepared state by assuming a conditioning on value q *i.e.* a very narrow conditioning window. Then, using $\langle q|1\rangle = qe^{i\phi}\langle q|0\rangle$, we can obtain the prepared state:

$$\rho_{\mathrm{C}} \propto \frac{0.9N_{\mathrm{II/I}}}{2}((1-R)q^2\,|0\rangle\langle 0|_{\mathrm{C}} + \eta\,|1\rangle\langle 1|_{\mathrm{C}} + q\sqrt{(1-R)\eta}(e^{i\phi}\,|0\rangle\langle 1|_{\mathrm{C}} + h.c.)) \\ +(1+0.1N_{\mathrm{II/I}} + \frac{0.9N_{\mathrm{II/I}}}{2}(1-\eta+R))\,|0\rangle\langle 0|_{\mathrm{C}}\,. \tag{7.16}$$

To see the quality of the input qubit created, we plot in figure 7.6 the size $|c_1|^2$ of the

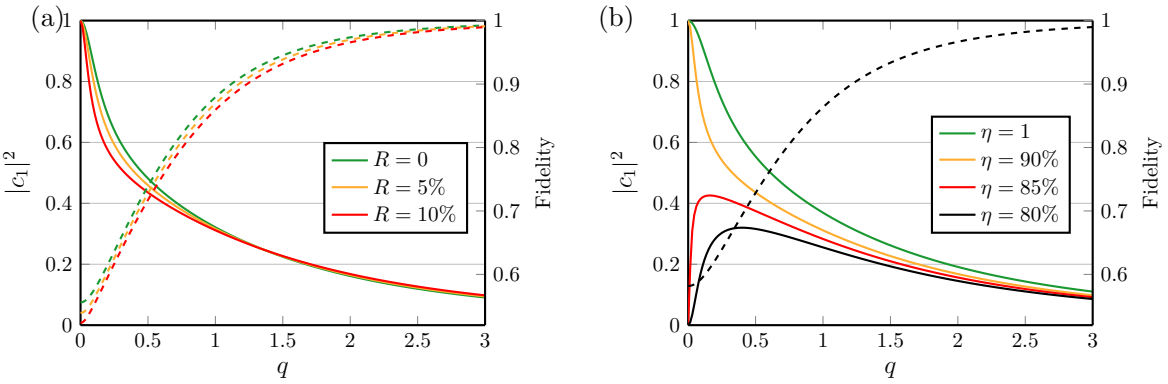

Figure 7.6: **Size and fidelity of the input state** remotely prepared by conditioning on q with the target qubit. Full lines: Value of $|c_1|^2$ of the target qubit closest in fidelity to the prepared state. Dashed lines: Corresponding fidelity between the prepared state and target qubit. (a): Evolution for different values of R and for $\eta = 90\%$. We get very little difference in terms of accessible qubit size for different values of R below 10%. (b): Evolution for different values of η. The losses in the delay line have a large impact for the preparation of states with higher population. The fidelity with the target state doesn't change much depending on η however. In both plots, when keeping states with fidelities above 80%, the two parameters have a narrow impact. Overall, it is possible to prepare with good fidelity only qubits where $|c_1|^2 \leq 0.3$.

target state closest in fidelity to the prepared state depending on q for different values of R and η. We show as well the fidelity between the two in dashed lines. All plots assume the 15% detection losses in the homodyne detection. We see that the escape efficiency and the homodyne losses are the limiting parameters that most restrict the accessible input qubits. In effect, when considering only states with fidelities above 80% with the target, the parameters of R and η have only a limited impact on the size and quality of the states we can prepare. Overall, we can create good qubits of size $|c_1|^2 \geq 0.3$ with a fidelity above 85% for $R \leq 10\%$ and $\eta \geq 90\%$. With a perfect delay line, we can create reliably states with $|c_1|^2 \geq 0.4$.

From these result, we can emphasise the benefits of using our method. Many quantum teleportation protocols are tested experimentally using coherent states as input qubits, for example in [161]. One may therefore question the benefits of using our more complicated setup for the preparation of the input qubits instead. The advantage of our method is that the input qubit will be limited to the $\{|0\rangle, |1\rangle\}$ subspace no matter the conditioning. The same cannot be said for coherent states for which, even at low values of $|\alpha|^2$, terms outside of $\{|0\rangle, |1\rangle\}$ will have a non-negligible contribution. As soon as $|\alpha|^2 \geq 0.2$ for example, the coherence terms $|\langle 0|\alpha\rangle \langle \alpha|2\rangle| \geq 0.1$. The problem in that case is that the Bell measurement will be degraded as terms proportional to $|3\rangle$ will be added to equation (6.22) and the results obtained will undermine the actual quality of the setup. It is possible to test reliably the system only at lower values of $|\alpha|$. Limiting ourselves to $|\alpha|^2 \leq 0.2$, means creating with good fidelity qubits with a maximal size of $|c_1|^2 \approx 0.15$. We see that with our method, we can explore a significantly larger range of input states, in realistic conditions with $|c_1|^2 > 0.3$.

In conclusion to this section, we have seen that the quality of the input states we can create depends on the losses introduced by the delay line. In a realistic context however, the escape efficiency and the losses on the homodyne characterization are large enough that improving the quality of the delay line beyond $\sim 85-90\%$ of losses will lead to small returns. We now present our experimental implementation of the delay line.

2.3 Experimental delay line

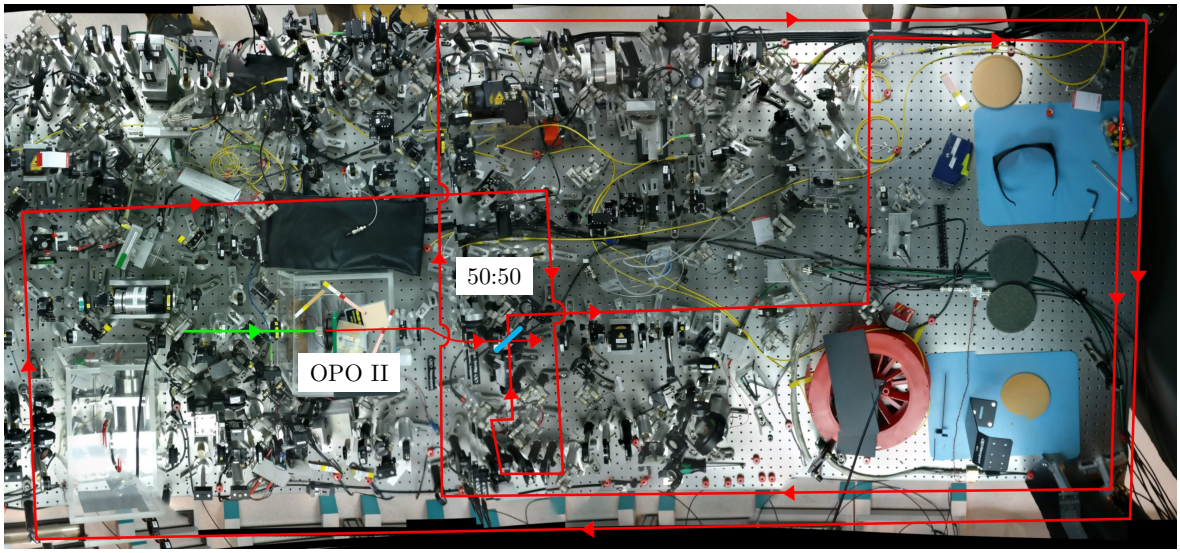

Figure 7.7: **Light path of the delay line on the optical table**. It passes through 15 independent mirrors, 4 lenses, 5 wave-plates and two polarizing beam-splitters. Its total optical length is 14.1m, which corresponds to a propagation time $t_{\mathrm{DL}} = 47$ ns. We estimate $1-\eta = 10\%$ of transmission losses and, when locked, a phase noise under 0.15 rad of standard deviation.

We now present the features of our experimental delay line. As we have seen it needs to introduce a delay significantly longer than 20 ns. We chose to make it close to 15 m long, which corresponds to $t_{\mathrm{DL}} = 50$ns. To limit losses, phase instability, and polarization instability, we decided to set it up in a free-space configuration. It is possible to obtain high transmission free-space delay lines by using only two mirrors as in [164, 165]. However, while having low losses is crucial to both these papers, we've seen in the previous section that the effect of transmission losses is secondary to that of escape efficiency and homodyne detection loss for our experiment. In consequence, we have built a very simple delay line made of standard independent mirrors set in an approximate spiral spread over the optical table. The light's path can be seen in the picture of figure 7.7. This span over the opposite corners of the optical table minimizes the number of mirrors used and therefore the losses, but it leads to increased instability.
We now report on measurements made to assess the transmission losses and phase stability of the delay line. In the case of transmission loss, we propose two distinct measurements, first in the continuous wave regime and then at the single photon level. We will see that the results are slightly different and conclude for the QT protocol.

2.4 Losses and phase stability of the delay line

The transmission of the delay line (DL) as a function of phase delay can be seen in figure 7.8 (a). We recover the expected behavior shown in figure 7.4 (b) and we have a good fit with a theoretical delay line with 10% intra-cavity losses. Next we consider its phase stability. The delay line has to be locked at a fixed phase that will be the relative phase between the input state and the DV mode of hybrid entanglement. We lock the phase by using a method similar to Hansch-Couillaud [166] locking. We place a half-wave plate in

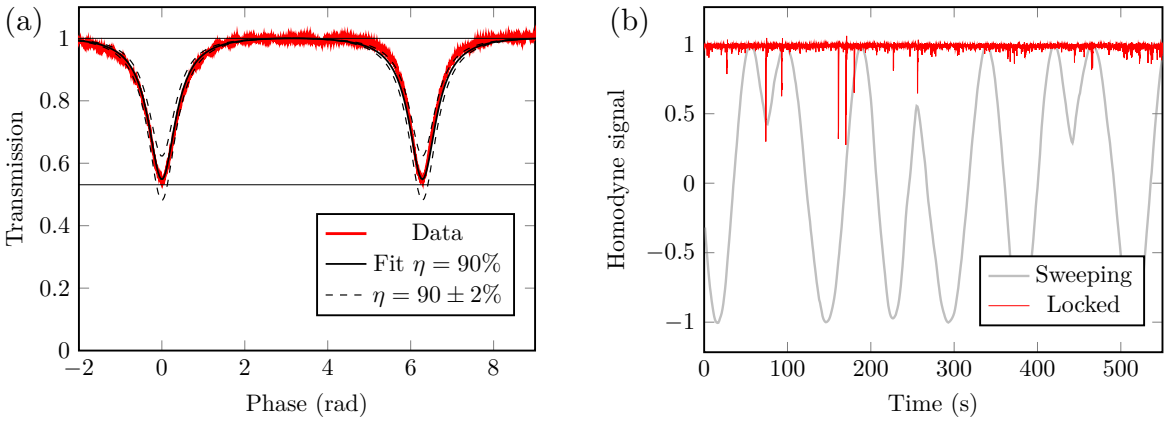

Figure 7.8: **Transmission and phase lock of the delay line**. (a): Transmission depending on the phase. We have the expected behavior of lower transmission at phases $\phi = 2n\pi$. A good fit is obtained with the theoretical curve for 90% of transmission. We also show in dashed lines the theoretical behavior for $\eta = 90 \pm 2\%$. All theoretical curves are normalized to get a maximum of 1. (b): Stability of the lock over 10 min. Some perturbations arise but the system quickly returns to the lock value. Overall we have about 0.15 rad or 10 degrees of standard deviation. The grey curve only serves as a visual aid to see the scale of the fringes.

the cavity turned at a small angle as compared to full transmission. It introduces a small orthogonal polarization component which will interfere with the input orthogonal field. We use this interference to build an error signal used to lock the phase via a standard analogue PID method. The quality of the locking is assessed in figure 7.8 (b). Here we evaluate the end impact on the phase of the input qubit. We directly monitor the interference between the local oscillator of the homodyne detection and the seed beam. When the delay line is locked, sweeping the phase leads to the interference fringe in gray. When locking additionally the local oscillator relative phase, we obtain the blue curve. The locking is maintained here for 10 min but is representative of the stability over longer periods. This plot therefore combines two locks and is a measurement of the phase stability of the input qubit. As the locking is made on phase π for the DL, a small variation of intensity leads to a significant change in phase. We measure a standard deviation close to 10 degrees for the phase of the qubit. The delay line can therefore be reliably locked at least with the same stability. We also note a quick return to the locking value after a perturbation.

2.5 Single photon through the delay line

In the previous section, we have measured the transmission losses in the delay line. One aspect of the setup that we have not yet characterized is the mode matching between the local oscillator and delay line modes. The homodyne detection is set experimentally to have optimal matching between the optical mode going straight through the balanced beam-splitter. It is therefore possible that the other mode, coupled to the homodyne detector on reflection is matched differently. In the context of QT, this would mean that the input state and the DV mode of hybrid entanglement have a different matching to the homodyne detection. As the Bell measurement includes homodyne conditioning, this can degrade the quality of the protocol.

This coupling is challenging to measure in the continuous wave regime because there is

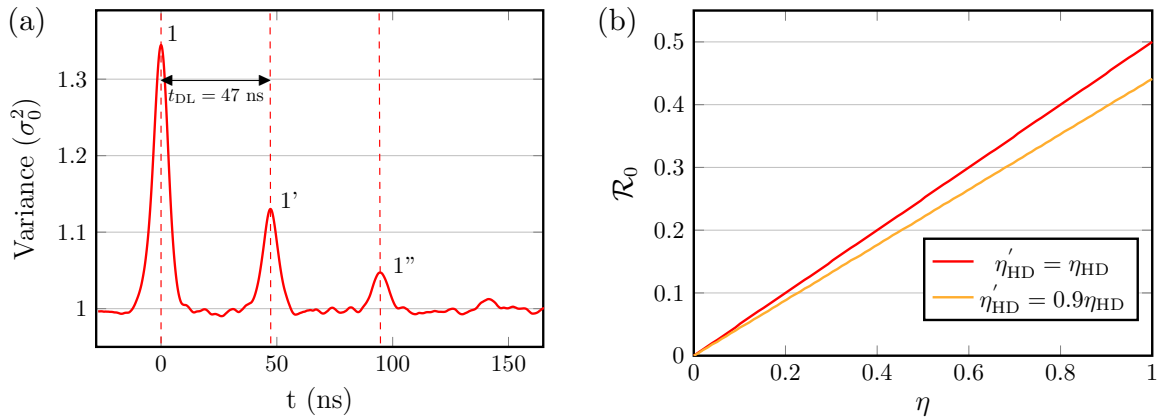

Figure 7.9: **Quadrature variance of a single photon through the delay line**. (a): Variance of the field quadrature depending on time after heralding a photon at time $t = 0$. We see several peaks corresponding to the direct transmission of the photon, detection after one pass through the delay line, and detection after two passes. The corresponding events can be discriminated thanks to the measured 47 ns it takes for a run through the delay line. (b): Ratio of consecutive peaks depending on the losses on the delay line and the input qubit c_1. All values are for homodyne losses of 15%.

no configuration in which we can observe interferences involving only the input mode and the local oscillator. It can be done however at the single-photon level by monitoring the variance of the homodyne signal. This is shown in figure 7.9 (a). We herald a single photon at time $t = 0$ and observe a peak labeled #1 with the corresponding Lorentzian temporal mode at that time. There are however other peaks that we call echoes and that correspond to the cases where the heralded single photon went through the delay line before impinging on the homodyne detector. We label the first two echo peaks #1′ and #1″ and the are as expected close to 50 ns and 100 ns away from peak #1. We have $t_{\mathrm{DL}} = 47.3$ ns. We see that the delay line is long enough to separate the temporal modes corresponding to a different number of passes before detection.

In a first approximation, the relative size between consecutive peaks is governed by the transmission losses $1 - \eta$ in the delay line. We note the ratio between the height of the first and of the second peak $\mathcal{R}_0$. Starting from a pure single photon at the output of OPO-II, we have:

$$\mathcal{R}_0 = \frac{\int q^2 |\frac{\eta}{2}\langle 1|q\rangle + (2 - \eta + \frac{\eta}{2})\langle 0|q\rangle|^2 dq - 4\sigma_0^2}{\int q^2 |\langle 1|q\rangle + \langle 0|q\rangle|^2 dq - 4\sigma_0^2}. \tag{7.17}$$

One can show that this equation is also valid in the case of an imperfect single photon as written in equation (7.11) and independent from the homodyne losses. The evolution is plotted in red in figure 7.9 (b). In the case of $\eta = 90\%$, we expect to have $\mathcal{R}_0 = 0.45$. We see experimentally a different result as we have $\mathcal{R}_{0,exp} = 0.4$. As explained before, this difference probably results from asymmetric matching to the homodyne. We can model this by introducing a new parameter defined from the coupling losses $1 - \eta_{\mathrm{HD}}$ between the DV mode of hybrid entanglement and the homodyne detector. This parameter, written η'_{HD} , is defined as the matching between the local oscillator and the input state modes. The yellow curve of figure 7.9 (b) corresponds to asymmetric losses $\eta'_{\mathrm{HD}} = 0.9 * \eta_{\mathrm{HD}}$ and is consistent with the measured ratio $\mathcal{R}_{0,xp} = 0.4$ for $\eta = 90\%$.

This difference in matching will lead to a degradation of the Bell measurement. As we condition on quadrature results close to zero, homodyne losses lead to a worse discrimination

between vacuum and single-photons. As the losses are asymmetric depending on the mode, the conditioning will be slightly biased towards the DV mode of entanglement. That being said, we expect the effect to be minimal or on the same level that the presence of two-photon components in the DV mode.

In this section, we have presented a theoretical model and experimental details for the delay line. We have shown in particular that, being longer than the temporal modes of the photons, it allows us to associate to particular times t the path followed by our quantum states. In the context of quantum teleportation, this ensures that the input qubit and hybrid entanglement are heralded consecutively. In the next section, we report on preliminary results for hybrid QT in the context of entanglement swapping.

3 Hybrid entanglement swapping: Preliminary results

In this section, we report on our first results for hybrid quantum teleportation, in the context of entanglement swapping. The current status of the cryo-cooler led us to temporarily adapt the setup to the use of two detectors instead of three. This leads to some changes in the quality of the protocol that we report on. One consequence is a decrease of the experiment's count rate which is significantly smaller than in other setups considered so far. In consequence we need to accumulate more data in order to give conclusive results. These first results are however consistent with a successful quantum teleportation protocol. We first characterize experimentally the input DV∞DV state and then detail the data analysis process and the effect of some parameter choices.

3.1 Input DV∞DV entanglement

Our first result is an experimental characterization of the input state. In the case of entanglement swapping, this is DV∞DV entanglement. This state was created and measured in an experiment separate from the teleportation protocol. The setup used is the same as in figure 7.2 with the difference that the delay line is not closed. Instead, we installed a third homodyne detection at its end. The input state is created by heralding a single photon and we perform quantum tomography on both output modes of the beam-splitter. We characterize the input state in the conditions of the QT experiment: We start from the mixed single photon of equation (7.4), and have the tapping beam splitter used for the Bell measurement on the DV mode of hybrid entanglement. This leads to an additional 10% of losses before homodyne tomography.

We have accumulated overall 100 000 events and the corresponding Wigner function is presented in figure 7.10 without correction for detection losses. We recover the expected DV∞DV entanglement with losses. In the $\langle 0|\,\hat{\rho}\,|0\rangle$ projection, we see a lossy single-photon state with a visible dip but no negativity of the Wigner function. In the $\langle 1|\,\hat{\rho}\,|1\rangle$ projection we recover vacuum. Finally we see the presence of coherence terms. We measure a negativity of entanglement of $\mathcal{N} = 0.08$. According to figure 6.7, this is in the regime where the entanglement swapping protocol should lead to a swapped state with a higher negativity than through direct transmission.

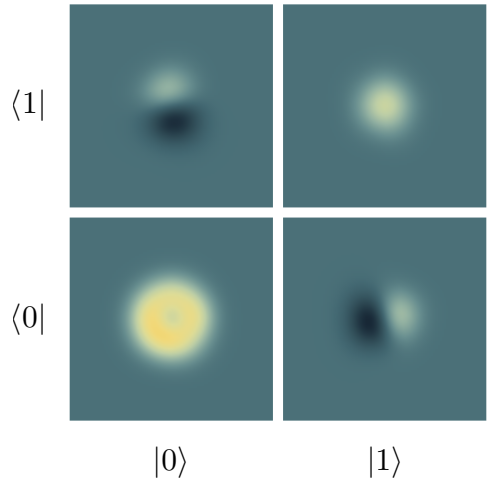

Figure 7.10: **Input DV∞DV entanglement**. Wigner functions of the projection on the DV mode of the input state recovered from 100000 events. We measure a negativity of entanglement $\mathcal{N} = 0.08$ without correction from detection losses.

3.2 Using two detectors, time filtering

The results we present in this section have been obtained by using just two detectors instead of the three required by the ideal setup shown in figure 7.2, and that we plan to implement once the cryo-cooler is fully operational. The setup adapted to the use of two SNSPDs is shown in figure 7.11. We use the same detector, called SNSPD 1, for the heralding of a single photon (HSP) and for the Bell detection. This is done by mixing the heralding and subtraction paths using a beam-splitter of reflectivity R_2. In the teleportation protocol, the time difference between the Bell detection click and the single-photon heralding is $t_{\mathrm{DL}} \approx 50$ ns. This duration is too short for our purpose of using in sequence the SNSPD for the two clicks as it has a dead time of the order of 100 ns. In consequence, we introduce a fibered optical delay on the subtraction path $\Delta t_{\mathrm{Bell}} \approx 150$ ns. The rest of the protocol is identical to figure 7.2, the other detector, SNSPD 2, is used to herald hybrid entanglement.

One issue that arises with this setup is the problem of coincidental clicks. Fixing the Bell detection event at time $t = 0$, the targeted sequence is:

- $t = -\Delta t_{\mathrm{Bell}} - t_{\mathrm{DL}}$: Heralded single photon on SNSPD 1.
- $t = -\Delta t_{\mathrm{Bell}}$: Heralded hybrid entanglement on SNSPD 2.
- $t = 0$: Bell detection on SNSPD 1.

Because we mix the HSP and Bell detection paths, it is not possible to distinguish this target sequence to the case where we have a two clicks coming from the heralding path at times $t = -\Delta t_{\mathrm{Bell}} - t_{\mathrm{DL}}$ and $t = 0$. Thankfully, this is in principle not a problem because the HSP and Bell detection clicks are correlated. To see this, let us assume we herald a pure single-photon at time $t = 0$. The photon will have a 50% chance to go through the balanced beam splitter, then with a probability R it will be sent to the subtraction path and finally with probability R_2 detected by the SNSPD at time Δt_{Bell}. We therefore have an overall conditional probability:

$$p(\mathrm{Bell@}\Delta t_{\mathrm{Bell}}|\mathrm{HSP@0}) = \frac{1}{2} R R_2. \tag{7.18}$$

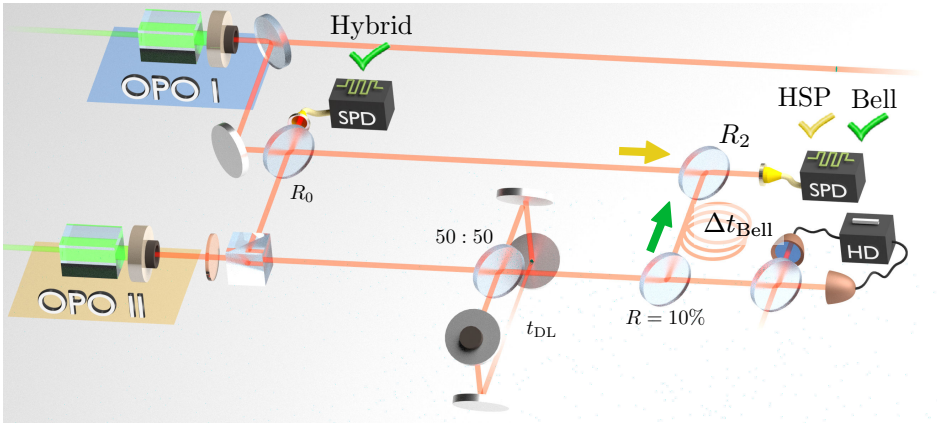

Figure 7.11: **Setup with two detectors**. We use the same detector for the heralding of the single photon (HSP) and the Bell detection (Bell). To do so, the heralding and detection paths are mixed using a beam-splitter with a coefficient of reflection R_2. The dead time of the SNSPD is to the order of 100 ns. As we want to condition on two detection event in sequence, it is necessary to delay the subtraction click. We introduce a fiber delay on the subtraction mode $\Delta t_{\text{Bell}} \approx 150$ ns. This setup works only because a Bell detection event at time $t = 0$ is correlated with a HSP click at time $t = -\Delta t_{\text{Bell}}$ so the targeted sequence is more likely than two coincidental clicks.

In the target sequence, we want the photon to propagate through the delay line of transmission η before being detected at time $\Delta t_{\text{Bell}} + t_{\text{DL}}$. We therefore have

$$p(\text{Bell@}\Delta t_{\text{Bell}} + t_{\text{DL}}|\text{HSP@0}) = \frac{1}{4}\eta R R_2. \tag{7.19}$$

The hybrid click is also correlated to the subtraction click. We can similarly compute the corresponding conditional probability, starting from the fact that if we have a hybrid click, we have a 50% chance to have a single photon on the DV mode. We get in the end

$$p(\text{Bell@}\Delta t_{\text{Bell}}|\text{Hybrid@0}) = \frac{1}{4}R R_2. \tag{7.20}$$

To take advantage of these correlations, we perform a conditioning on the timing of the clicks. This is done by triggering on three detection events, fixing the Bell measurement click at time $t = 0$. Then, we keep only clicks on SNSPD 1 and SNSPD 2 at the corresponding times t_1 and t_2 if they are in a given window of width $\Delta\tau$ around the target time:

$$\begin{aligned} -\Delta t_{\text{Bell}} - t_{\text{DL}} - \frac{\Delta\tau}{2} \leq t_1 \leq -\Delta t_{\text{Bell}} - t_{\text{DL}} + \frac{\Delta\tau}{2} \\ -t_{\text{DL}} - \frac{\Delta\tau}{2} \leq t_2 \leq -t_{\text{DL}} + \frac{\Delta\tau}{2}. \end{aligned} \tag{7.21}$$

The protocol with two detectors is equivalent to the ideal setup with three detectors if the probabilities (7.19) and (7.20) are much greater than the probability of having a coincidental click in the window $\Delta\tau$. This latter probability is, using the heralding rate from OPO II,

$$p(\text{HSP@}t_1|\text{HSP@0}) = R_0(1 - R_2)\mathcal{R}_{\text{II}}\Delta\tau. \tag{7.22}$$

Taking into account the temporal mode $f(t)$, we finally get the necessary condition for a successful protocol:

$$\frac{\eta R R_2}{4R_0(1 - R_2)\mathcal{R}_{\text{II}}} \frac{\int_{-\Delta\tau/2}^{+\Delta\tau/2} |f(t)|^2 dt}{\Delta\tau} \gg 1 \tag{7.23}$$

In the usual experimental conditions where $\mathcal{R}_{II} \approx 300$ kHz and $\mathcal{R}_I \approx 100$ kHz we have, from equation (7.1), $R_0 = 75\%$. Choosing a window as wide as the temporal mode $\Delta\tau = 20$ ns, we also have $\int_{-\Delta\tau/2}^{+\Delta\tau/2} |f(t)|^2 dt = 99\%$. We finally get, with $R_2 = 50\%$, $R = 10\%$ and $\eta = 90\%$

$$\frac{\eta R R_2}{4R_0(1-R_2)\mathcal{R}_{\mathrm{II}}} \frac{\int_{-\Delta\tau/2}^{+\Delta\tau/2} |f(t)|^2 dt}{\Delta\tau} \approx 5. \tag{7.24}$$

We are 5 times more likely to observe the right sequence of events than coincidental clicks in these conditions. This bias can be increased further by changing the value of R_2, in practice we set $R_2 = 60\%$, and the size $\Delta\tau$. It is preferable to set the conditioning window to be much narrower than the temporal mode. At vanishing $\Delta\tau$ we improve significantly the chance of selecting the right sequence but we increase dramatically the experimental duration. A good compromise is setting $\Delta\tau = 5$ ns. We then get

$$\frac{\eta R R_2}{4R_0(1-R_2)\mathcal{R}_{\mathrm{II}}} \frac{\int_{-\Delta\tau/2}^{+\Delta\tau/2} |f(t)|^2 dt}{\Delta\tau} \approx 20. \tag{7.25}$$

Note that, here, we have not taken into account all the experimental imperfections, for example the escape efficiency of the OPO is missing. In practice we can always adjust the parameters R_2 and R, as well as the pumping power applied to the OPOs to get in the right situation. In any case, this ratio has to be monitored as triggering on the wrong events amounts to adding losses.

3.3 Experimental settings and count rate

As can be expected from the protocol, this experiment has a very small count rate when compared to others presented in this thesis. Indeed, we combine two-clicks for the generation of a single photon and hybrid state, then an additional click for the Bell measurement and finally homodyne conditioning. Bringing everything together, the count rate depends on several parameters. Some have to be set during the data acquisition while others can be adjusted during the analysis. The former include the pumping power of both OPOs (and their ratio $N_{\mathrm{II/I}}$), the beam splitter reflectivity at the output of OPO I, and the reflectivity R of the tapping beam splitter for detection 3. As we are still in preliminary measurements, we adjust some parameters at the cost of state quality to have a reasonable count rate. First we increase the pumping power on both OPOs. We set respectively 20 mW and 5 mW of pump power at OPO I and OPO II. This leads to 5 dB of squeezing for the cat state generation and we keep the same reflectivity of 3% on the tapping mode. This increases the count rate but leads to a diminution of state purity. The five-fold increase on OPO II will lead to an increase of two-photon components that can potentially degrade the quality of the Bell measurement. We therefore have to monitor the weight of the higher Fock states in the final density matrix obtained. To preserve the quality of the Bell measurement, we kept a reasonably low reflectivity $R = 10\%$ for the Bell detection.

As we can apply the time filtering after the data acquisition, we first accumulate three click events happening in a wide time window of 250 ns. This is done by setting the triggers to have the Bell detection click at time $t_3 = 0$ and recording data when we happen to have prior detection events at times t_1 and t_2 such that -250 ns $\leq t_{1,2} \leq 0$. With these settings, we record triple coincidental events at a rate close to 50Hz.

This gives us a large amount of data from which we can check the presence of corre-

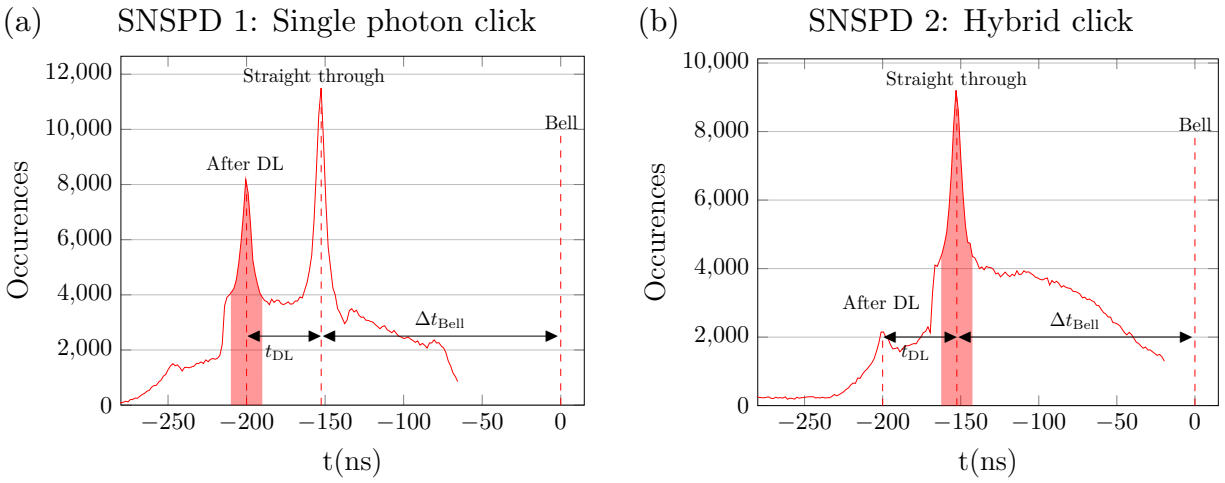

Figure 7.12: **Correlated detection events**. Histogram of detection times observed at the two detectors for state heralding given that we have a click at time $t = 0$ at the Bell measurement. Every registered event corresponds to a detection at time $t = 0$ on the Bell measurement and two prior independent detections at time $-250\text{ns} \leq t \leq 0$ on SNSPD 1 and 2 corresponding to the heralding respectively of a single photon, and of hybrid entanglement. We see that a detection during the Bell measurement is strongly correlated with the heralding of photons at SNSPD 1 and hybrid states at SNSPD 2 at some specific times. The relative size of the peaks and the noise floor are due to many parameters including losses in the delay line and the trigger pulses shapes. The shaded peaks correspond to the target protocol.

lations between clicks. In figure 7.12, we present histograms of detection times for a data set of 400 000 events. We indeed see that fixing the Bell measurement click at time $t_3 = 0$ favors specific times t_1 and t_2. In figure (a), we show the histogram for SNSPD 1 where we removed the triggers at time $t_3 = 0$. We see two main peaks that follow the temporal mode distribution. The peak at time $t_1 = -\Delta t_{\text{Bell}}$ corresponds to the case where the heralded single photon went straight through the balanced beam splitter before being detected. The shaded peak is the one of interest for the protocol and is at time $t_1 = -\Delta t_{\text{Bell}} - t_{\text{DL}}$. It corresponds to the single photon having gone through the delay line once before being detected at the Bell measurement. In figure (b), we also see two peaks corresponding to the case where the hybrid is heralded at $t_2 = -\Delta t_{\text{Bell}}$, and a smaller peak corresponding to the peak having gone through the delay line before detection. Note that the relative size of the peaks is due to our triggering setup on this oscilloscope. Through the addition of cable delays, we are actually set to trigger only on events such that $-215\text{ ns} \leq t_1 \leq 0$ and $-165\text{ ns} \leq t_2 \leq 0$. In consequence, we see a drop in the number of events at these times. The fact that we still record events at times prior is due to the irregular down slope of the SNSPD detection pulse that can lead to a trigger inside the selection window. This down slope also explains the general shape of the noise floor for SNSPD 1. As we wait for consecutive clicks on that detector, the closer the two detection events, the smaller the second pulse, and the probability of having coincidental events decreases.

Although the peaks are well defined, the noise floor is higher than expected. Among our setting choices, it is most likely due to the increase of pumping power on the OPO II. The shaded peaks are a little more than twice the height of the noise floor. This means that we

have close to 50% of wrong events on which we condition. Some experimental adjustments would improve the situation, by changing R_2, or R for example, or even by adding shutters on the heralding and subtraction paths. However, going to the setup with three detectors as we intend to do will completely remove this issue. Furthermore, this will eliminate the need for the beam-splitter R_2 and lead to a four-fold speedup of the experiment. Our current priority is to gain some insight into the protocol's functioning by completing the Bell measurement on our preliminary data set.

3.4 Effect of time filtering

Figure 7.12 obtained in the experimental conditions, is already a good indication that the protocol functions. The Bell-measurement click on which we trigger is correlated with the generation of a single photon and hybrid entanglement at privileged time. The effect of filtering on times t_1 and t_2 has on the measured variance scans on the two homodyne detections is shown in figure 7.13. These plots help to understand the different steps of the protocol and reveal some issues in our implementation, so we describe them in detail.

- In the top row, we see the initial variance scan without filtering and with t_3 set at time $t_3 = 0$. Peak #1 and the associated echos through the delay line #1′, #1″, and so on are due to the use of a single SNSPD for the heralding of a single photon and final subtraction. Without filtering the most likely reason for these peaks is single-photon heralding at time $t_1 = 0$. We have seen that the state heralded is mostly single-photon mixed with hybrid entanglement. For this reason we see a peak on both homodynes, but the strongest is seen on homodyne 2. A successful filtering should remove these peaks as they do not correspond to the right sequence of operations. The interesting data lies in times occurring before these peaks. The increase of variance over the one of vacuum is due to the fact that we heralded both single-photons and hybrid entanglement at negative times. As the precise moment of their creation is not set, there is an averaging effect and we don't see any well-defined peak, the signal is scrambled.

- Then, in the second row we have applied the time filtering, *i.e.* we've kept events in the shaded areas of figure 7.12. The plots correspond to $\Delta\tau = 12$ns. Let's look first at homodyne 1. Peak #1 is significantly reduced and a sharp peak #2 has appeared, centered at time $-\Delta t_{\text{Bell}}$. This peak is the variance of the CV mode of hybrid entanglement. We also see a small peak labeled #3 that is due to the imperfect single-photon heralding as was peak #1 before filtering. This plot is in agreement with what we expect, and the size of peaks #1 and #3 can be reduced by changing the value of $N_{\text{I/II}}$.

- Finally, in figure (d), we see the effect of filtering on homodyne 2. Peak #3 is due to the heralding of the single photon close to time $-\Delta t_{\text{Bell}} - t_{\text{DL}}$. Peak #2 results from two scenarios: the detection of the heralded single photon after one pass through the delay line or the DV mode of hybrid entanglement: This is a requirement for the teleportation protocol, both situations should be indistinguishable. The fact that this peak is as tall as #3 is an indicator of the relative probabilities of the two scenarios. Indeed, the echo peak #3′ (which is the same as peak #2) is about half as tall as #3 and so is the DV mode of hybrid entanglement. These peaks are expected and suggest the success of the protocol. However the fact that we have a peak #1 of comparable size is an issue. This means, as we had expected from figure 7.12, that we have the

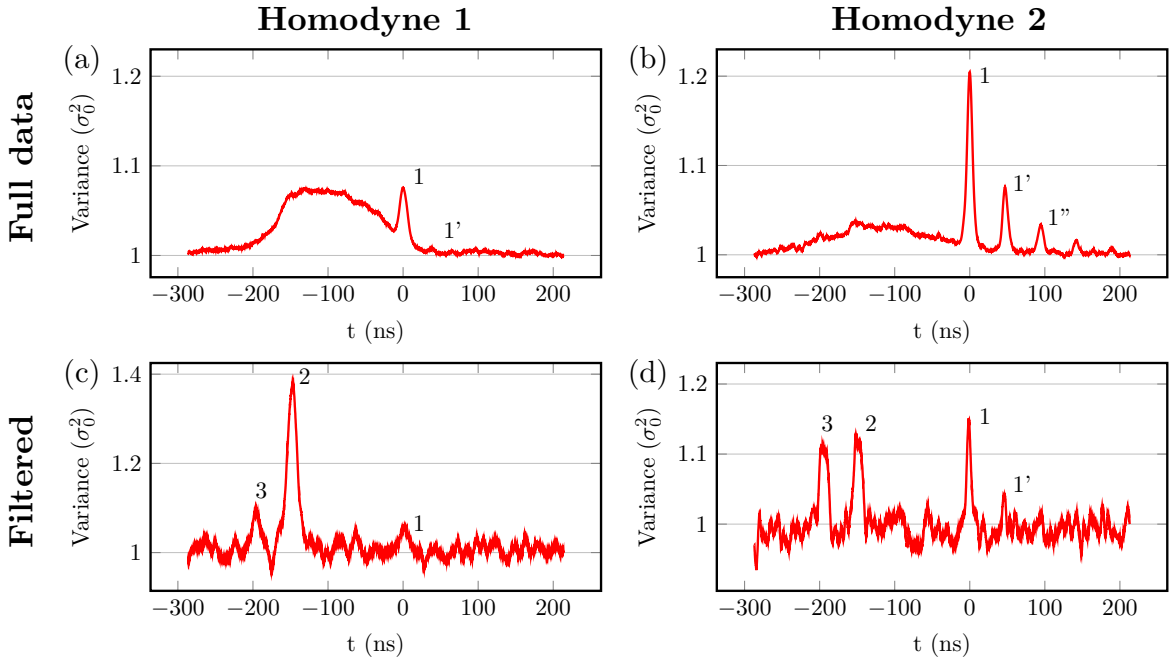

Figure 7.13: **Time filtering**. Variance of quadratures at the ouput of OPO I and OPO II before and after time filtering on a subset of $8 \cdot 10^5$ samples taken in one afternoon. Peaks #1 and the associated delay line echoes $\#1^{(n)}$ are due to the temporary setup with only two detectors and should disappear in the final protocol. Figure (a) and (b): Before filtering, the generation of single-photons and hybrid entanglement could have happened at any negative time starting from −200ns. As a result the variance is increased from vacuum but averaged over all possible times. Figures (c) and (d): After filtering. Peak #3: heralding of single photon. Peak #2: Hybrid entanglement created and echo of the single photon on the DV mode. Homodyne conditioning on peak #2 on the DV mode will complete the teleportation protocol.

same probability of completing the Bell measurement at time $t_3 = 0$ and of having an independent single-photon generation at that time. This is due exclusively to the use of a single detector for events t_1 and t_3 and will be solved with the setup using 3 detectors. In the meantime we can add an homodyne condtioning operation on this peak, *i.e.* condition on zero to remove the inappropriate events. With the number of measurements we currently have, this is not yet possible.

We therefore observe the expected features of a successful teleportation protocol, with some issues that are due to our temporary setup. What is left is homodyne conditioning on peak #3 of figure (d) to complete the Bell measurement. At the current stage, we need to acquire more data before performing that last step. Applying a suitable filtering window $\Delta\tau = 5$ ns, we have only about 500 events before the final homodyne conditioning. Overall these results are encouraging and will be very useful to choose the experimental parameters for the future experiment with three detectors.

3.5 Outlook: Qubit Quantum teleportation

Only one change to the setup has to be realized to perform qubit QT: remote state preparation of the input qubit. This means locking the homodyne phase at the desired qubit

relative phase and then see the effect of different conditionings on peak #3 of figure 7.13, *i.e.* when preparing different input qubits. This protocol will be even more time consuming because of this additional conditioning and the necessity of testing several qubit phases. With our temporary system, it is out of reach but with the use of a third detector it may be achieved in the near future. In parallel to this study, we are also in the very early stages of the addition of a new type-II OPO. This would allow us to start from a polarization qubit and then perhaps aim for a fully deterministic and active protocol.

4 Conclusion

In this chapter, we have presented a protocol for hybrid quantum teleportation using the same initial resources to create the input state and perform teleportation. Key to this protocol is a delay line that is used to propagate the input state before performing the Bell measurement. We have described some of the key features of our experimental delay line and made a theoretical study of its effect on the protocol. Finally we presented some preliminary results in the context of entanglement swapping. We have shown that we are able to create the input DV∞DV entangled state and the behavior of the system is consistent with a successful protocol. The addition of a third detector should enable us to complete the experiment, which would represent a significant stepping stone towards the realization of scalable hybrid quantum networks.

Conclusion

In this work, we have presented new protocols following an hybrid continuous- and discrete-variable approach to quantum communication. We first reported on methods for the generation of high-purity single-mode non-Gaussian states such as single-photons and Schödinger cat states. To that end, we presented in details key experimental resources, including optical parametric oscillators with high escape efficiency and superconducting nanowire single-photon detectors. We reported in particular on the installation of a new cryo-cooler used to bring these detectors into the superconducting regime and on the quantum efficiency characterization we performed. This study proved the highly-efficient nature of these detectors as we measured more than 90% system detection efficiency in the best cases.

We then presented the protocol used for the generation of hybrid entanglement of light. This resource, that links continuous- and discrete-variable encodings, opens the possibility of realizing quantum networks joining parties using dissimilar systems. It is with that mindset that we then explored a number of novel protocols exploiting hybrid entanglement. The first we reported on was the remote preparation of arbitrary CV-qubits by performing homodyne measurements on the DV mode of hybrid entanglement [68]. This first hybrid protocol having illustrated the usefulness of our entangled resource for quantum communication, we then tested its non-local features in order to evaluate its potential for either fully or one-sided device independent protocols. We reported first on a study of the loss-requirements for the experimental measurement of a Bell inequality violation. In this study, we considered a number of strategies in the particular framework of the CHSH inequality. We find that the demonstration is experimentally very challenging but may be accessible with a change of encoding on the DV mode, *i.e.* through the implementation of a polarization-based hybrid entangled state. From there, we turned to the intermediate challenge of Einstein-Podolsky-Rosen steering. We report first on the use of semi-definite-programming tools for the search of optimal steering inequalities for the hybrid resource. We then implemented the steering test using homodyne conditioning on the DV mode to steer the CV mode into an assemblage of 12 different states. We find that the influence measured cannot be explained by local models and we violate an optimal steering inequality by more than five standard-deviations [99].

Finally, in the last part of this manuscript, we reported on the current progress made towards the realization of hybrid quantum teleportation from DV to CV encoding. As the hybrid approach increases the range of accessible encodings, we first presented the protocols of qubit quantum teleportation and entanglement swapping and outlined the consequences of using different encodings in that context. We also reported on a new method for the implementation of a Bell measurement that combines single-photon subtraction and homodyne conditioning. The features of the method were presented and we find that the demonstration of quantum teleportation should be feasible with our system. The last chapter addresses the current implementation and gives preliminary results for entanglement swapping. We pre-

sented the experimental protocol in details and the delay line used in for the generation of the input state and hybrid entanglement in sequence with the same resources. Our preliminary results give us confidence in the future success of the experiment. Some adjustments such as the addition of a third detectors will make its implementation more efficient and of greater quality.

Perspectives

The short term perspective for the experiment is the realization of hybrid quantum teleportation in the ideal case. This will require finalizing the installation of the cryo-cooler which will enable us to use three detectors simultaneously and should dramatically increase the experiment's count rate and quality. In the longer term, we are currently working on the installation of a third optical parametric oscillator. This is in the hopes of implementing polarization-based hybrid entanglement following the protocol presented in [167]. This would open a number of new possibilities, as it would allow the implementation of a fully deterministic and active teleportation protocol from CV to DV. This demonstration would be facilitated as well by the addition of a local subtraction at the exit of OPO-I as we have done in the past [31, 32]. This would enable us to use the encoding $\{\hat{a}\hat{S}\left|0\right\rangle, \hat{a}^2\hat{S}\left|0\right\rangle\}$ on the CV mode which is close, up to a Hadamard gate, to the ideal CV encoding $\{\left|\alpha\right\rangle, \left|-\alpha\right\rangle\}$.

The addition of the delay line opens as well a number of possibilities, notably the exploration of time-bin encoding. A first implementation could be an adaptation of the protocol of entanglement swapping, starting with two hybrid DV∞CV entangled states, that would enable us to realize time-bin entanglement of the nature $\left|cat_+\right\rangle_t \left|cat_-\right\rangle_{t'} + \left|cat_-\right\rangle_t \left|cat_+\right\rangle_{t'}$. This new class of protocols may be suited as well for the realization of new non-locality tests.

Another general direction to pursue would be the realization of verified protocols. These combine in the same experiments quantum information protocols, such as quantum key distribution [80] or quantum computation [168, 169], with non-locality tests in order to verify that the operations have been performed by untrusted parties. This principle may be for example applied to our system, thus allowing us to perform verified quantum teleportation.

Bibliography

[1] E. Schrödinger. Die gegenwärtige Situation in der Quantenmechanik. *Naturwissenschaften*, 23(50):844–849, Dec. 1935. ISSN 1432-1904. doi: 10.1007/BF01491987. URL https://doi.org/10.1007/BF01491987. [Cited on pages v and 16.]

[2] A. Einstein, B. Podolsky, and N. Rosen. Can Quantum-Mechanical Description of Physical Reality Be Considered Complete? *Phys. Rev.*, 47(10):777–780, May 1935. doi: 10.1103/PhysRev.47.777. URL https://link.aps.org/doi/10.1103/PhysRev.47.777. [Cited on pages v, 18, 71, and 83.]

[3] J. S. Bell. On the Einstein Podolsky Rosen paradox. *Physics Physique Fizika*, 1(3): 195–200, Nov. 1964. doi: 10.1103/PhysicsPhysiqueFizika.1.195. URL https://link.aps.org/doi/10.1103/PhysicsPhysiqueFizika.1.195. [Cited on pages v and 71.]

[4] S. J. Freedman and J. F. Clauser. Experimental Test of Local Hidden-Variable Theories. *Phys. Rev. Lett.*, 28(14):938–941, Apr. 1972. doi: 10.1103/PhysRevLett.28.938. URL https://link.aps.org/doi/10.1103/PhysRevLett.28.938. [Cited on pages v and 71.]

[5] A. Aspect, J. Dalibard, and G. Roger. Experimental Test of Bell's Inequalities Using Time-Varying Analyzers. *Phys. Rev. Lett.*, 49(25):1804–1807, Dec. 1982. doi: 10.1103/PhysRevLett.49.1804. URL https://link.aps.org/doi/10.1103/PhysRevLett.49.1804. [Cited on pages v and 71.]

[6] L. K. Shalm, E. Meyer-Scott, B. G. Christensen, et al. Strong Loophole-Free Test of Local Realism. *Phys. Rev. Lett.*, 115(25):250402, Dec. 2015. doi: 10.1103/PhysRevLett.115.250402. URL https://link.aps.org/doi/10.1103/PhysRevLett.115.250402. [Cited on pages v and 71.]

[7] B. Hensen, H. Bernien, A. E. Dréau, et al. Loophole-free Bell inequality violation using electron spins separated by 1.3 kilometres. *Nature*, 526(7575):682–686, Oct. 2015. ISSN 1476-4687. doi: 10.1038/nature15759. URL https://www.nature.com/articles/nature15759. [Cited on pages v and 71.]

[8] M. Giustina, M. A. M. Versteegh, S. Wengerowsky, et al. Significant-Loophole-Free Test of Bell's Theorem with Entangled Photons. *Phys. Rev. Lett.*, 115(25):250401, Dec. 2015. doi: 10.1103/PhysRevLett.115.250401. URL https://link.aps.org/doi/10.1103/PhysRevLett.115.250401. [Cited on pages v and 71.]

[9] M. A. Nielsen and I. L. Chuang. *Quantum Computation and Quantum Information: 10th Anniversary Edition*. Cambridge University Press, New York, NY, USA, 10th edition, 2011. ISBN 978-1-107-00217-3. [Cited on pages vi and 10.]

[10] P. Shor. Polynomial-Time Algorithms for Prime Factorization and Discrete Logarithms on a Quantum Computer. *SIAM J. Comput.*, 26(5):1484–1509, Oct. 1997. ISSN 0097-5397. doi: 10.1137/S0097539795293172. URL https://epubs.siam.org/doi/10.1137/S0097539795293172. [Cited on page vi.]

[11] L. K. Grover. A Fast Quantum Mechanical Algorithm for Database Search. In *Proceedings of the Twenty-eighth Annual ACM Symposium on Theory of Computing*, STOC '96, pages 212–219, New York, NY, USA, 1996. ACM. ISBN 978-0-89791-785-8. doi: 10.1145/237814.237866. URL http://doi.acm.org/10.1145/237814.237866. [Cited on page vi.]

[12] R. L. Rivest, A. Shamir, and L. Adleman. A Method for Obtaining Digital Signatures and Public-key Cryptosystems. *Commun. ACM*, 21(2):120–126, Feb. 1978. ISSN 0001-0782. doi: 10.1145/359340.359342. URL http://doi.acm.org/10.1145/359340.359342. [Cited on page vi.]

[13] C. H. Bennett and G. Brassard. Quantum cryptography: Public key distribution and coin tossing. *Theoretical Computer Science*, 560:7–11, Dec. 2014. ISSN 0304-3975. doi: 10.1016/j.tcs.2014.05.025. URL http://www.sciencedirect.com/science/article/pii/S0304397514004241. [Cited on pages vi and 72.]

[14] N. Gisin and R. Thew. Quantum communication. *Nature Photonics*, 1(3):165–171, Mar. 2007. ISSN 1749-4893. doi: 10.1038/nphoton.2007.22. URL https://www.nature.com/articles/nphoton.2007.22. [Cited on page vi.]

[15] Y. Tamura, H. Sakuma, K. Morita, et al. The First 0.14-dB/km Loss Optical Fiber and its Impact on Submarine Transmission. *Journal of Lightwave Technology*, 36(1):44–49, Jan. 2018. ISSN 0733-8724, 1558-2213. doi: 10.1109/JLT.2018.2796647. URL http://ieeexplore.ieee.org/document/8267035/. [Cited on page vi.]

[16] C. H. Bennett, G. Brassard, C. Crépeau, R. Jozsa, A. Peres, and W. K. Wootters. Teleporting an unknown quantum state via dual classical and Einstein-Podolsky-Rosen channels. *Phys. Rev. Lett.*, 70(13):1895–1899, Mar. 1993. doi: 10.1103/PhysRevLett.70.1895. URL https://link.aps.org/doi/10.1103/PhysRevLett.70.1895. [Cited on pages vi, 62, and 112.]

[17] S. Pirandola, J. Eisert, C. Weedbrook, A. Furusawa, and S. L. Braunstein. Advances in quantum teleportation. *Nature Photonics*, 9(10):641–652, Oct. 2015. ISSN 1749-4893. doi: 10.1038/nphoton.2015.154. URL https://www.nature.com/articles/nphoton.2015.154. [Cited on page vi.]

[18] D. Bouwmeester, J.-W. Pan, K. Mattle, M. Eibl, H. Weinfurter, and A. Zeilinger. Experimental quantum teleportation. *Nature*, 390(6660):575–579, Dec. 1997. ISSN 1476-4687. doi: 10.1038/37539. URL https://www.nature.com/articles/37539. [Cited on pages vii and 118.]

[19] J.-G. Ren, P. Xu, H.-L. Yong, et al. Ground-to-satellite quantum teleportation. *Nature*, 549(7670):70–73, Sept. 2017. ISSN 1476-4687. doi: 10.1038/nature23675. URL https://www.nature.com/articles/nature23675. [Cited on pages vii and 118.]

[20] H. J. Kimble. The quantum internet. *Nature*, 453:1023–1030, June 2008. ISSN 1476-4687. doi: 10.1038/nature07127. URL `https://www.nature.com/articles/nature07127`. [Cited on pages vii and 112.]

[21] P. Kok, W. J. Munro, K. Nemoto, T. C. Ralph, J. P. Dowling, and G. J. Milburn. Linear optical quantum computing with photonic qubits. *Reviews of Modern Physics*, 79(1): 135–174, Jan. 2007. ISSN 0034-6861, 1539-0756. doi: 10.1103/RevModPhys.79.135. URL `https://link.aps.org/doi/10.1103/RevModPhys.79.135`. [Cited on page vii.]

[22] S. L. Braunstein and P. van Loock. Quantum information with continuous variables. *Quantum information with continuous variables*, 77(2):65, 2005. [Cited on page vii.]

[23] P. van Loock. Optical hybrid approaches to quantum information. *Laser & Photon. Rev.*, 5(2):167–200, Mar. 2011. ISSN 1863-8899. doi: 10.1002/lpor.201000005. URL `http://onlinelibrary.wiley.com/doi/10.1002/lpor.201000005/abstract`. [Cited on page vii.]

[24] U. L. Andersen, J. S. Neergaard-Nielsen, P. van Loock, and A. Furusawa. Hybrid discrete- and continuous-variable quantum information. *Nature Physics*, 11(9):713–719, Sept. 2015. ISSN 1745-2481. doi: 10.1038/nphys3410. URL `https://www.nature.com/articles/nphys3410`. [Cited on pages vii and 56.]

[25] U. L. Andersen and T. C. Ralph. High-Fidelity Teleportation of Continuous-Variable Quantum States Using Delocalized Single Photons. *Phys. Rev. Lett.*, 111(5):050504, Aug. 2013. doi: 10.1103/PhysRevLett.111.050504. URL `https://link.aps.org/doi/10.1103/PhysRevLett.111.050504`. [Cited on pages vii and 56.]

[26] S. Takeda, T. Mizuta, M. Fuwa, P. van Loock, and A. Furusawa. Deterministic quantum teleportation of photonic quantum bits by a hybrid technique. *Nature*, 500(7462):315–318, Aug. 2013. ISSN 1476-4687. doi: 10.1038/nature12366. URL `https://www.nature.com/articles/nature12366`. [Cited on pages vii, 56, and 118.]

[27] O. Morin, J.-D. Bancal, M. Ho, et al. Witnessing Trustworthy Single-Photon Entanglement with Local Homodyne Measurements. *Phys. Rev. Lett.*, 110(13):130401, Mar. 2013. doi: 10.1103/PhysRevLett.110.130401. URL `https://link.aps.org/doi/10.1103/PhysRevLett.110.130401`. [Cited on pages vii and 56.]

[28] H. Jeong, A. Zavatta, M. Kang, et al. Generation of hybrid entanglement of light. *Nature Photonics*, 8(7):564–569, July 2014. ISSN 1749-4885, 1749-4893. doi: 10.1038/nphoton.2014.136. URL `http://www.nature.com/articles/nphoton.2014.136`. [Cited on page vii.]

[29] O. Morin, K. Huang, J. Liu, H. Le Jeannic, C. Fabre, and J. Laurat. Remote creation of hybrid entanglement between particle-like and wave-like optical qubits. *Nat Photon*, 8(7):570–574, July 2014. ISSN 1749-4885. doi: 10.1038/nphoton.2014.137. URL `http://www.nature.com/nphoton/journal/v8/n7/abs/nphoton.2014.137.html`. [Cited on pages vii, 55, 57, and 60.]

[30] O. Morin. *Non-Gaussian states and measurements for quantum information*. Thesis, Université Pierre et Marie Curie - Paris VI, Dec. 2013. URL `https://tel.archives-ouvertes.fr/tel-01066655/document`. [Cited on pages viii, 5, 11, 20, 21, 27, 31, and 33.]

[31] K. Huang. *Optical hybrid architectures for quantum information processing*. Thesis, Université Pierre et Marie Curie - Paris VI, 2015. URL https://tel.archives-ouvertes.fr/tel-01661603v1. [Cited on pages viii and 156.]

[32] H. Le Jeannic. *Optical Hybrid Quantum Information processing*. Thesis, Université Pierre et Marie Curie - Paris VI, Dec. 2016. URL https://tel.archives-ouvertes.fr/tel-01665496/document. [Cited on pages viii, 33, 36, and 156.]

[33] A. Ketterer. *Modular variables in quantum information*. Thesis, Université Paris 7, Sorbonne Paris Cité, Oct. 2016. URL https://tel.archives-ouvertes.fr/tel-01502539/document. [Cited on pages viii, 75, and 77.]

[34] C. Cohen-Tannoudji, J. Dupont-Roc, and G. Grynberg. *Photons et atomes, 1. introduction à l'électrodynamique quantique*. Savoirs actuels. Ed. du Centre national de la recherche scientifique (CNRS), Paris, 1987. ISBN 978-2-7296-0156-0. [Cited on page 4.]

[35] G. Grynberg, A. Aspect, C. Fabre, and C. Cohen-Tannoudji. *Introduction to Quantum Optics: from the semi-classical approach to quantized light*. Cambridge university press edition, Sept. 2010. ISBN 978-0-511-77826-1. doi: 10.1017/CBO9780511778261. URL /core/books/introduction-to-quantum-optics/F45DCE785DC8226D4156EC15CAD5FA9A. [Cited on page 4.]

[36] G. B. Arfken, H. J. Weber, and F. E. Harris. *Mathematical Methods for Physicists: A Comprehensive Guide*. Academic Press, 2013. ISBN 978-0-12-384654-9. [Cited on page 6.]

[37] U. Fano. Description of States in Quantum Mechanics by Density Matrix and Operator Techniques. *Rev. Mod. Phys.*, 29(1):74–93, Jan. 1957. doi: 10.1103/RevModPhys.29.74. URL https://link.aps.org/doi/10.1103/RevModPhys.29.74. [Cited on page 7.]

[38] E. Wigner. On the Quantum Correction For Thermodynamic Equilibrium. *Phys. Rev.*, 40(5):749–759, June 1932. doi: 10.1103/PhysRev.40.749. URL https://link.aps.org/doi/10.1103/PhysRev.40.749. [Cited on page 7.]

[39] R. Jozsa. Fidelity for Mixed Quantum States. *Journal of Modern Optics*, 41(12):2315–2323, Dec. 1994. ISSN 0950-0340. doi: 10.1080/09500349414552171. URL https://doi.org/10.1080/09500349414552171. [Cited on page 8.]

[40] S. Haroche and J.-M. Raimond. *Exploring the Quantum: Atoms, Cavities, and Photons*. OUP Oxford, Aug. 2006. ISBN 978-0-19-850914-1. Google-Books-ID: ynwSDAAAQBAJ. [Cited on page 9.]

[41] A. Ourjoumtsev. *Etude théorique et expérimentale de superpositions quantiques cohérentes et d'états intriqués non-gaussiens de la lumière*. Thesis, Paris 11, Jan. 2007. URL http://www.theses.fr/2007PA112217. [Cited on page 17.]

[42] R. L. Hudson. When is the wigner quasi-probability density non-negative? *Reports on Mathematical Physics*, 6(2):249–252, Oct. 1974. ISSN 0034-4877. doi: 10.1016/0034-4877(74)90007-X. URL http://www.sciencedirect.com/science/article/pii/003448777490007X. [Cited on page 17.]

[43] A. I. Lvovsky. Iterative maximum-likelihood reconstruction in quantum homodyne tomography. *J. Opt. B: Quantum Semiclass. Opt.*, 6(6):S556, 2004. ISSN 1464-4266. doi: 10.1088/1464-4266/6/6/014. URL http://stacks.iop.org/1464-4266/6/i=6/a=014. [Cited on page 20.]

[44] P. Faist and R. Renner. Practical and Reliable Error Bars in Quantum Tomography. *Phys. Rev. Lett.*, 117(1):010404, July 2016. doi: 10.1103/PhysRevLett.117.010404. URL https://link.aps.org/doi/10.1103/PhysRevLett.117.010404. [Cited on pages 22, 93, 96, 97, 98, 103, and 106.]

[45] A. I. Lvovsky. Squeezed light. *arXiv:1401.4118 [physics, physics:quant-ph]*, Jan. 2014. URL http://arxiv.org/abs/1401.4118. arXiv: 1401.4118. [Cited on page 23.]

[46] J. Aasi, J. Abadie, B. P. Abbott, et al. Enhanced sensitivity of the LIGO gravitational wave detector by using squeezed states of light. *Nature Photonics*, 7(8):613–619, Aug. 2013. ISSN 1749-4893. doi: 10.1038/nphoton.2013.177. URL https://www.nature.com/articles/nphoton.2013.177. [Cited on page 23.]

[47] O. Morin, J. Liu, K. Huang, F. Barbosa, C. Fabre, and J. Laurat. Quantum State Engineering of Light with Continuous-wave Optical Parametric Oscillators. *JoVE (Journal of Visualized Experiments)*, (87):e51224, May 2014. ISSN 1940-087X. doi: 10.3791/51224. URL https://www.jove.com/video/51224/quantum-state-engineering-light-with-continuous-wave-optical. [Cited on page 27.]

[48] C. K. Hong and L. Mandel. Experimental realization of a localized one-photon state. *Physical Review Letters*, 56(1):58–60, Jan. 1986. ISSN 0031-9007. doi: 10.1103/PhysRevLett.56.58. URL https://link.aps.org/doi/10.1103/PhysRevLett.56.58. [Cited on page 29.]

[49] A. I. Lvovsky, H. Hansen, T. Aichele, O. Benson, J. Mlynek, and S. Schiller. Quantum State Reconstruction of the Single-Photon Fock State. *Physical Review Letters*, 87(5), July 2001. ISSN 0031-9007, 1079-7114. doi: 10.1103/PhysRevLett.87.050402. URL https://link.aps.org/doi/10.1103/PhysRevLett.87.050402. [Cited on page 29.]

[50] A. Zavatta, S. Viciani, and M. Bellini. Tomographic reconstruction of the single-photon Fock state by high-frequency homodyne detection. *Physical Review A*, 70(5), Nov. 2004. ISSN 1050-2947, 1094-1622. doi: 10.1103/PhysRevA.70.053821. URL https://link.aps.org/doi/10.1103/PhysRevA.70.053821. [Cited on page 29.]

[51] A. Ourjoumtsev, R. Tualle-Brouri, and P. Grangier. Quantum Homodyne Tomography of a Two-Photon Fock State. *Physical Review Letters*, 96(21), June 2006. ISSN 0031-9007, 1079-7114. doi: 10.1103/PhysRevLett.96.213601. URL https://link.aps.org/doi/10.1103/PhysRevLett.96.213601. [Cited on page 29.]

[52] Bahaa E. A. Saleh and M. C. Teich. *Fundamentals of Photonics, 2nd Edition*. Wiley, 2001. ISBN 978-0-471-35832-9. URL https://www.wiley.com/en-fr/Fundamentals+of+Photonics%2C+2nd+Edition-p-9780471358329. [Cited on page 30.]

[53] A. E. B. Nielsen and K. Mølmer. Single-photon-state generation from a continuous-wave nondegenerate optical parametric oscillator. *Phys. Rev. A*, 75(2):023806, Feb.

2007. doi: 10.1103/PhysRevA.75.023806. URL https://link.aps.org/doi/10.1103/PhysRevA.75.023806. [Cited on page 31.]

[54] O. Morin, C. Fabre, and J. Laurat. Experimentally Accessing the Optimal Temporal Mode of Traveling Quantum Light States. *Phys. Rev. Lett.*, 111(21):213602, Nov. 2013. doi: 10.1103/PhysRevLett.111.213602. URL https://link.aps.org/doi/10.1103/PhysRevLett.111.213602. [Cited on pages 31 and 35.]

[55] D. A. Shaddock, M. B. Gray, and D. E. McClelland. Frequency locking a laser to an optical cavity by use of spatial mode interference. *Opt. Lett., OL*, 24(21):1499–1501, Nov. 1999. ISSN 1539-4794. doi: 10.1364/OL.24.001499. URL https://www.osapublishing.org/ol/abstract.cfm?uri=ol-24-21-1499. [Cited on page 31.]

[56] R. W. P. Drever, J. L. Hall, F. V. Kowalski, J. Hough, G. M. Ford, A. J. Munley, and H. Ward. Laser phase and frequency stabilization using an optical resonator. *Appl. Phys. B*, 31(2):97–105, June 1983. ISSN 1432-0649. doi: 10.1007/BF00702605. URL https://doi.org/10.1007/BF00702605. [Cited on page 32.]

[57] K. Huang, H. Le Jeannic, J. Ruaudel, O. Morin, and J. Laurat. Microcontroller-based locking in optics experiments. *Review of Scientific Instruments*, 85(12):123112, Dec. 2014. ISSN 0034-6748. doi: 10.1063/1.4903869. URL https://aip.scitation.org/doi/10.1063/1.4903869. [Cited on page 33.]

[58] H. L. Jeannic, V. B. Verma, A. Cavaillès, et al. High-efficiency WSi superconducting nanowire single-photon detectors for quantum state engineering in the near infrared. *Opt. Lett., OL*, 41(22):5341–5344, Nov. 2016. ISSN 1539-4794. doi: 10.1364/OL.41.005341. URL https://www.osapublishing.org/ol/abstract.cfm?uri=ol-41-22-5341. [Cited on pages 36, 41, and 45.]

[59] K.-H. Luo, H. Herrmann, S. Krapick, et al. Direct generation of genuine single-longitudinal-mode narrowband photon pairs. *New J. Phys.*, 17(7):073039, 2015. ISSN 1367-2630. doi: 10.1088/1367-2630/17/7/073039. URL http://stacks.iop.org/1367-2630/17/i=7/a=073039. [Cited on page 36.]

[60] M. Bouillard, G. Boucher, J. F. Ortas, B. Kanseri, and R. Tualle-Brouri. High production rate of single-photon and two-photon Fock states for quantum state engineering. *arXiv:1807.05701 [quant-ph]*, July 2018. URL http://arxiv.org/abs/1807.05701. arXiv: 1807.05701. [Cited on page 37.]

[61] A. Ourjoumtsev, R. Tualle-Brouri, J. Laurat, and P. Grangier. Generating Optical Schrödinger Kittens for Quantum Information Processing. *Science*, 312(5770):83–86, Apr. 2006. ISSN 0036-8075, 1095-9203. doi: 10.1126/science.1122858. URL http://science.sciencemag.org/content/312/5770/83. [Cited on page 38.]

[62] J. S. Neergaard-Nielsen, B. M. Nielsen, C. Hettich, K. Mølmer, and E. S. Polzik. Generation of a Superposition of Odd Photon Number States for Quantum Information Networks. *Physical Review Letters*, 97(8), Aug. 2006. ISSN 0031-9007, 1079-7114. doi: 10.1103/PhysRevLett.97.083604. URL https://link.aps.org/doi/10.1103/PhysRevLett.97.083604. [Cited on page 38.]

[63] M. Dakna, T. Anhut, T. Opatrný, L. Knöll, and D.-G. Welsch. Generating Schr\"odinger-cat-like states by means of conditional measurements on a beam splitter. *Phys. Rev. A*, 55(4):3184–3194, Apr. 1997. doi: 10.1103/PhysRevA.55.3184. URL https://link.aps.org/doi/10.1103/PhysRevA.55.3184. [Cited on page 38.]

[64] G. N. Gol'tsman, O. Okunev, G. Chulkova, et al. Picosecond superconducting single-photon optical detector. *Applied Physics Letters*, 79(6):705, Aug. 2001. ISSN 0003-6951. doi: 10.1063/1.1388868. URL https://aip.scitation.org/doi/10.1063/1.1388868. [Cited on page 42.]

[65] F. Marsili, F. Najafi, E. Dauler, et al. Single-Photon Detectors Based on Ultranarrow Superconducting Nanowires. *Nano Lett.*, 11(5):2048–2053, May 2011. ISSN 1530-6984. doi: 10.1021/nl2005143. URL https://doi.org/10.1021/nl2005143. [Cited on page 43.]

[66] F. Marsili, V. B. Verma, J. A. Stern, et al. Detecting single infrared photons with 93% system efficiency. *Nature Photonics*, 7(3):210–214, Mar. 2013. ISSN 1749-4893. doi: 10.1038/nphoton.2013.13. URL https://www.nature.com/articles/nphoton.2013.13. [Cited on page 43.]

[67] W. E. Gifford. The Gifford-McMahon Cycle. In K. D. Timmerhaus, editor, *Advances in Cryogenic Engineering*, Advances in Cryogenic Engineering, pages 152–159. Springer US, 1966. ISBN 978-1-4757-0522-5. [Cited on page 47.]

[68] H. L. Jeannic, A. Cavaillès, J. Raskop, K. Huang, and J. Laurat. Remote preparation of continuous-variable qubits using loss-tolerant hybrid entanglement of light. *Optica, OPTICA*, 5(8):1012–1015, Aug. 2018. ISSN 2334-2536. doi: 10.1364/OPTICA.5.001012. URL https://www.osapublishing.org/optica/abstract.cfm?uri=optica-5-8-1012. [Cited on pages 55, 62, and 155.]

[69] P. van Loock and A. Furusawa. *Quantum Teleportation and Entanglement: A Hybrid Approach to Optical Quantum Information Processing*. 2011. ISBN 978-3-527-40930-3. URL https://www.wiley.com/en-fr/Quantum+Teleportation+and+Entanglement%3A+A+Hybrid+Approach+to+Optical+Quantum+Information+Processing-p-9783527409303. [Cited on page 56.]

[70] K. Park and H. Jeong. Entangled coherent states versus entangled photon pairs for practical quantum-information processing. *Phys. Rev. A*, 82(6):062325, Dec. 2010. doi: 10.1103/PhysRevA.82.062325. URL https://link.aps.org/doi/10.1103/PhysRevA.82.062325. [Cited on page 56.]

[71] T. C. Ralph, A. Gilchrist, G. J. Milburn, W. J. Munro, and S. Glancy. Quantum computation with optical coherent states. *Phys. Rev. A*, 68(4):042319, Oct. 2003. doi: 10.1103/PhysRevA.68.042319. URL https://link.aps.org/doi/10.1103/PhysRevA.68.042319. [Cited on page 56.]

[72] J. Preskill. Fault-tolerant quantum computation. Dec. 1997. URL https://arxiv.org/abs/quant-ph/9712048. [Cited on page 56.]

[73] A. P. Lund, T. C. Ralph, and H. L. Haselgrove. Fault-Tolerant Linear Optical Quantum Computing with Small-Amplitude Coherent States. *Phys. Rev. Lett.*, 100(3):030503,

Jan. 2008. doi: 10.1103/PhysRevLett.100.030503. URL https://link.aps.org/doi/10.1103/PhysRevLett.100.030503. [Cited on page 56.]

[74] A. Ourjoumtsev, A. Dantan, R. Tualle-Brouri, and P. Grangier. Increasing Entanglement between Gaussian States by Coherent Photon Subtraction. *Phys. Rev. Lett.*, 98(3):030502, Jan. 2007. doi: 10.1103/PhysRevLett.98.030502. URL https://link.aps.org/doi/10.1103/PhysRevLett.98.030502. [Cited on page 56.]

[75] H. Takahashi, J. S. Neergaard-Nielsen, M. Takeuchi, M. Takeoka, K. Hayasaka, A. Furusawa, and M. Sasaki. Entanglement distillation from Gaussian input states. *Nature Photonics*, 4(3):178–181, Mar. 2010. ISSN 1749-4893. doi: 10.1038/nphoton.2010.1. URL https://www.nature.com/articles/nphoton.2010.1. [Cited on page 56.]

[76] A. E. Ulanov, I. A. Fedorov, A. A. Pushkina, Y. V. Kurochkin, T. C. Ralph, and A. I. Lvovsky. Undoing the effect of loss on quantum entanglement. *Nature Photonics*, 9(11):764–768, Nov. 2015. ISSN 1749-4893. doi: 10.1038/nphoton.2015.195. URL https://www.nature.com/articles/nphoton.2015.195. [Cited on page 56.]

[77] S.-W. Lee and H. Jeong. Near-deterministic quantum teleportation and resource-efficient quantum computation using linear optics and hybrid qubits. *Phys. Rev. A*, 87(2):022326, Feb. 2013. doi: 10.1103/PhysRevA.87.022326. URL https://link.aps.org/doi/10.1103/PhysRevA.87.022326. [Cited on pages 56 and 58.]

[78] N. C. Menicucci, P. van Loock, M. Gu, C. Weedbrook, T. C. Ralph, and M. A. Nielsen. Universal Quantum Computation with Continuous-Variable Cluster States. *Phys. Rev. Lett.*, 97(11):110501, Sept. 2006. doi: 10.1103/PhysRevLett.97.110501. URL https://link.aps.org/doi/10.1103/PhysRevLett.97.110501. [Cited on page 56.]

[79] T. P. Spiller, K. Nemoto, S. L. Braunstein, W. J. Munro, P. v. Loock, and G. J. Milburn. Quantum computation by communication. *New J. Phys.*, 8(2):30, 2006. ISSN 1367-2630. doi: 10.1088/1367-2630/8/2/030. URL http://stacks.iop.org/1367-2630/8/i=2/a=030. [Cited on page 56.]

[80] J. Rigas, O. Gühne, and N. Lütkenhaus. Entanglement verification for quantum-key-distribution systems with an underlying bipartite qubit-mode structure. *Phys. Rev. A*, 73(1):012341, Jan. 2006. doi: 10.1103/PhysRevA.73.012341. URL https://link.aps.org/doi/10.1103/PhysRevA.73.012341. [Cited on pages 56 and 156.]

[81] C. Wittmann, J. Fürst, C. Wiechers, D. Elser, H. Häseler, N. Lütkenhaus, and G. Leuchs. Witnessing effective entanglement over a 2 km fiber channel. *Opt. Express, OE*, 18(5):4499–4509, Mar. 2010. ISSN 1094-4087. doi: 10.1364/OE.18.004499. URL https://www.osapublishing.org/oe/abstract.cfm?uri=oe-18-5-4499. [Cited on page 56.]

[82] K. Kreis and P. van Loock. Classifying, quantifying, and witnessing qudit-qumode hybrid entanglement. *Phys. Rev. A*, 85(3):032307, Mar. 2012. doi: 10.1103/PhysRevA.85.032307. URL https://link.aps.org/doi/10.1103/PhysRevA.85.032307. [Cited on page 56.]

[83] H. Kim, S.-W. Lee, and H. Jeong. Two different types of optical hybrid qubits for teleportation in a lossy environment. *Quantum Inf Process*, 15(11):4729–4746, Nov.

2016. ISSN 1573-1332. doi: 10.1007/s11128-016-1408-7. URL https://doi.org/10.1007/s11128-016-1408-7. [Cited on pages 58, 116, and 118.]

[84] H.-K. Lo. Classical-communication cost in distributed quantum-information processing: A generalization of quantum-communication complexity. *Phys. Rev. A*, 62(1):012313, June 2000. doi: 10.1103/PhysRevA.62.012313. URL https://link.aps.org/doi/10.1103/PhysRevA.62.012313. [Cited on page 62.]

[85] A. K. Pati. Minimum classical bit for remote preparation and measurement of a qubit. *Phys. Rev. A*, 63(1):014302, Dec. 2000. doi: 10.1103/PhysRevA.63.014302. URL https://link.aps.org/doi/10.1103/PhysRevA.63.014302. [Cited on page 62.]

[86] C. H. Bennett, D. P. DiVincenzo, P. W. Shor, J. A. Smolin, B. M. Terhal, and W. K. Wootters. Remote State Preparation. *Phys. Rev. Lett.*, 87(7):077902, July 2001. doi: 10.1103/PhysRevLett.87.077902. URL https://link.aps.org/doi/10.1103/PhysRevLett.87.077902. [Cited on page 62.]

[87] D. W. Berry and B. C. Sanders. Optimal Remote State Preparation. *Phys. Rev. Lett.*, 90(5):057901, Feb. 2003. doi: 10.1103/PhysRevLett.90.057901. URL https://link.aps.org/doi/10.1103/PhysRevLett.90.057901. [Cited on page 62.]

[88] J. L. O'Brien, A. Furusawa, and J. Vučković. Photonic quantum technologies. *Nature Photonics*, 3(12):687–695, Dec. 2009. ISSN 1749-4893. doi: 10.1038/nphoton.2009.229. URL https://www.nature.com/articles/nphoton.2009.229. [Cited on page 62.]

[89] N. A. Peters, J. T. Barreiro, M. E. Goggin, T.-C. Wei, and P. G. Kwiat. Remote State Preparation: Arbitrary Remote Control of Photon Polarization. *Phys. Rev. Lett.*, 94 (15):150502, Apr. 2005. doi: 10.1103/PhysRevLett.94.150502. URL https://link.aps.org/doi/10.1103/PhysRevLett.94.150502. [Cited on pages 62 and 63.]

[90] G.-Y. Xiang, J. Li, B. Yu, and G.-C. Guo. Remote preparation of mixed states via noisy entanglement. *Phys. Rev. A*, 72(1):012315, July 2005. doi: 10.1103/PhysRevA.72.012315. URL https://link.aps.org/doi/10.1103/PhysRevA.72.012315. [Cited on page 62.]

[91] W.-T. Liu, W. Wu, B.-Q. Ou, P.-X. Chen, C.-Z. Li, and J.-M. Yuan. Experimental remote preparation of arbitrary photon polarization states. *Phys. Rev. A*, 76(2):022308, Aug. 2007. doi: 10.1103/PhysRevA.76.022308. URL https://link.aps.org/doi/10.1103/PhysRevA.76.022308. [Cited on page 62.]

[92] S. A. Babichev, B. Brezger, and A. I. Lvovsky. Remote Preparation of a Single-Mode Photonic Qubit by Measuring Field Quadrature Noise. *Phys. Rev. Lett.*, 92(4):047903, Jan. 2004. doi: 10.1103/PhysRevLett.92.047903. URL https://link.aps.org/doi/10.1103/PhysRevLett.92.047903. [Cited on page 62.]

[93] M. G. A. Paris, M. Cola, and R. Bonifacio. Remote state preparation and teleportation in phase space. *J. Opt. B: Quantum Semiclass. Opt.*, 5(3):S360, 2003. ISSN 1464-4266. doi: 10.1088/1464-4266/5/3/370. URL http://stacks.iop.org/1464-4266/5/i=3/a=370. [Cited on pages 62 and 65.]

[94] J. Laurat, T. Coudreau, N. Treps, A. Maître, and C. Fabre. Conditional Preparation of a Quantum State in the Continuous Variable Regime: Generation of a sub-Poissonian State from Twin Beams. *Phys. Rev. Lett.*, 91(21):213601, Nov. 2003. doi: 10.1103/PhysRevLett.91.213601. URL https://link.aps.org/doi/10.1103/PhysRevLett.91.213601. [Cited on page 62.]

[95] Z. Kurucz, P. Adam, Z. Kis, and J. Janszky. Continuous variable remote state preparation. *Phys. Rev. A*, 72(5):052315, Nov. 2005. doi: 10.1103/PhysRevA.72.052315. URL https://link.aps.org/doi/10.1103/PhysRevA.72.052315. [Cited on page 62.]

[96] J. T. Barreiro, T.-C. Wei, and P. G. Kwiat. Remote Preparation of Single-Photon "Hybrid" Entangled and Vector-Polarization States. *Phys. Rev. Lett.*, 105(3):030407, July 2010. doi: 10.1103/PhysRevLett.105.030407. URL https://link.aps.org/doi/10.1103/PhysRevLett.105.030407. [Cited on page 62.]

[97] Y.-S. Ra, H.-T. Lim, and Y.-H. Kim. Remote preparation of three-photon entangled states via single-photon measurement. *Phys. Rev. A*, 94(4):042329, Oct. 2016. doi: 10.1103/PhysRevA.94.042329. URL https://link.aps.org/doi/10.1103/PhysRevA.94.042329. [Cited on page 62.]

[98] J. S. Neergaard-Nielsen, M. Takeuchi, K. Wakui, H. Takahashi, K. Hayasaka, M. Takeoka, and M. Sasaki. Optical Continuous-Variable Qubit. *Phys. Rev. Lett.*, 105 (5):053602, July 2010. doi: 10.1103/PhysRevLett.105.053602. URL https://link.aps.org/doi/10.1103/PhysRevLett.105.053602. [Cited on page 63.]

[99] A. Cavaillès, H. Le Jeannic, J. Raskop, et al. Demonstration of Einstein-Podolsky-Rosen Steering Using Hybrid Continuous- and Discrete-Variable Entanglement of Light. *Phys. Rev. Lett.*, 121(17):170403, Oct. 2018. doi: 10.1103/PhysRevLett.121.170403. URL https://link.aps.org/doi/10.1103/PhysRevLett.121.170403. [Cited on pages 69 and 155.]

[100] N. Brunner, D. Cavalcanti, S. Pironio, V. Scarani, and S. Wehner. Bell nonlocality. *Rev. Mod. Phys.*, 86(2):419–478, Apr. 2014. doi: 10.1103/RevModPhys.86.419. URL http://link.aps.org/doi/10.1103/RevModPhys.86.419. [Cited on pages 71 and 72.]

[101] J. F. Clauser, M. A. Horne, A. Shimony, and R. A. Holt. Proposed Experiment to Test Local Hidden-Variable Theories. *Phys. Rev. Lett.*, 23(15):880–884, Oct. 1969. doi: 10.1103/PhysRevLett.23.880. URL https://link.aps.org/doi/10.1103/PhysRevLett.23.880. [Cited on page 71.]

[102] V. Capasso, D. Fortunato, and F. Selleri. Sensitive observables of quantum mechanics. *Int J Theor Phys*, 7(5):319–326, Sept. 1973. ISSN 0020-7748, 1572-9575. doi: 10.1007/BF00669912. URL https://link.springer.com/article/10.1007/BF00669912. [Cited on page 72.]

[103] N. Gisin. Bell's inequality holds for all non-product states. *Physics Letters A*, 154 (5):201–202, Apr. 1991. ISSN 0375-9601. doi: 10.1016/0375-9601(91)90805-I. URL http://www.sciencedirect.com/science/article/pii/037596019190805I. [Cited on page 72.]

[104] D. Home and F. Selleri. Bell's theorem and the EPR paradox. *Riv. Nuovo Cim.*, 14 (9):1, Sept. 1991. ISSN 1826-9850. doi: 10.1007/BF02811227. URL https://link.springer.com/article/10.1007/BF02811227. [Cited on page 72.]

[105] R. F. Werner. Quantum states with Einstein-Podolsky-Rosen correlations admitting a hidden-variable model. *Phys. Rev. A*, 40(8):4277–4281, Oct. 1989. doi: 10.1103/PhysRevA.40.4277. URL https://link.aps.org/doi/10.1103/PhysRevA.40.4277. [Cited on page 72.]

[106] A. Peres. All the Bell Inequalities. *Foundations of Physics*, 29(4):589–614, Apr. 1999. ISSN 0015-9018, 1572-9516. doi: 10.1023/A:1018816310000. URL https://link.springer.com/article/10.1023/A:1018816310000. [Cited on page 72.]

[107] T. Moroder, O. Gittsovich, M. Huber, and O. Gühne. Steering Bound Entangled States: A Counterexample to the Stronger Peres Conjecture. *Phys. Rev. Lett.*, 113(5):050404, Aug. 2014. doi: 10.1103/PhysRevLett.113.050404. URL https://link.aps.org/doi/10.1103/PhysRevLett.113.050404. [Cited on page 72.]

[108] T. Vértesi and N. Brunner. Disproving the Peres conjecture by showing Bell nonlocality from bound entanglement. *Nature Communications*, 5:5297, Nov. 2014. ISSN 2041-1723. doi: 10.1038/ncomms6297. URL https://www.nature.com/articles/ncomms6297. [Cited on page 72.]

[109] C. H. Bennett, G. Brassard, and N. D. Mermin. Quantum cryptography without Bell's theorem. *Phys. Rev. Lett.*, 68(5):557–559, Feb. 1992. doi: 10.1103/PhysRevLett.68.557. URL https://link.aps.org/doi/10.1103/PhysRevLett.68.557. [Cited on page 72.]

[110] A. K. Ekert. Quantum cryptography based on Bell's theorem. *Phys. Rev. Lett.*, 67(6):661–663, Aug. 1991. doi: 10.1103/PhysRevLett.67.661. URL https://link.aps.org/doi/10.1103/PhysRevLett.67.661. [Cited on page 72.]

[111] A. Yao and D. Mayers. Quantum Cryptography with Imperfect Apparatus. In *Proceedings 39th Annual Symposium on Foundations of Computer Science (Cat. No.98CB36280)(FOCS)*, page 503, 1998. ISBN 978-0-8186-9172-0. doi: 10.1109/SFCS.1998.743501. URL doi.ieeecomputersociety.org/10.1109/SFCS.1998.743501. [Cited on page 73.]

[112] D. Mayers and A. Yao. Self Testing Quantum Apparatus. *Quantum Info. Comput.*, 4(4):273–286, July 2004. ISSN 1533-7146. URL http://dl.acm.org/citation.cfm?id=2011827.2011830. [Cited on page 73.]

[113] J. Barrett, L. Hardy, and A. Kent. No Signaling and Quantum Key Distribution. *Phys. Rev. Lett.*, 95(1):010503, June 2005. doi: 10.1103/PhysRevLett.95.010503. URL https://link.aps.org/doi/10.1103/PhysRevLett.95.010503. [Cited on page 73.]

[114] A. Acín, N. Gisin, and L. Masanes. From Bell's Theorem to Secure Quantum Key Distribution. *Phys. Rev. Lett.*, 97(12):120405, Sept. 2006. doi: 10.1103/PhysRevLett.97.120405. URL https://link.aps.org/doi/10.1103/PhysRevLett.97.120405. [Cited on page 73.]

[115] S. Pironio, A. Acín, S. Massar, et al. Random numbers certified by Bell's theorem. *Nature*, 464(7291):1021–1024, Apr. 2010. ISSN 1476-4687. doi: 10.1038/nature09008. URL https://www.nature.com/articles/nature09008. [Cited on page 73.]

[116] J. Wilms. Local realism, detection efficiencies, and probability polytopes. *Phys. Rev. A*, 78(3), 2008. doi: 10.1103/PhysRevA.78.032116. [Cited on page 74.]

[117] R. Chaves and J. B. Brask. Feasibility of loophole-free nonlocality tests with a single photon. *Phys. Rev. A*, 84(6):062110, Dec. 2011. doi: 10.1103/PhysRevA.84.062110. URL https://link.aps.org/doi/10.1103/PhysRevA.84.062110. [Cited on pages 75 and 77.]

[118] K. Banaszek and K. Wódkiewicz. Testing Quantum Nonlocality in Phase Space. *Phys. Rev. Lett.*, 82(10):2009–2013, Mar. 1999. doi: 10.1103/PhysRevLett.82.2009. URL https://link.aps.org/doi/10.1103/PhysRevLett.82.2009. [Cited on page 75.]

[119] D. Wilson, H. Jeong, and M. S. Kim. Quantum nonlocality for a mixed entangled coherent state. *Journal of Modern Optics*, 49(5-6):851–864, Apr. 2002. ISSN 0950-0340. doi: 10.1080/09500340110109449. URL https://doi.org/10.1080/09500340110109449. [Cited on page 76.]

[120] A. Laghaout and G. Björk. Feasibility of Bell tests with the W state. *Phys. Rev. A*, 81(3):033823, Mar. 2010. doi: 10.1103/PhysRevA.81.033823. URL https://link.aps.org/doi/10.1103/PhysRevA.81.033823. [Cited on page 77.]

[121] T. Guerreiro, F. Monteiro, A. Martin, et al. Demonstration of Einstein-Podolsky-Rosen Steering Using Single-Photon Path Entanglement and Displacement-Based Detection. *Phys. Rev. Lett.*, 117(7):070404, Aug. 2016. doi: 10.1103/PhysRevLett.117.070404. URL http://link.aps.org/doi/10.1103/PhysRevLett.117.070404. [Cited on page 78.]

[122] J. B. Brask and R. Chaves. Robust nonlocality tests with displacement-based measurements. *Phys. Rev. A*, 86(1):010103, July 2012. doi: 10.1103/PhysRevA.86.010103. URL https://link.aps.org/doi/10.1103/PhysRevA.86.010103. [Cited on page 78.]

[123] B. Vlastakis, A. Petrenko, N. Ofek, et al. Characterizing entanglement of an artificial atom and a cavity cat state with Bell's inequality. *Nature Communications*, 6:8970, Nov. 2015. ISSN 2041-1723. doi: 10.1038/ncomms9970. URL https://www.nature.com/articles/ncomms9970. [Cited on pages 78 and 79.]

[124] Z.-B. Chen, J.-W. Pan, G. Hou, and Y.-D. Zhang. Maximal Violation of Bell's Inequalities for Continuous Variable Systems. *Phys. Rev. Lett.*, 88(4):040406, Jan. 2002. doi: 10.1103/PhysRevLett.88.040406. URL https://link.aps.org/doi/10.1103/PhysRevLett.88.040406. [Cited on page 81.]

[125] R. Filip and L. Mišta. Violation of Bell's inequalities for a two-mode squeezed vacuum state in lossy transmission lines. *Phys. Rev. A*, 66(4):044309, Oct. 2002. doi: 10.1103/PhysRevA.66.044309. URL https://link.aps.org/doi/10.1103/PhysRevA.66.044309. [Cited on pages 81 and 82.]

[126] Y. Z. Law, L. P. Thinh, J.-D. Bancal, and V. Scarani. Quantum randomness extraction for various levels of characterization of the devices. *J. Phys. A: Math. Theor.*, 47 (42):424028, 2014. ISSN 1751-8121. doi: 10.1088/1751-8113/47/42/424028. URL http://stacks.iop.org/1751-8121/47/i=42/a=424028. [Cited on page 83.]

[127] E. Passaro, D. Cavalcanti, P. Skrzypczyk, and A. Acín. Optimal randomness certification in the quantum steering and prepare-and-measure scenarios. *New J. Phys.*, 17(11):113010, 2015. ISSN 1367-2630. doi: 10.1088/1367-2630/17/11/113010. URL http://stacks.iop.org/1367-2630/17/i=11/a=113010. [Cited on page 83.]

[128] G. Tóth, T. Moroder, and O. Gühne. Evaluating Convex Roof Entanglement Measures. *Phys. Rev. Lett.*, 114(16):160501, Apr. 2015. doi: 10.1103/PhysRevLett.114.160501. URL https://link.aps.org/doi/10.1103/PhysRevLett.114.160501. [Cited on page 83.]

[129] D. Cavalcanti, P. Skrzypczyk, G. H. Aguilar, R. V. Nery, P. H. S. Ribeiro, and S. P. Walborn. Detection of entanglement in asymmetric quantum networks and multipartite quantum steering. *Nature Communications*, 6:7941, Aug. 2015. ISSN 2041-1723. doi: 10.1038/ncomms8941. URL https://www.nature.com/articles/ncomms8941. [Cited on page 83.]

[130] W. McCutcheon, A. Pappa, B. A. Bell, et al. Experimental verification of multipartite entanglement in quantum networks. *Nature Communications*, 7:13251, Nov. 2016. ISSN 2041-1723. doi: 10.1038/ncomms13251. URL https://www.nature.com/articles/ncomms13251. [Cited on page 83.]

[131] E. Schrödinger and P. A. M. Dirac. Probability relations between separated systems. *Mathematical Proceedings of the Cambridge Philosophical Society*, 32(03):446, Oct. 1936. ISSN 0305-0041, 1469-8064. doi: 10.1017/S0305004100019137. URL http://www.journals.cambridge.org/abstract_S0305004100019137. [Cited on page 83.]

[132] H. M. Wiseman, S. J. Jones, and A. C. Doherty. Steering, Entanglement, Nonlocality, and the Einstein-Podolsky-Rosen Paradox. *Phys. Rev. Lett.*, 98(14):140402, Apr. 2007. doi: 10.1103/PhysRevLett.98.140402. URL http://link.aps.org/doi/10.1103/PhysRevLett.98.140402. [Cited on page 83.]

[133] D. Cavalcanti and P. Skrzypczyk. Quantum steering: a review with focus on semidefinite programming. *Rep. Prog. Phys.*, 80(2):024001, 2017. ISSN 0034-4885. doi: 10.1088/1361-6633/80/2/024001. URL http://stacks.iop.org/0034-4885/80/i=2/a=024001. [Cited on pages 84, 85, and 88.]

[134] L. Vandenberghe and S. Boyd. Semidefinite Programming. *SIAM Rev.*, 38(1):49–95, Mar. 1996. ISSN 0036-1445. doi: 10.1137/1038003. URL http://epubs.siam.org/doi/abs/10.1137/1038003. [Cited on page 85.]

[135] M. Fuwa, S. Takeda, M. Zwierz, H. M. Wiseman, and A. Furusawa. Experimental proof of nonlocal wavefunction collapse for a single particle using homodyne measurements. *Nature Communications*, 6:6665, Mar. 2015. ISSN 2041-1723. doi: 10.1038/ncomms7665. URL http://www.nature.com/ncomms/2015/150324/ncomms7665/full/ncomms7665.html. [Cited on page 93.]

[136] B. Efron and R. J. Tibshirani. *An Introduction to the Bootstrap*. CRC Press, May 1994. ISBN 978-0-412-04231-7. Google-Books-ID: gLlpIUxRntoC. [Cited on page 94.]

[137] R. Blume-Kohout. Optimal, reliable estimation of quantum states. *New J. Phys.*, 12(4):043034, 2010. ISSN 1367-2630. doi: 10.1088/1367-2630/12/4/043034. URL http://stacks.iop.org/1367-2630/12/i=4/a=043034. [Cited on page 96.]

[138] G. O. Roberts and J. S. Rosenthal. Optimal scaling for various Metropolis-Hastings algorithms. *Statist. Sci.*, 16(4):351–367, Nov. 2001. ISSN 0883-4237, 2168-8745. doi: 10.1214/ss/1015346320. URL http://projecteuclid.org/euclid.ss/1015346320. [Cited on page 97.]

[139] V. Ambegaokar and M. Troyer. Estimating errors reliably in Monte Carlo simulations of the Ehrenfest model. *American Journal of Physics*, 78(2):150–157, Jan. 2010. ISSN 0002-9505. doi: 10.1119/1.3247985. URL http://aapt.scitation.org/doi/abs/10.1119/1.3247985. [Cited on page 102.]

[140] D. Gottesman and I. L. Chuang. Demonstrating the viability of universal quantum computation using teleportation and single-qubit operations. *Nature*, 402(6760):390–393, Nov. 1999. ISSN 0028-0836, 1476-4687. doi: 10.1038/46503. URL http://www.nature.com/articles/46503. [Cited on page 112.]

[141] R. Raussendorf and H. J. Briegel. A One-Way Quantum Computer. *Physical Review Letters*, 86(22):5188–5191, May 2001. ISSN 0031-9007, 1079-7114. doi: 10.1103/PhysRevLett.86.5188. URL https://link.aps.org/doi/10.1103/PhysRevLett.86.5188. [Cited on page 112.]

[142] H.-J. Briegel, W. Dür, J. I. Cirac, and P. Zoller. Quantum Repeaters: The Role of Imperfect Local Operations in Quantum Communication. *Physical Review Letters*, 81(26):5932–5935, Dec. 1998. ISSN 0031-9007, 1079-7114. doi: 10.1103/PhysRevLett.81.5932. URL https://link.aps.org/doi/10.1103/PhysRevLett.81.5932. [Cited on pages 112 and 114.]

[143] M. Żukowski, A. Zeilinger, M. A. Horne, and A. K. Ekert. "Event-ready-detectors" Bell experiment via entanglement swapping. *Phys. Rev. Lett.*, 71(26):4287–4290, Dec. 1993. doi: 10.1103/PhysRevLett.71.4287. URL https://link.aps.org/doi/10.1103/PhysRevLett.71.4287. [Cited on page 114.]

[144] D. Collins, N. Gisin, and H. D. Riedmatten *. Quantum relays for long distance quantum cryptography. *Journal of Modern Optics*, 52(5):735–753, Mar. 2005. ISSN 0950-0340. doi: 10.1080/09500340412331283633. URL https://doi.org/10.1080/09500340412331283633. [Cited on page 114.]

[145] n. Massar and n. Popescu. Optimal extraction of information from finite quantum ensembles. *Phys. Rev. Lett.*, 74(8):1259–1263, Feb. 1995. ISSN 1079-7114. doi: 10.1103/PhysRevLett.74.1259. [Cited on page 115.]

[146] V. Scarani, S. Iblisdir, N. Gisin, and A. Acín. Quantum cloning. *Rev. Mod. Phys.*, 77(4):1225–1256, Nov. 2005. doi: 10.1103/RevModPhys.77.1225. URL https://link.aps.org/doi/10.1103/RevModPhys.77.1225. [Cited on page 115.]

[147] F. Grosshans and P. Grangier. Quantum cloning and teleportation criteria for continuous quantum variables. *Phys. Rev. A*, 64(1):010301, June 2001. doi: 10.1103/PhysRevA.64.010301. URL https://link.aps.org/doi/10.1103/PhysRevA.64.010301. [Cited on page 115.]

[148] D. Cavalcanti, P. Skrzypczyk, and I. Šupić. All entangled states can demonstrate nonclassical teleportation. *arXiv:1607.03249 [quant-ph]*, July 2016. URL http://arxiv.org/abs/1607.03249. arXiv: 1607.03249. [Cited on page 115.]

[149] N. Lütkenhaus, J. Calsamiglia, and K.-A. Suominen. Bell measurements for teleportation. *Phys. Rev. A*, 59(5):3295–3300, May 1999. doi: 10.1103/PhysRevA.59.3295. URL https://link.aps.org/doi/10.1103/PhysRevA.59.3295. [Cited on page 116.]

[150] J. Calsamiglia and N. Lütkenhaus. Maximum efficiency of a linear-optical Bell-state analyzer. *Appl Phys B*, 72(1):67–71, Jan. 2001. ISSN 1432-0649. doi: 10.1007/s003400000484. URL https://doi.org/10.1007/s003400000484. [Cited on page 116.]

[151] H. Jeong, M. S. Kim, and J. Lee. Quantum-information processing for a coherent superposition state via a mixedentangled coherent channel. *Phys. Rev. A*, 64(5):052308, Oct. 2001. doi: 10.1103/PhysRevA.64.052308. URL https://link.aps.org/doi/10.1103/PhysRevA.64.052308. [Cited on pages 116, 117, and 119.]

[152] K. Park, S.-W. Lee, and H. Jeong. Quantum teleportation between particlelike and fieldlike qubits using hybrid entanglement under decoherence effects. *Phys. Rev. A*, 86 (6):062301, Dec. 2012. doi: 10.1103/PhysRevA.86.062301. URL https://link.aps.org/doi/10.1103/PhysRevA.86.062301. [Cited on pages 117, 118, and 119.]

[153] D. Boschi, S. Branca, F. De Martini, L. Hardy, and S. Popescu. Experimental Realization of Teleporting an Unknown Pure Quantum State via Dual Classical and Einstein-Podolsky-Rosen Channels. *Phys. Rev. Lett.*, 80(6):1121–1125, Feb. 1998. doi: 10.1103/PhysRevLett.80.1121. URL https://link.aps.org/doi/10.1103/PhysRevLett.80.1121. [Cited on page 118.]

[154] E. Knill, R. Laflamme, and G. J. Milburn. A scheme for efficient quantum computation with linear optics. *Nature*, 409(6816):46–52, Jan. 2001. ISSN 1476-4687. doi: 10.1038/35051009. URL https://www.nature.com/articles/35051009. [Cited on page 118.]

[155] M. A. Nielsen, E. Knill, and R. Laflamme. Complete quantum teleportation using nuclear magnetic resonance. *Nature*, 396(6706):52–55, Nov. 1998. ISSN 1476-4687. doi: 10.1038/23891. URL https://www.nature.com/articles/23891. [Cited on page 118.]

[156] E. Lombardi, F. Sciarrino, S. Popescu, and F. De Martini. Teleportation of a Vacuum–One-Photon Qubit. *Phys. Rev. Lett.*, 88(7):070402, Jan. 2002. doi: 10.1103/PhysRevLett.88.070402. URL https://link.aps.org/doi/10.1103/PhysRevLett.88.070402. [Cited on page 118.]

[157] S. J. van Enk and O. Hirota. Entangled coherent states: Teleportation and decoherence. *Phys. Rev. A*, 64(2):022313, July 2001. doi: 10.1103/PhysRevA.64.022313. URL https://link.aps.org/doi/10.1103/PhysRevA.64.022313. [Cited on page 118.]

[158] J. S. Neergaard-Nielsen, Y. Eto, C.-W. Lee, H. Jeong, and M. Sasaki. Quantum tele-amplification with a continuous-variable superposition state. *Nature Photonics*, 7(6): 439–443, June 2013. ISSN 1749-4893. doi: 10.1038/nphoton.2013.101. URL https://www.nature.com/articles/nphoton.2013.101. [Cited on page 118.]

[159] X.-S. Ma, T. Herbst, T. Scheidl, et al. Quantum teleportation over 143 kilometres using active feed-forward. *Nature*, 489(7415):269–273, Sept. 2012. ISSN 1476-4687. doi: 10.1038/nature11472. URL https://www.nature.com/articles/nature11472. [Cited on page 118.]

[160] H. Jeong, S. Bae, and S. Choi. Quantum teleportation between a single-rail single-photon qubit and a coherent-state qubit using hybrid entanglement under decoherence effects. *Quantum Inf Process*, 15(2):913–927, Feb. 2016. ISSN 1573-1332. doi: 10.1007/s11128-015-1191-x. URL https://doi.org/10.1007/s11128-015-1191-x. [Cited on page 119.]

[161] A. E. Ulanov, D. Sychev, A. A. Pushkina, I. A. Fedorov, and A. I. Lvovsky. Quantum Teleportation Between Discrete and Continuous Encodings of an Optical Qubit. *Phys. Rev. Lett.*, 118(16):160501, Apr. 2017. doi: 10.1103/PhysRevLett.118.160501. URL https://link.aps.org/doi/10.1103/PhysRevLett.118.160501. [Cited on pages 119, 127, and 142.]

[162] D. V. Sychev, A. E. Ulanov, E. S. Tiunov, A. A. Pushkina, A. Kuzhamuratov, V. Novikov, and A. I. Lvovsky. Entanglement and teleportation between polarization and wave-like encodings of an optical qubit. *Nature Communications*, 9(1): 3672, Sept. 2018. ISSN 2041-1723. doi: 10.1038/s41467-018-06055-x. URL https://www.nature.com/articles/s41467-018-06055-x. [Cited on pages 119 and 127.]

[163] L.-M. Duan, M. D. Lukin, J. I. Cirac, and P. Zoller. Long-distance quantum communication with atomic ensembles and linear optics. *Nature*, 414(6862):413–418, Nov. 2001. ISSN 1476-4687. doi: 10.1038/35106500. URL https://www.nature.com/articles/35106500. [Cited on page 130.]

[164] M. Bouillard, G. Boucher, J. F. Ortas, B. Pointard, and R. Tualle-Brouri. Quantum storage of single-photon and two-photon Fock states with an all-optical quantum memory. *arXiv:1810.07419 [quant-ph]*, Oct. 2018. URL http://arxiv.org/abs/1810.07419. arXiv: 1810.07419. [Cited on pages 137 and 143.]

[165] S. Takeda, K. Takase, and A. Furusawa. On-demand photonic entanglement synthesizer. *arXiv:1811.10704 [quant-ph]*, Nov. 2018. URL http://arxiv.org/abs/1811.10704. arXiv: 1811.10704. [Cited on pages 137 and 143.]

[166] T. W. Hansch and B. Couillaud. Laser frequency stabilization by polarization spectroscopy of a reflecting reference cavity. *Optics Communications*, 35(3):441–444, Dec. 1980. ISSN 0030-4018. doi: 10.1016/0030-4018(80)90069-3. URL http://www.sciencedirect.com/science/article/pii/0030401880900693. [Cited on page 143.]

[167] H. Kwon and H. Jeong. Generation of hybrid entanglement between a single-photon polarization qubit and a coherent state. *Physical Review A*, 91(1), Jan. 2015. ISSN 1050-2947, 1094-1622. doi: 10.1103/PhysRevA.91.012340. URL https://link.aps.org/doi/10.1103/PhysRevA.91.012340. [Cited on page 156.]

[168] J. F. Fitzsimons and E. Kashefi. Unconditionally verifiable blind computation. *arXiv:1203.5217 [quant-ph]*, Mar. 2012. URL `http://arxiv.org/abs/1203.5217`. arXiv: 1203.5217. [Cited on page 156.]

[169] S. Barz, J. F. Fitzsimons, E. Kashefi, and P. Walther. Experimental verification of quantum computation. *Nat Phys*, 9(11):727–731, Nov. 2013. ISSN 1745-2473. doi: 10.1038/nphys2763. URL `http://www.nature.com/nphys/journal/v9/n11/abs/nphys2763.html`. [Cited on page 156.]

Adrien Cavaillès **14 février 2019**

Sujet : Tests de non-localité et protocoles de communication quantique utilisant l'intrication hybride optique

Résumé : Cette thèse est centrée sur la réalisation de protocoles d'information quantique utilisant conjointement les approches à variables discrètes et à variables continues de l'information quantique optique. Nous détaillons tout d'abord les protocoles utilisés pour la génération d'états hautement non classiques tels que les photons uniques, les chats de Schrödinger optiques et enfin l'intrication hybride entre variables discrètes et continues. Nous évaluons le potentiel de cette resource innovante en détaillant son utilisation dans un certain nombre de protocoles. Nous commençons par envisager la réalisation de tests de Bell utilisant l'intrication hybride et rapportons l'observation experimentale d'une violation d'inégalité de Steering, pour la première fois dans un contexte hybride. Enfin, nous détaillons l'état d'avancement de l'installation d'une nouvelle expérience de téléportation quantique entre variables discrètes et variables continues. Nos résultats prouvent l'intérêt de suivre une approche hybride et permettent d'envisager la réalisation de réseaux d'information quantique hybrides liant des systèmes de différentes natures.

Mots clés : Optique quantique, information quantique hybride, chats de Schrödinger, photon unique, intrication, téléportation quantique, tests de non-localité

Subject : Non-locality tests and quantum communication protocols using hybrid entanglement of light

Abstract: There are two traditionally-separated approaches to optical quantum information: the continuous- and discrete-variable strategies respectively linked to the wave-like and particle-like nature of light. This thesis work is focused on the novel hybrid approach aiming to join the capabilities of both strategies into single systems. Using hybrid methods, we report on the use of optical parametric oscillators and superconducting-nanowire single-photon detectors to generate highly non-classical non-Gaussian states such as high-purity single-photons, Schrödinger cat states and finally hybrid entanglement of light between continuous- and discrete-variable encoding. The potential of this resource is studied in a number of protocols. We first consider non-locality tests with hybrid entanglement such as Bell inequality violation and experimentally demonstrate the violation of Einstein-Podolsky-Rosen steering inequalities. We finally report on the progress made towards the implementation of a new setup for the demonstration of hybrid quantum teleportation between continuous and discrete-variable encodings. Our demonstrations prove the versatility of this hybrid resource and open the possibility of implementing scalable quantum networks linking systems of dissimilar nature.

Keywords : Quantum optics, hybrid quantum information, Schrödinger cat states, photon, entanglement, quantum teleportation, non-locality tests